LEABHARLANN CHOLÁISTE NA TRÍONÓIDE, BAILE ÁTHA CLIATH | TRINITY COLLEGE LIBRARY DUBLIN
Ollscoil Átha Cliath | The University of Dublin

Terms and Conditions of Use of Digitised Theses from Trinity College Library Dublin

Copyright statement

All material supplied by Trinity College Library is protected by copyright (under the Copyright and Related Rights Act, 2000 as amended) and other relevant Intellectual Property Rights. By accessing and using a Digitised Thesis from Trinity College Library you acknowledge that all Intellectual Property Rights in any Works supplied are the sole and exclusive property of the copyright and/or other IPR holder. Specific copyright holders may not be explicitly identified. Use of materials from other sources within a thesis should not be construed as a claim over them.

A non-exclusive, non-transferable licence is hereby granted to those using or reproducing, in whole or in part, the material for valid purposes, providing the copyright owners are acknowledged using the normal conventions. Where specific permission to use material is required, this is identified and such permission must be sought from the copyright holder or agency cited.

Liability statement

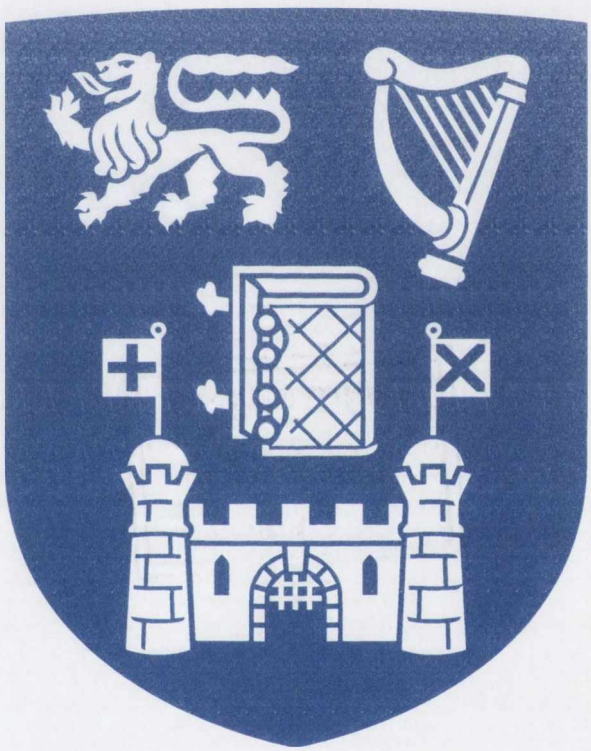
By using a Digitised Thesis, I accept that Trinity College Dublin bears no legal responsibility for the accuracy, legality or comprehensiveness of materials contained within the thesis, and that Trinity College Dublin accepts no liability for indirect, consequential, or incidental, damages or losses arising from use of the thesis for whatever reason. Information located in a thesis may be subject to specific use constraints, details of which may not be explicitly described. It is the responsibility of potential and actual users to be aware of such constraints and to abide by them. By making use of material from a digitised thesis, you accept these copyright and disclaimer provisions. Where it is brought to the attention of Trinity College Library that there may be a breach of copyright or other restraint, it is the policy to withdraw or take down access to a thesis while the issue is being resolved.

Access Agreement

By using a Digitised Thesis from Trinity College Library you are bound by the following Terms & Conditions. Please read them carefully.

I have read and I understand the following statement: All material supplied via a Digitised Thesis from Trinity College Library is protected by copyright and other intellectual property rights, and duplication or sale of all or part of any of a thesis is not permitted, except that material may be duplicated by you for your research use or for educational purposes in electronic or print form providing the copyright owners are acknowledged using the normal conventions. You must obtain permission for any other use. Electronic or print copies may not be offered, whether for sale or otherwise to anyone. This copy has been supplied on the understanding that it is copyright material and that no quotation from the thesis may be published without proper acknowledgement.

STATIC AND DYNAMIC MAGNETIC INTERACTIONS IN GRAPHENE AND RELATED MATERIALS.



John M. Duffy

A THESIS SUBMITTED FOR THE DEGREE OF
DOCTOR OF PHILOSOPHY

SCHOOL OF PHYSICS
TRINITY COLLEGE DUBLIN

2015

TRINITY LIBRARY
27 JUL 2016
DUBLIN
Thesis 10964

DECLARATION

I, John Michael Duffy, hereby declare: This thesis has not been submitted as an exercise for a degree at this or any other university; That it comprises work performed entirely by myself during the course of my Ph.D. studies at Trinity College Dublin; That I was involved in a number of collaborations, and where it is appropriate my collaborators are acknowledged for their contributions.

A copy of this thesis may be lended or copied by the Trinity College Library upon request by a third party provided it spans single copies made for study purposes only, subject to normal conditions of acknowledgement.

The crime that is inherent in us we do unto ourselves.

— J. M. Coetzee

ABSTRACT

Since its discovery in 2004, graphene has been the recipient of both intense research and media attention. Graphene's properties reads as a list of superlatives, and its applications are vast and diverse. However, in this thesis, we are most interested in its potential role in spintronics. Spintronics, the field that attempts to exploit the spin of the electron in solid state devices, emerged with the discovery of giant magnetoresistance in 1985 and has since enjoyed much commercial and fundamental success. One of the central challenges in the field is transporting electron spin coherently over device-sized distances, and it is here that graphene is expected to be useful. With its low spin-orbit and hyperfine interactions, spin waves suffer little dissipation in graphene, and hence it seems an ideal material for spintronics. However, graphene is non-magnetic, and hence any magnetic interactions must be created by adding impurities or exploiting defects. Furthermore, since it has only been discovered very recently, the fundamental properties of graphene are still under investigation.

There are a number of different mechanisms of magnetic alignment in graphene, but perhaps the most important is the indirect exchange coupling, whereby the itinerant electrons of the host mediate an interaction between magnetic moments. The indirect exchange coupling displays unique properties in graphene, and hence has been intensively studied. However, its behaviour in proximity to graphene's edges has received little attention, and this forms the core element of this thesis.

In order to examine this quantity, we utilise Green's functions, which prove a natural tool for investigating these effects. This allows us to examine the coupling in both semi-infinite graphene and graphene nanoribbons, and compare the results from both. We then show how our approach can be extended to more extended impurities, examining the effect of infinite lines of impurities in bulk graphene. In

later chapters, we move aways from static interactions entirely, and show how our approach can be modified to account for time dependent magnetic perturbations. Finally, we use the results of our thesis to motivate the study of the effect of impurities on the conductance. In doing so, we demonstrate the broad generality of our work, and how it might be extended to many different areas.

In this work, we constantly emphasise the importance of mathematical transparency and analysis. In our group we have developed a method of analytically approximating the Green's function, and this is used to extract strong general results from numerical findings. Furthermore, we pay great attention to the local density of states, and demonstrate its predictive power in many of the effects that we examine.

PUBLICATIONS

Publications resulting, and in preparation, from this work:

- **J. M. Duffy**, F.S.M. Guimaraes, A.T. Costa Jr, R.B. Muniz and M.S. Ferreira
  Dynamic RKKY Interaction between magnetic moments in edged-graphene
  In preparation.

- **J. M. Duffy**, J.A. Lawlor, C.H. Lewenkopf, and M. S. Ferreira
  Impurity conformation and conductance in graphene nanoribbons
  In preparation.

- P. D. Gorman, **J. M. Duffy**, S. R. Power, and M. S. Ferreira
  Strain-Modified RKKY Interaction in Carbon Nanotubes
  Physical Review B 92, 035411, 2015

- P. D. Gorman, **J. M. Duffy**, S. R. Power, and M. S. Ferreira
  RKKY Interaction Between Extended Magnetic Defect Lines in Graphene
  Physical Review B, 90, 125411, 2014.

- **J. M. Duffy**, P. D. Gorman, S. R. Power, and M. S. Ferreira
  Variable Range of the RKKY Interaction in Edged Graphene
  Journal of Physics: Condensed Matter, 26, 055007, 2014.

- P. D. Gorman, **J. M. Duffy**, M. S. Ferreira, and S. R. Power
  RKKY Interaction Between Adsorbed Magnetic Impurities in Graphene: Symmetry and Strain Effects
  Physical Review B, 88, 085405, 2013.

- S. R. Power, P. D. Gorman, **J. M. Duffy**, and M. S. Ferreira
  Strain-Induced Modulation of Magnetic Interactions in Graphene
  Physical Review B, 86, 195423, 2012.

ACKNOWLEDGEMENTS

I couldn't have done this without a lot of help. So now I'm going to thank it.

I'd like to acknowledge financial support from the Programme for Research in Third Level Institutions (PRTLI) under the HEA funding body as well as Science Foundation Ireland under Grant no. SFI 11/RFP.1/MTR/3083. I would also like to extend my gratitude to the School of Physics.

I'd like to thank Mauro for his (too?) lenient supervisory role. I'd like to thank my group and others who helped me including Stephen, James, Carlos, Claudia, Filipe, Antonio, Bechara, Tom and Colin. Particular thanks go to Paul and Eric, for making me even louder and more obnoxious than I was to begin with. Brendan and Kyle get a shout out too for lunches in the early years. I'd like to thank my family for their unwavering support, and I'd like to thank Judith, who was here for this all. I'm sure there are many that I've forgotten. I'm sorry.

I always imagined my acknowledgements would be full of lots of ribald humour and politically incorrect shtick. But unfortunately the writing of this thesis has coincided with a terrible period in my life, and I find myself lacking the stomach for it. Maybe that's for the best. Here is what I did.

CONTENTS

List of Figures xiv

Acronyms xvii

1 INTRODUCTION 1

1.1 Graphene . . . 2

1.1.1 Nanoribbons . . . 7

1.2 Spintronics . . . 9

1.3 Magnetism and the Indirect Exchange Coupling . . . 13

1.4 Conductance . . . 19

1.5 Thesis structure . . . 21

1.6 Parameters, Notation and Conventions . . . 23

2 MATHEMATICAL METHODS 25

2.1 Green's Functions . . . 25

2.1.1 The Local Density of States . . . 26

2.2 Dyson's equation . . . 27

2.3 Perturbations . . . 28

2.3.1 Substitutional . . . 29

2.3.2 Top adsorbed . . . 30

2.3.3 Center Adsorbed . . . 32

2.4 Recursive Methods . . . 32

2.4.1 The Rubio Sancho Method . . . 37

2.5 The Lloyd Formula . . . 39

2.6 Integrating over GFs . . . 41

2.7 Electron-Electron Interactions . . . 44

2.7.1 The Hartree Fock Approximation . . . 45

2.8 Chapter Summary . . . 48

3 GREEN'S FUNCTIONS 49
3.1 Graphene . . . 49
3.1.1 Band structure . . . 51
3.1.2 Green's functions . . . 52
3.1.3 Contour Integration . . . 56
3.1.4 The Stationary Phase Approximation . . . 58
3.2 Semi-Infinite Graphene . . . 61
3.2.1 Linear combination method . . . 61
3.2.2 Image method . . . 62
3.2.3 The SPA . . . 67
3.3 Nanoribbons . . . 68
3.3.1 Analytic . . . 69
3.3.2 Recursive . . . 70
3.4 Chapter Summary . . . 74
4 THE INDIRECT EXCHANGE COUPLING 76
4.1 Derivation . . . 78
4.1.1 The RKKY Coupling . . . 81
4.2 Graphene . . . 85
4.2.1 Substitutional Impurities . . . 85
4.2.2 Top-Adsorbed Impurities . . . 89
4.2.3 Center-Adsorbed Impurities . . . 89
4.3 Semi-Infinite Graphene . . . 94
4.4 Armchair Nanoribbons . . . 97
4.4.1 Analytic calculations . . . 98
4.5 Chapter Summary . . . 100
5 LINES OF IMPURITIES 102
5.1 The Green's Function . . . 104
5.2 The Perturbation . . . 105
5.3 The Indirect Exchange Coupling . . . 107

5.4 Numerical Results . . . 109
5.5 Analytical Results . . . 111
5.5.1 The SPA . . . 112
5.5.2 The Analytic Coupling . . . 114
5.6 The Finite Line of Impurities . . . 115
5.7 Chapter Summary . . . 117
6 THE DYNAMIC INTERACTION 118
6.1 The Spin Susceptibility . . . 120
6.2 Single Impurities . . . 126
6.3 Two Impurities . . . 128
6.4 3 or more impurities . . . 131
6.5 Chapter Summary . . . 132
7 THE CONDUCTANCE OF NANORIBBONS 136
7.1 The Kubo Formula . . . 139
7.2 The Conductance . . . 140
7.3 Configurational Averages . . . 143
7.4 An analytic approach . . . 148
7.5 Chapter Summary . . . 151
8 CONCLUSIONS 153
8.1 Future Work . . . 157

I APPENDIX 159
A DERIVATIONS 160
A.1 The Graphene Brillouin Zone . . . 160
A.2 Finding a contour . . . 162
A.2.1 Example: ZigZag Integration . . . 166
A.2.2 Armchair Integration . . . 167
B DETAILS 169
B.1 Block Matrix Inverse . . . 169

B.2 The Stationary Phase Approximation 171

B.3 Conjugate of the GF 172

BIBLIOGRAPHY 175

LIST OF FIGURES

Figure 1.1 A schematic representation of graphene. 3
Figure 1.2 Carbon in low dimensions 4
Figure 1.3 The bandstructure of graphene 6
Figure 1.4 Graphene nanoribbons 8
Figure 1.5 An illustration of a GMR stack 12
Figure 1.6 Schematic of Quantum Well Theory 15
Figure 2.1 A schematic of the different types of impurity 29
Figure 2.2 A system with two top-adsorbed impurities 31
Figure 2.3 An illustration of the recursive method 33
Figure 2.4 How to obtain off-diagonal elements recursively 35
Figure 2.5 Schematic of the Rubio Sancho method 37
Figure 2.6 A schematic of the integration contour. 42
Figure 2.7 A plot of the spin-split LDOS in the presence of an appropriate impurity. 47
Figure 3.1 A schematic of our graphene system 50
Figure 3.2 The graphene band structure 53
Figure 3.3 The LDOS of a graphene site 55
Figure 3.4 Plots the numerically calculated GF against its SPA equivalent. 60
Figure 3.5 Plots of the real parts of the numerically calculated GF against its SPA equivalent. 63
Figure 3.6 An illustration of the image method 65
Figure 3.7 The LDOS for SI graphene 66
Figure 3.8 SPA comparison for the SI GF. 67
Figure 3.9 An illustration of the graphene nanoribbon 68
Figure 3.10 The LDOS in metallic graphene nanoribbons. 71

Figure 3.11 The LDOS at $E_F = 0$ vs position in a GNR. 71
Figure 3.12 The DOS of a semiconducting graphene nanoribbons. 72
Figure 3.13 An illustration of different armchair nanoribbons 73
Figure 3.14 Impuritiy labelling in the armchair nanoribbon 75
Figure 4.1 A schematic demonstrating the potential of magnetic impurities as seen by electrons 79
Figure 4.2 A plot of the IEC in Bulk Graphene 86
Figure 4.3 A log-log plot of the IEC in Bulk Graphene 87
Figure 4.4 A plot of the IEC for at finite E_F 87
Figure 4.5 A plot of the IEC in Bulk Graphene, for top-adsorbed impurities 90
Figure 4.6 A plot of the IEC for a center-adsorbed impurity 91
Figure 4.7 The LDOS for a center adsorbed impurity in bulk graphene. . 92
Figure 4.8 A plot of the gamma term vs its SPA approximation 94
Figure 4.9 A plot of the IEC for SI graphene 95
Figure 4.10 The decay rate of the IEC in SI graphene. 96
Figure 4.11 A plot of the IEC in a AGNR 98
Figure 4.12 A plot of the IEC in a semiconducting AGNR 99
Figure 5.1 An illustration of an infinite line of impurities 106
Figure 5.2 A plot of the IEC for infinite lines of impurities 110
Figure 5.3 Log-log of the IEC for infinite lines of impurities 111
Figure 5.4 The IEC between infinite lines of impurities at non-zero E_F . . 112
Figure 5.5 A log-log plot of the IEC between infinite lines of impurities at non-zero E_F 113
Figure 5.6 The IEC between finite vs infinite lines of impurities 116
Figure 6.1 A schematic of our dynamic system 120
Figure 6.2 An illustration of a precessing magnetic moment. 121
Figure 6.3 A plot of the spin susceptibility for single impurities 127
Figure 6.4 The FWHM of the spin susceptibility for single impurities . . 128

Figure 6.5 A plot of χ_{00} against ω for non-VLDOS sites 130
Figure 6.6 A plot of FWHM against separation for the dynamic interaction between two impurities. 131
Figure 6.7 A plot of χ_{00} against ω for a single VLDOS site 132
Figure 6.8 A plot of FWHM against separation for the dynamic interaction between two impurities. 133
Figure 6.9 A plot of χ_{00} against ω for 3 impurities 134
Figure 6.10 A comparison of χ_{00} against ω for 3 and 2 impurities 135
Figure 7.1 A schematic of the RKKY scattering 137
Figure 7.2 A schematic of a nanoribbon with a scattering region 138
Figure 7.3 A plot of the conductance for pristine armchair nanoribbons. . 141
Figure 7.4 A plot of the conductance for substitutional impurities in a ribbon. 142
Figure 7.5 A plot of conductance for substitutional impurities vs position. 143
Figure 7.6 Comparison of the conductance for various kinds of impurity 144
Figure 7.7 An illustration of the configurational average 145
Figure 7.8 Configurational average of the conductance for various kinds of impurity 146
Figure 7.9 Random configurational average of the conductance for various kinds of impurity 147
Figure 7.10 Total configuration average vs concentration 148
Figure 7.11 Random configurational average vs concentration 149
Figure A.1 The graphene Brillouin zone 161
Figure A.2 Two areas equivalent to the Brillouin zone. 162
Figure A.3 The integration contour we use. 164
Figure B.1 A schematic of the stationary phase approximation. 173

COMMON ACRONYMS

GF Green's Function

IEC Indirect Exchange Coupling

LDOS Local Density of States

SI Semi-Infinite

AGNR Armchair graphene nanoribbon

ZGNR Zigzag graphene nanoribbon

SPA Stationary Phase Approximation

RKKY Ruderman-Kittel-Kasuya-Yosida

HF Hartree-Fock

RPA Random Phase Approximation

FWHM Full Width at Half Maximum

DFT Density Functional Theory

FM Ferromagnetic

AFM Antiferromagnetic

GMR Giant Magnetoresistance

MRAM Magnetoresistive Random Access Memory

STTRAM Spin Transfer Torque Random Access Memory

CMOS Complementary Metal-Oxide-Semiconductor

CVD Chemical Vapor Deposition

QED Quantum Electrodynamics

TEM Transmission Electron Microscopy

DNA Deoxyribonucleic acid

SPA Stationary Phase Approximation

1

INTRODUCTION

Physics, the most fundamental of the sciences, is inevitably focused on the very small. From a materials perspective, this is best represented by the field of nanoscience. The origin of nanoscience is often traced back to Richard Feynman's 1959 lecture "There's plenty of room at the bottom" [1]. Here Feynman discussed the possibility of manipulating matter on a small scale with the goals of information storage and computation, and described how the changing size range would influence the importance of the forces involved as gravity wanes and surface tension waxes. However, modern cultural anthropologists dispute this claim, and instead cite K. Eric Drexler's publication of "Engines of Creation: the coming era of nanotechnology" [2] as being responsible for popularising the field. Drexler's sometimes hyperbolic prose stoked commercial interest, and the field was buoyed by the simultaneous development of scanning tunnelling microscopy, which allows both imaging and manipulation of individual atoms [3]. However, the challenge of engineering devices on a quantum scale has proved appropriately tough, and hence the field shifted slightly from an application oriented approach, to a more fundamentally interested one.

Nanoscience has grown into a huge field today, and is accorded significant levels of both government and industry funding. The applications of the technology have been immense and are seen in fields as diverse as medicine and fundamental physics. As of the time of writing "The Project on Emerging Nanotechnologies" lists 1825 nano enabled consumer products [4]. The interest is heightened by problems in the world of computing, where integrated circuits have started to grapple with the kinds of quantum problems encountered at the nanoscale. All of this

serves to make nanotechnology an interesting area of research, and nanomaterials of great theoretical and practical importance.

Of all of the nanomaterials discovered, few have received as much attention as graphene. Graphene occupies an enviable place in the scientific spectrum, enjoying a wealth of properties that are both interesting from a fundamental and commercial perspective. It is graphene and its various forms that we examine in this thesis, and we introduce it in detail in the next section.

1.1 GRAPHENE

Graphene is just another word for a single layer of graphite (Fig.1.1). Graphene is a 2d material, with a hexagonal honeycomb lattice. The lattice can be formed by two interpenetrating triangular sublattices. Graphene is held together by incredibly strong in-plane σ bonds, with most of its electrical properties stemming from the out of plane π bonds. When stacked to form graphite, the individual planes of graphene interact via weak Van-der-Waals forces, which are easily broken to create graphite flakes (such as when a pencil is used). The existence of a flake consisting of just a single layer was long purported, however, isolation proved extremely challenging, and for a time was thought impossible. As early as 1962 Boehm examined ultra-thin carbon, noting that some of the flakes may have been as thin as a single layer [5], but lacking the technological nouse to prove it. In 1994 graphene was officially named [6] as a theoretical material, when its zero and one dimensional kin, buckyballs and nanotubes, had already been discovered (Fig.1.2). At this stage it was generally believed that graphene would remain a theoretical material, as calculations demonstrated the material to be thermodynamically unstable [7]. It would be 10 more years before Geim and Novoselov managed to isolate a sizeable enough flake (around $1\mu m$) to allow the graphene to be contacted and characterised [8]. Their success hinged on the brilliant realisation that a silicon substrate of a very

specific width (about 300nm) would render graphene visible. This discovery would win them a Nobel Prize, and precipitate a research goldrush which is still ongoing.

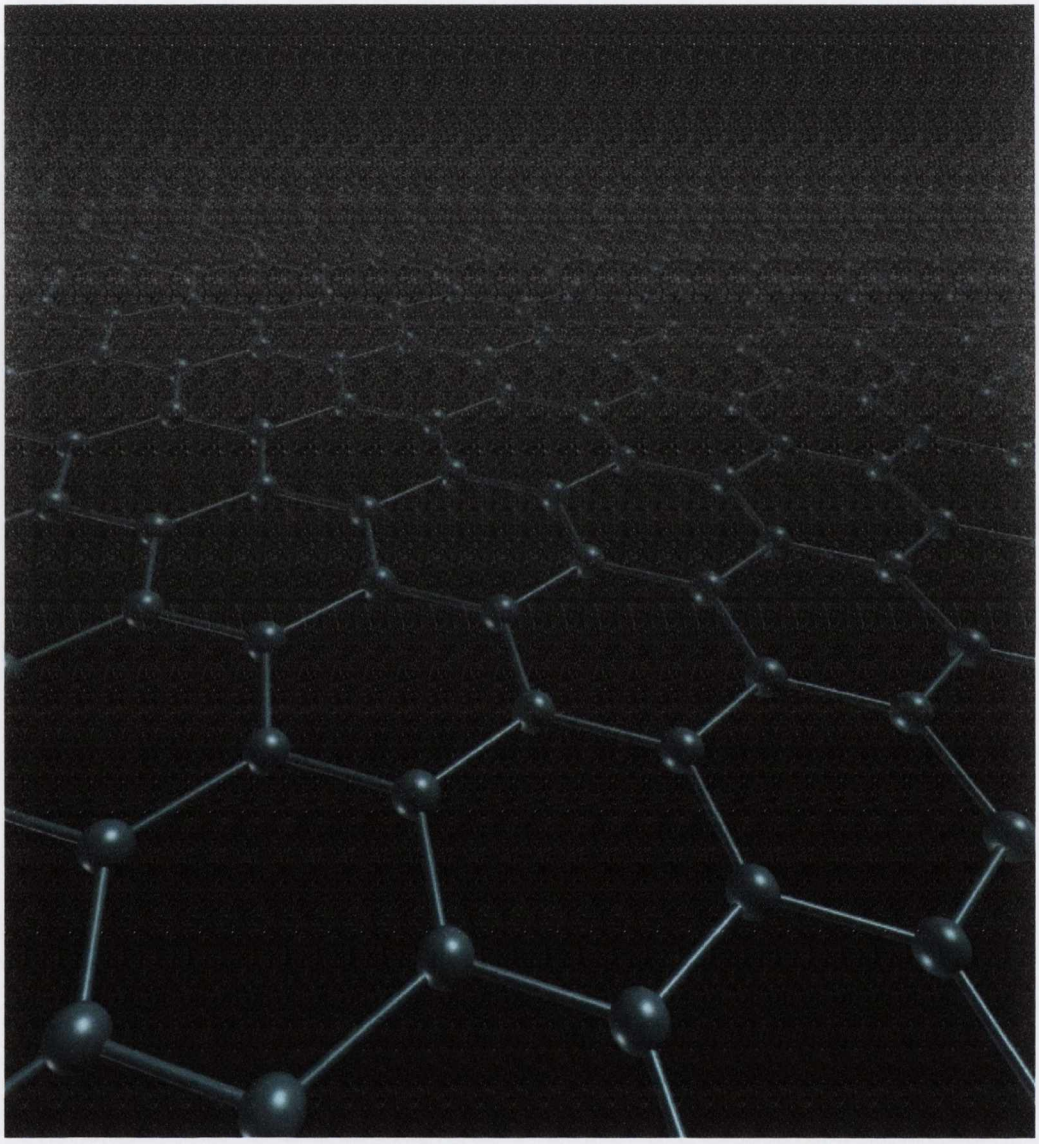


Figure 1.1: A schematic representation of graphene.

Geim and Novelsov isolated graphene by the repeated application of adhesive tape to a thin flake of graphite. The method was officially known as mechanical exfoliation, but became affectionately dubbed the "Scotch-Tape Method". Despite its apparently crudeness, the method actually remained the industry standard for

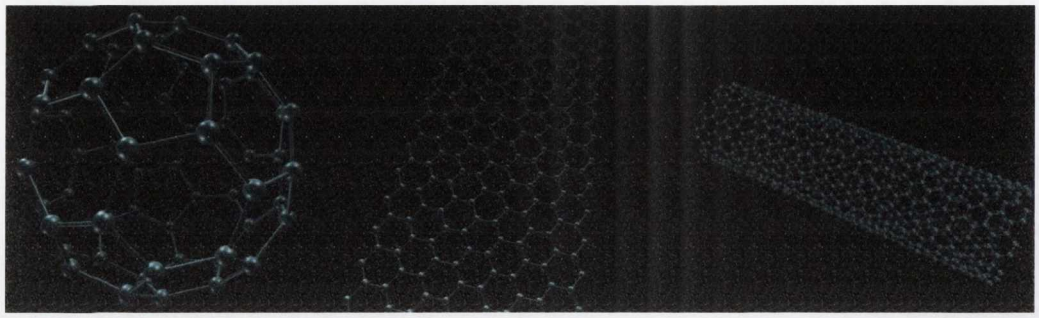


Figure 1.2: Carbon in low dimensions. From left to right we have a buckyball, a nanoribbon and a nanotube.

quite a while. However, intense research and industrial interest quickly produced a number of alternative routes to atomically thin carbon [9–16]. Among these are electrochemical exfoliation [9], molten salt corrosion [10], hydrothermal self-assembly [11] and the unzipping of carbon nanotubes [12].

Given the incredibly active state of research on graphene it is unsurprising that the standard of production is rapidly changing. For instance, where purity and electron mobility are considered, chemical vapour deposition (CVD) produces the best quality graphene [17–20]. Dramatic progress has been made recently in the speed at which the usually slow CVD process can be achieved, with Boyd *et. al.* reporting complete deposition in a single step [19]. Samsung have pushed the envelope on this technique with respect to size, reporting the growth of a full wafer of single crystal graphene [20]. Furthermore, the production of large graphene based samples for industry use is rapidly improving. A recent paper shows the production of large graphene laminates and fibres that demonstrate good mechanical and conductive properties [21]. And in Trinity College Dublin Paton *et. al.* have demonstrated the production of few-layer graphene in a household blender [22].

Graphene's already remarkable two dimensionality is complemented by a range of properties that distinguish it as a paragon of interest in the world of materials science. Among the list of its superlatives are its unparalleled mechanical strength [23], its electrical conductivity, and its thermal conductivity [24]. However, most

of the fundamental interest in graphene and much of the "buzz" stems from its unusual electronic structure. The bandstructure is shown in Fig.1.3, from which we can see the hexagonal structure of the Brillouin zone. However, more important are the points at the edge of the Brillouin zone, where the conduction and valence bands touch. These points are known as Dirac points, and the bandstructure is linear in this region (as also seen in the figure). Materials where the conduction and valence bands just touch are semi-metals, which can be alternately described as a metal with a vanishing Fermi surface, or a semiconductor with no gap. This means that graphene has a pronounced ambipolar electric field effect, meaning that its charge carriers may be continuously tuned between electrons and holes by means of an applied electric field [25]. Furthermore, electrons in the vicinity of the Dirac point are more easily described using the massless Dirac equation rather than the Schrodinger equation and hence mimic relativistic particles with an effective velocity of light $v_F \approx 10^6 m/s$ [25]. Part of the excitement arising from the discovery of graphene was the ability to probe the properties of QED outside of relativistic scenarios[26, 27].

The hullabaloo stemming from the discovery of graphene has led to proposals for its use in almost every conceivable technological area. Even the more sober predictions for the potential applications of graphene are incredibly broad, covering areas like filtration, lightweight composite materials and energy storage [24, 25, 28–30]. Indeed, graphene's atomic thinness and mechanical strength alone have lead to early application in the TEM of biomolecules [31], and its transparency, strength and conductivity makes it a leading candidate for transparent flexible displays. Graphene's unique optical properties make it a favourite for optical electronic devices and transistors [17]. Furthermore, graphene has been instrumental in the development of valleytronics, a recent field which attempts to harnass electron momentum for the manipulation of information [32]. Finally, some of graphene's most important contributions have been predicted to come in the areas of spintronics and sensors, areas which we will explore in greater depth later in this introduction.

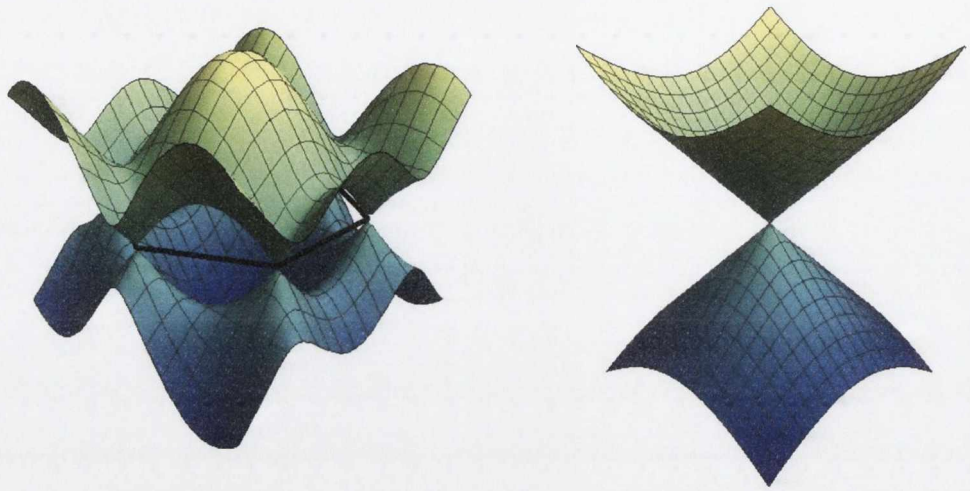


Figure 1.3: Two plots highlighting the bandstructure of graphene. On the left we show a plot of the bandstructure over the entire Brillouin zone (shown by the black hexagon), the hexagonal structure is obvious. On the right we examine a point at the edge of the Brillouin zone (one of the Dirac points), where the bandstructure can be approximated entirely linearly.

Although normally referred to as a two-dimensional crystal, graphene can also be seen as a giant organic molecule and can undergo a range of chemical reactions. Graphene can be reacted with fluorine to get fluorographene [33], or with hydrogen to get graphane [34, 35]. Furthermore, ab-initio calculations show that it may be stable in different phases, such as graphyne [36]. The progress made with graphene has led researchers to examine the possibility of other two-dimensional materials such as silicene [37, 38] and hexagonal boron nitride [39, 40]. The existence of other two-dimensional materials allows for the generation of heterostructures, formed by overlapping single-layer materials. One heterostructure that has been well studied involves stacking layers of graphene and boron nitride [41]. Given that boron nitride is insulating and graphene conducting, this allows for tuning of the coupling between layers.

It would be remiss of us to finish this section without talking about bilayer graphene, which is also explored in Geim and Novoselov's seminal 2004 paper [8]. The properties of bilayer graphene are distinct enough from its monolayer

or 3d relations that it can be viewed as a new material in its own right. Bilayer graphene has a parabolic gapless spectrum, describing chiral massive particles and leading to a host of interesting effects [42–44]. Although graphene can be reacted with various compounds to achieve different ends, one can observe entirely new properties simply by cutting it in the right direction, as we will see in the next section.

1.1.1 *Nanoribbons*

Many of graphene's local properties (e.g. transport, magnetic and mechanical) are drastically modified near the termination of the graphene lattice [45–52]. As such, edged graphene is an interesting material to study in its own right. Graphene nanoribbons (GNRs) consist of thin strips of graphene typically on the order of less than 50nm wide. They are usually examined with fixed edge orientations, armchair or zigzag edges being the most popular (Fig.1.4). Both orientations were examined theoretically by Misutaka Fujita in 1996 [53], who remarked on the appearance of a localised state at the zigzag edge. Nanoribbons can be patterned in bulk via nanotomy, which involves cutting graphite into nano-blocks with a diamond knife, and then exfoliating it. They may also be obtained from carbon nanotubes, either by cutting or unzipping [54]. Furthermore, extremely thin nanoribbons can be produced by narrowing existing ones by chemical etching [55].

Nanoribbons possess many of the same physical characteristics of graphene, and are given unique advantages by their size. As with graphene there are a wealth of potential applications for GNRs. Their high thermal and electrical conductivities make them an attractive candidate to replace copper in integrated circuit interconnects, and their semi-conducting properties allow them to be seen as an alternative to silicon semiconductors. They can be used to reinforce polymer nanocomposities for the clinical treatment of bone defects [56], or as contrast agents for photoacoustic and thermoacoustic tomography [57]. Finally, there are a number of proposals

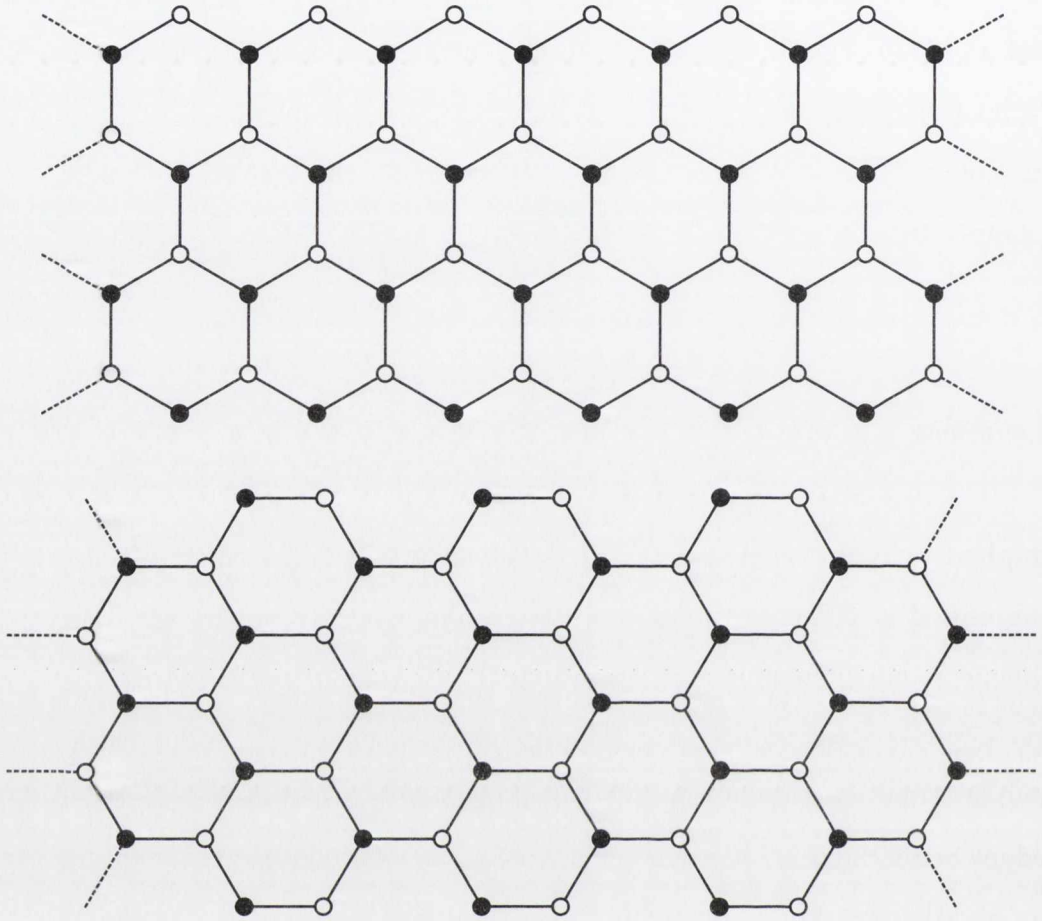


Figure 1.4: Graphene nanoribbons in different edge orientations. Zigzag is shown on top and armchair on the bottom.

for devices based on GNRs, such as in z-shaped nanoribbons, which can cause quantum confinement [58] thus allowing them to be used as quantum dots.

The edge orientation is extremely important, with tight binding calculations indicating that zigzag nanoribbons (ZGNRs) are always metallic whereas armchair nanoribbons (AGNRs) are either metallic or semi-conducting depending on width [53]. DFT calculations disagree, predicting that both armchair and zigag nanoribbons are semiconducting, with a gap inversely dependent on width [48, 59]. This viewpoint has been corroborated by some experiments [49]. Zigzag nanoribbons have a highly localised edge state as well as a sharp peak in the density of states (DOS) near the Fermi Energy. They have been predicted to demonstrate an ordered

magnetic edge state, and hence have felt the brunt of nanoribbon-based scrutiny [46, 53, 60, 61]. However, this edge state has not been observed experimentally, possibly because it is predicted to be highly sensitive to the edge geometry [61]. Fears that magnetism in zigzag nanoribbons may remain solely within the bounds of theoretical research are allayed by recent success in patterning more atomically exact edges [54, 55, 62]. Theoretical studies have also focused on predicting experimental methods that could potentially find the edge state [63]. The outcome of these experiments is of considerable theoretical and commercial interest, since the magnetically ordered edge state could be highly useful in the field of spintronics.

1.2 SPINTRONICS

Information technology involves the storage, retrieval, transport and manipulation of information. Currently, most of these operations are achieved with electric charge. Digital information is processed, transported, and, when required in rapid fashion, stored as electric charge. Non-volatile memory, on the other hand, is typically stored as spin (magnetic moments in hard drives). Furthermore, this information is read using a spin based process (spin valves). And while CMOS is one of the most successful technologies of all time, the conversion of spin into electric charge is necessarily a lossy process, and the manipulation of charge wastes energy due to Joule heating. The mish-mash of technologies and the limitations of working with information in the form of electric charge have led researchers to examine whether it would be better to switch to spin as the fundamental quantity in information, and the results have been impressive.

Spintronics, a portmanteau of "spin transport electronics", is the study of electron spin with a goal of increasing the efficiency and functionality of solid state devices. It is a necessarily broad field, encompassing the manipulation of single, localised spins (such as those found in quantum dots) on one extreme and spin

transport and dynamics in macroscale devices on the other. The origins of spintronics can be traced all the way back to 1930, with the theoretical proposal of spin waves [64], to their discovery, in 1957 [65]. Spin waves represent propagating disturbances caused by the collective precession of spins in ordered materials, and hold the potential to transport spin "information". However, it is commonly accepted that spintronics really began to emerge in the 1980s with the discovery spin injection from a ferromagnet [66] and of giant magnetoresistance (GMR) [67, 68]. GMR would earn both of its discoverers, Albert Fert and Peter Grünberg a Nobel prize. Already a picture was beginning to emerge wherein transport, storage, retrieval and processing of information was achieved by spin.

The retrieval of information was the first real success for spintronics. A GMR stack consists of two ferromagnetic layers connected by a metallic spacer and is shown in Fig.1.5. The central principle of GMR is that the resistance of the stack changes depending on whether the layers are in ferromagnetic or antiferromagnetic alignment. It is possible to engineer the alignment of the magnetic layers by changing the thickness of the spacer layer, and this was exploited by Fert and Grünberg to create a default magnetic alignment. They then used a small magnetic field to align the layers, and hence measured the GMR. Shortly after the discovery of GMR it was discovered that one of the layers could be pinned by an adjacent antiferromagnetic layer, hence creating a default magnetic alignment. This led to the creation of the *spin valve*. In a spin valve, only one layer is sensitive to the direction of a magnetic field, and hence the spin valve acts as a sensor for magnetic elements. It was later discovered that replacing the metallic spacer with an insulating layer led to more stable and robust devices [69, 70] and nowadays most spin valves are manufactured in this fashion. Spin valves have become the dominant way of reading non-volatile memory elements in modern computing, and are expected by many to be the first on a long road of successes for spintronics.

Later, the field would have another success in tackling storage. While non-volatile memory is generally stored in magnetic elements, until recently volatile

memory was still charge based. However, this has already begun to change with the development of magnetic random access memory (MRAM). MRAM stores memory in the same spin valves we have already examined in the context of GMR and TMR. The orientation of the "free" layer determines whether a 1 or a 0 is stored. MRAM seems destined for commercial success and many believe that the advantages are such that it will eventually become a universal memory (replacing all other forms of memory technology) [71]. MRAM might be further augmented by using spin-tranfer torque for switching, which is described as STT-RAM.

One of the remaining challenges for spintronics is the processing of spin as information, or a working spin-based logic device. However, considerable inroads have already been made on this hard problem. Most proposed logic devices are based around the concept of spin-transfer torque. Spin-transfer torque occurs when a spin-polarised current is passed into a ferromagnet. The dissipation of the spin current, in tandem with the conservation of angular momentum, can exert a torque on the magnetisation of the layer, changing its direction. Theoretical proposals for devices have been made based on this principle[72].

Despite the fact that considerable progress has been made on the more obviously challenging issues in spintronics, a surprisingly simple one still presents significant problems. The transport of spin as information would seem to have been among the simplest obstacles faced by spin based information technology. However, it has turned out to be one of the hardest. This is because spin currents tend to diffuse quickly, and one of the main barriers that inhibits the production of spintronic devices is the maintenance of a spin polarised population. The mechanisms of decay can be broadly classified into two main groups, *spin-flip scattering* and *spin dephasing*. The former refers to the possibility of a spin-flip occurring in conjunction with a scattering event, the latter to the fact that different rates of spin-precession leads to decoherence and decay over time. Two of the primary driving factors of these decay mechanisms are the spin-orbit and hyperfine interaction. Both of these

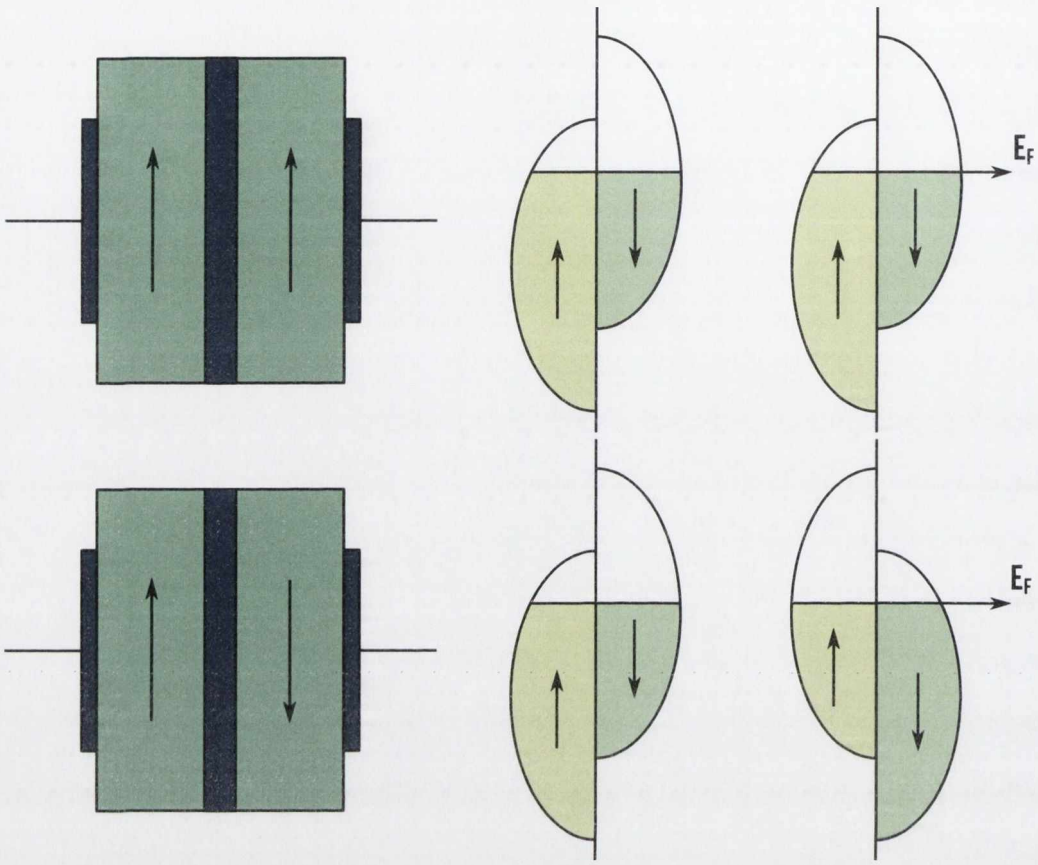


Figure 1.5: A schematic of the operation of the GMR stack. On the left are shown two GMR stacks consisting of two ferromagnetic layers with a metallic layer between. Above we show a case where both layers are aligned, and below we show the opposite case. The density of states of the various layers is shown on the right. In a ferromagnet, the density of states is split into two spin-dependent sub-bands. When the ferromagnetic layers in a GMR stack are aligned, the majority spin bands are also aligned and hence the electrons encounter little resistance passing through the device. When the ferromagnet layers are not aligned, the majority spin bands are different in each layer. This results in increased scattering, and hence resistance.

interactions are extremely weak in graphene [30, 73, 74], which has led to much speculation as to their role in the future of spintronics.

Despite the fact that it is non-magnetic, graphene already has a number of device proposals to its name [25]. Among the more interesting of these involves sharply straining parts of the graphene lattice to create "fins". These fins can have magnetic properties, and might be useful in an all-graphene spintronics device. This type of technology is dubbed "origami spintronics" [75]. Edged graphene has found

a home in spintronics as well. Thus far, most of the attention has been focused on edges with a zigzag geometry, where localized states were predicted to give rise to spin-polarized edges [46, 53, 60, 61]. Such magnetic-edged ribbons have inspired a number of theoretical device proposals [58, 76–78]. However, due to the sensitivity of the magnetic edge state to the nanoribbon, these devices may be difficult to achieve in practice. Nonetheless, zigzag nanoribbons maybe useful in spintronics anyway, as one paper shows zigzag nanoribbons becoming half metallic when in-plane magnetic fields are applied [77]. Half-metals are an interesting class of material with some special spin transport properties, acting as a conductor to electrons in one spin orientation, and a semi-conductor or insulator to those in the other. They have exciting possible applications in the field of spintronics and hence the possibility of tuning the spin transport properties of these materials has been well documented [53, 60].

1.3 MAGNETISM AND THE INDIRECT EXCHANGE COUPLING

While graphene's potential in spintronics is exciting, many of its application rely on doping or exploiting defect driven magnetic moments to achieve magnetic order. However, the existence of spin-order in graphene is debated and controversial. Early studies reported finding a ferromagnetic response [79] and a ferromagnetic response competing with an anti-ferromagnetic response at room temperature [80]. However, these initial successes were dogged by failed replications, with studies finding no ferromagetic response [81], not even paramagnetism due to edge effects [82]. Some studies concluded that much like graphite, graphene was diamagnetic [82]. Further problems for graphene arose when Nair *et. al.* found that defect induced magnetism in graphene was unlikely to lead to magnetic order due to clustering of adatoms and loss of structural stability in their presence [83]. At

this point, it seems unlikely that spin-order will be found in graphene, rather, it will have to be engineered. In order to do this, a knowledge of the fundamental interactions is essential.

When magnetic moments are embedded in a host medium, we may separate their coupling into two distinct contributions. The first, direct exchange, occurs when there is appreciable overlap of the electron wavefunctions. In a large graphene sheet, with a diffuse scattering of impurities, this kind of coupling is rare. The other kind, indirect exchange, occurs when electrons of the host medium interact with both impurities. Indirect exchange coupling (IEC) was first observed in metallic multilayers [84], where an oscillating interaction, with alignments switching between ferromagnetic and antiferromagnetic orientations, was observed [85]. Two main theories competed to better explaining the phenomenon. *Quantum Well Theory* explains the effect as one of quantum confinement by the magnetic impurities [86, 87]. Within this theory the oscillations of the interaction may be explained as the periodic effect of discrete energy levels crossing the Fermi energy as the impurities are moved apart (as illustrated in Fig.1.6). Alternatively, Ruderman-Kittel-Kasuya-Yosida (RKKY) theory was initially proposed by Ruderman and Kittel to explain broadening in nuclear spin resonance spectra [88]. It used second order perturbation theory to explain the indirect interaction as an effective direct interaction. It has since been extended to a wide variety of coupling phenomena [89–91].

Both theories shared a lot of the same predictions. They agreed that the interaction was host dependent, with the type of magnetic material having little or no effects on its properties. They agreed on the basic features of the interaction, that it was oscillatory, and that its amplitude decayed with the separation between the magnetic objects. Further investigation predicted the decay to be entirely dependent on the dimension of the host material and the period of its oscillations on its Fermi surface [92, 93]. Studies showed that the interaction decayed with the separation between impurities as D^{-d}, where D is the separation between impu-

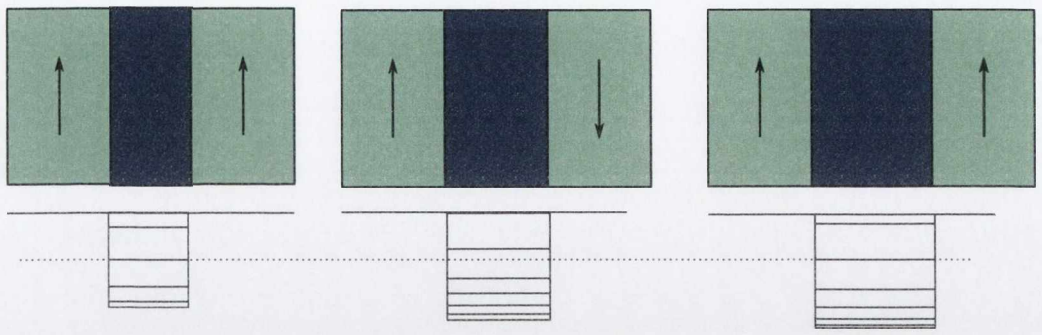


Figure 1.6: A rough schematic of Quantum Well Theory as seen through metallic multilayers. The addition of impurities can be modeled by localised potential and hence quantum confinement. As the imputites are moved apart the allowed energy levels in the spacer region changes. A periodic effect occurs as the energy levels cross the Fermi level. This periodicity is repeated in the oscillatory nature of the IEC.

rities and d the dimensionality of the host material. The investigation of the IEC in multilayer systems played a pivotal role in the development of the early spintronic devices, such as GMR stacks and spin valves [67, 68, 94]. Eventually, the RKKY was shown to be an approximation of quantum well theory, valid at large separations, and with simple oscillation periods [95–97]. However, the terminology is somewhat confused, and they are often used equivalently. In this thesis we will use the quantum well expression for the IEC, sometimes resorting to the RKKY approximation when looking for mathematical clarity.

The nature of the IEC in graphene has been the subject of much discussion in recent literature [46, 52, 76, 98–113]. Because pristine graphene is non-magnetic, and since the addition of defects has been shown to destabilize graphene, most studies are performed with added magnetic dopants. The exact nature of the interaction varies from study to study, with some even suggesting that Kondo screening dominates over the IEC at all distances for 2d/3d materials [114]. However, the general consensus from the literature is of an interaction that decays with the cube of the separation (D^{-3}). This is very surprising and breaks the dimensionality rule we introduced in the previous paragraph. The commonly cited reason for this bizarre behaviour is the unusual bandstructure of graphene, leading to a vanishing DOS

around the Dirac point. Another curiosity is the oscillatory nature of the interaction, which is evident in most materials but hidden in graphene by a commensurability effect between the oscillation periods and the underlying hexagonal lattice. It is found that magnetic moments on the same sublattice are always predicted to align ferromagnetically, whereas those on opposite sublattices will pair antiferromagnetically. This seems to be in accordance with the Lieb theorem for bipartite lattices and vacancies, which states that any magnetism must stem from a sublattice discrepancy[115]. As such, methods of introducing a sublattice discrepancy in graphene are under examination, and it is hoped that this may be achieved by partial hydrogenation [116]. Furthermore, a recent study indicates that if the bound states of the impurity interacts with the continuum of states in graphene, the resulting interaction could be of resonant character, being substantially enhanced, and breaking the sublattice symmetry, allowing for a net magnetic moment [117].

The IEC in edged graphene has also come under scrutiny, although in this case the body of work is surprisingly small [102, 104, 118–121]. Furthermore, most studies have been performed in zigzag nanoribbons, due to their magnetic edge state. The RKKY interaction mediated by the edge states in zigzag nanoribbons have been predicted to decay exponentially [102], however, the presence of electron-electron interactions has been predicted to lead to a distance-independent interaction [104]. Results in armchair nanoribbons are scarce, however, one study finds that the interaction is dependent on the distance of the impurities from the edge, and predicts the presence of both an exponential decay, and a *distance-independent* interaction [121], which is very surprising. Given previous experiments analysis of magnetism in nanoribbons, these results are unlikely to be particularly robust in the presence of disorder, and hence very difficult to measure with current experimental technology. However, success in the accurate patterning of graphene edges [54, 55, 62] means that these interactions may soon be observable in the lab, and hence make them an interesting topic of reseach at the moment.

Since the magnetic interactions in graphene decay quickly, methods are sought for extending its range. One possible route to this is by using extended magnetic objects. The idea of using extended objects to modify the properties of graphene is one that has become popular in the recent literature. In 2012 Salehi-Khoji *et. al.* examined line defects as a means of enhancing the chemical sensitivity of graphene, finding that graphene nanoribbons were particularly effective [122]. In the same year Winters *et. al.* announced the ability to create 3d structures in graphene using transfer printing [123], such as periodic steps and ripples. This same method would later be used to create graphene fins [124], which could display enhanced spin-orbit coupling and hence magnetism due to the intense strains involved [75]. Indeed, extended nanowires on graphyne have already been shown to demonstrate long range magnetic order and anisotropy [125]. This has led to interest in how ordered magnetic lines might interact. One paper examining the RKKY interaction between lines of defects find that the sublattice dependence of the interaction is broken, and the decay rate is the same, but the magnitude is greatly increased [126]. Further a recent paper has used stable crystographically ordered fluorine chains to generate spin order in graphene [127]. The impact of extended lines of impurities is likely to be broad and diverse, with studies already showing the potential of these structures to enhance valley polarization and propose valley valve device [128].

Long ranged magnetic interactions are quite difficult to treat effectively using DFT, since the computational intensity of the calculations tends to require small unit cells. Indeed this can, and has, lead to some wayward predictions in the past, due to failure to account for the inter-cell coupling [129]. However, DFT studies of the IEC can and have been performed [130–132], and are, among other things, the only way of obtaining a rough idea of the magnitude of the interaction. Most studies find an interaction strength in the range of 10s of meV at 10A [132, 133]. The studies have mostly confirmed the tight-binding model, finding a decay of $D^{-2.43}$, as well as the FM-AFM effect of different sublattices. They seem to agree that the coupling can be classified as an RKKY interaction [130]. The IEC has

also been studied using Quantum Monte Carlo simulations, which find that IEC is controllable in graphene via the spin orbit coupling and the chemical potential [134].

Of course, ideally we would like to measure the interaction between various magnetic impurities experimentally. Recently, there has been progress in doing exactly that [135–137]. Kaiser et. al used magnetic exchange force microscopy in order to map out both locations and spins of surface atoms on an atomic scale [135], then measured the difference between ferromagnetic and antiferromagnetic alignments. Meier et. al used a scanning tunneling microscope to obtain the magnetisation curves of individual magnetic atoms, and then extract the coupling from that [136]. The interaction strengths found are roughly on the order of 0.1meV at 10 angstroms [136, 137], 100 times weaker than the DFT predictions. However, greater interaction strengths may be accessible by arranging chains, or clusters of magnetic impurities [138, 139].

While there has been recent progress in examining the spin state of isolated impurities [140], there has been considerable experimental difficulty in detecting the IEC in graphene, which is surprising given the D^{-3} decay. This may be because many impurities adsorb at the center of the graphene hexagon, where they are alternately described as *plaquette* impurities or simply *center-adsorbed* impurities. Such impurites were initially predicted to display a greater rate of decay in carbon nanotubes [141], a result that was later extended to bulk graphene [101]. A low interaction strength spells doom for many important spintronic applications, however, it may be possible to increase the interaction range by causing the impurity spins to precess.

The dynamic magnetic interaction was initially examined in the context of metallic multilayers where it was shown to both considerably augment and extend the interaction [142, 143]. This was later extended to graphene where the same attributes were found, including a vastly decreased rate of decay D^{-1} [108]. Furthermore, there is reason to believe that the interaction may be augmented still, by using a

curved gated region as a lens for spin current [144]. This may lead to an easier route for detecting magnetic interactions in graphene [108], using inelastic scanning tunnelling spectroscopy [145]. The possible applications of this type of interaction are numerous, but two recent papers focus on graphene as a spin-pumping transistor [146] as well carbon nanotubes as waveguides for spin-current [147].

1.4 CONDUCTANCE

In the modern world, there is an ever present market for high conductance materials that minimise power loss. At room temperature, graphene's conductance is almost peerless, with carrier mobilities as high as 15,000 $cm^2V^{-1}s^{-1}$ being reported [8, 25, 148, 149]. Furthermore, these mobilities display the weak temperature dependence that indicates defect driven scattering, and hence it is expected that this value can be significantly improved. Graphene has been predicted to display superconductive properties under the right circumstances, with researchers recently finding evidence for superconductivity in Li-decorated monolayer graphene [150]. One of graphene's more unusual conductive properties is its finite minimum conductance with zero field and zero carrier density [25]. The presence of this minimum is a debated topic, but various theories posit that it originates from either the rippling of graphene, the presence of impurities or perhaps charge carriers from the substrate.

The conductive properties of graphene nanoribbons may be of even more import than the bulk, since many believe they will be useful as interconnects in integrated circuits [151]. However, the conductive properties of nanoribbons are under serious debate. A simple examination of the bandstructure within the tight binding scheme indicates that zigzag nanoribbons are always metallic, whereas armchair nanoribbons can be metallic or semiconducting depending on their width [48, 53]. However, subsequent calculations using more advanced techniques cast doubt on this simple picture [48, 152, 153]. Many studies predict gaps for both edge orienta-

tions [48, 153], some predict that zigzag nanoribbons may be metallic or semiconducing depending on their width, and even higher order tight binding calculations show significant changes to the bandstructure [154]. The difficulty in manufacturing nanoribbons with exact edges makes determining the validity of these claims difficult, but attempts have been made, which seem to verify the width dependent gap model in armchair edge nanoribbons, while obtaining contradictory results for zigzag nanribbons [49, 155]. Recently, the area has grown in excitement once again, as epitaxially grown graphene nanoribbons exceed the conductance of theoretical graphene by a factor of ten [156].

Since impurities are ubiquitous to all materials, their effect on the physical properties of any material is worthy of study. Their effect on the conductance is of particular importance, as they move the system away from the ballistic transport regime. Many studies have examined the effect of impurities on the conductance of nanoribbons [157–160]. Some show rapid suppression of the conductance with edge disorder due to Anderson localisation [160]. Others show the possibility of engineering the system with impurities, suggesting that impurities can be used to control the size of, or vanish, the bandgap in AGNRs [158]. The effect of impurities on the spin-dependence of the conductance is also of interest, and evidence suggests that hydrogen adsorbates may cause the spin-flip conductance (which is tiny in a pristine ribbon due to the weak spin orbit interaction) to become as large as its the spin-conserving counterpart in AGNRs [161].

Contaminants can be a serious problem in graphene, and adsorption of water or oxygen molecules can lead to large and non-repetitive hysteresis I-V characteristics. This problem has been significantly alleviated recently, as researchers have produced graphene coated with aluminium oxide. They found that the device was stable while being held in ambient conditions for a long period and remained so after chemical and heat treatments [162]. However, this sensitivity to impurities can be tuned to our advantage, and it may make graphene an ideal material for a sensor [163–165].

Graphene and sensors are a natural fit for a wide variety of reasons. Graphene's excellent conductivity is always a boon for device efficiency, its strength is important for stability, and its very two dimensionality allows for an unparalleled surface to volume ratio, which greatly enhances its sensitivity. For these reasons it is expected that graphene sensors will be smaller, lighter, more sensitive and more efficient than anything in the current generation. Graphene has already demonstrated excellent functionality as a DNA sensor [157] (for detecting nucleobases and nucleotides), and an almost extraordinary resolution as a gas sensor [163–165] being able to detect individual molecules [164]. The commercial properties are expansive, with Bosch collaborating with researchers at the Max-Planck Institute to create magnetic sensors claimed to be 100 times more sensitive than existing models, and Graphene Frontier raising 1.6 million dollars for sensors for a range of graphene-based chemical and biological sensors designed for use in medical applications.

1.5 THESIS STRUCTURE

In this thesis we will be using analytic and numerical methods to examine some of the problems introduced in this chapter.

In chapter 2 we will take a look at some of the mathematical techniques that form the backbone of this thesis. Many of our calculations in this thesis are based on Green's functions (GFs), and they are introduced in this chapter. We also introduce some techniques for manipulating GFs, such as the Dyson equation, which allows us to introduce perturbations into our systems. The energy changes in response to these perturbations are introduced as well, in the context of the Lloyd formula. Finally, we will conclude the chapter with a brief section on accounting for electron-electron interaction, as per the Hartree-Fock/Hubbard Model.

In chapter 3 we use some of the techniques developed in chapter 2 to examine the Green's functions of various graphene-like systems. We cover graphene and its edged variants, namely semi-infinite graphene and nanoribbons. We obtain the GFs numerically and analytically within an approximation, using an approach developed in our group. We also take the time to examine the local density of states (LDOS), which will play an important role in analysing many of our results.

In chapter 4 we will examine the IEC in edged graphene systems, making use of the GFs derived in chapter 3. This is achieved by using the Lloyd formula to determine the energy change caused by rotating magnetic impurities between ferromagnetic and antiferromagnetic arrangements. Then we examine the coupling both numerically, and analytically (using a technique developed in our group) in bulk graphene, semi-infinite graphene and graphene nanoribbons. We find a triadic pattern in the coupling near graphene edges, and explain it with reference to the LDOS. We also examine the effect of different impurity types on the interaction, which will prove important when examining the conductance.

In chapter 5 we extend our analysis of the IEC to infinite lines of impurities. We discuss how this might represent a reasonable approximation to some of the extended magnetic structures we see in graphene at the moment. We demonstrate how the IEC can be reformulated within this scheme, and reduced to a mathematically simple form. We examine the interaction both numerically and analytically, demonstrating a much stronger and longer ranged interaction. Furthermore, we show that the infinite line of impurities may be used as a reasonable proxy for small finite lines of impurities. This demonstrates the broad applicability of the result.

In chapter 6 we move away from the static regime, examining the dynamic magnetic interaction in graphene nanoribbons. We achieve this by inserting a number of top adsorbed impurities into our nanoribbon, and then perturbing one with a magnetic field, causing the impurities to communicate via spin-waves. We derive an expression for the dynamical transverse spin susceptibility, which we then use

to calculate the lifetime of excitation. We find a triadic pattern familiar to us from our work with the IEC and the LDOS. We demonstrate that impurities adsorbed on certain sites do not contribute to the interaction and hence propose a means by which the interaction may be probed by experiment.

In chapter 7 we examine the effect of various types of impurities on the conductance in nanoribbons. We do this to draw a correlation between the strength of the RKKY and the size of the conductance, since both are determined by scattering from impurities. We examine impurities of different conformation, and hope that we can correlate our results with those we attain in chapter 4. We examine the results in wide nanoribbons in the hope that they will generalise to graphene. We first examine the effect of impurities in isolation, and then show that our results generalise to large, random distributions of impurities. We hypothesise that graphene would not be as sensitive to center adsorbed impurities as other impurity types.

1.6 PARAMETERS, NOTATION AND CONVENTIONS

Since we are more interested in trends rather than absolutely values, all quantities in this thesis are calculated in units of convenience. Distances are calculated in units of the lattice parameter of graphene, in order to represent discrete atomic steps. Energies are calculated in units of the hopping parameter t, which is 2.7 eV [166, 167]. When we start performing dynamic calculations, we will set $\hbar = 1$, meaning that we will work in a system of natural units scaled by the hopping parameter. In this system, the frequency ω and dynamic susceptibility χ have units of energy and inverse energy respectively.

There are some parameters which will be used consistently throughout this thesis. For instance, impurities are often represented by an on-site energy ϵ and a hopping parameter τ. Electron-electron interactions are parametrised by the diago-

nal Coulomb integral U, which is chosen to satisfy the Stoner criterion in a simple single band model. And Green's functions are rendered advanced or retarded by means of a small imaginary part η. Typical values for these parameters are listed in the table below. Parameters are adjusted within reasonable ranges to see if they had a large effect on overall behaviour. Typically, we find that this influences the magnitude, but not the overall trend, of the examined quantities. We chose η to satisfy convergence. Our calculations typically converged with an $\eta = 1.0e-3$, and so most calculations were performed with $\eta = 1.0e-4$, to ensure accuracy.

ϵ	1.0
τ	1.0
U	10.0
η	1.0e-4

Sometimes we will reprint equations to save the reader the bother of needing to leaf back through several previous chapters. We will frequently use acronyms in order to conserve space, but will also occasionally resort to the full form to remind the reader. Finally, we commonly drop the argument list for a function once it is understood. For large, unwieldy equations, we feel like this brings some clarity and can increase comprehension.

Finally, I will frequently use a $[start, stop, step]$ notation which is common in computer science. In the usual mathematical notation, this refers to

$$[a, b, c] = \{a + cn | n \in \mathbb{N} \wedge a + cn < b\}. \tag{1.6.1}$$

2

MATHEMATICAL METHODS

In this chapter we will outline the mathematical procedures that form the backbone of this thesis. Much of our concern is with the generation and manipulation of Green's functions (GFs), which are introduced in some detail in this section. GFs have great utility in condensed matter physics and we use them for purposes ranging from calculating the local density of states of an atomic site to calculating the effect of a perturbed magnetic impurity on a system. Here we will develop general methods for dealing with impurities, finding the GFs of recursively generated systems and calculating energy differences upon the introduction of perturbations. We will also present some techniques that help to reduce the computational cost of our calculations.

2.1 GREEN'S FUNCTIONS

In its classical form the GF refers to a function used to solve differential equations subject to initial or boundary conditions. While the field of condensed matter often allows for a somewhat broader definition, for our purposes the original will suffice. The GF may be defined as the solution of the following equation

$$[z - L(\mathbf{r})]G(\mathbf{r}, \mathbf{r}'; z) = \delta(\mathbf{r} - \mathbf{r}'), \tag{2.1.1}$$

where z is a complex variable and $L(\mathbf{r})$ is a time-independent, linear, Hermitian differential operator with a complete set of eigenfunctions.

In condensed matter physics, the GF of interest is almost always that of the Schrödinger equation, and is given by

$$\hat{g} = \lim_{\eta \to 0} \left[(E \pm i\eta)\hat{I} - \hat{H} \right]^{-1}, \tag{2.1.2}$$

where $\hat{H}$ is the relevant Hamiltonian, $\hat{I}$ the identity matrix and E the energy. $i\eta$ is a small, positive, imaginary term that is added to resolve singularities. The limit can be taken with $i\eta$ positive or negative, leading to formulations for the *retarded* and *advanced* GFs respectively. In this thesis, all GFs are retarded unless otherwise specified.

2.1.1 *The Local Density of States*

The GF can be used to find the local density of states. If our Hamiltonian has eigenstates $|\phi_a\rangle$ and eigenvalues ϵ_a we can write

$$\hat{H} = \sum_a |\psi_a\rangle \epsilon_a \langle\psi_a|. \tag{2.1.3}$$

Entering this into our definition for the Green's function given in Eq. (2.1.2) gives

$$\hat{g} = \lim_{\eta \to 0} \sum_a |\psi_a\rangle \frac{1}{E + i\eta - \epsilon_a} \langle\psi_a|. \tag{2.1.4}$$

In tight-binding Hamiltonians, we may describe H by a basis of localised orbitals $|j\rangle$, centered on site j.

$$\begin{aligned} g_{jj} \equiv \langle j|\hat{g}|l\rangle &= \lim_{\eta \to 0} \sum_a \langle j|\psi_a\rangle \frac{1}{E + i\eta - \epsilon_a} \langle\psi_a|j\rangle \\ &= \lim_{\eta \to 0} \sum_a |\langle j|\psi_a\rangle|^2 \frac{E - i\eta - \epsilon_a}{(E - \epsilon_a)^2 + \eta^2}. \end{aligned} \tag{2.1.5}$$

And the imaginary part of this is given by

$$\mathrm{Im}(g_{jj}) = -\lim_{\eta\to 0}\sum_{a} |\langle j|\psi_a\rangle|^2 \frac{\eta}{(E-\epsilon_a)^2+\eta^2}. \tag{2.1.6}$$

The second part of this equation is just a delta function, given by

$$\delta(x) = \frac{1}{\pi}\lim_{a\to 0}\frac{a}{x^2+a^2}. \tag{2.1.7}$$

This allows us to write

$$-\frac{1}{\pi}\mathrm{Im}(g_{jj}) = \sum_{a} |\langle j|\psi_a\rangle|^2 \delta(E-\epsilon_a). \tag{2.1.8}$$

This is the definition of the LDOS. The LDOS can be used directly to quantify a number of the physical properties of a system, such as total energy, occupation number, etc. While simple to calculate, it is also very powerful, and we will return to it repeatedly in this thesis in order to explain far more complicated effects.

2.2 DYSON'S EQUATION

In tight binding, systems that exhibit translational invariance can be easily solved using Bloch's Theorem. However, Bloch's theorem is invalidated by even the slightest break of translational symmetry. When working with Green's functions, we are able to solve the translationally invariant system first, introducing any deviations in the form of a perturbing potential. It is important to remark that this is not perturbative in the sense that it stems from a truncated expansion, but simply by the fact that it represents a small additional term added to the pristine Hamiltonian. There are no approximations being used in this particular step.

Performing our calculations in this manner is enormously beneficial in terms of time and computational cost. If we let $\hat{g}$ be the GF of the translationally invariant

system (of Hamiltonian $\hat{H}_0$), and $\hat{G}$ be the GF of the perturbed system (of Hamiltonian $\hat{H} = \hat{H}_0 + \hat{V}$) we can write

$$\begin{aligned}\hat{G} &= \left[(E + i\eta)\hat{I} - (\hat{H}_0 + \hat{V})\right]^{-1} \\ &= \left[\hat{g}^{-1} - \hat{V}\right]^{-1} \\ &= \left[\hat{I} - \hat{g}\hat{V}\right]^{-1}\hat{g} \\ &= \hat{g} + \hat{g}\hat{V}\hat{G}.\end{aligned} \tag{2.2.1}$$

This is known as Dyson's equation. Within this scheme, the effects of a perturbation on physical quantities can be determined to any desired degree of accuracy (by expanding into higher terms if necessary). However, the applications of Dyson's equation are much broader than this would suggest, as we will see in the next sections.

It is sometimes advantageous to write Dyson's equation in terms of a "T" matrix $\hat{T} = \hat{V}\left[\hat{I} - \hat{g}\hat{V}\right]^{-1}$, from which we can find the perturbed GF using

$$\hat{G} = \hat{g} + \hat{g}\hat{T}\hat{g}. \tag{2.2.2}$$

This form will prove useful when we look at the Lloyd formula.

2.3 PERTURBATIONS

In this section we introduce various perturbations and show how to obtain some of the resulting GFs. While the calculations performed here serve as useful examples of our method, they double as specific circumstances that will be useful in later calculations. In this section, we assume a condensed matter system that is approximated within the tight-binding method, so all quantum mechanical terms may be written in terms of localised orbitals. Although the pictures in this section

use graphene as the default system (since it is applicable to our work), the results are more generally applicable.

2.3.1 *Substitutional*

The simplest type of impurity to add to the system is a substitutional impurity. Substitutional impurities replace a carbon atom at a certain site, and an example is shown in Fig.2.1. We seek the on-site GF, which can lead to important information about the new LDOS.

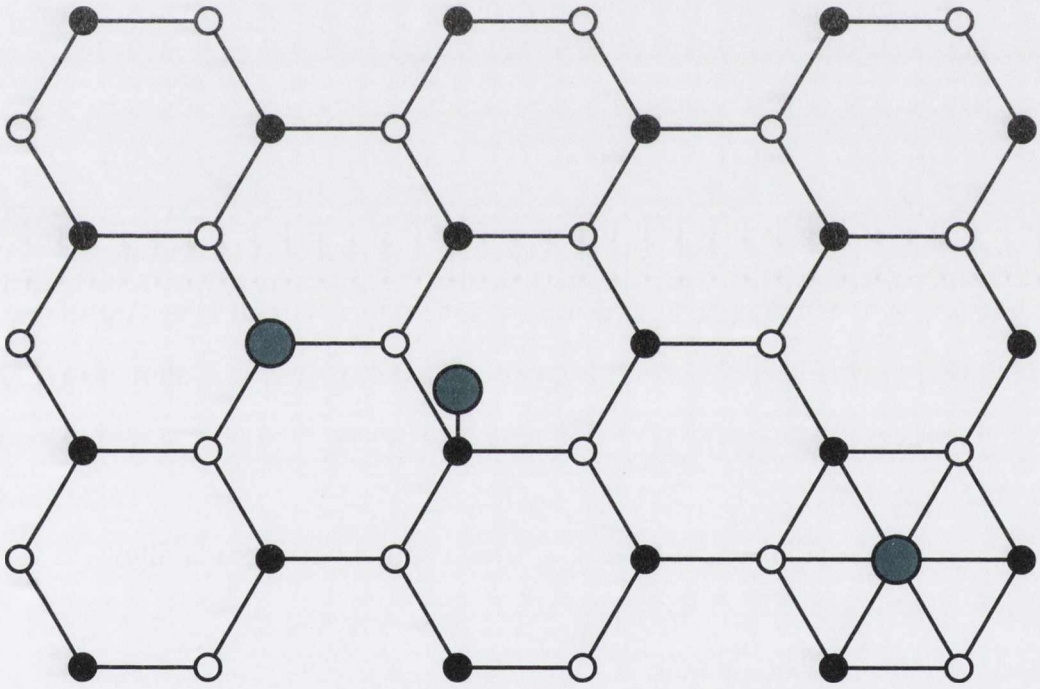


Figure 2.1: A schematic of the different types of impurity that we will investigate in this thesis. From left to right: a substitutional impurity, a top adsorbed impurity and a center adsorbed impurity.

To place a substitutional impurity at a site A we use a perturbation like

$$\hat{V} = |A\rangle\langle A|\epsilon. \tag{2.3.1}$$

Now the GF can be calculated using Dyson's equation to give

$$G_{AA} = g_{AA} + g_{Ai} V_{ij} G_{jA}. \tag{2.3.2}$$

And $\hat{V}_{ij} = \epsilon \delta_{iA} \delta_{jA}$, so we have

$$G_{AA} = g_{AA} + g_{AA} G_{AA} \epsilon. \tag{2.3.3}$$

Finally we get

$$G_{AA} = \frac{g_{AA}}{1 - g_{AA}\epsilon}. \tag{2.3.4}$$

2.3.2 *Top adsorbed*

A common adsorption method for an impurity to connect to a single lattice site. In this section we will add two top-adsorbed impurities to a system, at sites A and B and calculate G_{AB}, the GF between the impurities. Such a system is shown in Fig.2.2. This quantity is often useful when calculating magnetic interactions within the RKKY approximation.

We connect a top adsorbed impurity to our system using a perturbation like

$$\hat{V} = \tau(|A\rangle\langle a| + |a\rangle\langle A| + |B\rangle\langle b| + |b\rangle\langle B|). \tag{2.3.5}$$

And following similar methods from our substitutional section we get to find

$$G_{AB} = \tau g_{AA} G_{aB}. \tag{2.3.6}$$

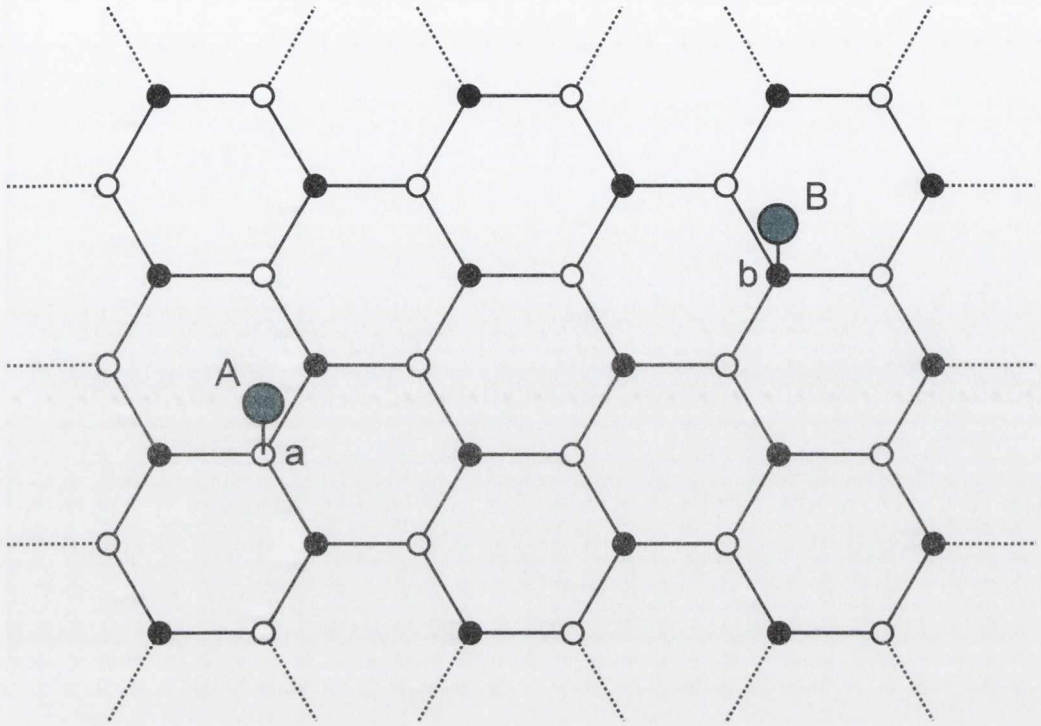


Figure 2.2: A schematic demonstrating our labelling convention for a system with two top-adsorbed impurities.

Where a large number of terms have disappeared because they are zero in the unconnected system. Now we continue calculating quantities until our equations outnumber our unknowns.

$$G_{AB} = \tau g_{AA} G_{aB} \tag{2.3.7}$$

$$G_{aB} = \tau g_{aa} G_{AB} + \tau g_{ab} G_{BB} \tag{2.3.8}$$

$$G_{BB} = g_{BB} + \tau g_{BB} G_{bB} \tag{2.3.9}$$

$$G_{bB} = \tau g_{bb} G_{BB} + \tau g_{ba} G_{AB}. \tag{2.3.10}$$

Solving the above equations gives

$$G_{AB} = \frac{\tau^2 g_{AA} g_{ab} g_{BB}}{(1 - \tau^2 g_{AA} g_{aa})(1 - \tau^2 g_{BB} g_{bb}) - \tau^4 g_{AA} g_{ab} g_{ba} g_{BB}}. \tag{2.3.11}$$

Obviously, similar calculations can be used to obtain G_{AA} and other matrix elements.

2.3.3 *Center Adsorbed*

The entire calculation of the center adsorbed impurity (pictured in Fig.2.1) is almost identical to the top adsorbed save for an additional sum. Our perturbation is now given by

$$V = \tau \sum_{i,k} (|a_i\rangle\langle A| + |A\rangle\langle a_i| + |b_k\rangle\langle B| + |B\rangle\langle b_k|). \tag{2.3.12}$$

Performing Dyson's equation now gives us

$$\begin{aligned} G_{AB} &= \tau \sum_i g_{AA} G_{a_i B} \\ G_{a_i B} &= \tau \sum_k (g_{a_i a_k} G_{AB} + g_{a_i b_k} G_{BB}) \\ G_{BB} &= g_{BB} + \tau \sum_i g_{BB} G_{b_i B} \\ G_{b_i B} &= \tau \sum_k (g_{b_i b_k} G_{BB} + g_{b_i a_k} G_{AB}). \end{aligned} \tag{2.3.13}$$

Introducing the Gamma term $\Gamma_{ab} = \tau^2 \sum_{i,k} g_{a_i b_k}$ allows us to write

$$G_{AB} = \frac{g_{AA}\Gamma_{ab} g_{BB}}{(1 - g_{BB}\Gamma_{bb})(1 - g_{AA}\Gamma_{aa}) - g_{AA}\Gamma_{ab}\Gamma_{ba} g_{BB}}. \tag{2.3.14}$$

2.4 RECURSIVE METHODS

Many of the systems we are interested in lack translational symmetry either partly or entirely. A standard way of building these systems is to connect together a large number of smaller "cells" as in Fig. 2.3. Cells may be connected via Dyson's equa-

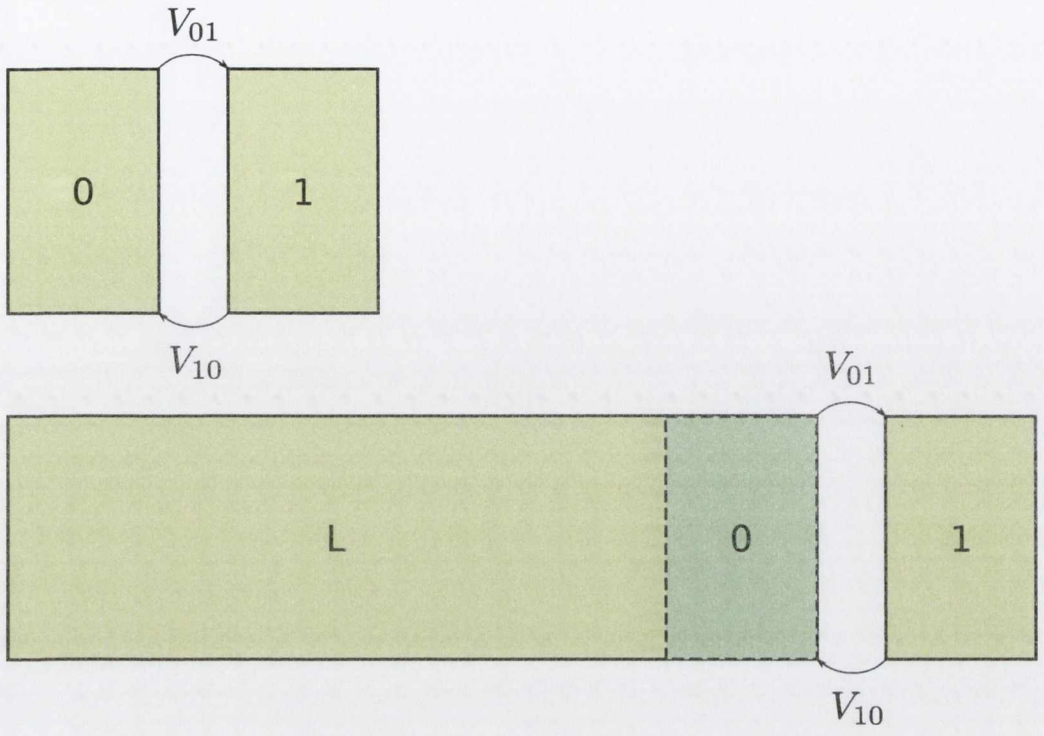


Figure 2.3: A schematic showing the perturbation introduced to update the edge element of a chain. The situation is identical to that of joining two individual cells together.

tions, and the GF of all or part of the connected system can be found. In practice, we are normally only interested in the GFs of a small region in the system, and it is possible to find these in a manner that is not too computationally expensive.

For the simple two cell system shown in Fig. 2.3, the GF of the disconnected system can be written in terms of the block matrix

$$\hat{g} = \begin{pmatrix} g_{00} & 0 \\ 0 & g_{11} \end{pmatrix}. \tag{2.4.1}$$

The perturbation used to connect the two systems is called the connection matrix and can be written in block form as

$$\hat{V} = \begin{pmatrix} 0 & V_{01} \\ V_{10} & 0 \end{pmatrix}. \tag{2.4.2}$$

Finally, the GF of the connected system may be represented as

$$\hat{G} = \begin{pmatrix} G_{00} & G_{01} \\ G_{10} & G_{11} \end{pmatrix}. \tag{2.4.3}$$

Since block matrix multiplication is identical to regular matrix multiplication we can use the Dyson equation to find the relevant cells. For example, updating cell one gives

$$G_{11} = g_{11} + g_{11} V_{10} G_{01} \tag{2.4.4}$$

$$G_{01} = g_{00} V_{01} G_{11}. \tag{2.4.5}$$

From which we get

$$G_{11} = (I - g_{11} V_{10} g_{00} V_{01})^{-1} g_{11}. \tag{2.4.6}$$

The second system in Fig. 2.3 appears more complicated, since now we have three cells to worry about, one of which is very large. However, a simple analysis shows the GFs of cells 0 and 1 are the only ones that matter. Our GF now has the following block matrix form

$$\hat{g} = \begin{pmatrix} \hat{g}_{00} & \hat{g}_{L0} & 0 \\ \hat{g}_{0L} & \hat{g}_{00} & 0 \\ 0 & 0 & \hat{g}_{11} \end{pmatrix}. \tag{2.4.7}$$

However, the elements in our connection matrix are still exactly the same.

$$\hat{V} = \begin{pmatrix} 0 & 0 & 0 \\ 0 & 0 & V_{01} \\ 0 & V_{10} & 0 \end{pmatrix}. \tag{2.4.8}$$

And writing out the Dyson equation it becomes clear that all elements like $\hat{g}_{0L}$ vanish and we have an identical formula to the simple two celled system. This equation therefore allows us to continually add cells to a system until we reach some arbitrary size. Indeed, we can go further, and add cells until the GF converges, at which point we may consider our lead to be semi-infinite. Furthermore, we can build SI leads in both directions, connecting them in the center to create a fully infinite system.

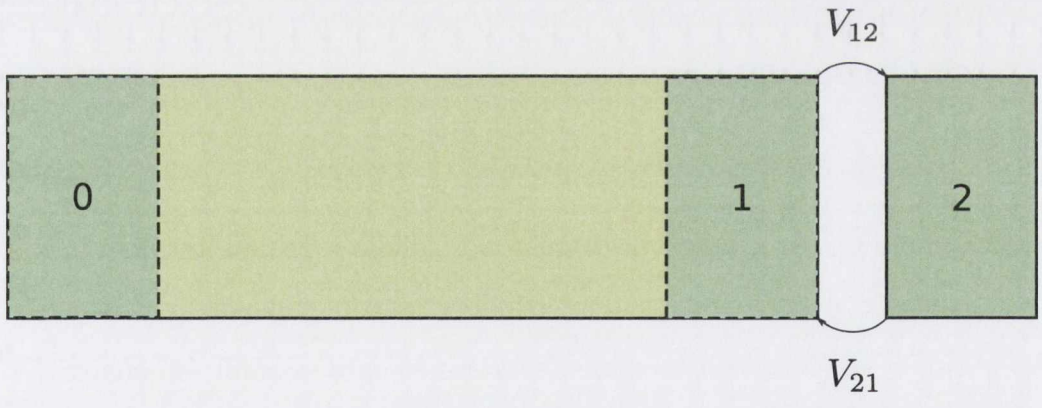


Figure 2.4: Calculating off-diagonal elements in a chain is more difficult than simply updating the Green's function on the edge, but the essential method is the same

We can also calculate off-diagonal elements, such as those shown in Fig 2.4. The equations become more involved, but the method remains the same.

$$G_{22} = (1 - g_{22}V_{21}g_{11}V_{12})^{-1}g_{22} \tag{2.4.9}$$

$$G_{20} = G_{22}V_{21}g_{10} \tag{2.4.10}$$

$$G_{00} = g_{00} + g_{01}V_{12}G_{20} \tag{2.4.11}$$

$$G_{02} = g_{01}V_{12}G_{22}. \tag{2.4.12}$$

For a single cell (as in Fig. 2.3), we may expect that 1 and 0 in the above equation simply become cell 0, and 2 becomes cell 1. Running through the Dyson equation shows that this is exactly the case

$$G_{11} = (1 - g_{11}V_{10}g_{00}V_{01})^{-1}g_{11} \tag{2.4.13}$$

$$G_{10} = G_{11}V_{10}g_{00} \tag{2.4.14}$$

$$G_{00} = g_{00} + g_{00}V_{01}G_{10} \tag{2.4.15}$$

$$G_{01} = g_{00}V_{01}G_{11}. \tag{2.4.16}$$

Where the order of the GFs is chosen specifically to facilitate repeated iteration in numerical calculations.

Calculating off-diagonal elements is obviously more computationally expensive than calculating their diagonal counterparts. Because of this, when working with infinite systems, it is best to calculate the off-diagonal elements of a finite system first, connecting semi-infinite leads to either side afterwards.

Of course, another avenue is to calculate the inverse of the Dyson Equation directly from its other form

$$\hat{G} = (\hat{1} - \hat{g}\hat{V})^{-1}\hat{g} \tag{2.4.17}$$

We have that

$$\hat{g}\hat{V} = \begin{pmatrix} 0 & g_{L1}V_{10} & g_{L0}V_{01} \\ 0 & g_{01}V_{10} & g_{00}V_{01} \\ 0 & g_{11}V_{10} & g_{10}V_{01} \end{pmatrix}. \tag{2.4.18}$$

When calculating the inverse we can therefore simply focus upon those elements from cells 0 and 1. For more information, see the Appendix.

Combining the methods listed above allows us to calculate the GF of almost any system. However, though the methods presented here all work, they are not always the most efficient way to approach the problem. One highly efficient algorithm for the rapid creation of SI systems is presented below.

2.4.1 *The Rubio Sancho Method*

While the above method of updating the edge cell will work, it is naive and computationally wasteful. A *much* faster way of obtaining the Green's function on the edge of a semi-infinite lead can be found using the *Rubio Sancho method* [168]. The Rubio Sancho method works by creating a formula to calculate cell N of a nanoribbon, then implements it recursively to find the Green's Function at the edge

We start by connecting cell N to the system shown in (Fig 2.5).

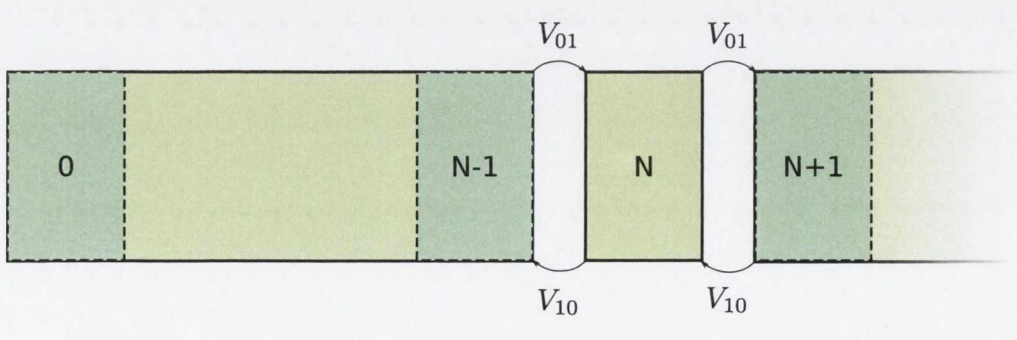


Figure 2.5: Schematic of the Rubio Sancho method: Reconnecting cell N

$$\hat{G}_{N0} = \hat{g}_C \hat{V}_{10} \hat{G}_{N-1,0} + \hat{g}_C \hat{V}_{01} \hat{G}_{N+1,0} \tag{2.4.19}$$

$$\equiv \hat{t}_0 \hat{G}_{N-1,0} + \hat{s}_0 \hat{G}_{N+1,0}. \tag{2.4.20}$$

Reusing this equation on terms $\hat{G}_{N-1,0}$ and $\hat{G}_{N+1,0}$ gives us

$$\hat{G}_{N0} = \hat{t}_0 \left[\hat{t}_0 \hat{G}_{N-2,0} + \hat{s}_0 \hat{G}_{N,0}\right] + \hat{s}_0 \left[\hat{t}_0 \hat{G}_{N,0} + \hat{s}_0 \hat{G}_{N+2,0}\right] \tag{2.4.21}$$

$$\equiv \hat{t}_1 \hat{G}_{N-2,0} + \hat{s}_1 \hat{G}_{N+2,0}. \tag{2.4.22}$$

Where

$$\hat{t}_1 = \left[\hat{I} - \hat{t}_0 \hat{s}_0 - \hat{s}_0 \hat{t}_0\right]^{-1} \hat{t}_0^2 \tag{2.4.23}$$

$$\hat{s}_1 = \left[\hat{I} - \hat{t}_0 \hat{s}_0 - \hat{s}_0 \hat{t}_0\right]^{-1} \hat{s}_0^2. \tag{2.4.24}$$

This process can easily be repeated to get

$$\hat{G}_{N0} = \hat{t}_i \hat{G}_{N-2^i,0} + \hat{s}_i \hat{G}_{N+2^i,0}, \tag{2.4.25}$$

and

$$\hat{t}_i = \left[\hat{I} - \hat{t}_{i-1} \hat{s}_{i-1} - \hat{s}_{i-1} \hat{t}_{i-1}\right]^{-1} \hat{t}_{i-1}^2 \tag{2.4.26}$$

$$\hat{s}_i = \left[\hat{I} - \hat{t}_{i-1} \hat{s}_{i-1} - \hat{s}_{i-1} \hat{t}_{i-1}\right]^{-1} \hat{s}_{i-1}^2. \tag{2.4.27}$$

Allowing $N = 2^i$ we get a sequence of equations

$$\hat{G}_{10} = \hat{t}_0 \hat{G}_{00} + \hat{s}_0 \hat{G}_{20} \tag{2.4.28}$$

$$\hat{G}_{20} = \hat{t}_1 \hat{G}_{00} + \hat{s}_1 \hat{G}_{40} \tag{2.4.29}$$

$$\vdots \tag{2.4.30}$$

$$\hat{G}_{2^i 0} = \hat{t}_i \hat{G}_{00} + \hat{s}_i \hat{G}_{2^{i+1} 0}. \tag{2.4.31}$$

Starting from the final equation, backsubstitution yields

$$\hat{G}_{10} = \left[\hat{t}_0 + \hat{s}_0\hat{t}_1 + \hat{s}_0\hat{s}_1\hat{t}_2 + \cdots + \hat{s}_0\hat{s}_1\cdots\hat{s}_{i-1}\hat{t}_i\right]\hat{G}_{00} + \hat{s}_n\hat{G}_{2^{i+1}0}, \tag{2.4.32}$$

where the final term can be made arbitrarily small. To utilize these equations we need to do a little bit more work.

From our previous equations we can write

$$\hat{G}_{00} = \left[\hat{I} - \hat{g}_{00}\hat{V}_{01}\hat{g}_{11}\hat{V}_{10}\right]^{-1}\hat{g}_{00} \tag{2.4.33}$$

$$\hat{G}_{10} = \hat{g}_{11}\hat{V}_{10}\hat{G}_{00}. \tag{2.4.34}$$

And introducing $\hat{T} = \hat{g}_{11}\hat{V}_{10}$ we can write

$$\hat{G}_{00} = \left[\hat{I} - \hat{g}_C\hat{V}_{01}\hat{T}\right]^{-1}\hat{g}_{00} \tag{2.4.35}$$

$$\hat{G}_{10} = \hat{T}\hat{G}_{00}. \tag{2.4.36}$$

Now we can clearly see the we have $\hat{T}$ in the expanded expression in our previous equation. This allows us to calculate $\hat{G}_{00}$ quickly and easily.

2.5 THE LLOYD FORMULA

One of the ways of determining the physical properties of the system is by seeing which configuration leads to the lowest energy. Examining the changes in energy produced by the introduction of impurities can tell us about how they align, distribute etc. These calculations can be performed by finding the total energy in both configurations and subtracting. In fact, this method is often used in *ab-initio* calculations. However, this is computationally wasteful, since the energy changes are often minuscule compared to the total energy of the system itself. A much more ef-

ficient technique is outlined by the Lloyd formula [169]. In this scheme, the change in energy in response to a perturbation is given by

$$\begin{aligned}\Delta E &= \int dE\, E(\rho(E) - \rho_0(E)) \\ &= -\frac{1}{\pi}\mathrm{Im}\sum_j \int dE\, E[G_{jj}(E) - g_{jj}(E)],\end{aligned} \tag{2.5.1}$$

where $\rho(E)$ is the density of states in the perturbed system and $\rho_0(E)$ the DOS in the unperturbed system.

Now

$$\sum_j (G_{jj} - g_{jj}) = \mathrm{Tr}\,(\hat{G} - \hat{g}), \tag{2.5.2}$$

and using the Dyson equation this can be written as

$$\mathrm{Tr}\,(\hat{G} - \hat{g}) = \mathrm{Tr}\,(\hat{g}\hat{V}(1 - \hat{g}\hat{V})^{-1}\hat{g}), \tag{2.5.3}$$

and using the properties of the trace we have

$$\mathrm{Tr}\,(\hat{G} - \hat{g}) = \mathrm{Tr}\,(\hat{g}^2\hat{V}(1 - \hat{g}\hat{V})^{-1}), \tag{2.5.4}$$

and we can differentiate the operator getting

$$\hat{g} = (E\hat{I} - \hat{H})^{-2} = -\frac{d}{dE}\hat{g}. \tag{2.5.5}$$

Which allows us drastically simplify our expression for the difference of Green's functions

$$\begin{aligned}\Delta G &= -\mathrm{Tr}[\hat{g}'\hat{V}(\hat{I} - \hat{g}\hat{V})^{-1}] \\ &= \mathrm{Tr}[(\hat{I} - \hat{g}\hat{V})'(\hat{I} - \hat{g}\hat{V})^{-1}] \\ &= \frac{d}{dE}\mathrm{Tr}\ln(\hat{I} - \hat{g}\hat{V}),\end{aligned} \tag{2.5.6}$$

where we have here used the identity $\mathrm{Tr}(\ln \hat{A})' = \mathrm{Tr}[\hat{A}'\hat{A}]$. This means that we can write the change in the DOS as

$$\Delta\rho(E) = -\frac{1}{\pi}\mathrm{Im}\Delta G(E). \tag{2.5.7}$$

This allows us to calculate a number of useful quantities, for example, we can calculate the change in occupation number upon the introduction of an impurity by

$$\begin{aligned}\Delta N(E_F) &= \int_{-\infty}^{E_F} dE\, \Delta\rho(E) \\ &= -\frac{1}{\pi}\mathrm{Im}\ln\left(\det(\hat{I} - \hat{g}\hat{V})\right)\Big|_{E_F}.\end{aligned} \tag{2.5.8}$$

Finally, we return to our original purpose, calculating the change in energy due to the introduction of an impurity

$$\begin{aligned}\Delta E &= -\frac{1}{\pi}\mathrm{Im}\int_{-\infty}^{E_F} dE\, E\frac{d}{dE}\ln(\det(\hat{I} - \hat{g}\hat{V})) \\ &= E_F\Delta N(E_F) + \frac{1}{\pi}\mathrm{Im}\int_{-\infty}^{E_F} dE\, E\ln(\det(\hat{I} - \hat{g}\hat{V})).\end{aligned} \tag{2.5.9}$$

In most problems that we work on, we expect no change in the occupation number following the introduction of our impurity. Therefore the first term in the equation vanishes and we are left with

$$\Delta E = \mathrm{Im}\int_{-\infty}^{E_F} dE\, E\ln(\det(\hat{I} - \hat{g}\hat{V})). \tag{2.5.10}$$

2.6 INTEGRATING OVER GFS

Numerical integration of Green's function is complicated by the presence of short sharp peaks coming from the poles (these correspond to Van Hove singularities when working with the DOS). Further problems are introduced when working

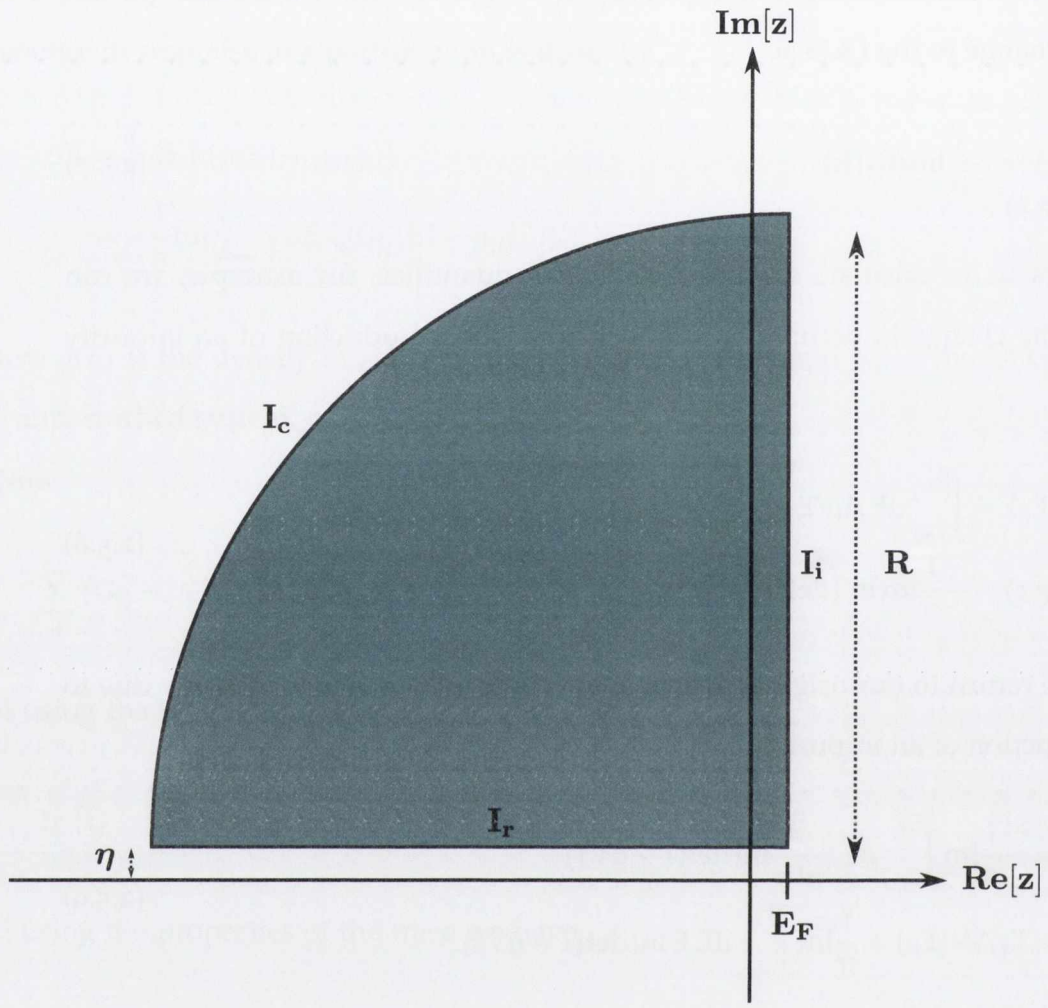


Figure 2.6: A schematic of the integration contour. There are no poles in the upper half plane, so integrating around the contour gives zero. If we let R go to infinity, the calculation of the crescent-shaped integral becomes trivial and the integral on the imaginary axis is far simpler than its real counterpart.

with perturbed systems, where bound states outside of the main energy band can make it difficult to choose an appropriate lower limit for the integral. We can remedy the first problem by noting that the retarded GF is analytic in the upper half plane, and therefore the integral around any contour in that region is equal to zero. This allows us to shift the integration from the real to the imaginary axis,

where the GF is generally much smoother. We use the example of the occupation at a single site. This is given by

$$n_i = \int_{-\infty}^{E_F} dE\, \rho_i(E) = -\frac{1}{\pi} \lim_{\eta \to 0} \mathrm{Im} \left[\int_{-\infty}^{E_F} dE\, G_{ii}(E + i\eta) \right]. \tag{2.6.1}$$

Our integration contour is shown in Fig. 2.6. Since the contour integral must vanish we write

$$I_r = -I_i - I_c. \tag{2.6.2}$$

In the limit where $R \to \infty$ we have $G \sim \frac{1}{z}$ and we can write the integral over the arc as

$$\begin{aligned} \lim_{R\to\infty} I_c &= \lim_{R\to\infty} \int_c dz \frac{1}{z} \\ &= \lim_{R\to\infty} \int_{\frac{\pi}{2}}^{\pi} (iRe^{i\theta} d\theta) \frac{1}{Re^{i\theta}} \\ &= \frac{i\pi}{2}. \end{aligned} \tag{2.6.3}$$

In cases where we have a product of GFs the integrand goes as z^{-2} and this contribution vanishes. Now we can write

$$\begin{aligned} n_i &= -\frac{1}{\pi} \mathrm{Im} \left[-i \lim_{\eta \to 0} \int_{\eta}^{\infty} dy\, G_{ii}(E_F + iy) - \frac{i\pi}{2} \right] \\ &= \frac{1}{2} + \frac{1}{\pi} \lim_{\eta \to 0} \int_{\eta}^{\infty} dy\, \mathrm{Re}[G_{ii}(E_F + iy)]. \end{aligned} \tag{2.6.4}$$

We still have the problem of the integration limit going to infinity. The substitution $y = \frac{1+\eta-t}{t}$ makes the limits more manageable.

$$n_i = \frac{1}{2} + \lim_{\eta \to 0} \frac{1+\eta}{\pi} \int_0^1 dt\, \frac{1}{t^2} \mathrm{Re} \left[G_{ii} \left(E_F + i \left(\frac{1+\eta-t}{t} \right) \right) \right]. \tag{2.6.5}$$

This technique allows us to vastly reduce the computational demand of our calculations, and is used every time we calculate the indirect exchange coupling in the next section.

2.7 ELECTRON-ELECTRON INTERACTIONS

Most of the time, when we build systems and examine their properties, we work in the absence of the electron-electron interaction. This dramatically simplifies our calculations, and most of the methods that we present in this chapter are invalid in its presence. However, the interaction is required in order to introduce magnetism into our system, so we need some manner of including it while still being able to use the mathematical techniques that we have so far presented. In this section, we show how to combine a Hubbard model with a self-consistency procedure in order to create magnetic objects while maintaining some of the benefits of the regular tight-binding scheme.

Since electron-electron interactions are a many body effect, it is easiest to start the calculation in second quantised form

$$H_{TB} = \sum_{ij\sigma} t_{ij} c^{\dagger}_{j\sigma} c_{i\sigma}. \tag{2.7.1}$$

This is the standard tight binding Hamiltonian, and the fact that it cannot lead to the formation of magnetic moments can be seen trivially by the fact that it is spin-degenerate. The creation of magnetic moments requires the presence of the coulomb interaction, which can be written in operator form as

$$V_{ab} = \frac{1}{2} \sum_{ijkl} \langle i, j | \frac{e^2}{r_{ab}} | k, l \rangle \sum_{\sigma\sigma'} c^{\dagger}_{i\sigma} c^{\dagger}_{j\sigma'} c_{k\sigma'} c_{l\sigma}. \tag{2.7.2}$$

And the expectation value can be written as

$$\langle i,j|\frac{e^2}{r_{ab}}|k,l\rangle = \int d\mathbf{r}_a \int d\mathbf{r}_b \psi_i^*(\mathbf{r}_a)\psi_j^*(\mathbf{r}_b)\frac{e^2}{r_{ab}}\psi_k(\mathbf{r}_b)\psi_l(\mathbf{r}_a). \tag{2.7.3}$$

The Hubbard model makes the assumption that electron screening restricts the interaction to on-site elements only, which corresponds to setting $i = j = k = l$ inside the above equations. Since the interaction is restricted to electrons sharing the same orbital, by the Pauli exclusion principal we have $\sigma \neq \sigma'$. The Hubbard Hamiltonian can now be written as

$$H_{Hub} = \frac{U}{2}\sum_{i\sigma} \hat{n}_{i\sigma}\hat{n}_{i\bar{\sigma}}, \tag{2.7.4}$$

where U is the diagonal Coulomb integral, and $\hat{n}_{i\sigma} = c_{i\sigma}^\dagger c_{i\sigma}$ is the occupation. So now our complete Hamiltonian looks like

$$H = \sum_{ij\sigma} t_{ij} c_{j\sigma}^\dagger c_{i\sigma} + \frac{U}{2}\sum_{i\sigma} \hat{n}_{i\sigma}\hat{n}_{i\bar{\sigma}}. \tag{2.7.5}$$

2.7.1 *The Hartree Fock Approximation*

We have simplified the interaction quite a bit, however, it is still not in a form that we can reliably calculate using the methods in this chapter. In order to do this, we use the Hartree Fock approximation which involves a simple substitution and then iteration until the field is self consistent.

We first make the trivial substitution

$$\hat{n}_{i\sigma} = \langle \hat{n}_{i\sigma}\rangle + (\hat{n}_{i\sigma} - \langle \hat{n}_{i\sigma}\rangle), \tag{2.7.6}$$

and then neglect terms of order $(n - \langle n \rangle)^2$. Within this approximation we get

$$\hat{n}_{i\sigma}\hat{n}_{i\bar{\sigma}} \approx \hat{n}_{i\sigma}\langle\hat{n}_{i\bar{\sigma}}\rangle + \hat{n}_{i\bar{\sigma}}\langle\hat{n}_{i\sigma}\rangle - \langle\hat{n}_{i\sigma}\rangle\langle\hat{n}_{i\bar{\sigma}}\rangle. \tag{2.7.7}$$

Now, we write the average occupation as

$$n_i = \langle\hat{n}_{i\uparrow}\rangle + \langle\hat{n}_{i\downarrow}\rangle, \tag{2.7.8}$$

and we write the dimensionless magnetic moment as

$$m_i = \langle\hat{n}_{i\uparrow}\rangle - \langle\hat{n}_{i\downarrow}\rangle. \tag{2.7.9}$$

So finally our Hamiltonian may be written so that

$$H = \sum_i \left(\frac{U}{2}(n_i \mp m_i) - U\langle\hat{n}_{i\sigma}\rangle\langle\hat{n}_{i\bar{\sigma}}\rangle\hat{n}_{i\sigma} \right). \tag{2.7.10}$$

Where the minus sign applies for spin up and the plus sign for spin down.

Casting our Hamiltonian within the Hartree Fock approximation means that the electron electron interaction can be approximated by a spin independent bandcenter shift

$$\delta_i = U\left(\frac{n_i}{2} - \langle\hat{n}_{i\sigma}\rangle\langle\hat{n}_{i\bar{\sigma}}\rangle\right), \tag{2.7.11}$$

and a spin dependent exchange splitting

$$\Delta_i = U m_i, \tag{2.7.12}$$

Therefore, the whole effect can be modelled as an on-site potential

$$V_{ii}^{\sigma} = \delta_i \mp \frac{\Delta_i}{2}, \tag{2.7.13}$$

where the minus sign applies for the spin up case and vice versa.

A schematic of the effect is shown in Fig.2.7. The spin up band is more occupied than the spin down equivalent and hence a magnetic moment is formed.

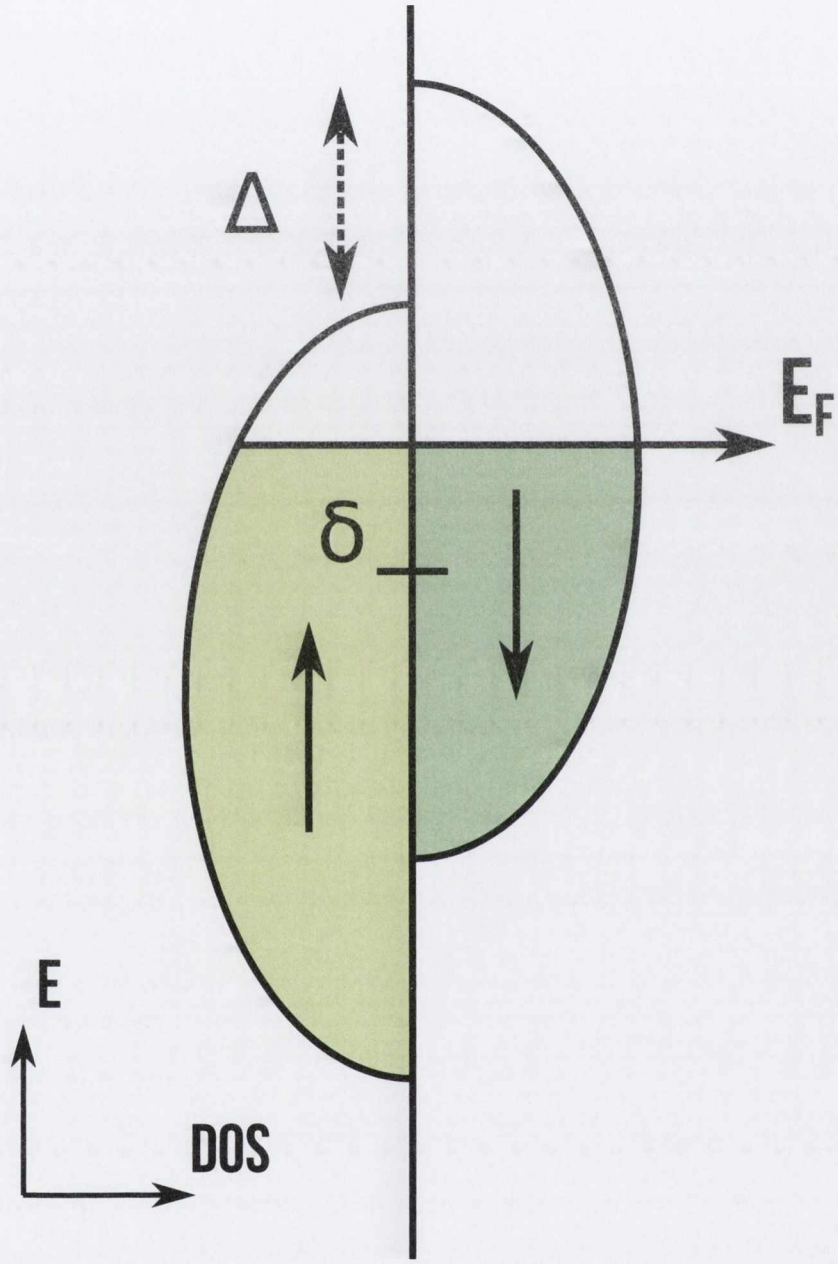


Figure 2.7: A plot of the spin-split LDOS in the presence of an appropriate impurity.

There are many cases where the quantities we are interested in are not highly sensitive to the type of impurity added, and therefore picking a representative bandcenter shift and exchange splitting is fine. However, in other situations, we

have to be very careful about the exact values of these quantities, and small deviations can lead to completely different results. In these situations an iterative self-consistency is employed, which works roughly as follows:

To start with we guess realistic values for the local magnetic moments, represented in vector form as $\mathbf{m}_0$. Then

1. We obtain the appropriate bandcenter shifts numerically using the formula

$$n_i = n_{i\uparrow}(\delta_1) + n_{i\downarrow}(\delta_1), \tag{2.7.14}$$

   where the n_i are obtained by integrating over the LDOS to the Fermi level.

2. New values for the local magnetic moments are obtained via

$$m_i^1 = n_{i\uparrow}(\delta_1)u - n_{i\downarrow}(\delta_1). \tag{2.7.15}$$

And these two steps are repeated until the desired level of convergence is obtained.

2.8 CHAPTER SUMMARY

In this chapter we introduced the mathematical methods that form the core of our thesis. We introduced the Green's function, and demonstrated how it could be used to find the LDOS in condensed matter systems. We also examined the Dyson equation as a means of introducing perturbations, and demonstrated its applicability to various impurity conformations. We demonstrated the calculations of energy differences by means of the Lloyd formula. We also showed how the GFs can be used in tandem with the Dyson equation to generate structures recursively. Finally, we finished with a discussion of electron-electron interactions, and how they may be approximated at certain sites. These techniques are used repeatedly throughout this thesis, and in the next chapter, we examine GFs in various graphene systems.

3

GREEN'S FUNCTIONS

Green's functions are used as part of a technique for solving partial differential equations. The basic method is to solve a simple equation $LG = \delta(x)$ as a proxy for solving the more complicated equation $LG = f(x)$. GFs turn up in a broad range of areas, but are particularly useful in condensed matter. In this work alone, GFs are used to determine the density of states, the indirect exchange coupling, the transverse magnetic susceptibility and the conductance of a variety of graphene systems.

In this chapter we will derive the GFs of the different graphene systems that we encounter in this thesis. We will examine various methods of deriving these functions, as well as different approximations that can be used to enhance the computational speed of calculations, and bring mathematical clarity to expressions. In each case the GFs will be used to obtain the LDOS, which in turn will influence the behaviour of many of the properties we will examine in this work. We begin our analysis with bulk graphene, introducing its edge variants afterwards.

3.1 GRAPHENE

We have already covered graphene thoroughly in the introduction, but we will review the essential elements here. At its most basic graphene consists of a 2d plane of carbon atoms arranged in a hexagonal, honeycomb lattice. It is very stable, due to strong σ bonds between the hybridised sp^2 orbitals. The band structure close to the Fermi level, however, is mostly due to the bonding of the out of plane π_z orbitals. For this reason, it is usual for calculations to take only these orbitals

into account, and we perform our calculations within this approximation. We break graphene into two separate triangular sublattices, represented by the black and white sites in Fig.3.1. In the figure we show our choice of unit cell, basis vectors, and a representative separation between sites, in order to illustrate our notation.

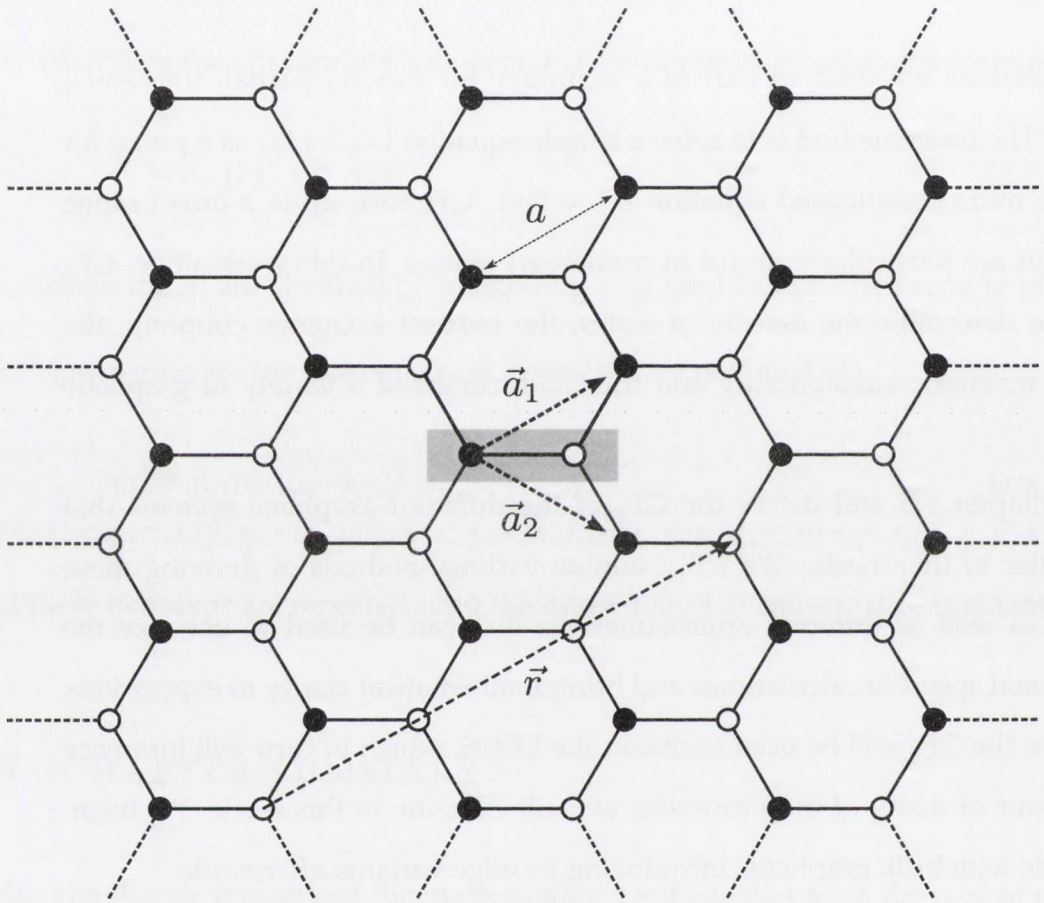


Figure 3.1: A schematic of our graphene system. Here we show both triangular sublattices in the black and white sites. Our choice of unit cell is shown by the black box surrounding both a black and white site. The nearest neighbour distance is given for a single sublattice by a. Our choice of basis vectors is shown by $\mathbf{a}_1$ and $\mathbf{a}_2$. Shown is a sample separation that can be alternately described by $m = 3, n = 0$ or $D_A = 3, D_Z = 3$ depending on the notation used.

3.1.1 *Band structure*

To calculate the band structure of graphene we need to first calculate the Hamiltonian. We use a nearest-neighbour tight-binding approximation for our Hamiltonian, where the eigenvectors $|\mathbf{r}, \alpha\rangle$ represent the electrons in the π_z orbitals at position $\mathbf{r}$ on sublattice α (where $\bullet$ and $\circ$ represent the black and white sublattices).

$$\hat{H} = \sum_{\mathbf{r}',\mathbf{r},\alpha,\beta} |\mathbf{r}, \alpha\rangle t \langle \mathbf{r}', \beta| \tag{3.1.1}$$

We can view its representation in reciprocal space using a Fourier transform

$$\hat{H} = \sum_{\mathbf{k}} f(\mathbf{k})|\mathbf{k}, \bullet\rangle\langle \mathbf{k}, \circ| + f^{\dagger}(\mathbf{k})|\mathbf{k}, \circ\rangle\langle \mathbf{k}, \bullet|, \tag{3.1.2}$$

where we have introduced $f(\mathbf{k}) = 1 + 2e^{ik_x \frac{\sqrt{3}}{2} a} \cos(\frac{k_y a}{2})$. Now the Hamiltonian can be written in the form of a simple 2x2 matrix.

$$\hat{H} = t \begin{pmatrix} 0 & f \\ f^{\dagger} & 0 \end{pmatrix}. \tag{3.1.3}$$

The eigenvalues of the matrix are given by

$$\epsilon_{\pm}(\mathbf{k}) = \pm t \sqrt{1 + 4\cos\left(k_x \frac{\sqrt{3}}{2} a\right)\cos\left(\frac{k_y a}{2}\right) + 4\cos^2\left(\frac{k_y a}{2}\right)}, \tag{3.1.4}$$

and they can be used to plot the bandstructure as shown in Fig.3.2, from which we can see the hexagonal Brillouin zone of graphene, and the linear dispersion around the Dirac Point. The corresponding eigenvectors are

$$\frac{1}{\sqrt{2}}\begin{pmatrix} 1 \\ \frac{f^\dagger}{|f|} \end{pmatrix} = |\mathbf{k}, +\rangle, \tag{3.1.5}$$

and

$$\frac{1}{\sqrt{2}}\begin{pmatrix} 1 \\ -\frac{f^\dagger}{|f|} \end{pmatrix} = |\mathbf{k}, -\rangle. \tag{3.1.6}$$

3.1.2 *Green's functions*

Recall from Eq.2.1.2 that the general GF is defined as

$$\hat{g} = \lim_{\eta \to 0} \left[E\hat{I} - \hat{H}\right]^{-1}, \tag{3.1.7}$$

where we have assumed that the small imaginary part is included in E (we work with the *retarded* GF). By working in the eigenbasis of graphene we can diagonalise the above expression and perform the inverse trivially

$$\begin{aligned} \hat{G} &= \sum \frac{|\psi\rangle\langle\psi|}{E - \epsilon} \\ &= \sum \frac{|\mathbf{k}, +\rangle\langle\mathbf{k}, +|}{E - \epsilon_+} + \frac{|\mathbf{k}, -\rangle\langle\mathbf{k}, -|}{E - \epsilon_-} \\ &= \sum \frac{|\mathbf{k}, +\rangle\langle\mathbf{k}, +|}{E - \epsilon_+} + \frac{|\mathbf{k}, -\rangle\langle\mathbf{k}, -|}{E + \epsilon_+}. \end{aligned} \tag{3.1.8}$$

This can be projected onto the position basis to get

$$\langle \mathbf{r}, \alpha | G | \mathbf{r}', \beta \rangle = G^{\alpha\beta}_{\mathbf{r}\mathbf{r}'}(E) = \frac{1}{N} \sum_{\mathbf{k}} \frac{N^{\alpha\beta} e^{i\mathbf{k}\cdot(\mathbf{r}'-\mathbf{r})}}{E^2 - \epsilon_+^2}, \tag{3.1.9}$$

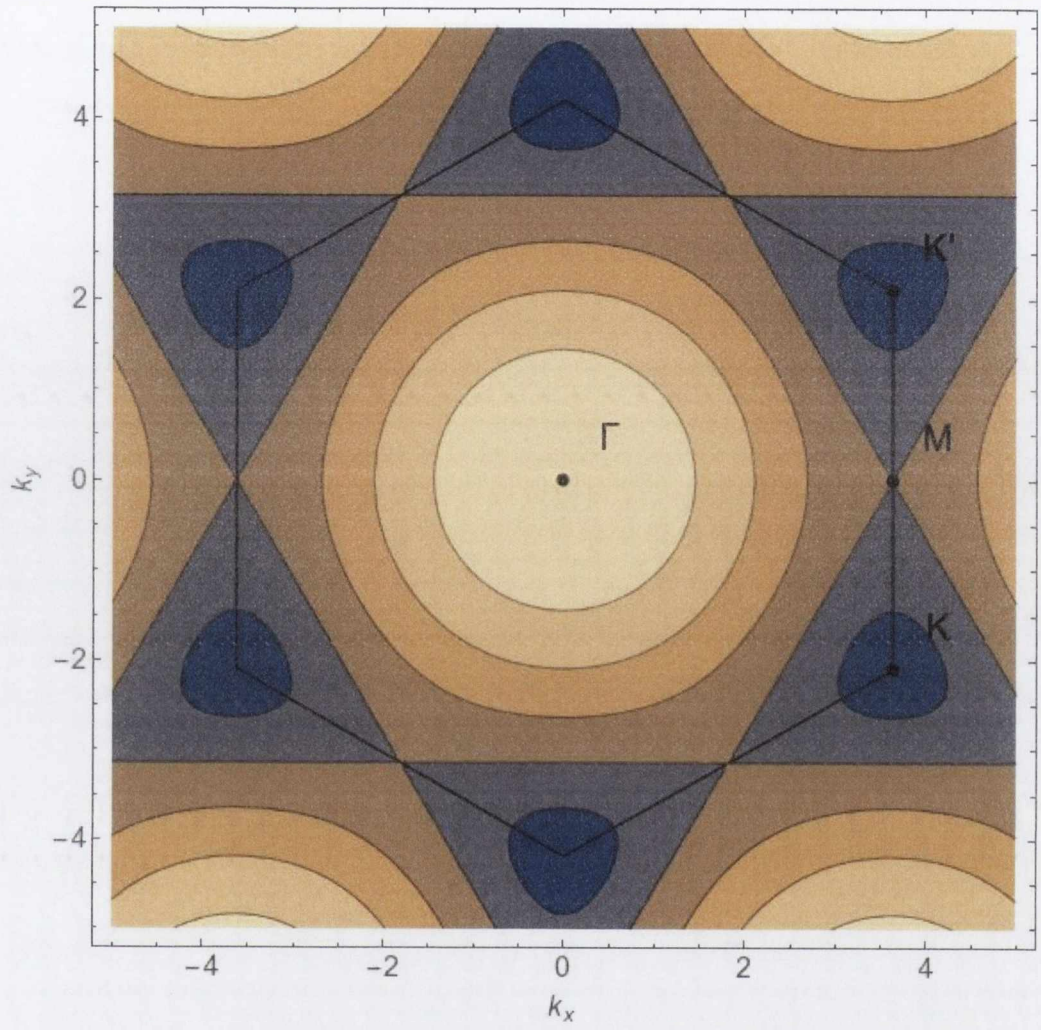


Figure 3.2: A contour plot of the graphene bandstructure. The symmetry points have been labelled. The hexagonal structure and Dirac points can clearly be seen.

where $N^{\alpha\beta}$ is a sublattice dependent term given by

$$N^{\alpha\beta} = \begin{cases} E & (\bullet,\bullet),(\circ,\circ) \\ tf & (\bullet,\circ) \\ tf^{\dagger} & (\circ,\bullet). \end{cases} \tag{3.1.10}$$

The sum in our expression for the GF may be taken over the Brillouin zone, and due to the infinite nature of the lattice is more naturally cast as an integral. The integration is complicated if conducted naively, since the BZ of graphene is

hexagonal, leading to an awkward choice of limits. However, it is possible to form equivalent periodic regions that we may integrate over, and this is approach is shown in the Appendix (Sec.A.1). This region may be constructed in two different ways, and this leads to two different choices of integration limits.

$$\sum_{k_x,k_y} \to \frac{\sqrt{3}a^2}{8\pi^2} \int_{-\frac{2\pi}{a}}^{\frac{2\pi}{a}} dk_y \int_{-\frac{\pi}{\sqrt{3}a}}^{\frac{\pi}{\sqrt{3}a}} dk_x, \tag{3.1.11}$$

and

$$\sum_{k_x,k_y} \to \frac{\sqrt{3}a^2}{8\pi^2} \int_{-\frac{\pi}{a}}^{\frac{\pi}{a}} dk_y \int_{-\frac{2\pi}{\sqrt{3}a}}^{\frac{2\pi}{\sqrt{3}a}} dk_x. \tag{3.1.12}$$

Both of these are acceptable choices and both will prove useful when we try to get the GF in a fully analytic form.

Our GF can now be written as

$$g^{\alpha\beta}_{\mathbf{r}\mathbf{r}'} = \frac{a^2\sqrt{3}}{8\pi^2} \int dk_y \int dk_x \frac{N^{\alpha\beta} e^{i\mathbf{k}\cdot(\mathbf{r}'-\mathbf{r})}}{E^2 - t^2|f|^2}. \tag{3.1.13}$$

Using the basis defined in Fig. 3.1, we can rewrite the difference in position vectors as

$$\begin{aligned} \mathbf{r}' - \mathbf{r} &= m\mathbf{a}_1 + n\mathbf{a}_2 \\ &= (m+n)\frac{\sqrt{3}}{2}a\mathbf{i} + (m-n)\frac{1}{2}a\mathbf{j}. \end{aligned} \tag{3.1.14}$$

Thus we can write our GF in the following form

$$g^{\alpha\beta}_{\mathbf{r}\mathbf{r}'} = \frac{a^2\sqrt{3}}{8\pi^2} \int dk_y \int dk_x \frac{N^{\alpha\beta} e^{ik_x(m+n)\frac{\sqrt{3}}{2}a + ik_y\frac{a}{2}(m-n)}}{E^2 - t^2|f|^2}. \tag{3.1.15}$$

We can further simplify this expression by using dimensionless variables $\frac{\sqrt{3}}{2}ak_x = k_A$ and $\frac{k_y a}{2} = k_Z$. Our final expression for the double integral version of our GF is

$$g^{\alpha\beta}_{\mathbf{r}\mathbf{r}'} = \frac{1}{2\pi^2}\int dk_Z \int dk_A \frac{N^{\alpha\beta} e^{ik_A(m+n)+ik_Z(m-n)}}{E^2 - t^2|f|^2}, \tag{3.1.16}$$

where in our new basis $f = 1 + 2e^{ik_A}\cos(k_Z)$.

The graphene GF can be used to examine a vast range of quantities. The easiest quantity to calculate is the LDOS, which is given in Eq.2.1.8 as $-\frac{\mathrm{Im}(g)}{\pi}$. A plot of the LDOS is shown in Fig.3.3 which again displays the linear behaviour around the Dirac point. This is responsible for a great deal of the unusual and exciting properties of graphene, and will influence our calculations in later chapters.

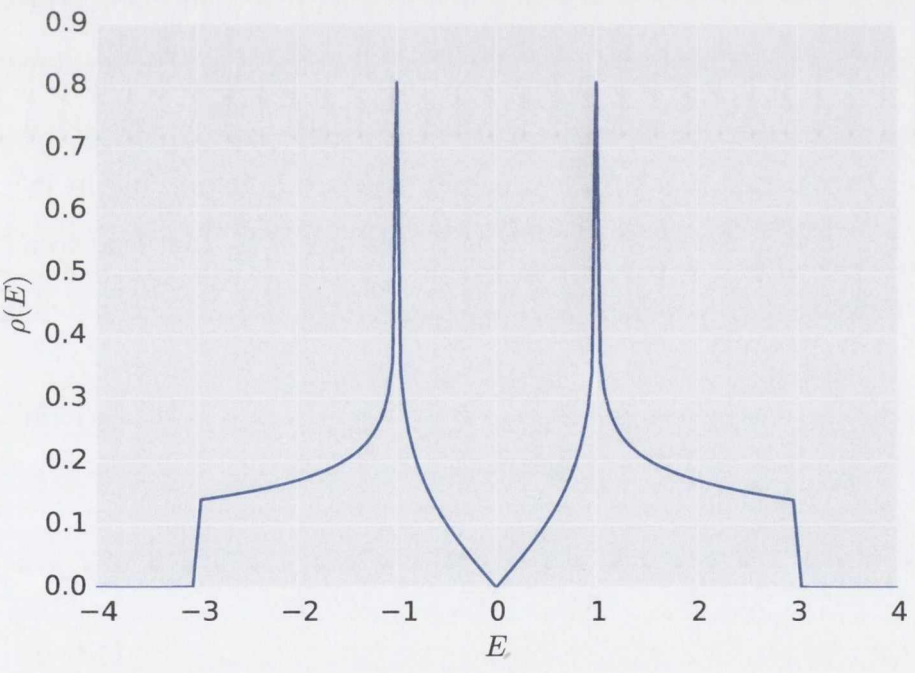


Figure 3.3: The LDOS at an atomic site in Graphene

3.1.3 *Contour Integration*

The GF given above in Eq.3.1.16 can be performed numerically. However, the double integration is costly, and hence it is beneficial to proceed analytically as far as possible. One of the integrals in our equations for the graphene GF can be performed by contour integration, hence allowing its more expedient evaluation when performed as part of an overall simulation.

Our two different choices of integration limits offer us two different ways of performing the contour integration. We first look at the integral over k_Z.

$$g^{\alpha\beta}_{\mathbf{r}\mathbf{r}'} = \frac{1}{2\pi^2}\int_{-\frac{\pi}{2}}^{\frac{\pi}{2}} dk_A \int_{-\pi}^{\pi} dk_Z \frac{N^{\alpha\beta} e^{ik_A(m+n)+ik_Z(m-n)}}{E^2 - t^2|f|^2} \tag{3.1.17}$$

We can rewrite this integral as a closed contour around the upper half plane. The details are not given here, but may be found in the appendix (Sec.A.2). The residue of a function $f(z) = \frac{g(z)}{h(z)}$ with a pole at z_0 is given by $\mathrm{Res}[f(z)] = \frac{g(z_0)}{h'(z_0)}$ (provided the pole is simple and the numerator and denominator are holomorphic in its neighbourhood). The poles are found by looking for values of k_A that lead to a vanishing denominator.

$$E^2 - t^2(1 + 4\cos(k_A)\cos(k_Z) + 4\cos^2(k_Z)) = 0 \tag{3.1.18}$$

$$\Rightarrow \cos(k_A) = \frac{-4\cos(k_A) \pm \sqrt{16\cos^2(k_A) - 4(1 - \frac{E^2}{t^2})}}{8} \tag{3.1.19}$$

$$\Rightarrow q^{\pm}(k_A) = \boxed{\pm}\cos^{-1}\left[\frac{1}{2}(-\cos(k_A) \pm \sqrt{\frac{E^2}{t^2} - \sin^2(k_A)}\right] \tag{3.1.20}$$

There are two poles ($\pm$) and the overall sign change ($\boxed{\pm}$) is chosen in order to bring the pole inside the contour. The residue is

$$\mathrm{Res}(g,q) = \frac{1}{t^2}\frac{N^{\alpha\beta}(k_A, q^{\pm})e^{i[k_A(m+n)+q^{\pm}(m-n)]}}{4\cos(k_A)\sin(q^{\pm}) + 8\cos(q^{\pm})\sin(q^{\pm})}, \tag{3.1.21}$$

and the GF may be written as

$$g^{\alpha\beta}_{\mathbf{r}\mathbf{r}'} = \frac{i}{4\pi t^2}\sum_{\pm}\int_{-\frac{\pi}{2}}^{\frac{\pi}{2}} dk_A \frac{N^{\alpha\beta}e^{i[k_A(m+n)+q^{\pm}(m-n)]}}{\cos(k_A)\sin(q^{\pm}) + \sin(2q^{\pm})}. \tag{3.1.22}$$

If we wish to perform the armchair integral first, we use a different, but equivalent choice of limits.

$$g^{\alpha\beta}_{\mathbf{r}\mathbf{r}'} = \frac{1}{2\pi^2}\int_{-\frac{\pi}{2}}^{\frac{\pi}{2}} dk_Z \int_{-\pi}^{\pi} dk_A \frac{N^{\alpha\beta}e^{ik_A(m+n)+ik_Z(m-n)}}{E^2 - t^2|f|^2}, \tag{3.1.23}$$

and poles are found in exactly the same manner.

$$q = \boxed{\pm}\cos^{-1}\left[\frac{E^2 - t^2 - 4t^2\cos^2(k_Z)}{4t^2\cos(k_Z)}\right] \tag{3.1.24}$$

And now the residue is given by

$$\mathrm{Res}(g,q) = \frac{\pi i}{2t^2}\frac{e^{iq(m+n)+ik_Z(m-n)}}{\cos(k_Z)\sin(q)}, \tag{3.1.25}$$

and

$$g^{\alpha\beta}_{\mathbf{r}\mathbf{r}'} = \frac{i}{4\pi t^2}\int_{-\frac{\pi}{2}}^{\frac{\pi}{2}} dk_Z \frac{N^{\alpha\beta}e^{iq(m+n)+ik_Z(m-n)}}{\cos(k_Z)\sin(q)}. \tag{3.1.26}$$

It is often convenient to work in a basis wherein $D_A = (m+n)$ and $D_Z = (m-n)$. Now D_A can be thought of as representing atomic steps in the armchair direction, and D_Z represents the same thing in the zigzag direction.

$$g^{\alpha\beta}_{\mathbf{r}\mathbf{r}'} = \frac{i}{4\pi t^2}\int_{-\frac{\pi}{2}}^{\frac{\pi}{2}} dk_Z \frac{N^{\alpha\beta}e^{iqD_A+ik_ZD_Z}}{\cos(k_Z)\sin(q)} \tag{3.1.27}$$

3.1.4 *The Stationary Phase Approximation*

Analytic work with graphene GFs is typically performed in the linear dispersion regime [99, 100]. While this is useful, it is only valid at low energies. Examination of the GF across the energy band can be performed at large separations using a different approximation, known as the Stationary Phase Approximation (SPA). The SPA works by assuming that highly oscillatory integrands cancel over the bulk of the integration range, and may be evaluated solely by looking at individual *stationary points*. The derivation is shown in the appendix (Sec.B.2), and can be summarised by saying that integrals of the form

$$I(x) = \int dy\, f(y) e^{i\phi(y)x}, \tag{3.1.28}$$

can be approximated by

$$I_{y_0}(x) = f(y_0) e^{i\phi(y_0)x} \sqrt{\frac{2i\pi}{\phi''(y_0)x}}, \tag{3.1.29}$$

where x is very large.

3.1.4.1 *Zigzag*

The stationary phase approximation simplifies dramatically for the two high symmetry direction in graphene. In the zigzag direction, our Green's function is

$$g^{\bullet\bullet}_{rr'} = \frac{i}{4\pi t^2} \sum_{\pm} \int_{-\pi}^{\pi} dk_A \frac{N^{\alpha\beta} e^{i[k_A D_A + q^{\pm} D_Z]}}{\cos(k_A)\sin(q^{\pm}) + \sin(2q^{\pm})}. \tag{3.1.30}$$

We work in the zigzag direction, where we have $D_A = 0$

$$g^{\bullet\bullet}_{rr'} = \frac{i}{4\pi t^2} \sum_{\pm} \int_{-\pi}^{\pi} dk_A \frac{E e^{iq^{\pm} D_Z}}{\cos(k_A)\sin(q^{\pm}) + \sin(2q^{\pm})}. \tag{3.1.31}$$

Now we can write our entire GF within the SPA as

$$g^{\bullet\bullet}_{rr'} = \frac{i}{4\pi t^2}\sum_{\pm}\int_{-\pi}^{\pi} dk_A \frac{Ee^{iq^0_{\pm}D_Z}}{\cos(k^0_A)\sin(q^0_{\pm})+\sin(2q^0_{\pm})}\sqrt{\frac{2i\pi}{q^0_{\pm}{}''D_Z}}. \tag{3.1.32}$$

To find the stationary point, we solve the equation $q'_{\pm}(k_A) = 0$, which has solution $k_A = 0$

We now need to evaluate all of the relevant quantities at the stationary point. We get

$$q^0_{\pm} = \boxed{\pm}\cos^{-1}\left[\frac{1}{2}\left(-1 \pm \sqrt{\frac{E^2}{t^2}}\right)\right], \tag{3.1.33}$$

and

$$q^0_{\pm}{}'' = \boxed{\mp}\frac{1 \mp \frac{1}{\sqrt{\frac{E^2}{t^2}}}}{2\sqrt{1-\frac{1}{4}\left(-1 \pm \sqrt{\frac{E^2}{t^2}}\right)^2}}. \tag{3.1.34}$$

Now we look at the relevant trigonometric quantities.

$$\begin{aligned}\cos(q^0_{\pm}) &= \frac{1}{2}\left(-1 \pm \sqrt{\frac{E^2}{t^2}}\right)\\ \sin(q^0_{\pm}) &= \boxed{\pm}\sqrt{1-\frac{1}{4}\left(1 \mp \sqrt{\frac{E^2}{t^2}}\right)^2}\end{aligned} \tag{3.1.35}$$

Now, substituting all of these terms into our GFs and simplifying we get

$$g^{\bullet\bullet}_{rr'} = \boxed{\pm}\sum_{\pm}\pm\frac{i}{2\pi t^2}\frac{Ee^{\boxed{\pm}iD_Z\cos^{-1}\left[\frac{1}{2}\left(-1\pm\sqrt{\frac{E^2}{t^2}}\right)\right]}}{\left[4-\left(1\mp\sqrt{\frac{E^2}{t^2}}\right)^2\right]^{\frac{1}{4}}}\sqrt{\boxed{\mp}\frac{i\pi}{D_Z\left(\frac{E^2}{t^2}+\sqrt{\frac{E^2}{t^2}}\right)}}. \tag{3.1.36}$$

3.1.4.2 *Armchair*

We can perform the exact same treatment in the Armchair direction, except now we find two poles. Going through the same steps as before we get

$$g^{\bullet\bullet}_{rr'} = \boxed{\pm}\frac{iEe^{\boxed{\pm}iD_A\cos^{-1}\left(\frac{E^2-5t^2}{4t^2}\right)}}{[(E^2-9t^2)(-E^2+t^2)]^{\frac{1}{4}}}\sqrt{\boxed{\mp}\frac{i}{D_A\pi(3t^2+E^2)}} \\ \boxed{\pm}\frac{iEe^{\boxed{\pm}iD_A\cos^{-1}\left(\sqrt{1-\frac{E^2}{t^2}}\right)}}{(E^2(t^2-E^2))^{\frac{1}{4}}\sqrt{3t^2+E^2}}\sqrt{\boxed{\pm}\frac{i}{\pi D_A}}. \tag{3.1.37}$$

The excellent match of the SPA in both directions is illustrated in Fig. 3.4.

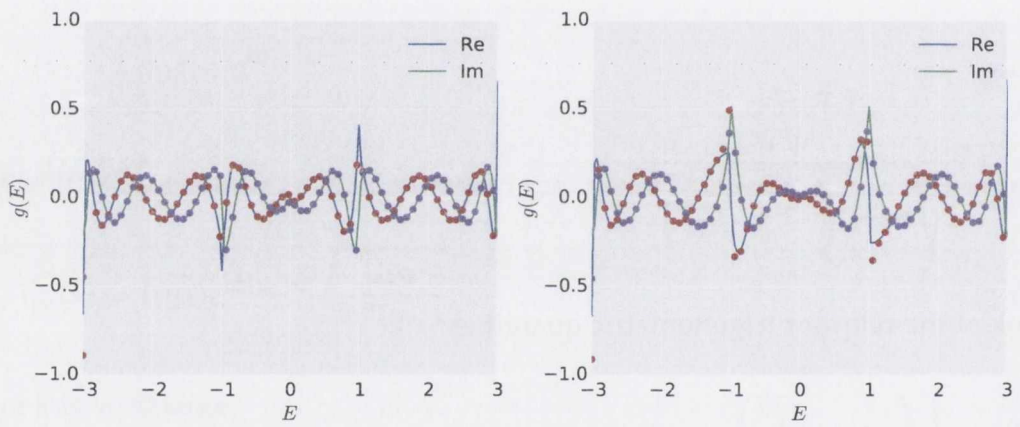


Figure 3.4: Plots the numerically calculated GF against its SPA equivalent. The plot on the left shows a separation of 3 unit cells in the armchair direction and the plot on the right a separation of 5 in the zigzag direction. The lines represent the real and imaginary parts of the numerically calculated GF and the dots the SPA. It can be seen that a good match is achieved even at a low separation.

The results of the SPA can be summarised as a GF of the form

$$G_{BA}(E) = \frac{\mathcal{A}(E)e^{iQ(E)D}}{\sqrt{D}}, \tag{3.1.38}$$

which is essential to our analytic determination of the IEC decay rates.

3.2 SEMI-INFINITE GRAPHENE

Edged graphene is interesting as a material in its own right, as many of graphene's properties are drastically modified in the presence of an edge. In this section we examine semi-infinite graphene, or graphene with a single edge. Armchair edges are more naturally introduced from a mathematical perspective, and tend to be less examined in the literature, so we focus on them here. With this in mind, we derive the GFs of semi-infinite graphene with a single armchair edge. This will allow us to examine the LDOS and demonstrate some interesting features.

Many of the techniques necessary to derive the semi-infinite (SI) graphene GFs have already been developed in the previous section and will be glossed over here. The SI GF may be derived using the *linear combination method* which leads to an integral form of the GF similar to what we have already found in bulk. It may also be derived using the *image method* which allows us to write the SI GF directly in terms of its bulk counterparts. This can provide additional insight into the relationship between bulk and edged behaviours.

3.2.1 *Linear combination method*

Any linear combination of the eigenstates of a linear operator is itself an eigenstate. Therefore we can form a new eigenbasis for our graphene Hamiltonian using the eigenstates below

$$|\phi_{\mathbf{k}}, \pm\rangle = \frac{1}{\sqrt{2}} \left(|(k_x, k_y), \pm\rangle - |(k_x, -k_y), \pm\rangle \right), \tag{3.2.1}$$

which have the exact same eigenvalues as our original basis. However, these eigenstates have no projection along the line $y = 0$ (Fig.3.5), meaning that we have broken our graphene sheet up into two halves, both terminating in armchair edges.

The Green's functions are obtained in the exact same manner as before, and our general expression for the GF becomes

$$\hat{g}(E) = \sum \frac{|\phi_{\mathbf{k}}, +\rangle\langle\phi_{\mathbf{k}}, +|}{E - \epsilon_+} + \frac{|\phi_{\mathbf{k}}, -\rangle\langle\phi_{\mathbf{k}}, -|}{E + \epsilon_+}. \tag{3.2.2}$$

Projecting this onto the position basis gives us

$$\begin{aligned}\langle \mathbf{r}_1, \alpha|g(E)|\mathbf{r}_2, \beta\rangle = \frac{a^2\sqrt{3}}{4\pi} \int dk_y \int dk_x \\ \times \frac{N^{\alpha\beta} e^{ik_x(x_2 - x_1)} \sin(k_y y_1) \sin(k_y y_2)}{E^2 - t^2|f|^2}.\end{aligned} \tag{3.2.3}$$

Reducing this to single integral form by contour integration is almost identical to the procedure in bulk.

$$g^{\alpha\beta}_{\mathbf{r}_1\mathbf{r}_2} = \frac{i}{2\pi t^2} \int_{-\frac{\pi}{2}}^{\frac{\pi}{2}} dk_Z \frac{N^{\alpha\beta} e^{iqD_A} \sin(k_Z D_{Z1} D_{Z2})}{\cos(k_Z)\sin(q)} \tag{3.2.4}$$

And the meaning of our particular notation is best shown through example in Fig.3.5.

We look at armchair separations so often that it will be convenient to put this in a form suitable for such work. For armchair separations we have $D_{Z1} = D_{Z2} = D_Z$ and we can write

$$g(D_A, D_Z, E) = \frac{i}{2\pi t^2} \int_{-\frac{\pi}{2}}^{\frac{\pi}{2}} dk_Z \frac{E e^{iqD_A} \sin^2(k_Z D_Z)}{\cos(k_Z)\sin(q)}. \tag{3.2.5}$$

3.2.2 *Image method*

When working with the linear combination method, we form a SI GF by working with combinations of bulk eigenstates. The fact that this is possible makes it natural to consider whether we can write the GFs of SI graphene in terms of those in bulk.

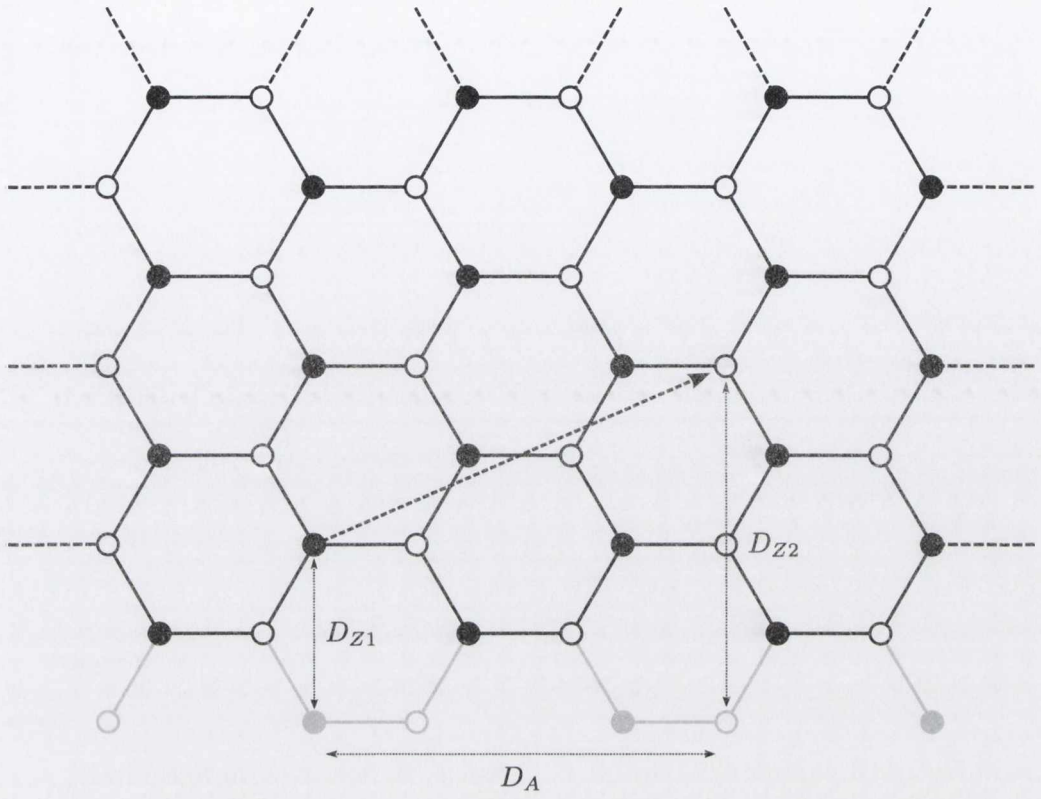


Figure 3.5: A schematic of the SI system demonstrating our notation. Particular attention should be paid to D_{Z1} and D_{Z2} which give the distances from the edge of the two sites. For a GF between the sites shown we have $D_A = 3$, $D_{Z1} = 2$, $D_{Z2} = 4$ and $s = 1$.

It turns out that this is both possible, and results in a simple geometric picture, analogous to the image method in electrostatics.

If we can expand out Eq. 3.2.2 in terms of the bulk eigenvectors, it is quickly clear that some of the terms resemble bulk GFs. In particular

$$\hat{g}_{AB}(E) = \sum \frac{|(k_x, k_y), +\rangle\langle(k_x, k_y), +|}{E - \epsilon_+} + \frac{|(k_x, k_y), -\rangle\langle(k_x, k_y), -|}{E + \epsilon_+}, \tag{3.2.6}$$

is instantly recognisable as the standard bulk GF (our choice of notation in $\hat{g}_{AB}$ will become apparent later). However, most terms contain a $-k_y$, and this is where the difficulty arises. And example of such a term is given by

$$\hat{g}_{AB'}(E) = \sum \frac{|(k_x, k_y), +\rangle\langle(k_x, -k_y), +|}{E - \epsilon_+} + \frac{|(k_x, k_y), -\rangle\langle(k_x, -k_y), -|}{E + \epsilon_+}. \tag{3.2.7}$$

These do not fit our criteria for bulk GFs, however, it is possible to show that the minus sign in the k basis may be translated to the position basis upon projection. Examining the term $\langle \mathbf{r}, \alpha|\mathbf{k}, \pm\rangle$ through a Fourier transform we can write

$$\begin{aligned}\langle \mathbf{r}, \alpha|\mathbf{k}, \pm\rangle &= \langle \mathbf{r}, \alpha|\frac{1}{\sqrt{2N}} \sum_{\mathbf{r}'} e^{-i\mathbf{k}\cdot\mathbf{r}'} \left(|\mathbf{r}', \bullet\rangle \pm \frac{f^\dagger(\mathbf{k})}{|f(\mathbf{k})|} |\mathbf{r}', \circ\rangle \right) \\ &= e^{-i\mathbf{k}\cdot\mathbf{r}} \mathcal{F}(k_x, k_y, \alpha).\end{aligned} \tag{3.2.8}$$

Here $\mathcal{F}$ is a sublattice dependent function of k_x and k_y which is symmetric in k_y, and therefore we can write

$$\begin{aligned}\langle (x, y), \alpha|(k_x, -k_y), \pm\rangle &= e^{-ik_x x + ik_y y} \mathcal{F}(k_x, k_y, \alpha) \\ &= \langle (x, -y)|(k_x, k_y), \pm\rangle.\end{aligned} \tag{3.2.9}$$

Therefore a change in the sign of k_y is equivalent to reflecting the vector $\mathbf{r}$ around the x-axis. Thus $\langle \mathbf{r}_1, \alpha|\hat{g}_{AB'}(E)|\mathbf{r}_2, \beta\rangle$ can be seen as the GF between $\mathbf{r}_1$ and the reflection of $\mathbf{r}_2$. Expanding out our SI eigenstates, it is now easy to see that our SI GF is equal to a sum of all of the bulk GFs between the relevant atoms and their images. A geometric view of these results is shown in Fig. 3.6, which demonstrates that the calculation of the semi-infinite GFs is analogous to the image method found in electrostatics, and makes our notation clear.

$$\begin{aligned}g^{SI}_{AB}(E) &= \frac{1}{2}\left(g_{AB}(E) - g_{AB'}(E) - g_{A'B}(E) + g_{A'B'}(E)\right) \\ &= g_{AB}(E) - g_{AB'}(E)\end{aligned} \tag{3.2.10}$$

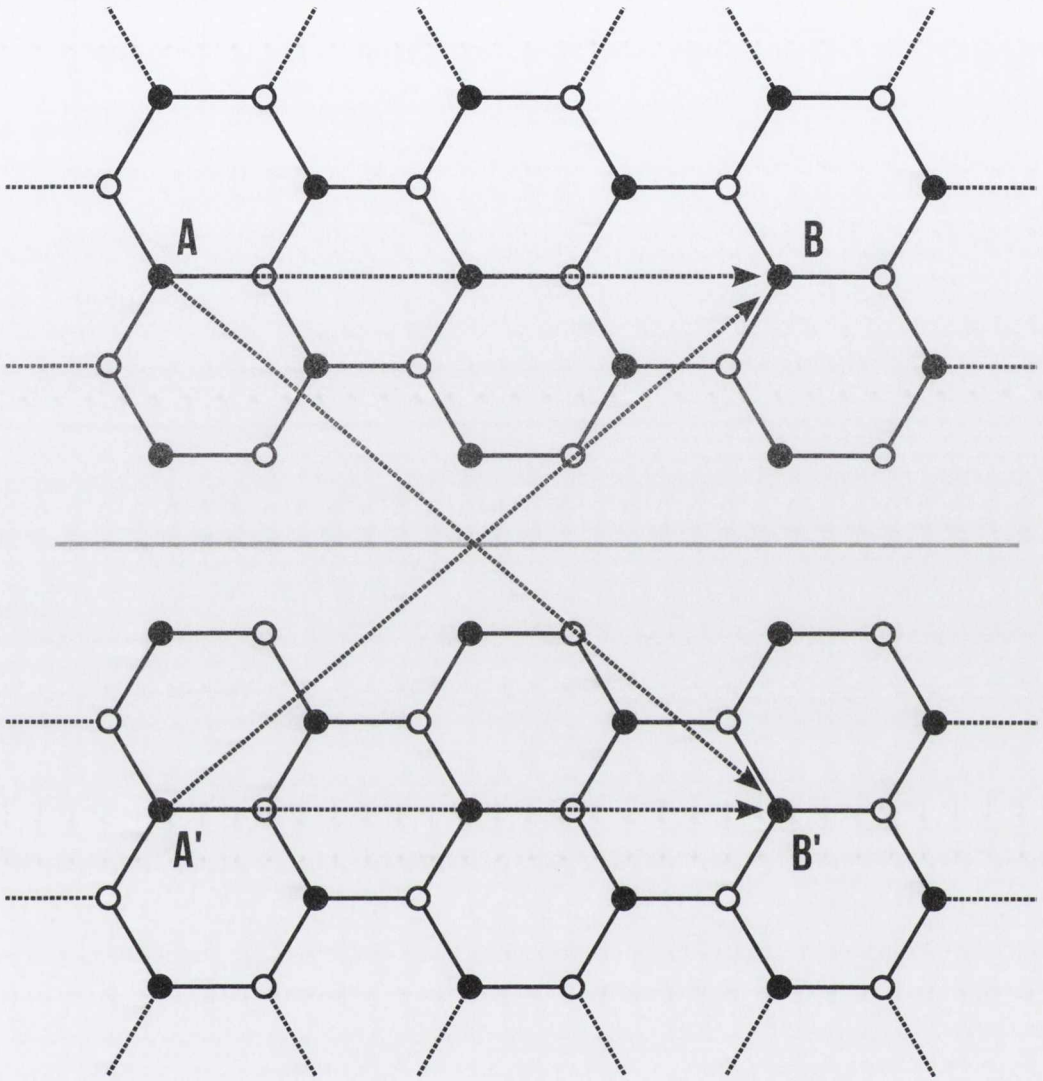


Figure 3.6: A figure illustrating the image method, for a GF with $n_E = 3$, $D = 3$. A single GF in SI graphene can be written as a combination four bulk GFs connecting the relevant atoms with their images in another SI sheet.

Where we have eliminated two of the GFs by symmetry. We note here that as we move away from the edge the amplitude of $g_{AB'}(E)$ declines much faster than $g_{AB}(E)$, and we recover the bulk GFs.

Now that we have the GFs we can plot the LDOS. In Fig.3.7 we plot the LDOS for the first 3 sites from the edge. In the first two plots the LDOS is linear around the Dirac point, identical to the behaviour we get in bulk graphene. However, at the third point we find the LDOS is significantly more smooth, indicative of vanishing

derivatives. When we repeat this calculation for sites further into the sheet, we find that the pattern repeats. Thus we end up with a triadic pattern in the smoothness of the LDOS, which we will later find has important consequences for the indirect exchange coupling, and marks the middle ground between bulk and nanoribbon forms of graphene. Finally, when we move far enough into the sheet, we start to find that the linear behaviour around the Dirac point starts to become ubiquitous again.

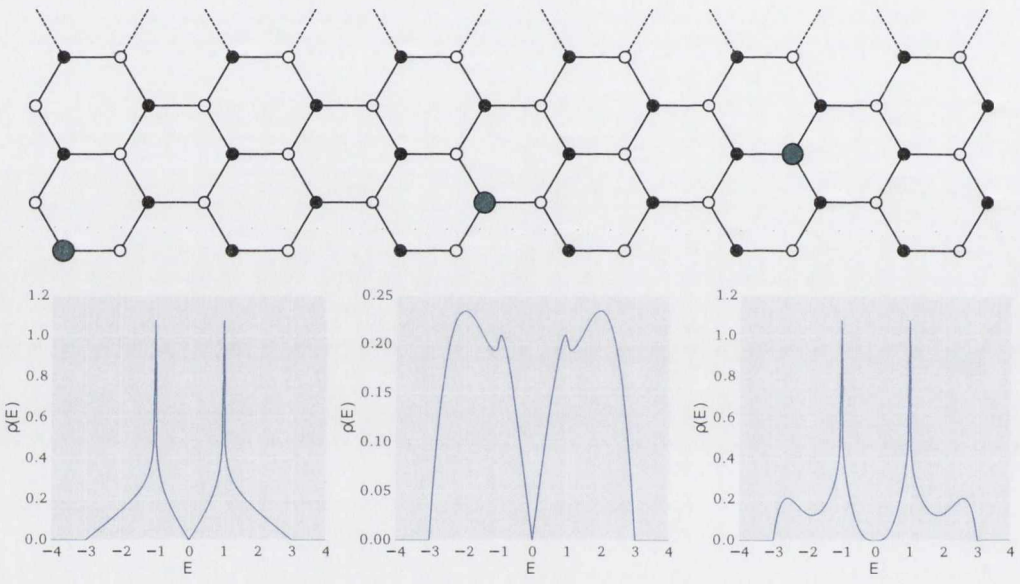


Figure 3.7: The LDOS for SI graphene at the first three atomic sites from the edge ($D_Z \in \{1, 2, 3\}$). The third site is significantly smoother around the Dirac point. The is the beginning of a triadic pattern that continues well into the sheet.

3.2.3 *The SPA*

Just as when working in bulk, we can use the SPA to find an analytic expression for the GF. The procedure is the same as that outlined in our bulk section, and our SPA GF is given by

$$g(D_A, D_Z, E) = \pm 2iEe^{\pm iD_A \cos^{-1}\left(\frac{\sqrt{t^2-E^2}}{t}\right)} \times \frac{\sin^2\left[D_Z \sin^{-1}\left(\frac{\sqrt{E^2+3t^2}}{2t}\right)\right]}{\sqrt{E^2+3t^2}\,[E^2(t^2-E^2)]^{\frac{1}{4}}} \sqrt{\pm\frac{2i}{D_A\pi}}, \tag{3.2.11}$$

where $\pm = -\text{Sign}[E]$. Plots of the SPA against the numerically integrated GF are shown in figure 3.8, and indicate that best results are found close to the edge and at large separations. As stated in the section on bulk graphene the true advantage of the SPA is the ability to put the GF in the form of Eq.3.1.38. This will be beneficial when we look at the indirect exchange coupling in the next chapter.

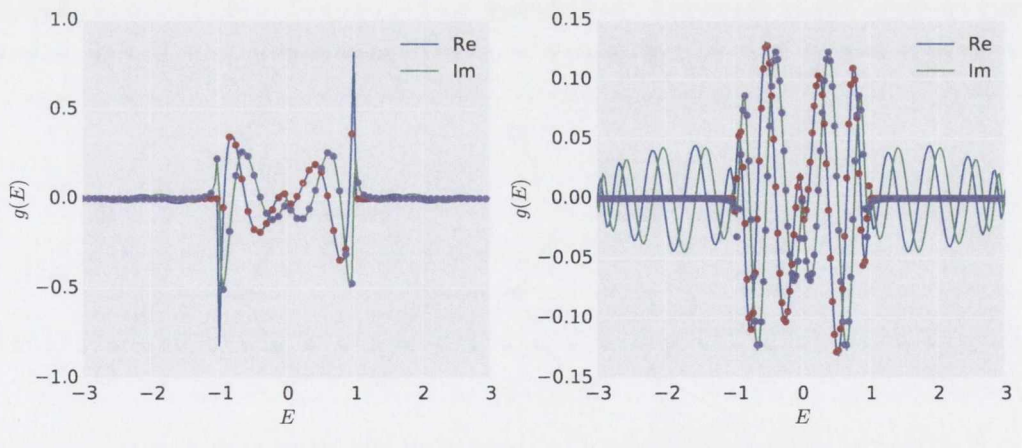


Figure 3.8: A comparison of the SPA against numerical obtained GFs for different distances from the edge and separations. The figure on the left is calculated for $D_Z = 1$ and $D_A = 3$. The figure on the right is calculated for $D_Z = 2$ and $D_A = 5$. The lines represent our numerical calculations and the dots the SPA. As can be seen, the approximation is best close to the edge and at large armchair separations.

3.3 NANORIBBONS

Similar to our work with SI graphene, when working with nanoribbons we normally examine those with armchair edges. Armchair graphene nanoribbons are characterised by the number of atoms N in a zigzag strip and are only metallic for $N = 3n + 2 \quad n \in \mathbb{N}$ [48, 53]. We will generally work in metallic nanoribbons, where many of the physical effects we examine are more important (such as the IEC and the conductance). However, semi-infinite nanoribbons offer a good way to test some of our calculations.

The GFs for graphene nanoribbons are normally calculated using the recursive techniques shown in Sec.2.4. Hence this is the perfect place for us to give an introduction to the practical application of these methods. However, the GF of the AGNR can also be derived completely analytically (without recourse to the SPA), and we begin by showing this derivation.

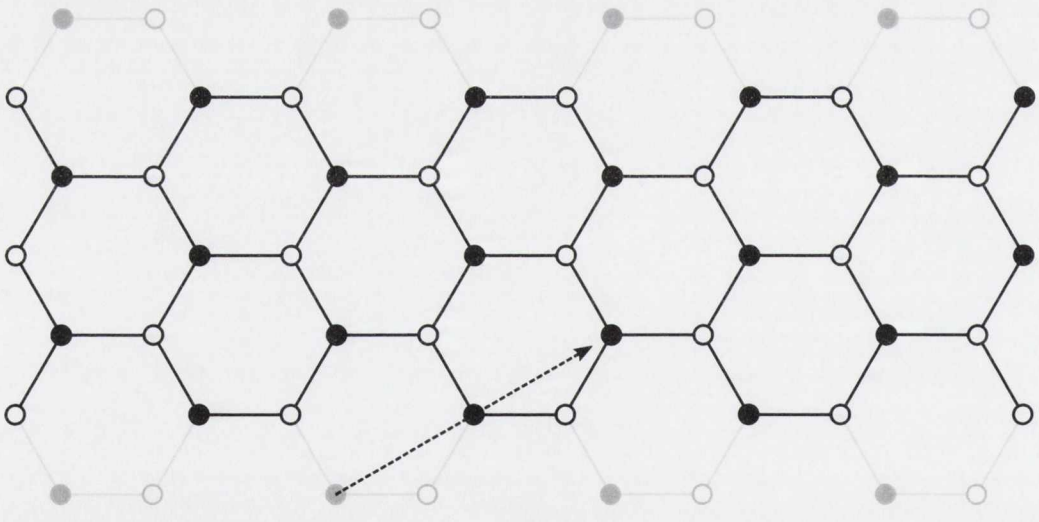


Figure 3.9: A figure illustrating the analytic construction of the graphene nanoribbons. The faded sites vanish, leaving a nanoribbon. The case shown has $n_E = 6$. Positions are determined from the lower vanishing edge, as shown.

3.3.1 *Analytic*

We start with the eigenvectors of our SI Hamiltonian

$$|\phi_{\mathbf{k}}, \pm\rangle = \frac{1}{\sqrt{2}}\left(|(k_x, k_y), \pm]\rangle - |(k_x, -k_y), \pm\rangle\right). \tag{3.3.1}$$

These can be written as

$$|\phi_{\mathbf{k}}, \pm\rangle = \frac{1}{2}\left[\left(|k_x, k_y, \bullet\rangle - |k_x, -k_y, \bullet\rangle\right) \pm \left(|k_x, k_y, \circ\rangle - |k_x, -k_y, \circ\rangle\right)\right]. \tag{3.3.2}$$

And a Fourier transform gives

$$|k_x, k_y, \alpha\rangle - |k_x, -k_y, \alpha\rangle = -2i \sum_{x,y} e^{-ik_x x} \sin(k_y y)|x, y, \alpha\rangle. \tag{3.3.3}$$

Now we want the projection $\langle x, n_E \frac{a}{2}|\phi_k\rangle$ to vanish, as shown in Fig.3.9. We are introducing the variable n_E, which given the number of sites between vanishing edges, and can simply be written as $N + 1$. However, n_E is more appropriate for analytic calculations.

$$-2ie^{-ik_x x} \sin(k_y n_E \frac{a}{2}) = 0 \tag{3.3.4}$$

Which gives us $k_y = \frac{2\pi j}{n_E a}$.

Our resulting GF is almost identical to the SI case, save for the presence of a sum.

$$\hat{g} = \frac{\sqrt{3}a}{2\pi N_y} \sum_{k_y} \int_{-\frac{2\pi}{\sqrt{3}a}}^{\frac{2\pi}{\sqrt{3}a}} dk_x \, \frac{N^{\alpha\beta} e^{ik_x(x_2 - x_1)} \sin(k_y y_1) \sin(k_y y_2)}{E^2 - t^2|f|^2} \tag{3.3.5}$$

Performing the usual transformations gives us

$$\frac{i}{2n_E t^2} \sum_j \frac{N^{\alpha\beta} e^{iq(m_2 + n_2 - m_1 - n_1)} \sin[\frac{\pi j}{n_E}(m_2 - n_2)] \sin[\frac{\pi j}{n_E}(m_1 - n_1)]}{\cos(\frac{\pi j}{n_E}) \sin(q)}. \tag{3.3.6}$$

While this form of nanoribbon GF will prove useful in our examination of the indirect exchange coupling, it is slightly more cumbersome when calculating the conductance. That is because the conductance (Chapter 7) requires the implementation of a large scattering region, which is far less computationally intensive using recursive methods. As a consequence, we take the time here to introduce some recursive techniques that we will be using.

Now that we have our GF we can go about examining the DOS. Plots of the LDOS in a metallic nanoribbon are given in Fig.3.10 and show an alternating pattern whereby everything third site has a bandgap. Since this bandgap extended across the entire lines of sites with $D_Z = 3$ we refer to these as lines of vanishing local density of states (VLDOS). It is immediately apparent that this is the extreme version of the triadic pattern seen in semi-infinite graphene, and thus we can see the progression between our different systems and how each is the limiting case of the other. For easy of visualisation a plot of the LDOS vs distance from the edge is shown in Fig.3.11. Since the LDOS is a strong predictor of various material properties, we would expect the various quantities we examine in this thesis to show a strong dependence on adsorption position, and in future chapters we will see that this is the case. The nanoribbon LDOS will prove very useful in future chapters, as we examine the indirect exchange coupling, dynamic interaction and conductance. Finally, we plot the DOS for an entire nanoribbon where we do not have $N = 3n + 2$ in Fig.3.12, and show that it is indeed semi-conducting, as predicted.

3.3.2 *Recursive*

We can also build nanoribbons using the recursive techniques outlined in Sec.2.4. In order to build our nanoribbons, we first need to have an idea of our unit cell. Examples are shown in Fig. 3.13, from which it is obvious that odd and even nanoribbons

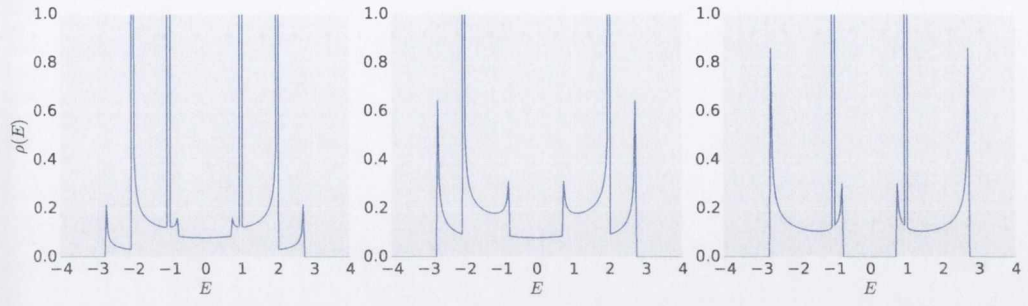


Figure 3.10: The LDOS in a $n_E = 6$ GNR at the first 3 atomic sites from the edge. Every third atom displays a bandgap.

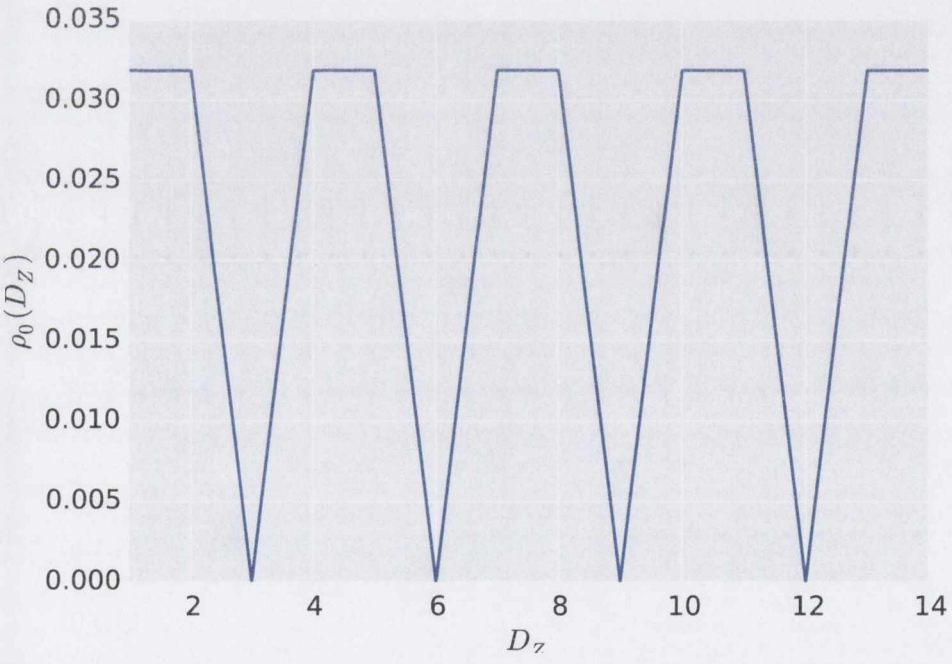


Figure 3.11: A plot of the LDOS at $E_F = 0$ vs edge distance in a AGNR with $n_E = 15$. Shows the triadic behaviour that we expect

need to be built in a slightly different way. However, with a bit of care it is possible to write a general Hamiltonian for both cases.

$$H = t \sum_{i \in S_1 \bigcup S_2} |i\rangle\langle i+1| + t \sum_{i \in S_3} |i\rangle\langle i+N| + h.c. \tag{3.3.7}$$

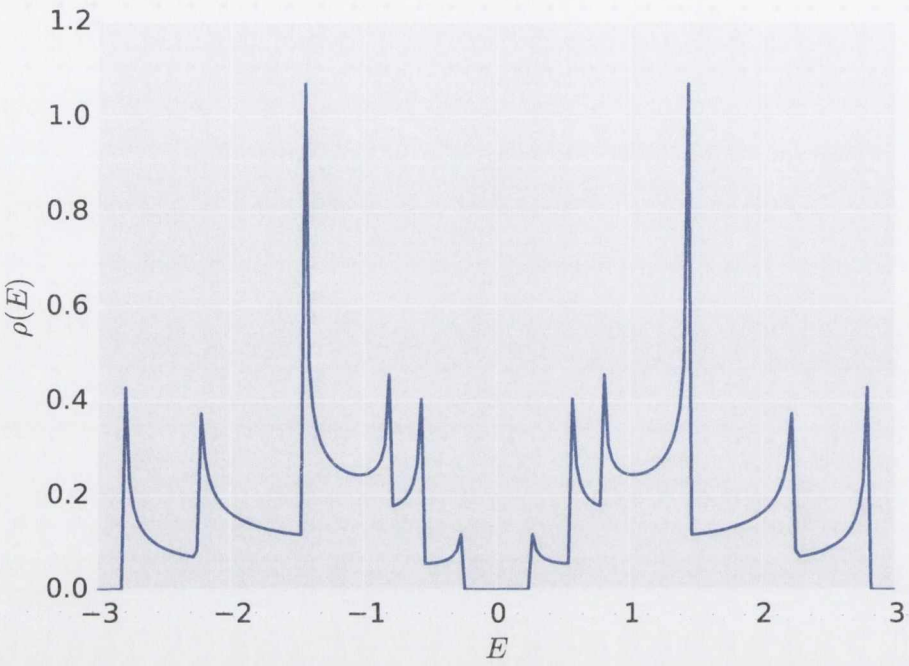


Figure 3.12: The DOS of a $n_E = 7$ GNR, demonstrating an obvious bandgap

The first term in the Hamiltonian gives the hopping between numerical adjacent sites, the second term gives the hopping between the other, horizontally connected sites. The appropriate sets for summing over are given by

$$S_1 = [0, N-2] \tag{3.3.8}$$

$$S_2 = [N, 2N-2] \tag{3.3.9}$$

$$S_3 = \{i \in [0, N-1, 2]\}, \tag{3.3.10}$$

from which we can see that S_1 and S_2 sum over the left and right sides of the strips, whereas S_3 sums over the middle section.

Using similar methods we can define the connection matrices as

$$V_{LR} = t \sum_{i \in C} |i + N\rangle\langle i| \tag{3.3.11}$$

$$V_{RL} = t \sum_{i \in C} |i\rangle\langle i + N|, \tag{3.3.12}$$

for

$$C = \{i \in [1, N-1] | i \text{ odd}\}. \tag{3.3.13}$$

Obviously one of the next steps we would like to perform would be adding

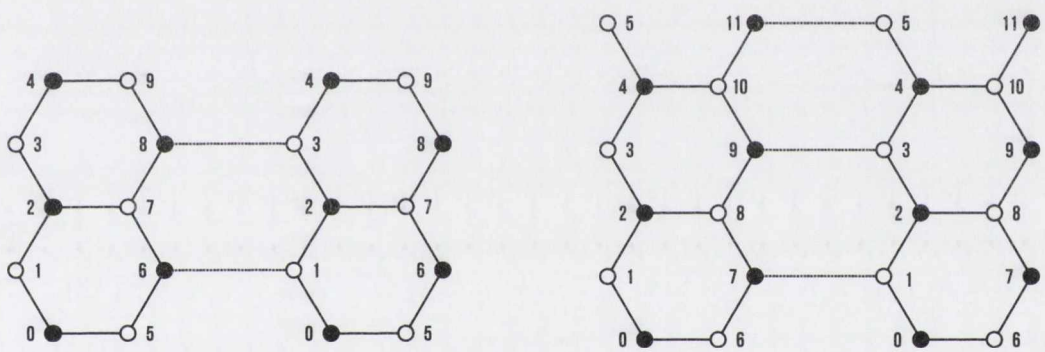


Figure 3.13: Examples of different nanoribbons. On the left we have odd nanoribbons with $N = 5$ on the right even nanoribbons with $N = 6$. Two nanoribbons are included in each case in order to see how the connection matrices might be built.

impurities. These can be added either by using Dyson techniques familiar from previous sections, or by simply adding them directly to the relevant unit cell.

Adding impurities in the recursive regime is relatively easy, and we show the method for single impurities here (a schematic is shown in Fig.3.14). Extension to the multiple impurity case should be obvious. First of all we introduce a perturbative Hamiltonian that contains our impurities

$$\hat{H} = \hat{H}_0 + \hat{H}_I \tag{3.3.14}$$

For the substitutional case where we have a substitutional impurity at site i this can be represented as a change in the on-site energy and we get

$$\hat{H}_I^S = |i\rangle\langle i|\epsilon. \tag{3.3.15}$$

A top adsorbed impurity connecting to a site i (note that the impurity itself is at site 2N) gives us a Hamiltonian of

$$\hat{H}_I^T = |i\rangle\langle 2N|\tau + h.c. \tag{3.3.16}$$

A center adsorbed impurity has a Hamiltonian of

$$\hat{H}_I = \sum_{j\in S_C} (|j\rangle\langle 2N| + h.c.). \tag{3.3.17}$$

where

$$S_C = [i, i+2] \cup [i+N, i+N+2]. \tag{3.3.18}$$

3.4 CHAPTER SUMMARY

In this chapter we examined the Green's functions of the various edged graphene systems that we encounter throughout the text. We used a contour integration to simplify the numerical calculation of these quantities, and examined them fully analytically within the SPA approximation. We also presented a practical application of the recursive technique, in this case, using armchair graphene nanoribbons. In every system presented, we examined the LDOS, and showed how a triadic pattern could be observed in the edged cases. It is reasonable to expect that this triadic pat-

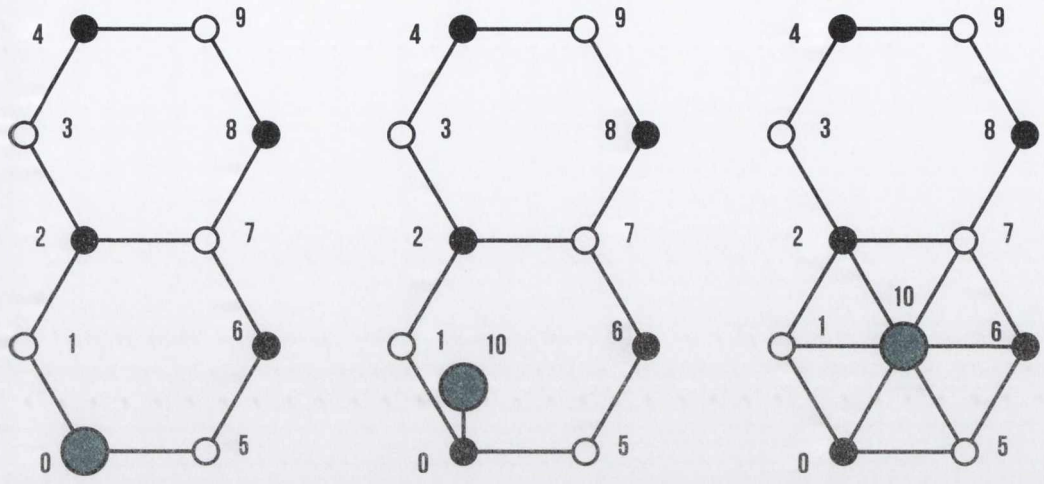


Figure 3.14: Examples of adding impurities to an armchair nanoribbon N = 5. From left to right we have substitutional, top-adsorbed and center-adorbed impurities. It should be clear that the formulas from the text identify the appropriate sites.

tern will be observed again in other physical quantities, and we will see in later chapters that this is the case.

4

THE INDIRECT EXCHANGE COUPLING

When magnetic impurities are embedded in a metallic host, they have two main forms of interaction. When the impurities are close, and there is appreciable overlap of their electron wavefunctions, they may interact via direct exchange. However, when the impurities are at appreciable distance, direct exchange is negligible, and so they interact via *indirect exchange*, where they are coupled by the itinerant electrons of the host. In a large metallic object, with a diffuse scattering of impurities, indirect exchange is generally the dominant interaction term and plays an important role in determining magnetic alignment. There are two commonly used approaches to estimate the IEC; Quantum Well Theory and the RKKY approximation. The RKKY interaction has been shown to be a first order approximation of quantum well theory [95–97], and so we generally perform our numerical calculations within the latter, using the former for our simplified mathematical analysis.

The IEC possesses a number of properties that are common to almost all metals. First, it is an oscillatory interaction, oscillating between ferromagnetic and antiferromagnetic couplings with the separation between impurities. Second, the decay of its amplitude is related to the dimensionality of the material in question (D^{-d} where D is the separation and d the dimensionality) [93]. It is also worth noting that the IEC has been studied in semiconductors, where it decays exponentially. This result will become useful when we study graphene nanoribbons.

The IEC has been extensively studied in graphene, partly because of its role in governing magnetic alignment, partly because its properties there are particularly unusual. Graphene is neither metal nor semiconductor, and the IEC it exhibits is different from both. Around the Dirac point, the IEC displays a power law decay, but at an unusual rate for its dimensionality (D^{-3}) [46, 52, 76, 98–113]. Furthermore,

the oscillations in sign seen in metals do not occur in graphene, with impurities on the same sublattice exhibiting a ferromagnetic interaction, and impurities on opposite sublattices demonstrating an antiferromagnetic one. This is due to the commensurability of the Fermi wavevector with the lattice.

Edged graphene has similar but distinct properties to its bulk counterpart. It is also expected to have a large role in the future of spintronics. However, despite this, there has been little work performed on the IEC in these systems, possibly due to the fact that there has been some controversy over the exact bandstructure of these systems. It might also be because of the experimental difficulty in manufacturing exact edges, and the disappointing properties of nanoribbons without clearly defined edge orientations [61]. However, the latter problem is currently being solved [54, 55, 62], and hence now is a good time to start examining magnetic interactions. Indeed, one paper has done just that for armchair ribbons, finding both an exponential decay, and a *distance independent* interaction [121].

In this chapter we examine the IEC in graphene and its edged variants. Though the IEC in bulk graphene has already been subject to a great deal of examination, it is important to replicate results, and performing this analysis will allow us to introduce the theoretical machinery that forms the backbone of this chapter. Furthermore, it is easier to examine a wide variety of impurities in bulk graphene, and this will prove useful in later chapters. We will then examine the same interaction in semi-infinite graphene and graphene nanoribbons, both with armchair edges. By examining all of these cases we should be able to see the connection between the different regimes, since bulk graphene can be viewed as the asymptotic limit of SI graphene, which is the limit of graphene nanoribbons.

We begin by deriving a general expression for the IEC, and we demonstrate how this may be approximated within the RKKY to obtain a series expansion of the coupling in terms of decay rates. We then will examine the various types of edged graphene following the structure of our Green's functions chapter, looking at the bulk first and then introducing one and two edges. We will calculate the IEC

using the GFs already derived, and use both numerical and analytic techniques to portray a clear picture of the interaction in the systems examined. Finally, we will repeatedly reference our results for the LDOS obtained in the previous chapter, demonstrating the IEC is highly dependent on the presence of itinerant electrons around the Fermi energy.

4.1 DERIVATION

The IEC between two impurities can be calculated by examining the energy difference between their ferromagnetic and antiferromagnetic alignments [86, 87]. This is often calculated by building both systems separately, calculating the total energy in each case, and then inspecting the difference between them. However, the energy difference between alignments is often tiny, and hence it is far more efficient to calculate them directly using the Lloyd formula from Eq. 2.5.10.

We derive the coupling between impurities by starting our system in a ferromagnetic state and then using the Lloyd formula to calculate the energy change from rotating one of the impurities by π radians. The forms of the IEC and RKKY interaction shown here are system independent and we need only the system specific GFs in order to calculate the appropriate interaction. Impurities are added as a result of the self-consistency calculation on the Hubbard Hamiltonian, which we have already shown in Sec.2.7. However, here we break down the resulting perturbation into two parts, one containing the spin-independent contribution (the bandcenter shift) and the other containing the spin dependent contribution (the exchange splitting). These are applied separately (using the Dyson Formula from Eq.2.2.1), and we assume that the bandcenter shift has already been applied in the calculations that follow. Here we define the exchange splitting as $V_{ex} = \frac{\Delta}{2}$, which puts our equations in a more readable and compact form. The spin-dependent part is then

added in the form of a perturbation that puts both impurities in a ferromagnetic alignment, which is described in Fig.4.1.

$$V^{\uparrow} = -V_{ex}(|A\rangle\langle A| + |B\rangle\langle B|) \tag{4.1.1}$$

$$V^{\downarrow} = V_{ex}(|A\rangle\langle A| + |B\rangle\langle B|) \tag{4.1.2}$$

Application of these potentials to the spin degenerate $\hat{g}$ yields the spin-dependent GFs $\hat{g}^{\uparrow}$ and $\hat{g}^{\downarrow}$.

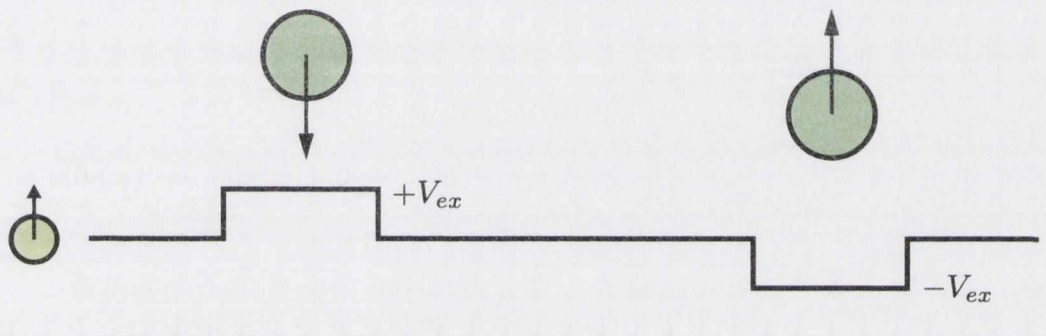


Figure 4.1: A schematic demonstrating the potential of magnetic impurities as seen by electrons. A spin up electron encounters a greater potential barrier at a spin down impurity and vice versa.

The magnetic moment can be rotated using the following perturbation (written in the spin basis $|\uparrow\rangle, |\downarrow\rangle$), which we have performed for an arbitrary θ to keep our calculations as general as possible.

$$\hat{V}(\theta) = -V_{ex}\begin{pmatrix} \cos\theta - 1 & \sin\theta \\ \sin\theta & 1 - \cos\theta \end{pmatrix} \tag{4.1.3}$$

It can be seen that a rotation of π leads to a perturbation of $2V_{ex}$ on the up band and $-2V_{ex}$ on the down band, exactly in line with what we expect. Generally this perturbation is applied to impurity B, and we follow this convention. We can

then calculate the energy difference from the Lloyd Formula (Eq.2.5.10), which we reprint here for convenience.

$$\Delta E = \mathrm{Im} \int_{-\infty}^{E_F} dE\, E \ln(\det(\hat{I} - \hat{g}\hat{V})) \tag{4.1.4}$$

It is easiest to examine this in parts, and we start with the determinant

$$\det(\hat{I} - \hat{g}_{BB}\hat{V}(\theta)) = \left| \begin{pmatrix} 1 & 0 \\ 0 & 1 \end{pmatrix} + V_{ex} \begin{pmatrix} g^{\uparrow}_{BB} & 0 \\ 0 & g^{\downarrow}_{BB} \end{pmatrix} \begin{pmatrix} \cos\theta - 1 & \sin\theta \\ \sin\theta & 1 - \cos\theta \end{pmatrix} \right|, \tag{4.1.5}$$

which can be expanded to get

$$\det(\hat{I} - \hat{g}_{BB}\hat{V}(\theta)) = 1 + V_{ex}(g^{\uparrow}_{BB} - g^{\downarrow}_{BB})(\cos\theta - 1) - 2V_{ex}^2 g^{\uparrow}_{BB} g^{\downarrow}_{BB}(\cos\theta - 1). \tag{4.1.6}$$

We can simplify this expression further by using the Dyson equation (remembering that we need to apply the perturbation on both A and B to get $\hat{g}^{\uparrow}$ and $\hat{g}^{\downarrow}$) to write

$$g^{\downarrow}_{BB} = g^{\uparrow}_{BB} + 2V_{ex}(g^{\uparrow}_{BB} g^{\downarrow}_{BB} + g^{\uparrow}_{BA} g^{\downarrow}_{AB}), \tag{4.1.7}$$

and we can use this formula to simplify our determinant

$$\det(\hat{I} - \hat{g}_{BB}\hat{V}(\theta)) = 1 - 2V_{ex}^2 g^{\uparrow}_{BA} g^{\downarrow}_{AB}(\cos\theta - 1). \tag{4.1.8}$$

Performing the rotation for $\theta = \pi$ we get

$$\det(\hat{I} - \hat{g}_{BB}\hat{V}(\pi)) = 1 + 4V_{ex}^2 g^{\uparrow}_{BA} g^{\downarrow}_{AB}, \tag{4.1.9}$$

which allows us to write the indirect exchange coupling in a much simplified form

$$J_{BA} = -\frac{1}{\pi}\mathrm{Im}\int_{-\infty}^{\infty} dE\, f(E)\ln(1+4V_{ex}^2 g_{BA}^{\uparrow}(E)g_{AB}^{\downarrow}(E)). \tag{4.1.10}$$

The vast majority of the time we work in the low temperature limit where $f(E) \approx 1$. Furthermore, we almost always calculate the IEC over the imaginary axis (as shown in Sec.2.6) when doing numerical work, as it is much smoother and easier to integrate.

For analytic purposes, it is hard to work with the integral in Eq.4.1.10, and it is best to expand it in the RKKY approximation, which is shown in the next section.

4.1.1 *The RKKY Coupling*

The Ruderman-Kittel-Kasuya-Yosida or RKKY interaction initially referred to the indirect interaction between two nuclear magnetic moments. However, it has been significantly extended since then and sometimes even used interchangeably with the IEC in the literature. It is generally written in the form

$$J_{ab} = -\frac{1}{16\pi^2}\lambda^2 h^2 \chi_a b. \tag{4.1.11}$$

This can be found by expanding the IEC for small perturbations. We find that we can write the RKKY in the form of a series, which, when combined with our ability to derive completely analytic forms of the GFs, allows us to predict the decay of the coupling completely analytically. We show that these predictions agree with our numerical results for small perturbations and large separations.

In the limit of small perturbations the IEC reduces to the RKKY coupling. We expand the natural log in a Taylor series

$$\ln(1+x) = x - \frac{x^2}{2} + \frac{x^3}{3} + \ldots, \tag{4.1.12}$$

and use the fact that the Dyson equation can be written as a series (Eq.2.2.1) to write

$$G = g + gVg + gVgVg + \dots \tag{4.1.13}$$

If V_{ex} is very small we can chop both of these series to leading order, and then use the symmetry of the GF to get the RKKY approximation

$$J_{BA} \approx -\frac{4V_{ex}^2}{\pi} \mathrm{Im} \int dE\, f(E) g_{BA}^2(E). \tag{4.1.14}$$

We note that this can be written in the form

$$J_{BA}^{RKKY} = -2V_{ex}^2 \chi_{BA}^0, \tag{4.1.15}$$

where χ_{BA}^0 is the non-interacting spin-susceptibility. This is formally identical to Eq.4.1.11.

The main advantage of the RKKY approximation is that it can be combined with the fully analytic GF in the SPA to make fully analytic predictions about the decay rate of the interaction. From Eq.3.1.38, we know that we can write our GF within the SPA as

$$g_{BA}(E) = \frac{A(E)e^{iQ(E)D}}{\sqrt{D}}, \tag{4.1.16}$$

and we square this to get

$$g_{BA}^2(E) = \frac{B(E)e^{2iQ(E)D}}{D}, \tag{4.1.17}$$

where $B(E) = A(E)^2$. Now the RKKY coupling can be written as

$$J_{BA}^{RKKY} = -\frac{4V_{ex}^2}{\pi D} \mathrm{Im} \int dE\, \frac{B(E)e^{2iQ(E)D}}{1 + e^{\beta(E-E_F)}}. \tag{4.1.18}$$

This equation can be solved via contour integration in the upper half plane (after distorting the contour by a small imaginary part). The poles of the denominator occur when $1 + e^{\beta(E_p - E_F)} = 0$, or when

$$E_p = E_F + (1 + 2p)\pi k_B T \qquad p \in \mathbb{Z}. \tag{4.1.19}$$

These are known as the Matsubara frequencies. Performing the contour integral gives us

$$J_{BA}^{RKKY} = -\frac{4V_{ex}^2}{\pi D} \mathrm{Im}\left(2\pi i \,\mathrm{Res}\left[\sum_p \frac{B(E)e^{2iQ(E)D}}{1 + e^{\beta(E-E_F)}}\right]\Bigg|_{E=E_p}\right), \tag{4.1.20}$$

and the residue can be calculated in the usual fashion to get

$$\begin{aligned}\mathrm{Res}\left[\sum_p \frac{B(E)e^{2iQ(E)D}}{1 + e^{\beta(E-E_F)}}\right]\Bigg|_{E=E_p} &= \sum_p \frac{B(E)e^{2iQ(E)D}}{\beta e^{\beta(E-E_F)}}\Bigg|_{E=E_p} \\ &= -\sum_p k_B T B(E_p) e^{2iQ(E_p)D}.\end{aligned} \tag{4.1.21}$$

This allows us put the coupling in the form

$$J_{BA}^{RKKY} = -\frac{V_{ex}^2 k_B T}{D} \mathrm{Im} \sum_p 2\pi i B(E_p) e^{2iQ(E_p)D}. \tag{4.1.22}$$

Now we expand both the coefficient $B(E)$ and the wavevector $Q(E)$ around the Fermi Energy, the latter only up to its first derivative.

$$B(E) = \sum_l \frac{1}{l!} B^{(l)} (E - E_F)^l, \tag{4.1.23}$$

$$Q(E) = Q^{(0)} + Q^{(1)}(E - E_F), \tag{4.1.24}$$

where $B^{(l)} = \frac{d^l}{dE^l} B(E)\Big|_{E=E_F}$ and $Q^{(l)}$ is defined similarly. Within this approximation the coupling may be written as

$$J_{BA}^{RKKY} = \frac{8V_{ex}^2 k_B T}{D} \mathrm{Im} \sum_l \frac{i}{l!} B^{(l)} e^{2iQ^{(0)}D} \sum_p (E_p - E_F)^l e^{2iQ^{(1)}(E_p - E_F)D}, \tag{4.1.25}$$

Now we can use

$$\frac{d^a}{dD^a} e^{2iQ^{(1)}(E_p - E_F)D} = [2iQ^{(1)}(E_p - E_F)]^a e^{2iQ^{(1)}(E_p - E_F)D}, \tag{4.1.26}$$

to write our coupling as

$$J_{BA}^{RKKY} = \frac{8V_{ex}^2 k_B T}{D} \mathrm{Im} \sum_l \frac{i}{l!} B^{(l)} e^{2iQ^{(0)}D} \frac{d^l}{dD^l} \sum_p \frac{e^{2iQ^{(1)}(E_p - E_F)D}}{(2iQ^{(1)})^l}. \tag{4.1.27}$$

Furthermore, the sum can be reduced to

$$\begin{aligned} \sum_p e^{2iQ^{(1)}(E_p - E_F)D} &= \sum_p e^{2iQ^{(1)} i(2p+1)\pi k_B T D} \\ &= e^{-2Q^{(1)}\pi k_B T D} \sum_p \left(e^{-4Q^{(1)}\pi k_B T D}\right)^p \\ &= \frac{e^{-2Q^{(1)}\pi k_B T D}}{1 - e^{-4Q^{(1)}\pi k_B T D}} \\ &= \frac{1}{2\sinh[2Q^{(1)}\pi k_B T D]}, \end{aligned} \tag{4.1.28}$$

and now we have only one sum

$$J_{BA}^{RKKY} = \frac{8V_{ex}^2 k_B T}{D} \mathrm{Im} \sum_l \frac{i}{l!} \frac{B^{(l)} e^{2iQ^{(0)}D}}{(2iQ^{(1)})^l} \frac{d^l}{dD^l} \frac{1}{2\sinh[2Q^{(1)}\pi k_B T D]}. \tag{4.1.29}$$

If we work in the low temperature limit we can expand out the sinh to first order. Then, using $\frac{d^l}{dD^l} D^{-1} = (-1)^l l! D^{-1-l}$ we can finally write

$$\mathcal{J}_{BA}^{RKKY} = V_{ex}^2 \mathrm{Im} \sum_l \frac{B^{(l)} e^{2iQ^{(0)}D} (-1)^l}{(2iQ^{(1)})^{l+1} D^{l+2}}, \tag{4.1.30}$$

and we can see how the rate of decay is determined by the degree to which the derivatives $B^{(l)}$ vanish. This result will prove extremely powerful, predicting the decay rates of impurities of different conformation type, under different edge effects and after being extended across the lattice.

4.2 GRAPHENE

As discussed in the introduction, the indirect exchange coupling in graphene is well studied. The general consensus is of an interaction that decays with the cube of the separation (D^{-3}), with ferromagnetic alignment for same sublattice cases, and antiferromagnetic alignement otherwise. We repeat these calculations in graphene as a means of testing our method, replicating previous results, and introducing techniques that will be used in subsequent sections. Furthermore, graphene can be thought of as the limiting case of semi-infinite graphene, in that far enough from the edge we should reproduce bulk graphene results. Hence the calculation of results in bulk graphene both acts as a useful check for our calculations and a tool to flesh out our narrative. The simplest impurity form to calculate is the *substitutional impurity* which we examine in the next section. Then we will examine the highly similar *top-adsorbed impurities* and more complicated (but more interesting) *center-adsorbed impurities*.

4.2.1 *Substitutional Impurities*

Substitutional impurities replace carbon atoms in the graphene lattice as shown in Fig. 3.1. They are easily modelled by introducing a perturbation that changes the on-site energy (as shown in Sec.2.3), and calculating the IEC using Eq. 4.1.10.

A plot of the coupling for both armchair and zigzag separations is shown in Fig. 4.2. From this we can see a roughly power-law decay in both cases, with a

monotonic decay in the armchair direction and a periodic one in the zigzag direction. The decay rate of the interaction is most easily determined through a log-log plot (where power law decays become linear) and such a plot is shown in Fig.4.3. Interpolation shows that the coupling decays at a rate of roughly D^{-3} in both directions, in agreement with what is commonly predicted. We note that the armchair direction decays monotonically, whereas the zigzag direction displays a triadic pattern, which is identical to the commensurability between the relevant Fermi wavevector and lattice sites. The negativity of the coupling indicates that the impurities align ferromagnetically, and subsequent calculations show that this is always true for impurities on the same sublattice, with impurities on opposite sublattices exhibiting antiferromagnetic alignment. This is in contrast to general predictions of the IEC, which indicates an interaction that oscillates between alignments. We also performed the calculations for a Fermi level away from the Dirac point, where graphene's unique properties should not be as apparent (Fig.4.4). The decay rate returns to D^{-2} in this regime, and a general oscillatory pattern appears, as expected for a usual 2d material.

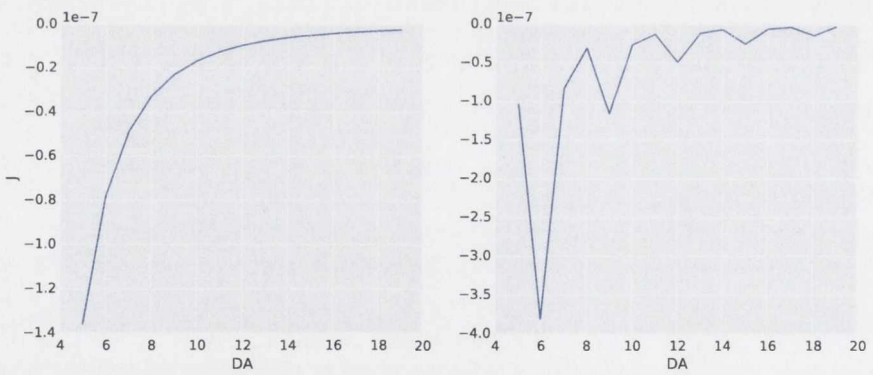


Figure 4.2: A plot of the IEC in bulk graphene between substitutional impurities at the Dirac point. The figure on the left show the interaction between impurities in the armchair direction and the figure on the right the zigzag directions. The power law decay and unchanging sign (indicating a constant ferromagnetic interaction) are clearly seen. A monotonic decay is apparent in the armchair direction and a triadic pattern emerges in the zigzag direction.

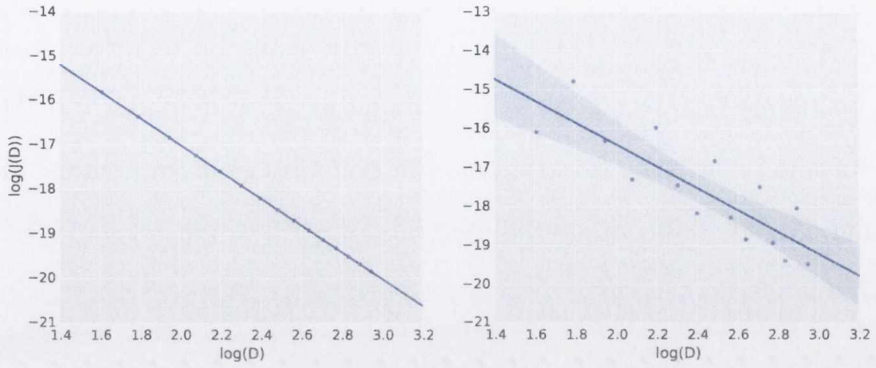


Figure 4.3: A log-log plot of the IEC between substitutional impurities in bulk graphene at the Dirac point. The linear nature of the decay indicates a power-law behaviour. Interpolation shows the decay to be D^{-3}. Better agreement with smaller error margins can be obtained at larger distances.

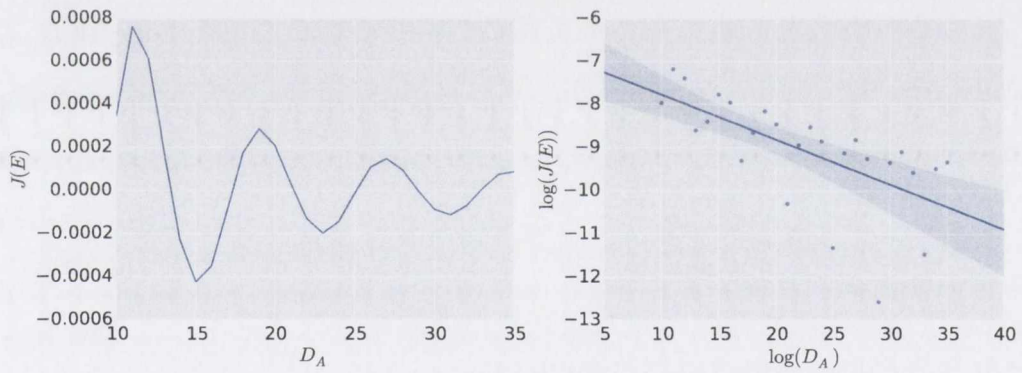


Figure 4.4: On the left we show a plot of the IEC for a substitutional impurity in the armchair direction for $E_F = 0.2$. The commensurability is destroyed and an oscillatory pattern is beginning to emerge. On the right we show a log-log plot, which can be interpolated to get a decay rate of roughly D^{-2}. We observe a substantial increase in the magnitude of the interaction, around 3 orders of magnitude, presumably due to the increased availability of charge carries.

It is worth comparing these results with our plots of the LDOS in chapter 3. Away from the Dirac point the LDOS is finite and the results replicate what is expected of a general 2d material. However, at the Dirac point the LDOS is zero, we have less conduction electrons, and the decay rate increases to D^{-3}. This indicates the LDOS is highly correlated with the IEC, and we will see more of this in the future.

4.2.1.1 *Analytic Decay*

As discussed in Sec.4.1.1, we can calculate the decay rate of the RKKY interaction fully analytically by using Eq.4.1.30. We expect that this should match the IEC well for small perturbations at large separations. For substitutional impurities, the appropriate GF can be determined using the methods in Sec.2.3. We get

$$G_{AB} = \frac{g_{AB}}{(1 - g_{AA}V_{AA})(1 - g_{BB}V_{BB}) - g_{AB}V_{BB}g_{BA}V_{AA}} \tag{4.2.1}$$

However, the only separation dependent term here is g_{AB}, and since the factor in the denominator vanishes for small V, the decay of the interaction can be reliably approximated by the pristine GFs.

The SPA for pristine bulk GFs is given in Sec.3.1.4. Here we work in the armchair direction, since that is more appropriate when dealing with SI graphene and armchair GNRs. The SPA in the armchair direction is given in Eq.3.1.37 and from it $B(E)$ can be written as

$$B(E) = \boxed{\mp}\frac{iE}{\pi(3t^2 + E^2)\sqrt{E^2(t^2 - E^2)}} \tag{4.2.2}$$

We evaluate its derivatives at the Dirac point, finding

$$B^{(0)} = 0 \tag{4.2.3}$$

and

$$B^{(1)} = \boxed{\mp}\frac{i\sqrt{t^2}}{3\pi t^4} \tag{4.2.4}$$

Therefore the first derivative is our leading term in Eq.4.1.30 and the interaction decays with D^{-3}. This corroborates our numerical results.

A similar calculation may be conducted in the zigzag direction. However, the zigzag direction will be less useful once we begin to work in edged graphene, and hence it is more illuminating to look at the armchair case.

4.2.2 *Top-Adsorbed Impurities*

Top-adsorbed impurities are expected to show many of the same characteristics as substitutional impurities. Top adsorbed impurities can be introduced with the perturbation shown in Sec.2.3. Top adsorbed impurities are interesting in part because they share the decay and features of a substitutional impurity, while having an identical form to a center-adsorbed impurity.

In Fig.4.5 we plot the top-adsorbed IEC for both high symmetry directions. The immediate similarity to the substitutional case is apparent and interpolation shows roughly the same rate of decay. The only difference is the substantially weaker nature of the top-adsorbed coupling. The effects of different sublattice arrangements and non-zero Fermi energy are also similar to the substitutional case.

Getting the decay rates analytically for zigzag impurities is almost identical to the substitutional case. The appropriate GFs for top-adsorbed impurities are given by Eq.2.3.11 in the Methods section. Here, the only separation dependent term is again the bulk GF. Hence the pristine GF may again be used, in identical fashion to the substitutional case, leading to identical results.

4.2.3 *Center-Adsorbed Impurities*

A common adsorption site for magnetic impurities embedded in graphene is at the center of the hexagons (shown in Fig. 3.1). If the IEC demonstrated rapid decay at these sites it would go some way to explaining the difficulties in finding experimental evidence of the IEC in graphene.

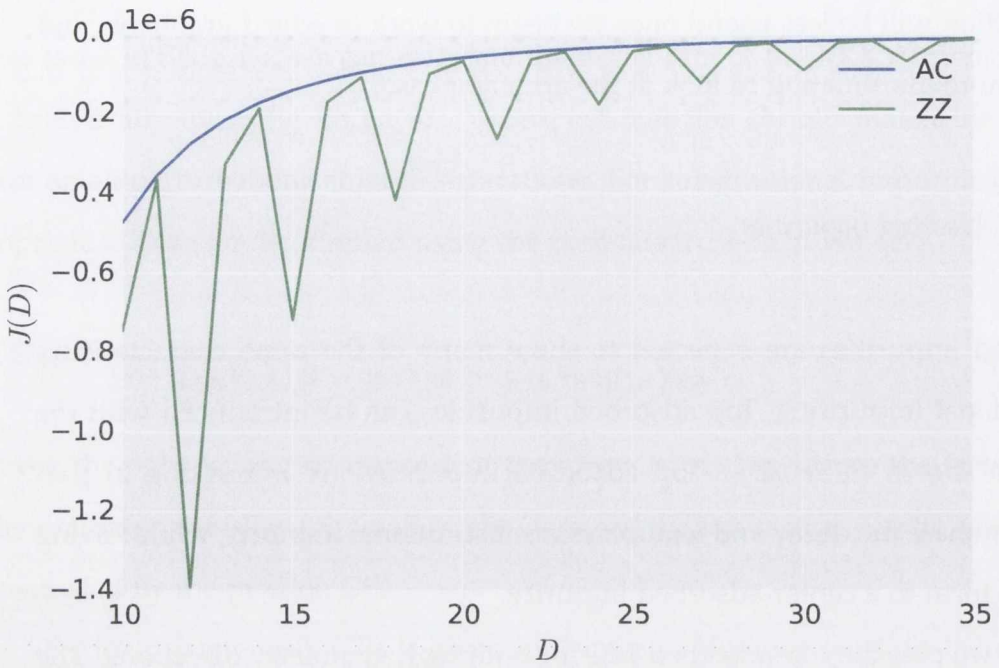


Figure 4.5: A plot of the IEC for top-adsorbed impurities. The armchair direction is shown on the left and the zigzag on the right. The similarity to the substitutional case is striking.

A plot of the relevant couplings in the zigzag and armchair directions (Fig.4.6) reveals something qualitatively similar to the substitutional and top-adsorbed couplings, but with a far more rapid decay. Interpolation shows that the decay rate is now given as D^{-7}, considerably larger than for other impurity types. It is worth asking where this larger decay comes from. We already know that the larger decay in graphene comes from the unusual electronic structure around the Dirac point. With this in mind, we examine the LDOS for a center adsorbed impurity. This is shown in Fig.4.7. We see that one again, the LDOS is zero at the Dirac point, but now the structure around the Dirac point is much flatter. We posit that this leads to a decrease in the number of itinerant electrons available to propagate the interaction, and hence a greater rate of decay. Initially reported by Uchoa *et. al.* [103] this was later explained analytically by our group [111].

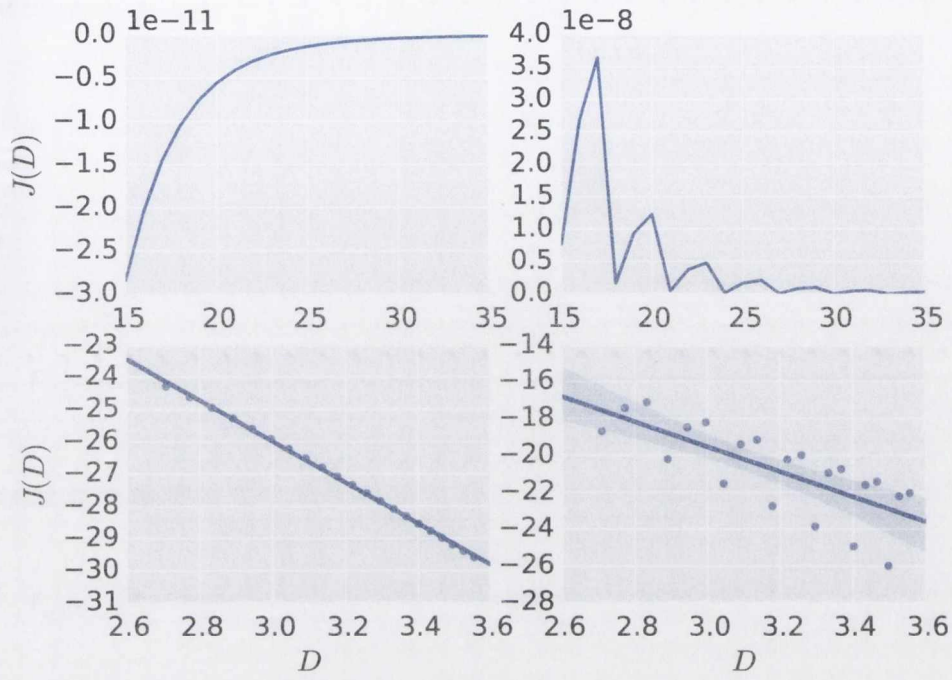


Figure 4.6: The IEC plotted for the center-adsorbed impurity. As usual we have the armchair coupling on the left and the zigzag on the right. The rapid decay of the interaction is apparent.

We would like to treat the center-adorbed impurities within the RKKY approximation, the same as we have for other impurity types. However, now using the pristine GFs in Eq.4.1.30 is inappropriate. This is because the relevant GFs are given by Eq.2.3.14 as

$$G_{AB} = \frac{g_{AA}\Gamma_{ab}g_{BB}}{(1 - g_{BB}\Gamma_{bb})(1 - g_{AA}\Gamma_{aa}) - g_{AA}\Gamma_{ab}\Gamma_{ba}g_{BB}}. \tag{4.2.5}$$

where $\Gamma_{ab} = \tau^2 \sum_{i,k} g_{a_i b_k}$. Mathematically, the only difference between top and center-adsorbed impurities is the introduction of a sum. This, however, makes treating the interaction far more difficult. We can see that all of the separation dependence is contained in Γ_{ab} and hence this is the appropriate term to use when calculating the derivatives of $B(E)$. Thus in order to determine the decay of the IEC analytically, we must calculate the gamma term within the bounds of the SPA. We

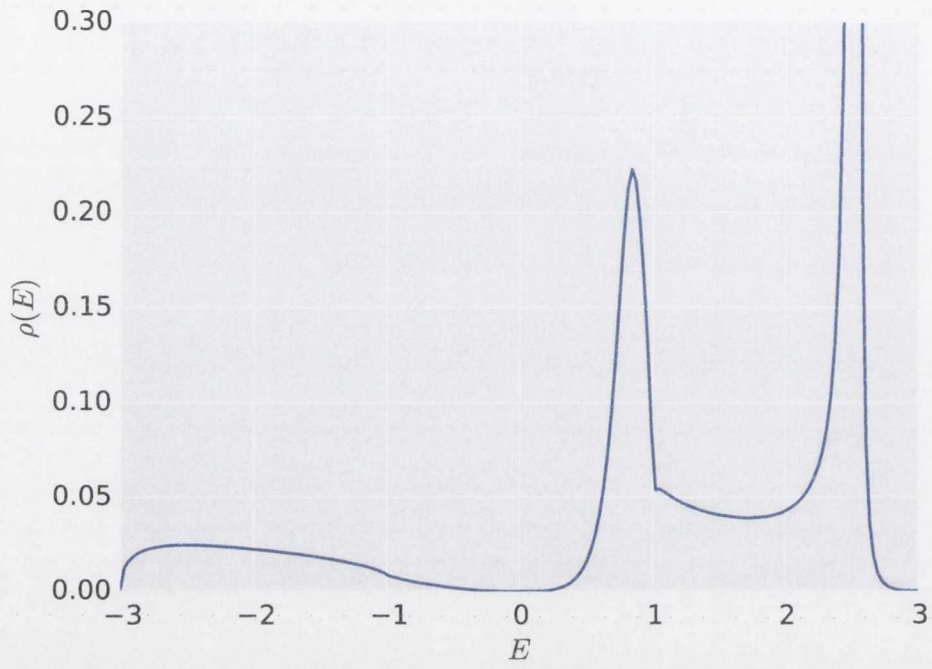


Figure 4.7: The LDOS for a center adsorbed impurity in bulk graphene. As usual we have the armchair coupling on the left and the zigzag on the right. The rapid decay of the interaction is apparent.

perform the calculation in the armchair direction, which will be more relevant in our future work.

Collecting the relevant GFs and simplifying is a tedious process, but it allows us to substantially reduce the form of the gamma term

$$\Gamma_{ab} = \frac{1}{2\pi^2} \frac{(2E|f|^2 + te^{-2ik_A} f^3 + te^{2ik_A} (f^\dagger)^3)(e^{ik_A(m+n)+ik_Z(m-n)})}{E^2 - t^2|f|^2} \tag{4.2.6}$$

The contour integral can be performed as usual to get

$$\Gamma_{ab} = \frac{i}{4\pi t^4} \frac{(2E^2 + t^3 f^3 e^{-2iq} + t^3 (f^\dagger)^3 e^{2iq}) e^{iq(m+n)+ik_Z(m-n)}}{\cos(k_Z)\sin(q)} \tag{4.2.7}$$

Finally, the gamma term can be written in the SPA approximation, which in the armchair direction has two poles

$$\Gamma^a_{ab} = \boxed{\pm}\frac{i(E-t)(E+3t)^3 e^{\boxed{\pm}2i|D_A|\cos^{-1}\left(\frac{E^2-5t^2}{4t^2}\right)}}{4t^3[(E^2-9t^2)(t^2-E^2)]^{\frac{1}{4}}}\sqrt{\boxed{\mp}\frac{i}{\pi|D_A|(3t^2+E^2)}} \tag{4.2.8}$$

and

$$\Gamma^b_{ab} = \boxed{\pm}\frac{i2E^3(t-E)e^{\boxed{\pm}2i|D_A|\cos^{-1}\left(-\sqrt{1-\frac{E^2}{t^2}}\right)}}{t^3\sqrt{3t^2+E^2}(E^2(t^2-E^2))^{\frac{1}{4}}}\sqrt{\boxed{\pm}\frac{i}{\pi|D_A|}} \tag{4.2.9}$$

The entire gamma term is given by

$$\Gamma_{ab} = \Gamma^a_{ab} + \Gamma^b_{ab} \tag{4.2.10}$$

The gamma SPA can be plotted against its bulk equivalent and shows good agreement, as seen in Fig. 4.8. However, it generally requires that we move to greater separations than the usual bulk SPA.

By using the gamma term in the SPA approximation we can finally get a result for the analytic coupling. We have that

$$B(E) = \boxed{\pm}\frac{4iE^6(t-E)^2}{\pi t^6(3t^2+E^2)\sqrt{E^2(t^2-E^2)}} \tag{4.2.11}$$

and we find that all derivatives disappear up to $B^{(5)}$, which is given by

$$B^{(5)} = \boxed{\mp}i\frac{160}{\pi t^7} \tag{4.2.12}$$

This leads to a decay rate of D^{-7}.

To this point, these results have already been produced by other members of our group. In order to find new and interesting effects, we must start to examine edged graphene systems.

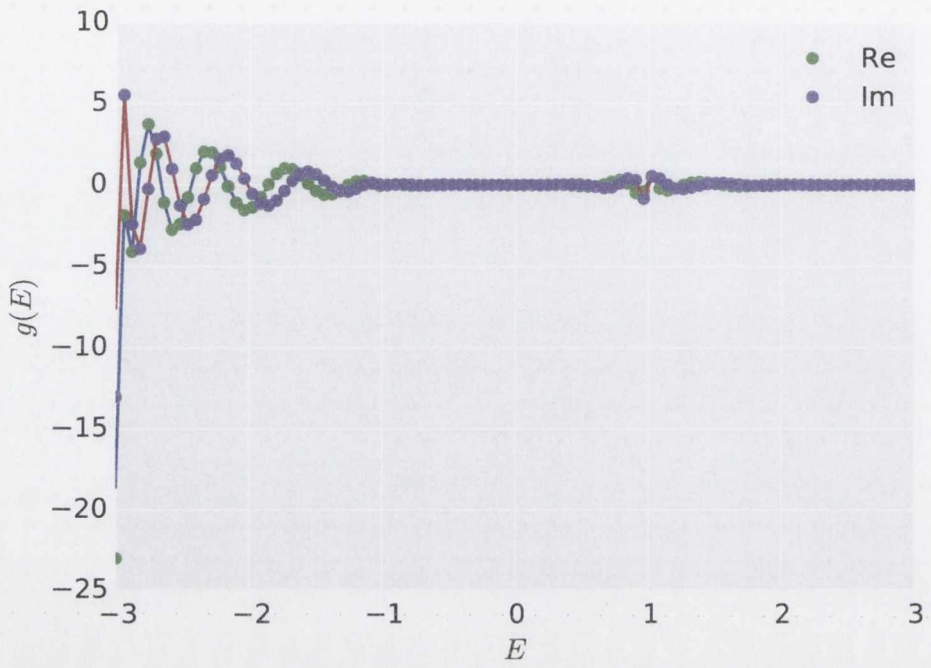


Figure 4.8: The gamma term calculated fully analytically against its stationary phase approximation equivalent for $D_A = 5$.

4.3 SEMI-INFINITE GRAPHENE

We have already examined the GFs of SI graphene in Sec.3.2. There we examined the LDOS in proximity to the edge, and demonstrated the emergence of a periodic triadic pattern. However, it must be stressed at this point that the IEC is generally considered to be a dimensionality dependent problem and not particularly dependent on edge effects. In Fig. 4.9, we plot the IEC between two substitutional impurities in SI graphene for the first three sites from the edge. We see that, contrary to our expectations, 3 sites from the edge the decay is significantly more rapid. In Fig. 4.10 we plot the rate of decay (as α where the decay is $D^{-\alpha}$) as we move into the graphene sheet. We find the presence of two different decay rates, one that is very similar to bulk graphene, the other, considerably higher, whenever D_Z is a multiple of 3 from the edge. Both converge to the bulk value far enough into

the sheet. It is hard to believe that the triadic pattern that we have found in both the IEC and LDOS of SI graphene are unrelated. It seems considerably more likely that the smoothness of the LDOS around the Dirac point results in less itinerant electrons being available to propagate that interaction and hence a quicker rate of decay.

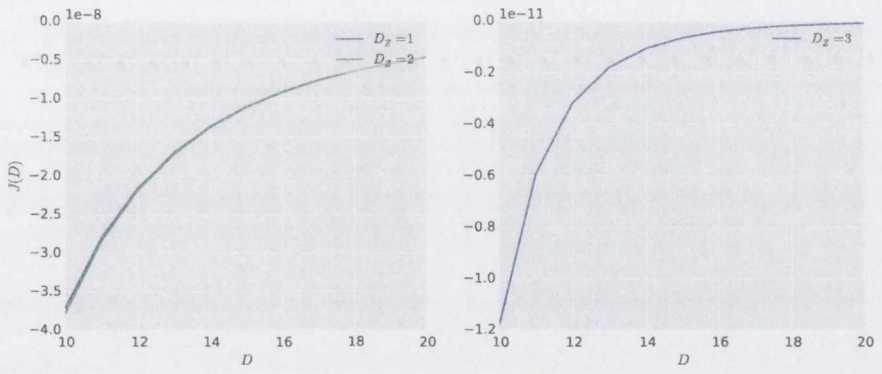


Figure 4.9: A plot of the coupling J against armchair separation D_A. On the left we show the IEC for the first two sites from the edge $D_Z = 1, 2$. On the right we plot the coupling for $D_Z = 3$ which clearly exhibits a much greater decay.

We can use Eq. 4.1.30 to calculate the decay rate. From our Eq.3.2.11 for the SI SPA we can write $B(E)$ as

$$B(E) = \mp \frac{8iE^2 \sin^4[D_Z \sin^{-1}\left(\frac{\sqrt{E^2+3t^2}}{2t}\right)]}{\pi(E^2+3t^2)\sqrt{E^2(t^2-E^2)}} \tag{4.3.1}$$

When $\mathcal{B}(E)$ is evaluated at the Fermi level it vanishes identically. However, its first derivative and second derivative have the forms

$$B^{(1)} = \frac{4i \sin^4\left[\frac{n_E \pi}{3}\right]}{3\pi t^3}, \tag{4.3.2}$$

and

$$B^{(2)} = \frac{4i \sin\left[\frac{n_E \pi}{3}\right]^3 \left(4\sqrt{3} n_E \cos\left[\frac{n_E \pi}{3}\right] + \sin\left[\frac{n_E \pi}{3}\right]\right)}{3\pi t^5}. \tag{4.3.3}$$

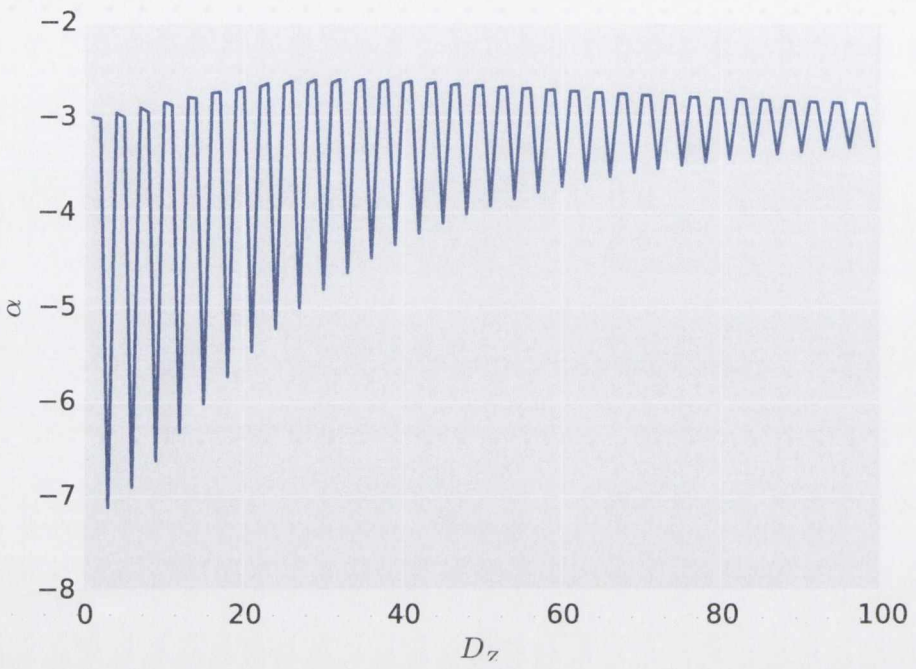


Figure 4.10: Here we plot D_Z against the decay rate α (where the IEC decays as $D^{-\alpha}$), as the impurity pair moves further into the graphene sheet. The triadic pattern is instantly observable. Both the slow and fast decays converge to 3 as we move further into the sheet.

which implies that a D^{-3} decay is felt in general, with every third atom from the edge experiencing a higher rate of decay.

Some studies indicate that introducing stronger hopping parameters (by about 12%) next to the graphene edge results in a better match with experiment [48]. This is known as the *edge correction*, which was not included when calculating the numerical results in this section. We find that the presence of an edge correction perturbs our results very close to the edge, but converges to our original results rapidly as we move into the graphene sheet.

4.4 ARMCHAIR NANORIBBONS

Finally, we examine armchair graphene nanoribbons, which will complete our panoply of edged graphene. Our hope is to find results that are both interesting, and also plausibly complete the spectrum of edged graphene. As mentioned before, we work chiefly in nanoribbons with $N = 3n + 2$, which are metallic.

The coupling may be determined numerically by using the appropriate GFs (from Sec.3.3) and is plotted in Fig. 4.11. The similarity to the SI is apparent immediately. We get the triadic pattern of slow and fast decays, but here the effect is even more pronounced. Determining the exact type of decay is best performed in a log-log plot, from which it is clear that we are seeing both power law and exponential decays. By fitting the plots we can determine that for D_Z equal to 1 or 2 the coupling decays as D^{-1}, which matches some predictions for armchair nanoribbons [121], nanotubes [170] and is what would be expected in a 1d electron gas [91]. However, when D_Z is equal to 3, we find that our plots are better fitted with an exponential decay. This behaviour has been verified for a wide range of different D_Z, confirming that the triadic pattern is ubiquitous, and strengthening the link between the various forms of edged graphene.

The fact that we find an exponential decay for certain D_Z values is not surprising when we examine the LDOS of metallic armchair nanoribbons. The LDOS is shown in Fig.3.10 in our chapter on Green's functions, where it shows the same triadic pattern that we find in the IEC here. The vanishing LDOS means that there are no conducting states around the Fermi energy and thus the interaction decays exponentially for these D_Z values, as it would in a semiconductor [170].

Increasing the ribbon width has no effect on the decay rates, but can be seen to decrease the magnitude of the slow decay, while increasing the magnitude of the fast one, thus bringing both closer to their values in semi-infinite graphene. We note that this behaviour is similar to that reported previously in the literature [121], however we do not observe the non-decaying interaction predicted for certain cases

in that work. Finally, we plot the IEC for a non-metallic nanoribbon in Fig.4.12. It shows the exponential decay that we expect from a semiconducting material.

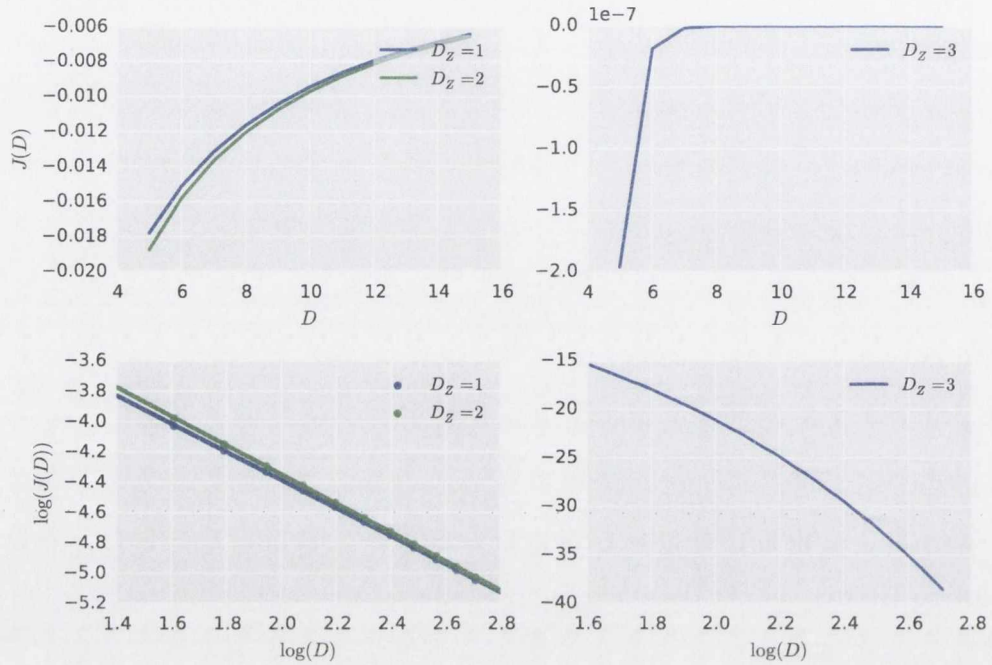


Figure 4.11: A plot of the IEC in a GNR. The plots are taken in the armchair direction. The top row gives a plot of the IEC in the armchair direction as D_Z ranges between 1 and 3. We can see a pattern similar to the triadic SI pattern beginning to emerge. The bottom row repeats the calculations in a log-log plot. From this we can see that the 3rd site from the edge does not have a power-law decay, it is in fact exponential. The calculations were performed in a ribbon of width $n_E = 6$.

4.4.1 *Analytic calculations*

With some small changes to the methods used in previous sections we can calculate the decay rate. Since our GF is already in analytic form, there is no need to calculate

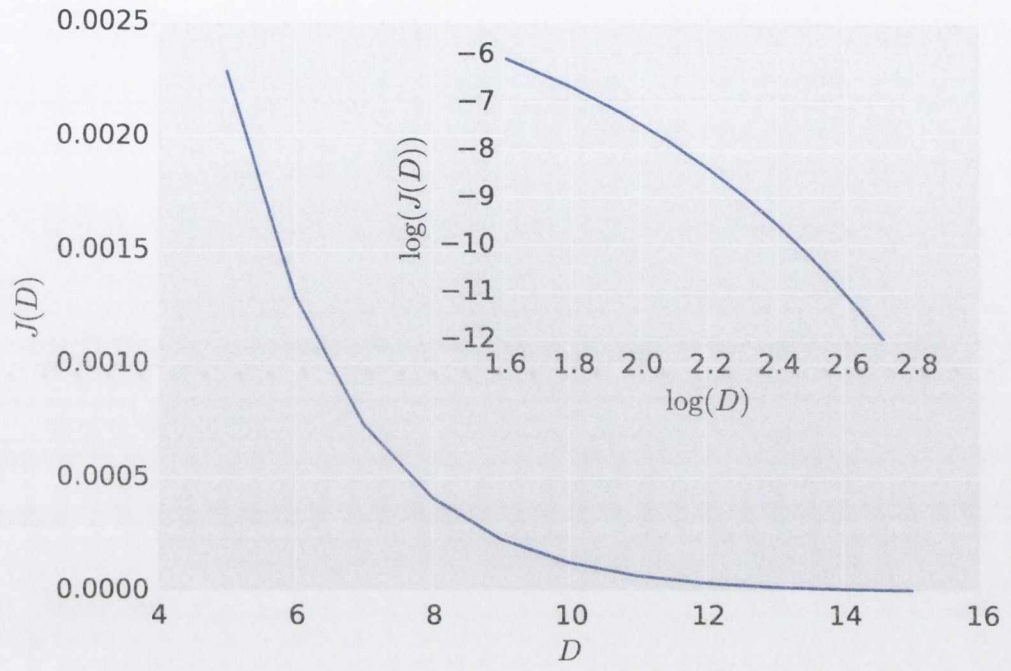


Figure 4.12: A plot of the coupling J against armchair separation D_A for a semiconducting ($n_E = 7$) nanoribbon. A log-log plot is inset. It displays an exponential decay, as expected.

it within the SPA. We can write the full expression for our GF in simplified form as

$$g_{BA}(E) = A(E)e^{iQ(E)D} \tag{4.4.1}$$

This is identical to Eq.3.1.38, and hence we can repeat our analytic derivation of the RKKY (Sec.4.1.1) to get

$$\mathcal{J}_{BA}^{RKKY} = V_{ex}^2 \mathrm{Im} \sum_l \frac{B^{(l)} e^{2iQ^{(0)}D}(-1)^l}{(2iQ^{(1)})^{l+1} D^{l+1}} \tag{4.4.2}$$

which is identical to Eq.4.1.30 aside from the power of D in the denominator.

It is clear that in order to replicate our numerical calculations we need $B^{(0)}$ to remain finite. Obviously, given the form of the GF, $B(E)$ is a complex product of

cross terms. However, when examined in the appropriate limit, almost all of these terms vanish. The only terms that remain are those that are just squares of regular terms in $A(E)$

$$b(E,j) = \frac{16t^4E^2 \sin\left(\frac{D_{Z1}j\pi}{n_E}\right)^2 \sin\left(\frac{D_{Z1}j\pi}{n_E}\right)}{16t^4 \cos\left(\frac{j\pi}{n_E}\right) - \left(-E^2 + t^2 + 4t^2\cos(\frac{j\pi}{n_E})^2\right)^2} \tag{4.4.3}$$

and now we make the substitution $j = \frac{n_E}{3}$, remember that this is always possible in a metallic nanoribbon since we have $n_E = 3n$. With this substitution the whole expression simplifies dramatically and we get

$$b(E) = 4t^2 \sin\left(\frac{D_{Z1}\pi}{3}\right) \sin\left(\frac{D_{Z2}\pi}{3}\right) \tag{4.4.4}$$

This expression remains in all situations where one of the impurities does not lie on a line of VLDOS, and hence we get the decay of D^{-1} in all of the situations we expect. Proving that the decay is higher in situations where the nanoribbon is semiconducting or one of the impurities is situated on one of the line of VLDOS is harder, but is strongly suggested by the form of this expression.

4.5 CHAPTER SUMMARY

In this chapter, we examined the indirect exchange coupling between different impurity types in different edged graphene systems. We first derived an expression for the coupling, using Lloyd's formula to quantify it as the difference between ferromagnetic and antiferromagnetic alignments of impurities. We then demonstrated that coupling can be written in an equivalent series form, which is useful for the analytic extraction of the decay rate of the interaction. We then examined its form in the various kinds of edged graphene that we encounter in this thesis. We began with bulk, replicating the known graphene behaviour for substitutional and

top adsorbed cases. We showed that these interactions are always ferromagnetic on same sublattice sites and antiferromagnetic otherwise. We demonstrated that the magnitude of the interaction is monotonically decreasing with the separation, at a rate of D^{-3} at the Dirac point, and D^{-2} away from it (where the interaction resumes its oscillatory nature). We also looked at center adsorbed impurities, which exhibit a much greater rate of decay, D^{-7}, at the Dirac point, and demonstrated how this decay arises by the cancelling of GFs. Finally, we examined semi-infinite graphene and armchair graphene nanoribbons. We showed that the interaction takes on a triadic form in these materials, with a greater rate of decay every third site from the edge. We found that this decay rate eventually converges to the bulk decay rate far enough into the SI sheet, but found an exponential character in graphene nanoribbons. All of the results in this chapter were justified using an analytic approach originating in our group. The results are also strongly correlated with the LDOS, which we examined in the previous chapter. Anywhere the LDOS is small, we expect a decrease in the number of itinerant electrons available to propagate the interaction, and hence a decrease in its strength. Our approach here is limited to two impurity systems, and methods of expanding this approach are explored in the next section. The results in this chapter were examined as part of *RKKY Interaction Between Extended Magnetic Defect Lines in Graphene* (Physical Review B, 90, 125411, 2014).

5

LINES OF IMPURITIES

Single site impurities are often used as proxies for finite sized objects. We would like to calculate these quantities directly, but doing this requires that we sacrifice a certain amount of mathematical transparency. In this chapter, we strike a compromise between the two approaches. An infinite line of impurities can be seen as a reasonable proxy for an extended magnetic object, while at the same time we are able to describe it within a relatively simple mathematical scheme.

Furthermore, there are a growing number of cases were such a model may be appropriate. In 2012 Salehi-Khoji et. al. examined line defects as a means of enhancing the chemical sensitivity of graphene, finding that graphene nanoribbons were particularly effective [122]. In the same year Winters et. al. announced the ability to create 3d structures in graphene using transfer printing [123]. This same method would later be used to create graphene fins [124], which could display enhanced spin-orbit coupling and hence magnetism due to the intense strains involved [75]. All of these systems may, as a first approximation, be modeled by unidirectional infinite lines with a modified on-site energy, exactly as for impurities.

Increased interest is being shown in extended magnetic impurities in graphene systems. Indeed, extended nanowires on graphyne have already been shown to demonstrate long range magnetic order and anisotropy [125]. This has led to interest in how ordered magnetic lines might interact. One paper examining the RKKY interaction between lines of defects finds that the sublattice dependence of the interaction is broken, and the decay rate is the same, but the magnitude is greatly increased [126]. Further a recent paper has used stable crystographically order fluorine chains to generate spin order in graphene [127].

Furthermore, the observance of the RKKY interaction in such structures may be more easily experimentally observable than in the single impurity case. Work is already being performed in this direction. In 2006 Hirjibehedin et. al. engineered linear chains of magnetic objects and examine the coupling experimentally, finding an AFM coupling strength of 3 to 6 meV [138]. However, this only examined the coupling between nearest neighbours. More recently, a study was performed examining the coupling between two clusters of magnetic impurities. They found large couplings at less than 1nm, up to 92meV. However, these quickly decayed to 0.1meV at 1nm [139].

So far, we have only defined the indirect exchange coupling for two impurity systems. In this chapter we extend that definition to work with infinite lines of impurities. Calculations of this kind are greatly facilitated by using a mixed representation, where the Green's function is Fourier transformed along one direction. This allows us to work in a system that is discrete and continuous where appropriate.

In this chapter we demonstrate the mathematical techniques necessary to deal with extended impurity systems. First we introduce the formalism necessary to model these systems (namely, the mixed representation) and then we show how the coupling may be obtained within that formalism. We calculate the coupling numerically, showing that the extended lines effectively reduce the dimensionality of the system. Finally, we use the methods that we have already developed to show that the decay rate of the interaction can be predicted entirely analytically. We also show how the finite results of a small number of impurities quickly converges to the infinite result.

In this chapter we will only work with substitutional impurities, but the method is obviously applicable to other impurity conformations.

5.1 THE GREEN'S FUNCTION

We have already calculated the GF of graphene in the position (x,y) and reciprocal space (k_x,k_y) bases. Here we wish to write it in the mixed representation (x,k_y). The GF in bulk graphene can be written as

$$\hat{g} = \sum_{\mathbf{k}} \left(\frac{|\mathbf{k},+\rangle\langle\mathbf{k},+|}{E-\epsilon_+} + \frac{|\mathbf{k},-\rangle\langle\mathbf{k},-|}{E+\epsilon_+} \right), \tag{5.1.1}$$

where our eigenvectors are give by

$$|\mathbf{k},\pm\rangle = \frac{1}{\sqrt{2}} \left(|k,\bullet\rangle \pm \frac{f^\dagger}{|f|}|k,\circ\rangle \right). \tag{5.1.2}$$

We can calculate the projection over a mixed representation basis to be

$$\langle k_x, k_y, \alpha | x, k_y, \alpha \rangle = \frac{1}{\sqrt{N_x}} e^{ik_x x}. \tag{5.1.3}$$

which allows us to determine the GF in the mixed representation

$$g^{\alpha\beta}_{xx'}(k_y) = \frac{1}{N_x} \sum_{k_x} \frac{N^{\alpha\beta} e^{ik_x(x'-x)}}{E^2 - t^2|f|^2}. \tag{5.1.4}$$

Following the usual procedure we replace the sum with an integral whose limits are given by the modified BZ

$$g^{\alpha\beta}_{xx'}(k_y) = \frac{\sqrt{3}a}{4\pi} \int_{-\frac{2\pi}{\sqrt{3}a}}^{\frac{2\pi}{\sqrt{3}a}} dk_x \, \frac{N^{\alpha\beta} e^{ik_x(x'-x)}}{E^2 - t^2|f|^2}, \tag{5.1.5}$$

and we introduce the dimensionless variable $k_A = \frac{\sqrt{3}a}{2}k_x$ while noting that $k_A \frac{2}{\sqrt{3}a}(x'-x) = D_A k_A$. This gives

$$g^{\alpha\beta}_{D_A}(k_y) = \frac{1}{2\pi} \int_{-\pi}^{\pi} dk_A \, \frac{N^{\alpha\beta} e^{ik_A D_A}}{E^2 - t^2|f|^2}, \tag{5.1.6}$$

where

$$f(k_A, k_y) = 1 + 2e^{ik_A}\cos(\frac{k_y a}{2}). \tag{5.1.7}$$

Now we can perform the contour integration in the usual fashion to get

$$g^{\alpha\beta}_{D_A}(k_y) = \frac{i}{4t^2}\frac{N^{\alpha\beta}e^{iq(k_y)D_A}}{\cos(\frac{k_y a}{2})\sin(q(k_y))}, \tag{5.1.8}$$

with

$$q(k_y) = \boxed{\pm}\cos^{-1}\left[\frac{E^2 - t^2 - 4t^2\cos^2(\frac{k_y a}{2})}{4t^2\cos(\frac{k_y a}{2})}\right], \tag{5.1.9}$$

and

$$f(k_y) = 1 + 2e^{iq(k_y)}\cos(\frac{k_y a}{2}). \tag{5.1.10}$$

The advantage of having the GF in the mixed representation is that it makes the application of perturbations with translational symmetry trivial to apply. Such perturbations can easily be cast in the mixed representation and then the Dyson equation can be applied as usual, as shown in the next section.

5.2 THE PERTURBATION

We seek to apply a perturbation that is infinite in the y direction at two different x coordinates. The appropriate form is given by

$$\hat{V} = \sum_y (V_{AA}|A, y\rangle\langle A, y| + V_{BB}|B, y\rangle\langle B, y|). \tag{5.2.1}$$

This can be Fourier transformed to get the same perturbation in the mixed representation

$$\hat{V} = \sum_{k_y} (V_{AA}|A, k_y\rangle\langle A, k_y| + V_{BB}|B, k_y\rangle\langle B, k_y|). \tag{5.2.2}$$

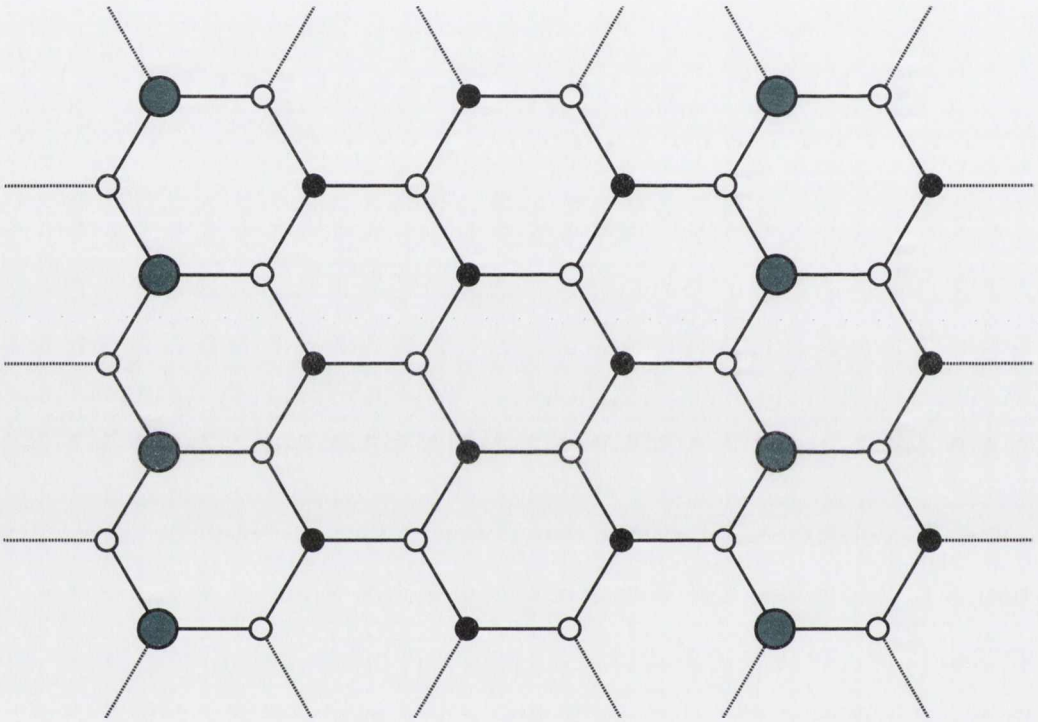


Figure 5.1: A schematic of the infinite line of impurities. Shown in an armchair separation of $D_A = 4$.

The perturbed GF can now be calculated as usual using the Dyson equation (Eq.2.2.1)

$$\hat{G} = (1 - \hat{g}\hat{V})^{-1}\hat{g}, \tag{5.2.3}$$

in the appropriate basis. In matrix form, the argument looks like

$$\hat{I} - \hat{g}\hat{V} = \hat{I} - \begin{pmatrix} \hat{g}_{AA} & \hat{g}_{AB} & \cdots \\ \hat{g}_{BA} & \hat{g}_{BB} & \\ \vdots & \vdots & \end{pmatrix} \begin{pmatrix} \hat{V}_{AA} & 0 & \cdots \\ 0 & \hat{V}_{BB} & \\ \vdots & \vdots & 0 \end{pmatrix}, \tag{5.2.4}$$

where all of the GF matrices are block matrices in k_y space.

$$\hat{g}_{AA} = \sum_{k_y} |A, k_y\rangle\langle A, k_y| g_{AA}(k_y) \tag{5.2.5}$$

However, since the matrices are also diagonal in k_y, we can use Eq.B.1.7 from the appendix to perform the inversion trivially. Now that we have the appropriate GFs, the next step is to get an appropriate form of the IEC.

5.3 THE INDIRECT EXCHANGE COUPLING

The indirect exchange coupling can now be calculated as the energy difference (per impurity) between the *entire lines* when they are aligned ferromagnetically and antiferromagnetically. The procedure is very similar to the one shown in chapter 4, save that the quantities we are dealing with are infinite dimensional matrices. We start from the Lloyd formula (Eq.2.5.10)

$$\Delta E(E_F) = \frac{1}{\pi} \mathrm{Im} \int dE\, f(E) \ln[\det(\hat{I} - \hat{g}\hat{V})]. \tag{5.3.1}$$

The appropriate perturbation is given in the mixed representation by

$$\hat{V} = \sum_{k_y} \hat{V}_\theta |B, k_y\rangle\langle B, k_y|, \tag{5.3.2}$$

and where $\hat{V}_\theta$ is the 2d spin perturbation matrix given in (Eq.4.1.3). Multiplication of block matrices is identical to regular matrix multiplication and we get

$$\det(\hat{I} - \hat{g}\hat{V}) = \det[1 + V_{ex}(\hat{g}^{\uparrow}_{BB} - \hat{g}^{\downarrow}_{BB})(\cos\theta - 1) + 2V_{ex}^2 \hat{g}^{\uparrow}_{BB}\hat{g}^{\downarrow}_{BB}(\cos\theta - 1)]. \quad (5.3.3)$$

We recall that all the quantities here are infinite matrices in k_y space

$$\hat{g}^{\uparrow}_{BB} = \sum_{k_y} g^{\uparrow}_{BB}(k_y)|k_y\rangle\langle k_y|, \quad (5.3.4)$$

and since

$$\det(\sum_a f_a|a\rangle\langle a|) = \prod_a f_a, \quad (5.3.5)$$

we get

$$\det(\hat{I} - \hat{g}\hat{V}) = \prod_{k_y}[1 + V_{ex}(g^{\uparrow}_{BB}(k_y) - g^{\downarrow}_{BB}(k_y))(\cos\theta - 1) + 2V_{ex}^2 g^{\uparrow}_{BB}(k_y)g^{\downarrow}_{BB}(k_y)(\cos\theta - 1)], \quad (5.3.6)$$

Evaulating this expression at $\theta = \pi$ gives us

$$N_y \mathcal{J}_{BA} = -\frac{1}{\pi}\mathrm{Im}\int_{-\infty}^{E_F} dE\, f(E) \ln \prod_{k_y}[1 + 4V_{ex}^2 g^{\uparrow}_{BA}(E, k_y)g^{\downarrow}_{AB}(E, k_y)] \quad (5.3.7)$$

$$= -\frac{1}{N_y\pi}\mathrm{Im}\int_{-\infty}^{E_F} dE \sum_{k_y} \ln[1 + 4V_{ex}^2 g^{\uparrow}_{BA}(E, k_y)g^{\downarrow}_{AB}(E, k_y)], \quad (5.3.8)$$

where we have defined the coupling per unit atom as $\mathcal{J}_{BA}$.

Once again we convert the sum into an integral over the modified BZ (Sec.A.1))

$$\mathcal{J}_{BA} = -\frac{a}{2\pi^2}\mathrm{Im}\int_{-\infty}^{E_F} dE\, f(E) \int_{-\frac{\pi}{a}}^{\frac{\pi}{a}} dk_y \ln[1 + 4V_{ex}^2 g^{\uparrow}_{BA}(E, k_y)g^{\downarrow}_{AB}(E, k_y)]. \quad (5.3.9)$$

Now that the coupling is in integral form it can be simplified by introducing the dimensionless variable $k_Z = \frac{a}{2}k_y$ to get

$$-\frac{1}{\pi^2}\mathrm{Im}\int_{-\infty}^{E_F} dE\, f(E)\int_{-\frac{\pi}{2}}^{\frac{\pi}{2}} dk_Z\, \ln\left[1+4V_{ex}^2 g^{\uparrow}_{AB}(E,k_Z)g^{\downarrow}_{AB}(E,k_Z)\right], \tag{5.3.10}$$

where

$$g^{\alpha\beta}_{D_A}(k_Z) = \frac{i}{4t^2}\frac{N^{\alpha\beta}e^{iq(k_Z)D_A}}{\cos(k_Z)\sin(q(k_Z))}. \tag{5.3.11}$$

We note that this is symmetric in k_Z and therefore it is possible to halve our integration region.

$$-\frac{2}{\pi^2}\mathrm{Im}\int_{-\infty}^{E_F} dE\, f(E)\int_{0}^{\frac{\pi}{2}} dk_Z\, \ln\left[1+4V_{ex}^2 g^{\uparrow}_{AB}(E,k_Z)g^{\downarrow}_{AB}(E,k_Z)\right] \tag{5.3.12}$$

Much like in chapter 4, we perform most of our calculations in the low temperature limit where $f(E) \approx 1$, and when calculating the coupling numerically we normally project of the imaginary axis.

5.4 NUMERICAL RESULTS

Now that we have the indirect exchange coupling in integral form, we can start to make numerical calculations. The IEC is plotted for two lines in Fig.5.2. The interaction has the usual graphene features, such as commensurability with the lattice, ferromagnetic alignment in same sublattice cases and antiferromagnetic alignment in opposite sublattice cases etc. As per the double impurity case the decay appears to follow a power law, however, the decay seems more gradual, which may be confirmed by the log-log plot shown in Fig.5.3. The linear form of the plots clearly indicates a power-law decay, and interpolating the results gives a decay of roughly D^{-2} for all cases. However, this decay rate does appear to change slightly with

larger separations (on the order of D = 1000), appearing to converge towards $D^{-2.1}$ for the same sublattice case and $D^{-2.3}$ for opposite sublattices.

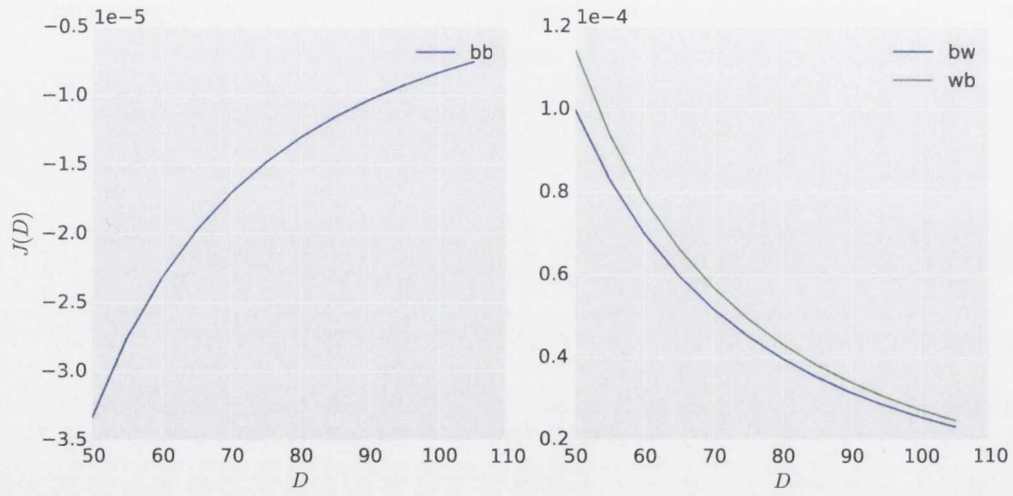


Figure 5.2: The indirect exchange coupling for infinite lines of impurities. On the left we plot the (••) case and on the right we plot the (•○) and (○•) cases. We see that the interaction is commensurate with the lattice, has a power-law behaviour and the usual configurations produce the usual alignments.

We also calculate the interaction away from the Dirac point, where we expect the special characteristics of graphene to vanish. Such a plot is shown in Fig.5.4. We immediately see an oscillatory interaction, indicating that our coupling is no longer commensurate with the lattice and we are out of the Dirac point regime. It also appears to be decaying more slowly, and this is confirmed by the log-log plot in Fig.5.5 which appears to exhibit a power law but oscillatory decay. The oscillatory nature of the interaction makes finding a reliable decay rate by interpolation more difficult, but in general we find a decay of roughly $D^{-1.5}$. Ideally, this would be confirmed by our analytic approach, and we explore this in the next section.

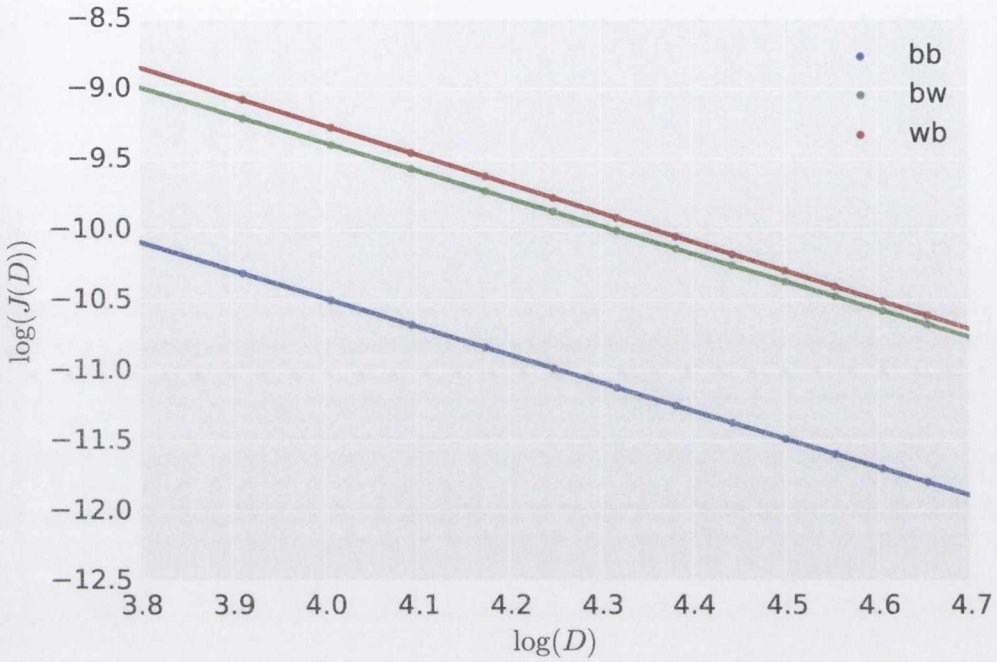


Figure 5.3: Shown is a log-log plot of the IEC for infinite lines of impurities. The dots indicate numerically calculated values and the lines the interpolation, which is around D^{-2} for all cases.

5.5 ANALYTICAL RESULTS

In order to calculate the coupling analytically it is first necessary to work in the RKKY approximation. We recall from chapter 4 that this is achieved by expanding to first order in V_{ex}^2, giving us

$$\mathcal{J}_{BA} \approx -\frac{4V_{ex}^2}{\pi^2} \mathrm{Im} \int_{-\infty}^{E_F} dE \int_{-\frac{\pi}{2}}^{\frac{\pi}{2}} dk_z \, g_{AB}(E, k_z)^2. \tag{5.5.1}$$

where we note that it is important to use the larger integration area to accurately capture the stationary points. In order to get a completely analytic result, we first need to approximate the inner integral within the SPA.

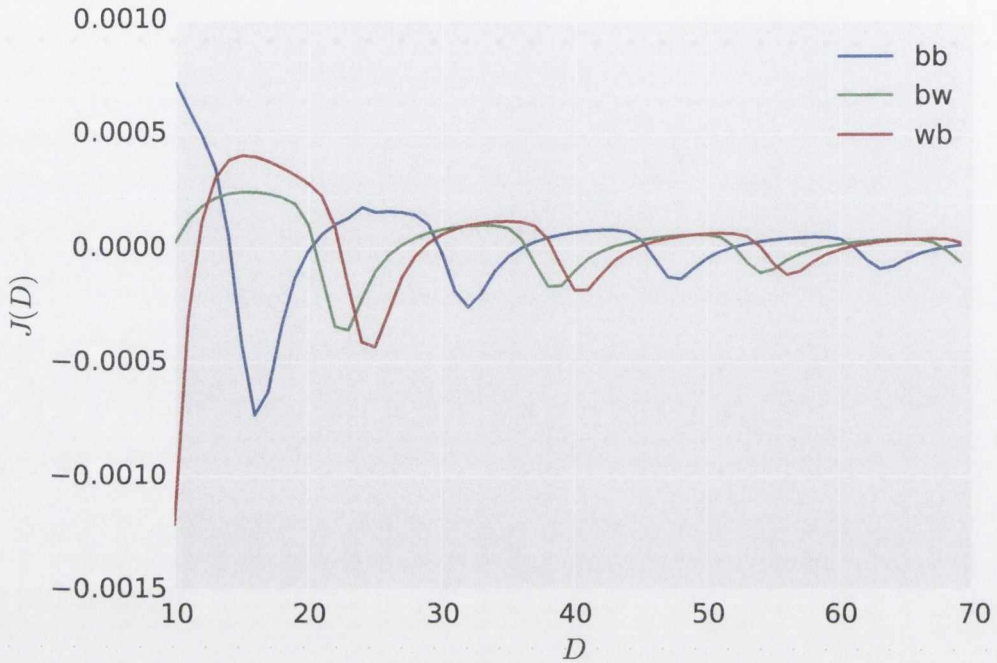


Figure 5.4: A plot of the IEC coupling for infinite lines of impurities away from the Dirac point ($E_F = 0.1$). The commensurability with the lattice disappears and the interaction oscillates.

5.5.1 *The SPA*

Our GF can be written entirely analytically in the mixed representation, which seems to make a calculation of the SPA unnecessary. However, in order to make an analytic calculation of the coupling in Eq.5.5.1, it is first necessary to solve the integral over k_Z. The procedure is similar to that found in Sec.3.1.4 and we note that a detailed discussion of the SPA can be found in the appendix (Sec.B.2).

The integral we have to approximate is

$$I_k = \int_{-\frac{\pi}{2}}^{\frac{\pi}{2}} dk_Z \, g_{D_A}^{\alpha\beta}(E, k_Z)^2. \tag{5.5.2}$$

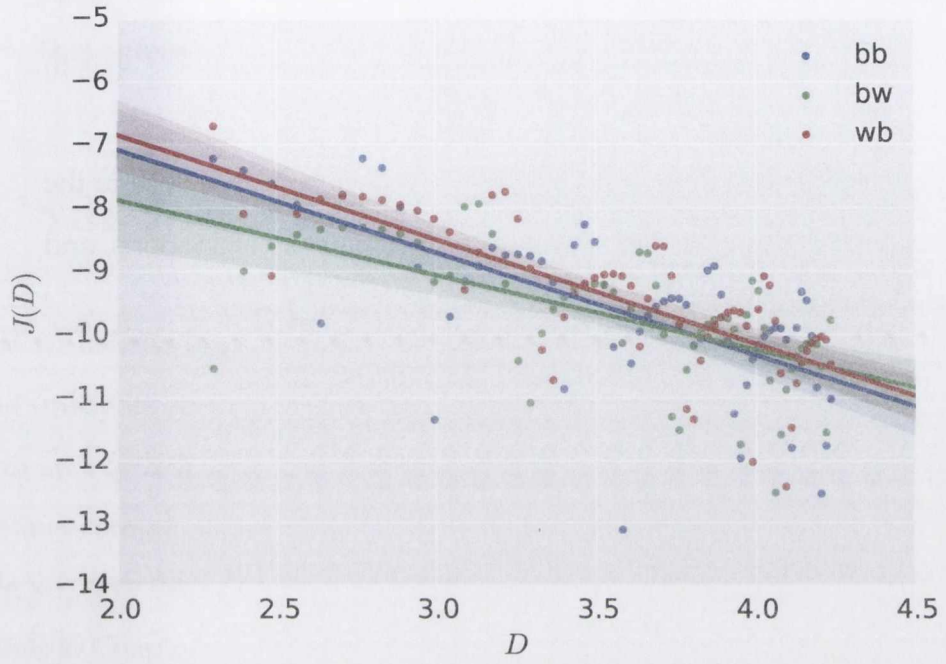


Figure 5.5: A log-log plot of the IEC coupling for infinite lines of impurities away from the Dirac point ($E_F = 0.1$). The oscillating dots represent the coupling and the straight lines the interpolation. We end up with a decay of roughly $D^{-1.5}$.

The GF can be expanded as

$$I_k = -\frac{1}{16t^4}\int_{-\frac{\pi}{2}}^{\frac{\pi}{2}} dk_Z \, \frac{N^{\alpha\beta}(E, k_Z)^2 e^{2iq(k_Z)D_A}}{\cos^2(k_Z)\sin^2(q(k_Z))}. \tag{5.5.3}$$

And the whole expression may be written within the SPA as

$$I_k \approx -\frac{1}{16t^4}\frac{N^{\alpha\beta}(E, k_Z^0)^2 e^{2iq(k_Z^0)|D_A|}}{\cos^2(k_Z^0)\sin^2(q(k_Z^0))}\sqrt{\frac{i\pi}{q''(k_Z^0)|D_A|}}. \tag{5.5.4}$$

We find two different stationary points (as is normal when working in the armchair direction), and substitute for $q(k_Z^0)$ and $q''(k_Z^0)$ to get

$$I_k^a = -\frac{E^2 e^{\boxed{\pm} 2i|D_A|\cos^{-1}\left(\frac{E^2-5t^2}{4}\right)}}{(-E^4+10E^2t^2-9t^4)^{\frac{3}{4}}}\sqrt{\frac{i\pi}{\boxed{\mp}|D_A|(E^2+3t^2)}}, \tag{5.5.5}$$

$$I_k^b = -\frac{2E^2 e^{\boxed{\pm} 2i|D_A|\cos^{-1}\left(-\sqrt{1-\frac{E^2}{t^2}}\right)}}{4(E^2t^2 - E^4)^{\frac{3}{4}}} \sqrt{\boxed{\pm}\frac{i\pi}{|D_A|(E^2+3t^2)}}, \tag{5.5.6}$$

where our full expression is given by $I_k \approx I_k^a + I_k^b$. Only I_k^b contributes close to the Dirac point and hence it is the most import quantity for analytic calculations, and the quantity that we examine in the next section.

5.5.2 *The Analytic Coupling*

The SPA allows us to write the integral in the following general form

$$\int_{-\frac{\pi}{2}}^{\frac{\pi}{2}} g_{AB}(E, k_Z)^2 = \frac{e^{2iQ(E)D}B(E)}{\sqrt{D}}. \tag{5.5.7}$$

After that, we need only make some small changes to the RKKY derivation in Sec.4.1.1 to get

$$\mathcal{J}_{BA}^{RKKY} = \pi V_{ex}^2 \mathrm{Im} \sum_l \frac{B^{(l)} e^{2iQ^{(0)}D}(-1)^l}{(2iQ^{(1)})^{l+1} D^{l+\frac{3}{2}}}. \tag{5.5.8}$$

This term is highly similar to its two impurity counterpart Eq.4.1.30, and it allows us to make a completely analytic prediction of the decay rate of the coupling by looking at the leading term $B^{(l)}$. However, there is a change in the prefactor, and more importantly a change in the power of D, which leads to non-integer decay rates. This leads credence to the idea that the infinite lines of impurities somehow reduce the dimensionality, meaning that we are working in neither a truly one-dimensional nor two-dimensional system.

$B(E)$ is given for an infinite line by

$$B(E) = -\frac{2E^2}{4(E^2t^2 - E^4)^{\frac{3}{4}}} \sqrt{\boxed{\pm}\frac{i\pi}{|D_A|(E^2+3t^2)}}, \tag{5.5.9}$$

and we find that the $B^{(0)}$ disappears at the Dirac point, leading to a decay rate of $D^{-2.5}$. Away from the Dirac point $B^{(0)}$ is finite and that leads to a decay rate of $D^{-1.5}$. This agrees well with our numerical results in Fig.5.3 and Fig.5.5.

5.6 THE FINITE LINE OF IMPURITIES

While an infinite line of impurities makes for a nice mathematical model, its real world utility its restrained by its ability to describe finite lines. In this section, we derive an expression for a finite line of substitutional impurities, and examine its coupling, comparing it to its infinite equivalent. The system we examine is similar to Fig.5.1, save for the fact the lines are finite. The IEC can derived in a very similar manner to Chapter 4, however, now our perturbation matrices for the up and down spin electrons are given by

$$V^{\uparrow} = -V_{ex}(\sum_{A} |A\rangle\langle A| + \sum_{B} |B\rangle\langle B|) \tag{5.6.1}$$

$$V^{\downarrow} = V_{ex}(\sum_{A} |A\rangle\langle A| + \sum_{B} |B\rangle\langle B|). \tag{5.6.2}$$

Where the sum is over all sites in line A/B. Similarly the rotation matrix can be written as

$$\begin{aligned}\hat{V}(\theta) = -V_{ex}\sum_{B}[&(\cos(\theta)-1)|B,\uparrow\rangle\langle B,\uparrow| + \sin(\theta)|B,\uparrow\rangle\langle B,\downarrow| + \\ &\sin(\theta)|B,\downarrow\rangle\langle B,\uparrow| + (1-\cos(\theta))|B,\downarrow\rangle\langle B,\downarrow|].\end{aligned} \tag{5.6.3}$$

We go through the steps as before and arrive at an expression that looks very similar to our two impurity indirect exchange coupling

$$J_{BA} = -\frac{1}{\pi}\mathrm{Im}\int_{-\infty}^{\infty} dE\, f(E)\ln(1 + 4V_{ex}^2 g^{\uparrow}_{BA}(E) g^{\downarrow}_{AB}(E)). \tag{5.6.4}$$

However, note that g_{BA} and g_{AB} are now block matrices, containing all of the sites in A and B.

Now that the derivation has been performed we can start to plot the coupling for both finite and infinite lines. This is shown in Fig.5.6, and we can see that we begin to see good agreement for very small lines, with almost complete convergence for lines consisting of 10 impurities.

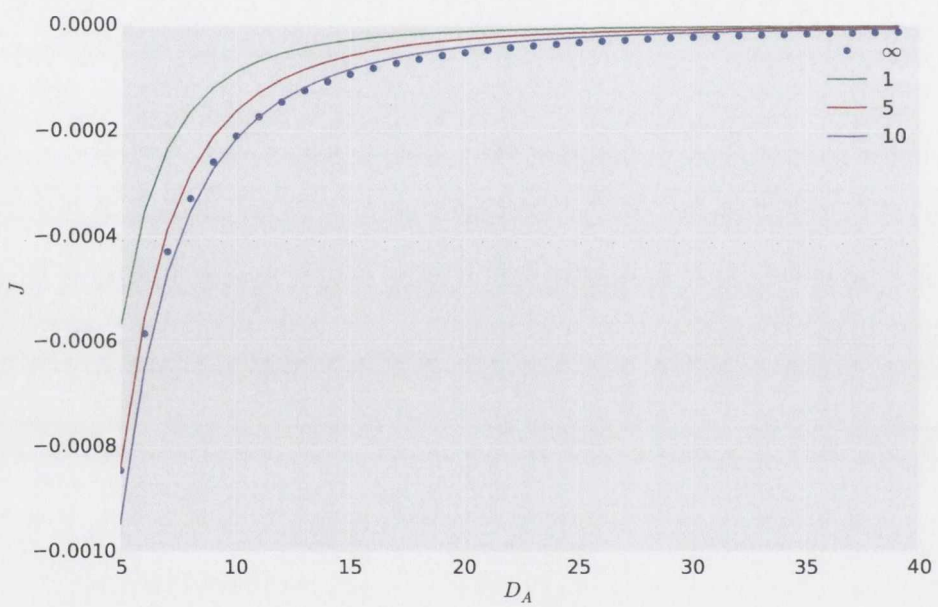


Figure 5.6: The IEC between finite vs infinite lines of impurities

This indicates that an infinite line of impurities is a reasonable approximation for even relatively small finite lines. Furthermore, due to the simplified nature of the mathematical formalism involved, it is vastly less computationally taxing than obtaining the coupling for large finite lines. This should be taken as an indication that our theoretically interesting model actually contains a powerful and general result.

5.7 CHAPTER SUMMARY

In this chapter we examined the IEC for infinite lines of impurities in bulk graphene This necessitates the introduction of the *mixed representation* where our GFs are Fourier transformed in one direction but not in the other. We derived both numerical and analytic expressions for the IEC within this scheme. Examining the IEC numerically, we found some of the same trademarks of graphene at the Dirac point; a ferromagnetic interaction for the same sublattice case, an antiferromagnetic interaction elsewhere, and a monotonically decreasing magnitude. However, the decay rates differ from the two impurity case. At the Dirac point, we found that the interaction decays at a rate of $D^{-2.1}$ for the same sublattice case and $D^{-2.3}$ otherwise. Away from Dirac point we found that the interaction begins to oscillate again, and the decay falls to $D^{-1.5}$. Furthermore, we found that the magnitude of the interaction is much greater than in the two impurity case. Finally, we examined finite impurity lines. After deriving an appropriate form of the interaction, we examined the coupling there and find that it is not substantially different from the infinite case, even at low impurity concentration. This lends greater generality to our work in this chapter.

The work in this chapter was published as *RKKY Interaction Between Extended Magnetic Defect Lines in Graphene* (Physical Review B, 90, 125411, 2014). This concludes our examination of IEC effects in this thesis. In the next chapters we will examine the dynamic interaction between impurities and also the conductance in ribbons. For a discussion of results and future work, please go to the conclusions section.

6

THE DYNAMIC INTERACTION

While the static interactions we have explored in the previous chapters are important for overall alignment, performing calculations in the static regime fails to take into account all of graphene's remarkable properties. In particular, graphene's low spin orbit and hyperfine interactions [30, 73, 74] indicate a material in which dissipation of spin waves is low, and hence has good potential for long range dynamic magnetic interactions. It is these properties that make graphene highly interesting to the field of spintronics, where a number of different applications have been proposed such as using graphene as a spin-pumping transistor [146] and using carbon nanotubes as waveguides [147]. Furthermore, there are many fundamentally interesting dynamic effects present in graphene, such as the non-local behaviour of spin currents around the Dirac point [171]. In this chapter, we move away from the static regime and examine the dynamic magnetic interaction in armchair graphene nanoribbons.

Among all of the strategies for introducing a dynamic magnetic perturbation to a system, one that seems particularly viable is to set the magnetic moments of the impurities in precessional motion. This type of calculation was performed in metallic multilayers by Šimánek and Heinrich in 2003 [142, 172], who demonstrated the increased magnitude and range of the interaction in this scheme. This can be understood in terms of the spin currents emanating from precessing moments. In this case, angular momentum from the moving magnetization is transferred to the conduction electrons, creating a spin disturbance that propagates throughout the conducting material [172]. In 2012 this type of calculation was extended to graphene by Power et. al. [108] again showing the signatures of a vastly increased magnitude and reduced rate of decay. Furthermore, there is reason to believe

that the interaction can be further augmented by the inclusion of a gated region [144]. The dynamic interaction is of particular interest because it is more accessible experimentally than its static equivalent. Dynamic interactions may be examined by ferromagnetic resonance [172] or other methods [173, 174], and Power et. al. have suggested a method whereby the dynamic signal may be obtained in bulk graphene [108], using inelastic scanning tunnelling spectroscopy [140, 145].

Magnetism in edged graphene structures tends to attract less attention than its bulk variant [102, 104, 118–121, 175]. Furthermore, most of this attention is mainly devoted to zigzag edges, with the armchair equivalent receiving substantially less fanfare. This also holds true for dynamic interactions [175], which is surprising since the size and properties of GNRs make them an obvious conduit for spin current in future spintronic devices [58, 76–78]. Given the recent success in manufacturing exact edges [54, 55, 62], we expect that the interest in these structures will grow considerably in the near future. As such, it seems obvious that the study of the dynamic interactions in armchair nanoribbons should be of great interest.

Previously in this thesis, we have examined armchair edge structures, and shown that they exhibit an unusual triadic behaviour. We found that at sites a multiple of 3 from the edge, the IEC exhibited a much more rapid decay. This we attributed to the VLDOS at these locations, determining the lack of itinerant electrons available to propagate the interaction resulted in an exponential decay. It would be interesting to see if perturbing the magnetic impurities and examining the dynamic interaction would cause these triadic effects to vanish. If not, it would be interesting to see how the triadic pattern manifests itself in a dynamic interaction.

In this chapter, we examine the dynamic interaction in armchair graphene nanoribbons. We do this by inserting one or more impurities into pristine nanoribbons, and then perturbing one of them with a small rotating magnetic field (Fig.6.2 and Fig.6.1). We derive an expression for the transverse dynamic spin susceptibility, which contains the complete details of the magnetic response of the system. We use this quantity to determine the lifetime of the interactions in our system, and

determine whether the same triadic behaviour that we previously observed with the IEC is replicated here. We focus on the same sublattice case, due to extra complications introduced in the opposite sublattice case. This is reasonable, a single sublattice distribution of impurities has been theoretically shown to be attainable at low concentrations [116].

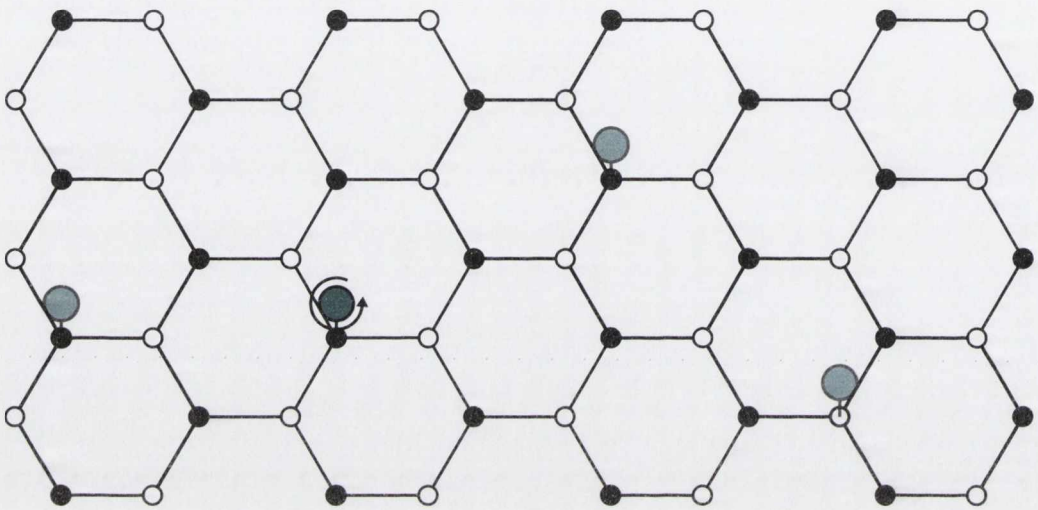


Figure 6.1: A schematic of our dynamic system. The system is populated with one or more impurities, and a rotational magnetic field is applied at a single site, creating a dynamic magnetic perturbation.

6.1 THE SPIN SUSCEPTIBILITY

The first step in examining this interaction is to introduce our Hamiltonian.

$$\hat{H} = \sum_{i,j,\sigma} t\hat{c}^{\dagger}_{i\sigma}\hat{c}_{j\sigma} + \frac{U}{2}\sum_{l,\sigma}\hat{n}_{l\sigma}\hat{n}_{l\bar{\sigma}} + g\mu_B h_Z \sum_{l}\hat{S}^{z}_{l}. \tag{6.1.1}$$

It should be clear that this is the same as the Hamiltonian we have been using for the bulk of this thesis (defined in Sec.2.7), with the addition of a single additional operator. This operator represents an on-site Zeeman field term at the impurity sites, and is used to create a default magnetic alignment. Here, g is the Landé

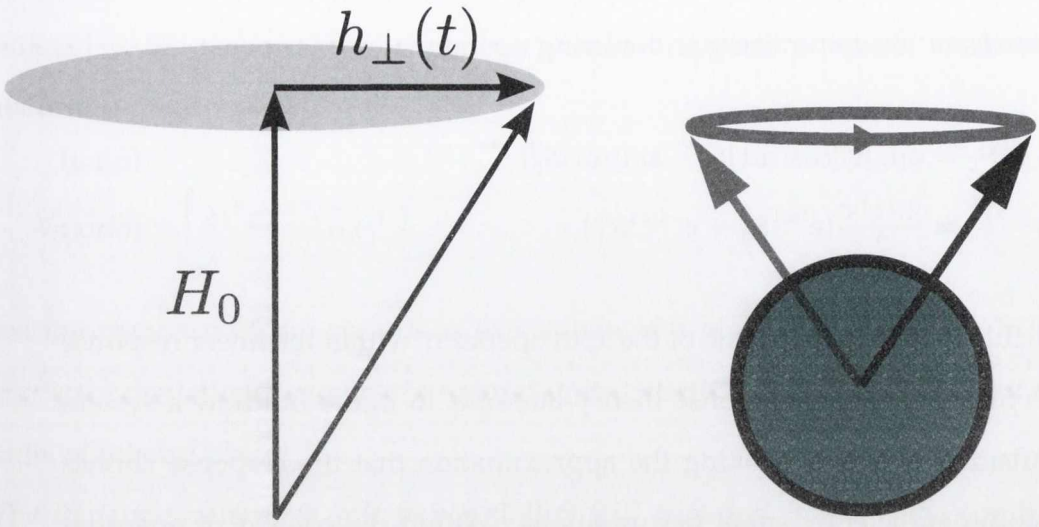


Figure 6.2: A schematic of a precessing magnetic moment driven by the appropriate field.

g-factor, μ_B is the Bohr magneton, h_Z the magnetic field intensity and $\hat{S}^z$ the spin projection operator. As has become common practice in this thesis, we can model this Hamiltonian by breaking it into parts

$$\hat{H} = \hat{H}_0 + \hat{H}_{imp}, \tag{6.1.2}$$

which allows us to calculate the GF of the pristine system first ($\hat{H}_0$), and introduce the magnetic impurities ($\hat{H}_{imp}$) later using the Dyson equation.

Now we introduce the dynamic element of our calculation, for which we choose a time-dependent rotating magnetic field

$$\mathbf{h}_\perp = h_0[\cos(\omega t)\hat{x} - \sin(\omega t)\hat{y}], \tag{6.1.3}$$

situated at one of the impurity sites. The corresponding Hamiltonian term can be written in terms of the spin raising an lowering operators.

$$g\mu_B \mathbf{h}_\perp \cdot \mathbf{S}_0 = g\mu_B h_0[\cos(\omega t)S_0^x - \sin(\omega t)S_0^y] \tag{6.1.4}$$

$$= \frac{g\mu_B h_0}{2}(e^{i\omega t}S_0^+ + e^{-i\omega t}S_0^-) \tag{6.1.5}$$

Now we calculate the change in one of the spin operators within the linear response approach [176, 177]. Linear response theory attempts to figure out how a system reacts to outside influences, making the approximation that the response should be linear within sufficiently small perturbations. Within the context of quantum mechanics, this takes the form of a Kubo formula. We can apply this method to the spin raising operator at site i getting

$$\delta\langle S_i^+(t)\rangle = \frac{g\mu_B h_0}{2}\int_{-\infty}^{\infty} dt'[e^{i\omega t'}\chi_{i0}^{++}(t-t') + e^{-i\omega t'}\chi_{i0}^{+-}(t-t')], \tag{6.1.6}$$

where the spin susceptibilities are given by

$$\chi_{ij}^{+-}(t) = -\frac{i}{\hbar}\Theta(t)\langle[S_i^+(t), S_j^-(0)]\rangle. \tag{6.1.7}$$

Now, the Hamiltonian is invariant under spin rotations around z, hence, the spin projection operator in the z direction S_z is conserved. This means that terms of the form χ^{++} are zero and we can write

$$\delta\langle S_i^+(t)\rangle = \frac{g\mu_B h_0}{2}\int_{-\infty}^{\infty} dt' e^{-i\omega t'}\chi_{i0}^{+-}(t-t'). \tag{6.1.8}$$

This gives the dynamic transverse spin susceptibility by

$$\chi_{m,l}^{+-}(t) = -\frac{i}{\hbar}\Theta(t)\langle[\hat{S}_m^+(t), \hat{S}_l^-(0)]\rangle, \tag{6.1.9}$$

where $\hat{S}^+$ and $\hat{S}^-$ are the spin raising and lowering operators and the quantity calculated is the response at site m due to a field applied at site l. Its Fourier transform

$$\chi^{+-}_{m,l}(\omega) = \int dt' \, e^{i\omega t'} \chi^{+-}_{m,l}(t'), \tag{6.1.10}$$

gives the response of the system to excitations of a given frequency ω. In our numerical calculations we work in natural units, where ω has units of energy and χ units of inverse energy.

The dynamic transverse spin susceptibility χ^{+-}_{i0} contains within it the complete dynamic response of the system. In order to write it in terms of single particle GFs, it must be written within the Hartree Fock approximation, which has already been discussed in Sec.2.7. Within the HF approximation, the susceptibility can be written in terms of the single particle GFs of the system as

$$\begin{aligned}
\chi^0_{ij}(\omega) =& \frac{i\hbar}{2\pi} \int_{-\infty}^{\infty} d\omega' \, f(\omega') \{ G^{R\uparrow}_{ji}(\omega') G^{R\downarrow}_{ij}(\omega + \omega') \\
& - G^{A\downarrow}_{ij}(\omega') G^{A\uparrow}_{ji}(\omega' - \omega) \\
& + [G^{R\downarrow}_{ij}(\omega') G^{A\uparrow}_{ji}(\omega' - \omega) - G^{A\uparrow}_{ji}(\omega') G^{R\downarrow}_{ij}(\omega + \omega')] \} \\
=& I_1 + I_2 + I_3.
\end{aligned} \tag{6.1.11}$$

Where G^R and G^A represent the advanced and retarded GFs. So far in this thesis we have only worked with retarded GFs. The choice of advanced or retarded GFs is the choice in the small imaginary part of the energy, which we discussed in chapter 2. As shown in the above equation the susceptibility can be divided into three integrals. If we wish to perform the integration in a computationally efficient fashion, all of these integrals need to be handled differently. I_1 can be integrated over the imaginary axis, as shown in Sec.2.6.

$$I_1 = \frac{i\hbar}{2\pi} \int_{\eta}^{\infty} dy \, G^{R\uparrow}_{ji}(\omega_F + iy) G^{R\downarrow}_{ij}(\omega_F + \omega + iy) \tag{6.1.12}$$

The same trick can be performed with I_2, except that now we need to perform the calculation in the lower half plane, since this is where the poles of the advanced GF lie.

$$I_2 = \frac{i\hbar}{2\pi}\int_{\eta}^{\infty} dy\, G_{ij}^{A\downarrow}(\omega_F - iy)G_{ji}^{A\uparrow}(\omega_F - \omega - iy) \tag{6.1.13}$$

The final integral contains a combination of advanced and retarded GFs and hence cannot be transformed onto the imaginary axis in either plane. To simplify this integral we follow an approach similar to that outlined by Muniz and Mills [178]. We make the transformation $\omega' \to \omega' + \omega$ in the first term

$$I_3 = \frac{i\hbar}{2\pi}\int_{-\infty}^{\infty} d\omega'[f(\omega' + \omega) - f(\omega')]G_{ji}^{A\uparrow}(\omega')G_{ij}^{R\downarrow}(\omega + \omega'), \tag{6.1.14}$$

and evaluate the whole quantity at $T = 0$ to get

$$I_3 = -\frac{i\hbar}{2\pi}\int_{\omega_F - \omega}^{\omega_F} d\omega' G_{ji}^{A\uparrow}(\omega')G_{ij}^{R\downarrow}(\omega + \omega'). \tag{6.1.15}$$

Now we have all of our integrals in a form that can be easily calculated.

The advantage of the HF approximation is that it can be easily written in terms of single particle GFs. The disadvantage is that it treats both spin channels as independent, and hence is limited in the kinds of excitation it can describe. In particular, HF calculations are limited to examine spin-flip excitations, and ineffective at examining collective excitations. In order to examine more complicated dynamic response we have to work within the random phase approximation (RPA), which is appropriate for describing collective magnetic excitation at low temperature [178–182]. The RPA approximation involves a replacement

$$\hat{c}_i^\dagger \hat{c}_j \hat{c}_k^\dagger \hat{c}_l \approx \langle \hat{c}_i^\dagger \hat{c}_j \rangle \hat{c}_k^\dagger \hat{c}_l - \langle \hat{c}_i^\dagger \hat{c}_l \rangle \hat{c}_k^\dagger \hat{c}_j + \langle \hat{c}_k^\dagger \hat{c}_l \rangle \hat{c}_i^\dagger \hat{c}_j - \langle \hat{c}_k^\dagger \hat{c}_j \rangle \hat{c}_i^\dagger \hat{c}_l, \tag{6.1.16}$$

where all the expectation values are evaluated in the HF ground state. The RPA can be written in terms of the HF susceptibility using

$$\hat{\chi}^{+-}(\omega) = \hat{\chi}^{0}(\omega) - \hat{\chi}^{0}(\omega)\hat{U}\hat{\chi}^{+-}(\omega) \tag{6.1.17}$$

$$= [\hat{I} + \hat{\chi}^{0}(\omega)\hat{U}]\hat{\chi}^{0}(\omega), \tag{6.1.18}$$

which is similar in form to the Dyson equation. Here $\hat{U}_{mn} = U_m\delta_{mn}$.

Analysis of the structure of $\chi^{+-}_{m,m}(\omega)$ shows that it is the retarded Green function associated with the operator that creates local spin excitations. Accordingly, its imaginary part plays the role of the spectral density for local spin excitations. In principle one would look for poles in $\chi^{+-}_{m,m}(\omega)$ in order to find the spin excitation energies. However, for magnetic objects in contact with nonmagnetic metallic substrates, $\chi^{+-}_{m,m}(\omega)$ does not have true poles, but only sharp resonances. This stems from the fact that spin excitations are not exact eigenstates of those systems, but may decay into Stoner excitations [177]. This interpretation is strongly suggested by the form of the RPA equation, which relates $\chi^{+-}(\omega)$ to its mean-field version $\chi^{0+-}(\omega)$. Here specifically,

$$\chi^{+-}(\omega) = \frac{\chi^{0+-}(\omega)}{1 + U\chi^{0+-}(\omega)}. \tag{6.1.19}$$

Thus, the transverse susceptibility displays resonances with line widths determined by $\mathrm{Im}\chi^{0+-}(\omega)$, which is the spectral density for Stoner (single particle spin flip) excitations. In most metallic systems $\mathrm{Im}\chi^{0+-}(\omega) \neq 0$, and collective spin excitations of all energies have finite lifetimes. There are very particular situations, however, for which some collective excitations may "decouple" from the Stoner continuum, as we will show later.

A schematic of our system is shown in Fig.6.1. We again constrain our work to metallic ribbons where $N = (3n + 2)$. As in previous chapters, the vertical positions of the impurities are denoted with respect to a line below the sheet located where the next atomic site would be. We label our impurities starting from zero. The goal

of this chapter is to examine multiple impurities systems, but we will start with a single impurity.

6.2 SINGLE IMPURITIES

In Fig.6.3 we can see χ_{00} as a function of ω for a single impurity at the edge of a nanoribbon. The real part crosses zero at the point of the excitation, identifying it as a true collective excitation. The onsite spectral density $\chi_{00}(\omega) \equiv \mathrm{Im}\chi^{+-}_{0,0}(\omega)$ is given by the imaginary part of the susceptibility and allows us to probe the life and character of the excitations. The peak in χ_{00} occurs around $g\mu_B h_Z$, indicating that resonance occurs around the Larmor frequency, as we would expect. There is, however, a non-negligible shift from the "bare" resonance frequency, that we attribute to the coupling between the spin excitation and the continuum of Stoner excitations in the host. Also noticeable is the finite linewidth of the peak, implying a finite lifetime for this excitation (the lifetime is inversely proportional to the linewidth of the excitation peak). As we mentioned before, the origin of the finite lifetime is the decaying of the spin excitation into Stoner excitations. This decay process results in a transfer of spin angular momentum from the magnetic adatom to the non-magnetic substrate, which is known as *spin pumping*.

Fig.6.3 shows the same calculation on a line of VLDOS $D_Z = 3$. Again, the real part of the susceptibility crosses zero, indicating a collective excitation. Furthermore, the spectral density shows the same features, a single peak, located at roughly the same position as before. However, the peak width has narrowed considerably, resembling a delta function in appearance. This indicates that the excitation has an extremely long lifetime. Repeated calculations demonstrate that this kind of peak is ubiquitous on VLDOS lines, with the peak obtained in Fig.6.3 being standard everywhere else. Fig.6.4 we show how the full width at half maximum height (FWHM) varies with position in the nanoribbon, and demonstrates the familiar tri-

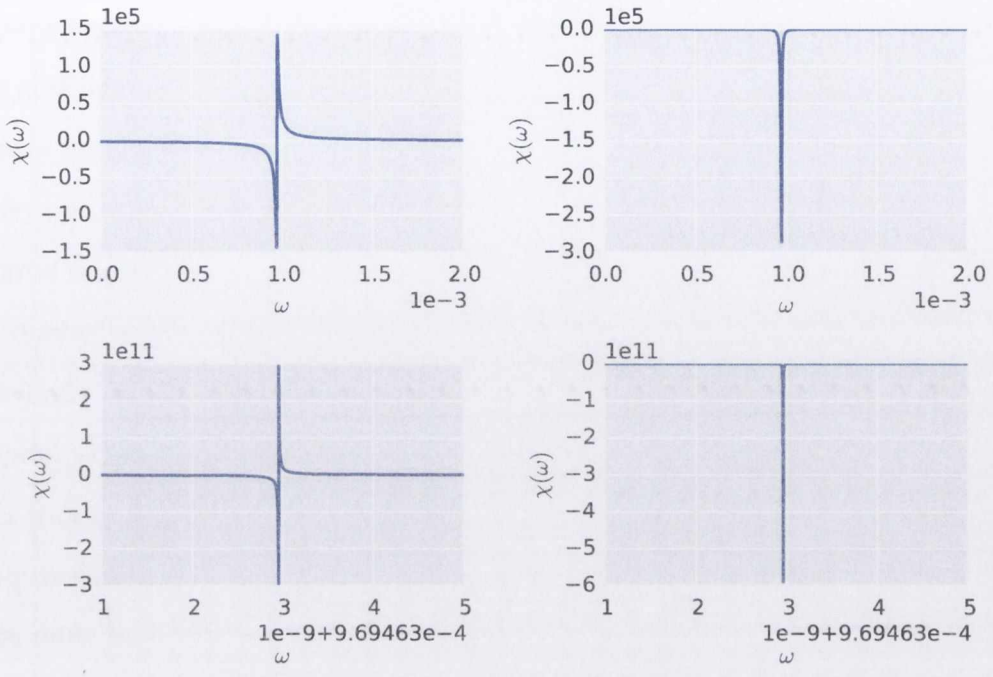


Figure 6.3: Plots of χ_{00} for a single impurity in a nanoribbon. From left to right are the real and imaginary parts. Top represents a single impurity on the edge of a nanoribbon ($N = 5$, $D_Z = 1$), and bottom shows the spin susceptibility of a magnetic impurity in a position with VLDOS ($N = 5$, $D_Z = 3$).

adic pattern that we have already observed elsewhere. It should be clear that this is another pattern emerging from the periodic VLDOS in nanoribbons. The likely mechanism underlying this is the lack of itinerant electrons at the Fermi level in the host. This strongly reduces the coupling between the magnetic adatom and the host, making the adatom's magnetization behave essentially as an isolated spin. Since our model is strictly spin-rotation invariant the spin excitations are infinitely lived, and hence the linewidth vanishes. Given the extraordinary sensitivity to position of the FWHM, it is will be interesting to see how this influences the coupling between impurities.

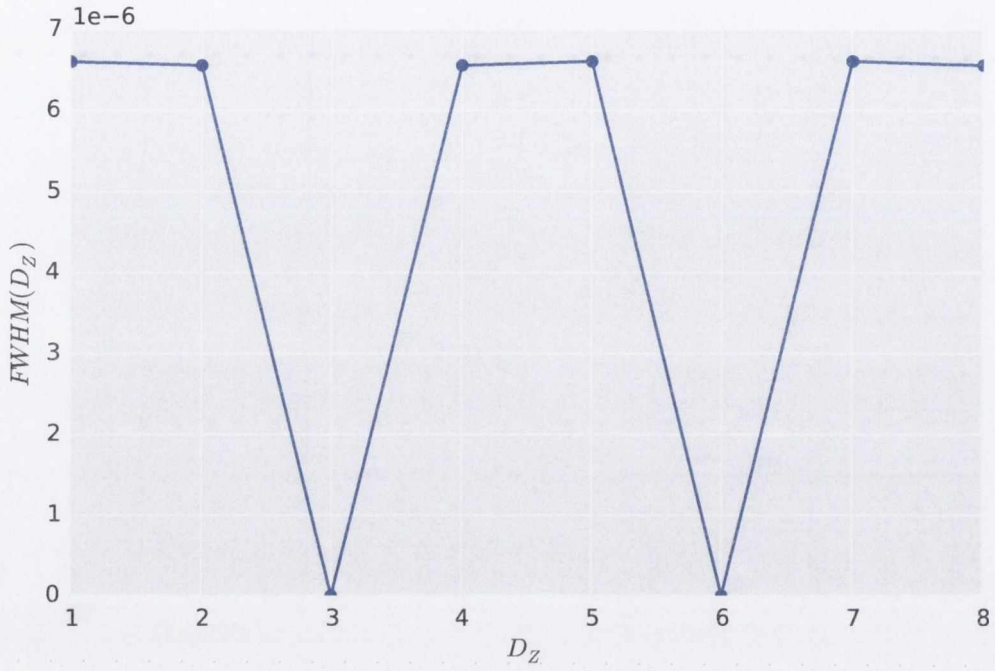


Figure 6.4: A plot of the FWHM of the peaks against D_Z across a nanoribbon of width N = 8

6.3 TWO IMPURITIES

When two magnetic adatoms are adsorbed to different substrate sites there will be two kinds of indirect magnetic interaction between them, both mediated by the electrons in the host. One is the static IEC, which emerges from the spin polarization of the host's electron density due to the coupling to the adatoms. The other is the dynamic interaction that appears as one of the adatoms' magnetization is disturbed and pumps transverse spin moment into the host, which will be partially absorbed by the other adatom and disturb its own spin moment.

It is reasonable to expect that cases with two interacting impurities can be divided into three distinct situations: both impurities off VLDOS lines, one on, and both on. In Fig.6.5 we plot the on site and the off diagonal matrix elements of the spectral density, $\chi_{00}(\omega)$ and $\chi_{10}(\omega)$, for two impurities away from VLDOS sites.

They represent the transverse spin component acquired by adatom 0 (1) due to a pumping field applied to adatom 0. It is clear that the first peak has the same phase and intensity in both adatoms, but the second peak changes sign in χ_{10}. This indicates that, at the frequency of the second peak, the phase of the disturbance in adatom 1 relative to the pumping field is π, whereas the phase of the disturbance in adatom 0 relative to the pumping field is 0. Thus, we usually refer to these modes as "acoustic" and "optical". The most obvious feature of the onsite susceptibility is the severely reduced width of the optical mode in comparison to that of the acoustic mode. This is highly unusual, since in most metallic systems the density of Stoner modes increases with energy. However, since the adatoms are adsorbed to two equivalent sites the spin excitations of a given parity can only decay into Stoner modes with the same parity. Thus the relevant quantity to determine the lifetime of the optical mode is the equivalent optical Stoner mode. In this particular case the optical Stoner mode has negligible spectral density, thus leading to a vanishing linewidth of the optical spin excitation mode.

We now wish to examine the linewidth of the acoustic mode in the 2 impurity configuration. We find that it is strongly reduced from the single impurity situation, indicating that the excitation has a longer lifetime. The obvious interpretation is that the spin current pumped by each of the impurities constantly effects the other, and this interference will be either constructive or destructive. We expect that this could lead to either suppression or augmentation of the overall interaction. As such, we examine the change in linewidth with separation to extremely high distances in Fig.6.6. We can see an oscillatory dependence of the linewidth, and hence lifetime, on the separation. This would seem to validate our model. Furthermore, we see that the result eventually converges to the single impurity case, as we require for consistency. Subsequent calculations show that these results are common to all cases where neither impurity occupies sites with a finite LDOS.

Now we perform similar calculations where only a single impurity occupies a VLDOS site. Here we would expect the interaction between impurities, and hence

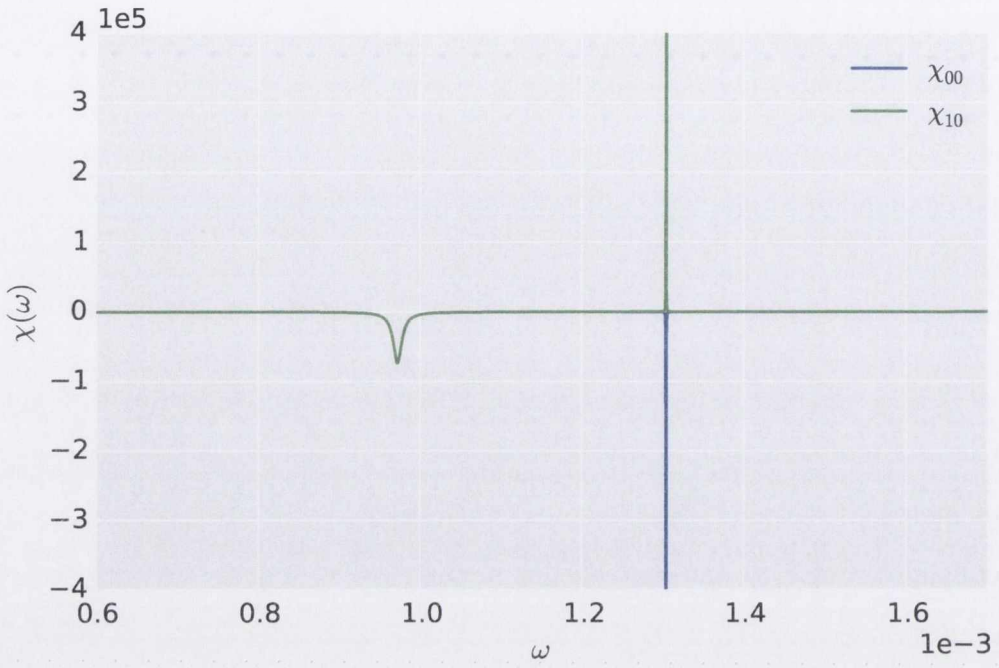


Figure 6.5: A plot of the on and off site susceptibilities, χ_{00} and χ_{10}, against ω. Both impurities are located away from VLDOS sites. Shown is a nanoribbon of with N and impurities at positions $D_{Z1} = 1, D_{Z2} = 1$ and $D_A = 10$.

the deviation in linewidth, to be extremely low. In Fig.6.7 we plot the susceptibility against the frequency for two cases where a single impurity occupies a VLDOS site. It can clearly be seen that even a relatively small increase in separation causes the peaks to converge. This signals that there is little to no interaction between impurities. This is confirmed by a plot of the FWHM against separation, shown in Fig.6.8. We see that convergence to the static case is extremely rapid, both for the VLDOS impurity and the finite LDOS impurity. This is the first indication we have that impurities situated on VLDOS sites simply vanish from the interaction, with their presence only slightly affecting impurities within an extremely close range. In a large nanoribbon, with a diffuse scattering of impurities, we might expect the impurities adsorbed on VLDOS sites to vanish from the interaction altogether.

Finally, the case where both impurities occupy VLDOS sites is very similar to the case where one does. Two peaks are observed at exceptionally close separations,

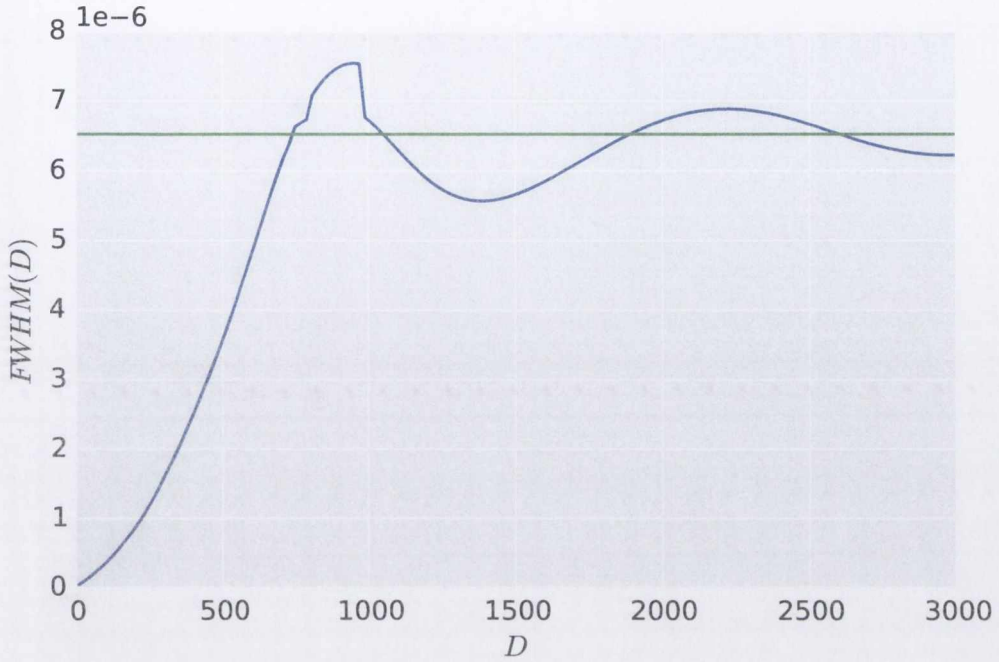


Figure 6.6: A plot of the FWHM of the acoustic peak against separation for the dynamic interaction between two impurities on the edge of the nanoribbon. There is a large dip in the FWHM where the optical peak is absorbed, but afterwards, we find that it oscillates around the single impurity value.

with both the picture, and the FWHM, converging to the single impurity after that. This demonstrates, once again, the lack of interaction between the impurities and the host, and indicates that with a large distribution of impurities, these cases may be excluded from the interaction.

6.4 3 OR MORE IMPURITIES

In order to confirm our predictions from the previous section, we need to start examining a higher number of impurities. In Fig.6.9 we plot the susceptibility against ω for three impurities, where none of the impurities occupy VLDOS sites. We get roughly the result we expect, where we now have three modes of descending width.

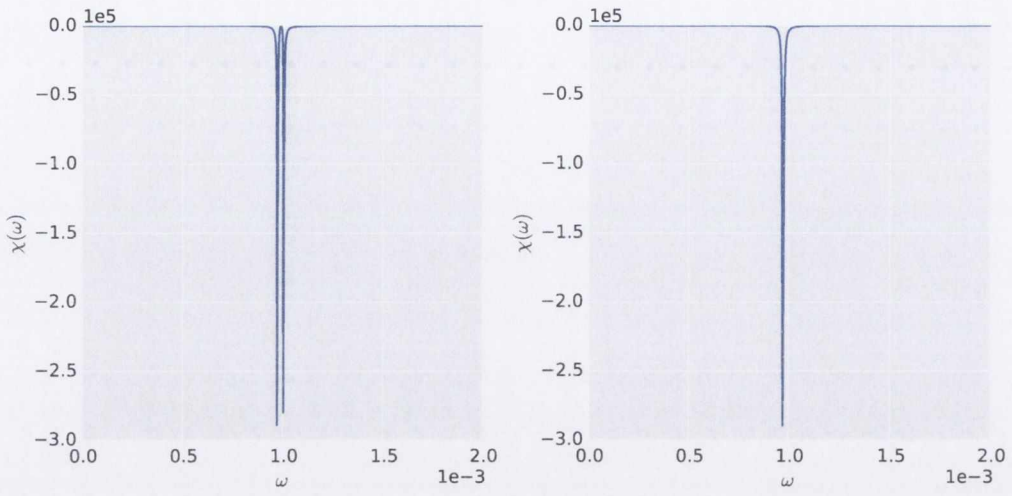


Figure 6.7: A plot of χ_{00} against ω where impurity 1 occupies a VLDOS site. We work in a nanoribbon of with N. On the left we show two impurities in locations $D_{Z1} = 1, D_{Z2} = 3$ and $D_A = 2$. On the right we show two impurities in locations $D_{Z1} = 1, D_{Z2} = 3$ and $D_A = 6$. The optical peak quickly converges with the acoustic peak, returning to the single impurity situation.

Now we examine the same system where one of the impurities occupies a VLDOS site. In Fig.6.10, we plot the susceptibility against the frequency for such a system. Now we are reduced to two peaks, and furthermore, we plot the equivalent two impurity system against it, resulting in an exact match. This goes some distance to confirming our hypothesis that VLDOS sites simply do not participate in the dynamic interaction and hence do not affect the lifetime of excitations. The fact that one third of a diffuse scattering of impurities do not interact with the others at all, and display a very different signal, should make this an effect that is easily probed by experimental methods, such as ferromagnetic resonance (FMR).

6.5 CHAPTER SUMMARY

In this chapter we examined dynamic magnetic interactions between top-adsorbed impurities in graphene nanoribbons. Dynamic magnetic interactions occur in the

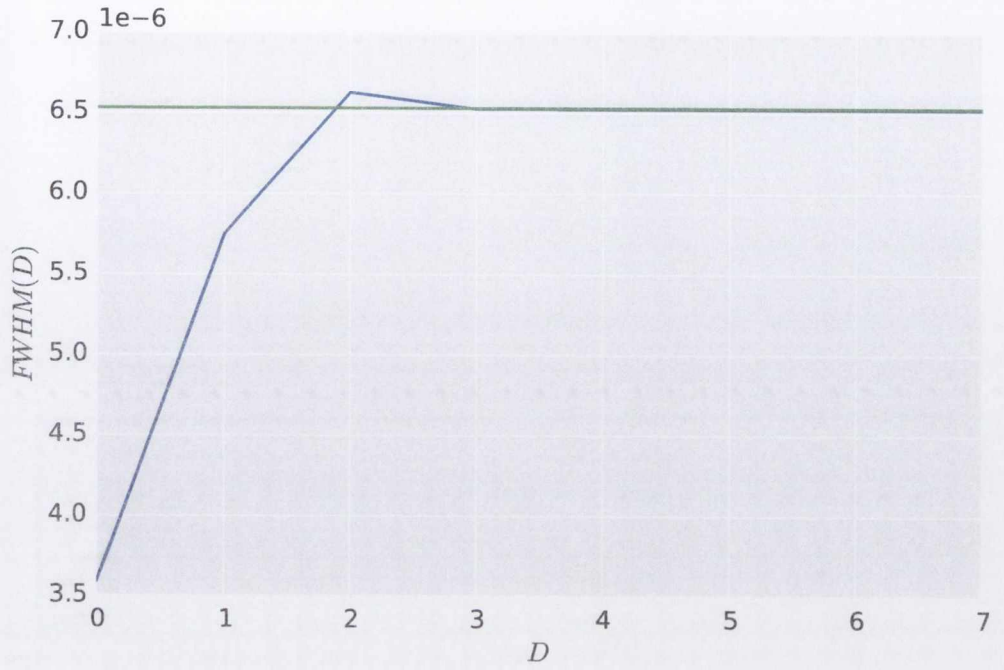


Figure 6.8: A plot of FWHM against separation for the dynamic interaction between two impurities where one occupies a VLDOS sites. We can see quick convergence to the single impurity case.

presence of a time dependent magnetic perturbation. The quantity most appropriate for examining this interaction is the dynamic spin susceptibility, and we derived an expression for it in this chapter. We began by examining the susceptibility of single magnetic impurities, demonstrating the familiar triadic pattern seen in previous chapters, but this time in the excitation lifetime. We found that impurities located on VLDOS sites had a far higher excitation lifetime, and interpreted this as an effect of the impurities being decoupled from the conduction electrons. Furthermore, when we examined 2 and 3 impurities, we found that impurities in such locations did not participate in any interactions. Therefore, we propose that it should be possible to find an experimental signature for this effect. The results in this chapter are in preparation for publication.

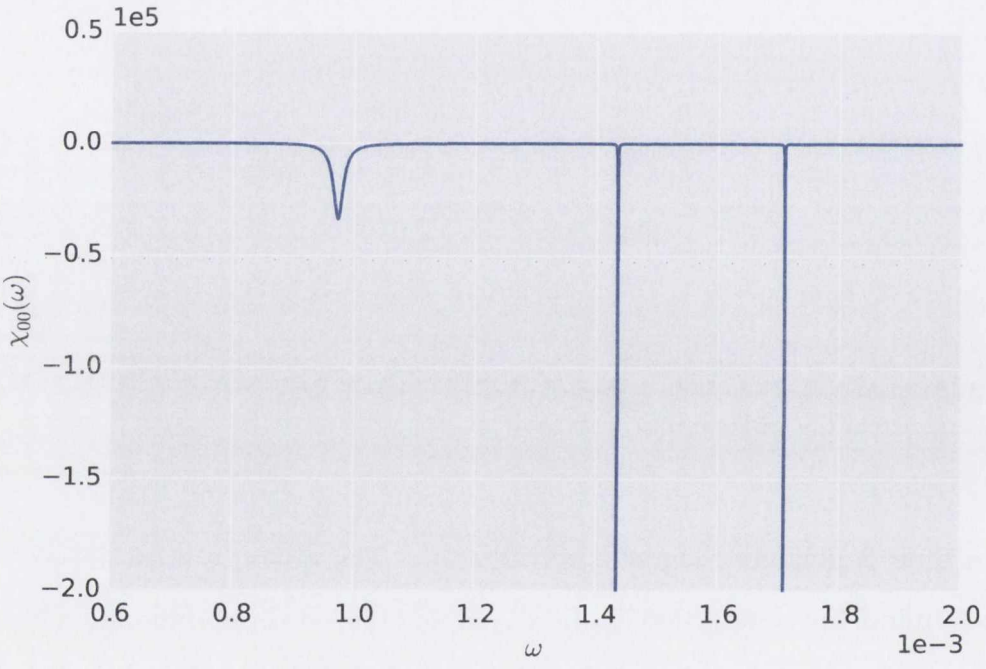


Figure 6.9: A plot of χ_{00} against ω for three impurities. We work in a nanoribbon of width $N = 5$ and have impurities located at $m1, n1, m2, n2, m3, n3 = 6, 1, 0, 4, 3, 8, 7$ (where we return to (m, n) notation since it is more appropriate for multiple impurity situations).

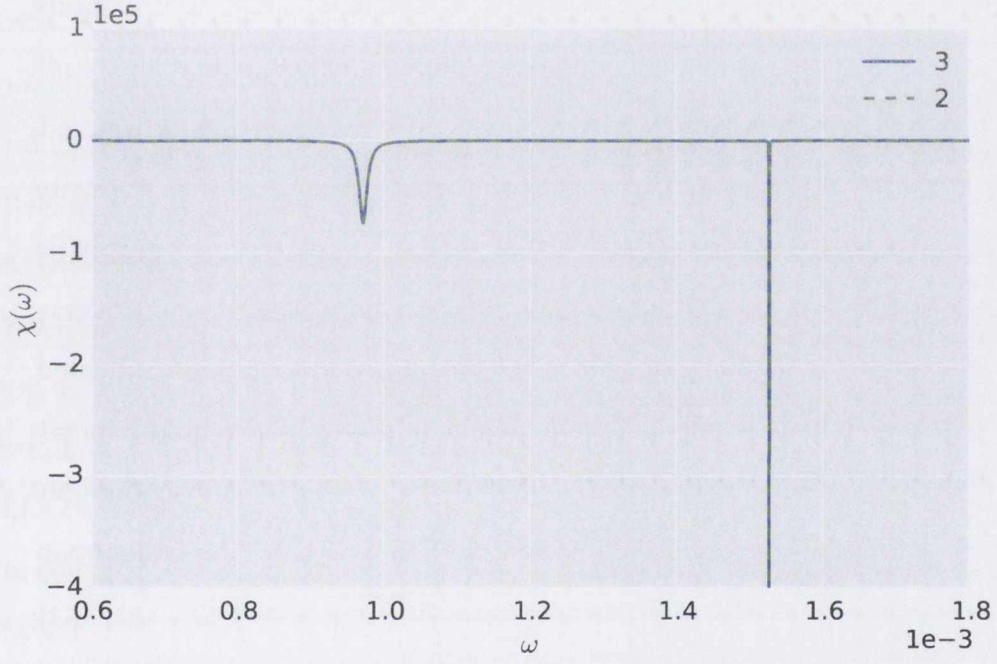


Figure 6.10: In this plot we compare χ_{00} against ω for three impurities where one occupies a VLDOS site, and the equivalent two impurity system. We work in a nanoribbon of width $N = 5$ and our impurities are located at $m1, n1, m2, n2, m3, n3 = 6, 1, 0, 4, 3, 10, 7$. We find the impurity on the site of VLDOS does not interact with the other sites since the two plots are identical.

7

THE CONDUCTANCE OF NANORIBBONS

Graphene, a semi-metal, exhibits remarkable conductance by any standard. At room temperature, there are few materials that can compare to it, as it exhibits mobilities as high as $15,000 cm^2 V^{-1} s^{-1}$ for both charge carriers [8, 25, 148, 149]. Furthermore, it is believed that even these figures can be substantially improved, as the weak temperature dependence of the conductance indicates that impurity scattering is the dominant contribution. Although the conductance of graphene nanoribbons might be expected to be similar to bulk, there is some controversy surrounding the conductance of GNRs. Initial tight-binding calculations indicated that zigzag GNRs were always metallic, whereas the armchair case could be metallic or semi-conducting depending on their width [48, 53]. However, subsequent ab-initio work has cast doubt on these assumptions, predicting a width dependent gap for armchair nanoribbons and conflicting results for the zigzag case [48, 152, 153]. Recent experiments seem to both confirm this model for the armchair case and continue the controversy in the zigzag case [49, 155]. However, even more recent experimental evidence has demonstrated ballistic transport in epitaxially grown GNRs [156], with conductance properties exceeding those of the bulk by a factor of ten. As such, it is reasonable to expect excitement about the conductance of nanoribbons to remain at a high level for the foreseeable future.

Part of the interest in graphene's conductance stems from its use in simply transporting charge with great speeds and low costs. However, perhaps of even more importance is graphene's potential as a *sensor*. Graphene's extraordinary conductive properties are considered a boon in sensor technology, but its peerless surface to volume ratio makes it attractive in fields where the detection of a very small fraction of impurities is necessary. Indeed, graphene has already shown great potential

in this area [157, 163–165]. As such, there is great interest in the kinds of impurities that graphene can detect. Work has already been performed in this area [158–160], but has focused on individual impurity species rather than any general quality. In this section, we want to show how the bonding symmetry is a dominant factor in the conductance.

As we have shown in chapter 4, the RKKY interaction is highly sensitive to impurity conformation, decaying at drastically different rates depending on the type of impurity. We also showed that it is highly correlated with the LDOS. But the RKKY is fundamentally a scattering process (Fig.7.1) and the intensity of the scattering determines the strength of the coupling. The conductance is also fundamentally a scattering process, scattering is determined by the impurity and related to the LDOS. Therefore we might expect that the results we have already achieved for the RKKY will be mirrored by the conductance. Strong scatterers, like substitutional and top-adsorbed impurities should contribute heavily to scattering and reduce the conductance. Weak scatterers, like center-adsorbed impurities and impurities on VLDOS lines should barely effect the conductance. In this chapter, we examine the effect of different impurities on the conductance, and see if our predictions prove correct.

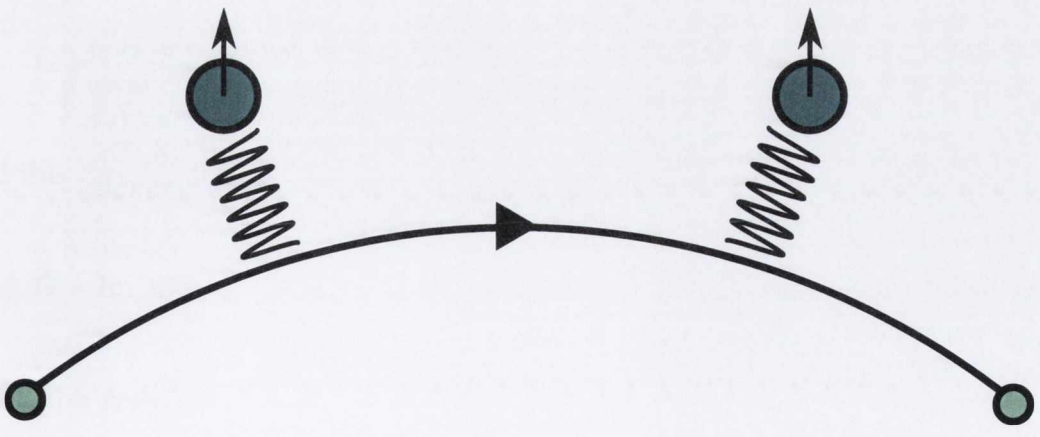


Figure 7.1: The RKKY interaction arises from a double scattering event of an electron off magnetic impurities. In practice it is calculated by means of a Feynmann diagram, which we have illustrated schematically here.

In this chapter we will examine the conductance in armchair nanoribbons using the tight binding method. While there are reasons to believe that tight-binding may not replicate the band gap seen in the DFT literature, it is the only method that will allow us to handle disorder at the kind of impurity densities that we need to prove a general result. Furthermore, the comparative computational lightness of the tight-binding method allows us to handle nanoribbons of much greater width than DFT processes, and hence we might expect that our results will provide a reasonable approximation to the result in graphene. We build systems similar to that shown in Fig.7.2 and then examine the conductance using the Kubo formula introduced in the next section. Our nanoribbons will generally have a scattering region (since we want to know the effect of the impurity conformation on the conductance) and hence are built recursively using the methods from Sec.2.4.

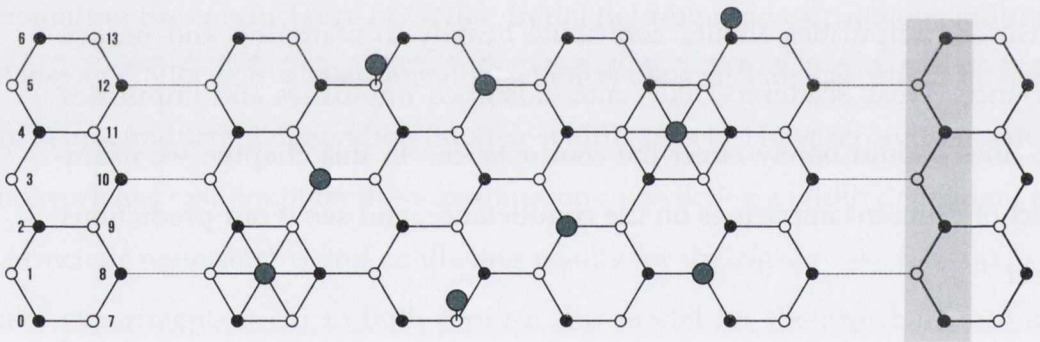


Figure 7.2: A schematic of the scattering region in a nanoribbon. We can add any kind of impurity to our scattering region and this is shown by the green circles in the figure. In practice, we generally add impurities homogeneously (i.e. all top or center). The central region in the figure has $N = 7$ and $p = 4$. The grey area shows the contour we use when calculating the Kubo Formula. The strip on the left shows our numbering convention.

7.1 THE KUBO FORMULA

We can calculate the conductance by means of the Kubo formula, which is given by [183]:

$$\Gamma(\omega) = \frac{\pi}{\omega}\int dE \sum_{\substack{k,k' \\ \epsilon(k)<E_F<\epsilon(k')}} |\langle k|\hat{I}|k'\rangle|^2 \delta(E+\hbar\omega-\epsilon(k'))\delta(E-\epsilon(k)) \tag{7.1.1}$$

where $\hat{I}$ is the current operator, ω is the frequency, and the sum extends over all eigenstates of the system satisfying $\epsilon(k) < E_F < \epsilon(k')$. It is desirable to replace these eigenstates, which we do not know, with Green's functions which we do, and this can be achieved by following a procedure similar to that of Mathon [184] to get

$$\Gamma(E_F) = \frac{4e^2}{h} \mathrm{Tr}\left[\tilde{G}_{00}(E_F)V_{01}\tilde{G}_{11}(E_F)V_{10} - V_{01}\tilde{G}_{10}(E_F)V_{01}\tilde{G}_{10}(E_F)\right] \tag{7.1.2}$$

where the leading term originates from the current operator, and the units of the GF and connection potentials cancel (inverse energy and energy respectively). Here

$$\tilde{G} = \frac{1}{2i}(G^A - G^R) \tag{7.1.3}$$

and this can be written as

$$\tilde{G} = \mathrm{Im}(G^R) \tag{7.1.4}$$

using the results from the Appendix. With this formula, and the recursive GFs from chapter 3, we can start to calculate the conductance of some nanoribbons.

7.2 THE CONDUCTANCE

Before we begin performing our calculations we should take a moment to discuss our notation. Our nanoribbons are built using recursive methods, which are discussed in the context of graphene nanoribbons in Sec.3.3.2. Many of our notative conventions originate in that chapter, such as the labelling of sites from the edge and using the bottom left site to label center-adsorbed impurities. These notations are revised again in the context of our current system in Fig.7.2. In this chapter, N gives the size of the nanoribbon, i the site of the impurity and p the size of the scattering region (in number of unit cells).

We start by examining a pristine metallic ribbon as shown in the left panel of Fig.7.3 in units of $\frac{2e^2}{h}$ (which will be our default unit of conductance for the remainder of the chapter). The structure of the plot makes it clear that we are in the ballistic transport regime, with every subband contributing a quantum of conductance. Since we are working within the tight binding approximation and are examining a nanoribbon of width $N = 8$, no gap is apparent. The limitations of this approach have already been discussed and we hope that they are less apparent for wider ribbons. Such a case is shown in the top right sub-panel in Fig.7.3, and we can see how the structure begins to approach that of pristine graphene. Although we expect that our results are more applicable in wide nanoribbons, we will often make use of the thinner variety for illustrative purposes, since any effects are more easily visible. Finally, in the bottom right panel of Fig.7.3 we plot results for a semiconducting nanoribbon, where the bandgap is obvious.

Obviously the goal of this chapter is to examine the effect of various impurities on the conductance and we follow the structure of previous chapters by examining substitutional impurities first. In Fig.7.4 we plot the conductance against Fermi energy for a substitutional impurity occupying one of the first three sites from the edge. The first two sites show a considerable dip in the conductance around the Dirac point, while the third shows almost no change from the pristine case. The re-

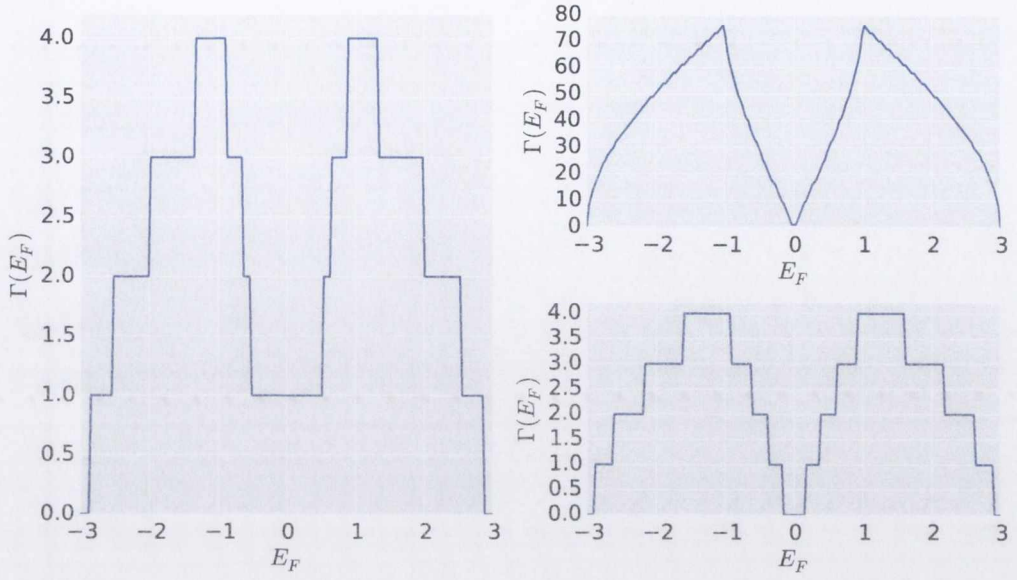


Figure 7.3: A plot of the conductance for pristine armchair nanoribbons. On the left, in the large panel, we show a thinner nanoribbon (N = 8) for clarity. From this we can clearly see that we are in the ballistic transport regime and clearly see the quantisation of the conductance. There is no gap at the center of the band indicating that the nanoribbon is metallic. In the upper right panel we have performed the same plot for much wider nanoribbon (N = 150) and we can see that we are beginning to achieve the conductance of prisine graphene. Finally, in the bottom left panel we plot the conductance of a semiconducing nanoribbon (N = 9), where the gap at the center is apparent.

sults are easily interpreted with reference to the LDOS which has been examined in chapter 3. In general, we expect the introduction of impurities to lower the conductance by breaking the symmetry of the nanoribbon and increasing the scattering cross-section. However, on examining the LDOS, we can see that impurities on sites a multiple of three from the edge have zero LDOS at the Dirac point. We have examined this before in the context of the IEC interaction, and it is interesting to see the same effect apparent in a different physical quantity. Further calculations show that this triadic pattern repeats across the width of the nanoribbon, which mirrors our results for both the LDOS and the IEC (Fig.7.5). We also examined the same effect in top-adsorbed impurities, where an identical pattern was observed. That the adsorption site can change the value of the conductance is an important

result, that can be useful in determining which impurities would be detected in graphene sensors.

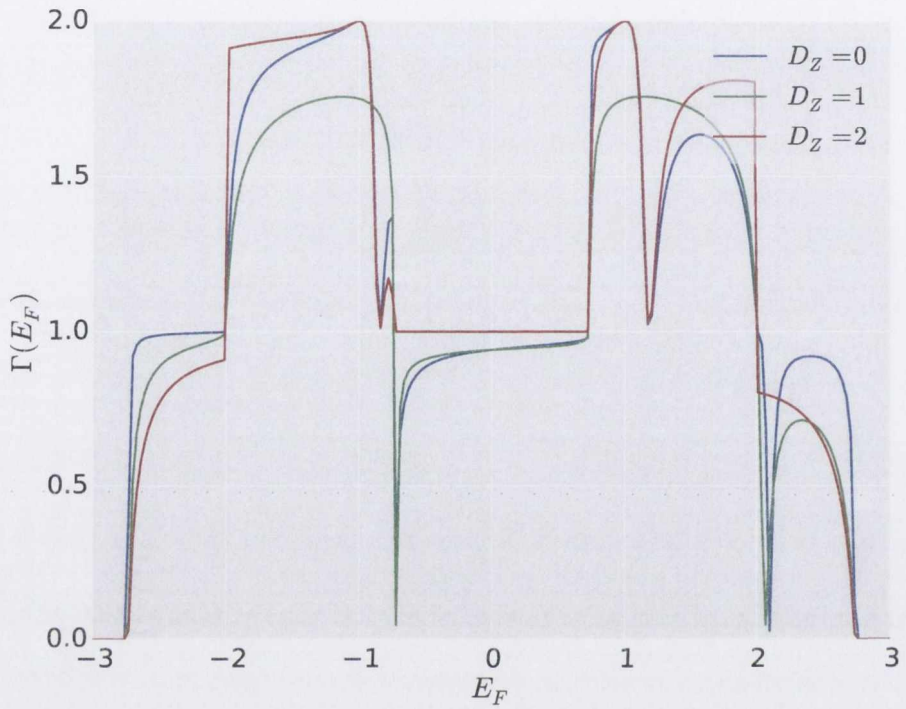


Figure 7.4: Conductance for substitutional impurities in a ribbon with N = 5. The final position is a VLDOS site and the conductance around the Dirac point is relatively unaffected by the addition of the impurity. We have performed the calculation in a narrow ribbon for clarity, but a similar picture emerges in wider ribbons.

The last impurity type that we wish to examine is the center-adsorbed impurity. We expect this type of impurity to have a much smaller effect on the conductance, as it exhibits a much smaller IEC as well as a much flatter LDOS than the other impurity types, indicating that it is a weaker scatterer. In Fig.7.6, we plot the conductance against energy for substitutional, top, and center-adsorbed impurities at representative sites. It is immediately clear that the top-adsorbed and substitutional impurities suffer a much greater dip in conductance around the Dirac point than the center-adsorbed case. Repeated calculations show that the effect is consistent across a wide range of ribbon widths and positions, except in the case where

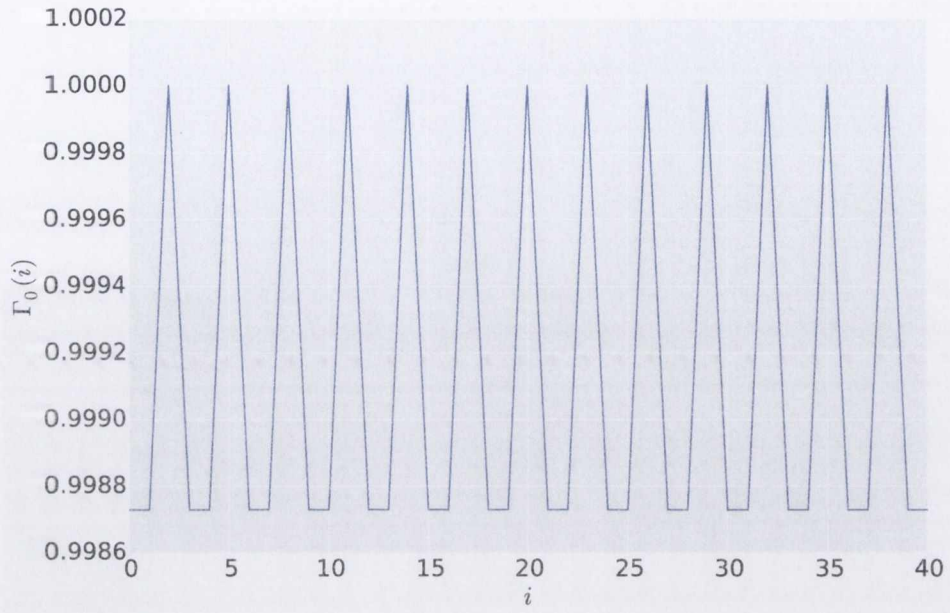


Figure 7.5: Conductance of substitutional impurities at the Dirac point vs position. The triadic pattern is apparent. The calculations were performed in a ribbon of width N = 41.

top-adsorbed and substitutional impurities occupy VLDOS sites. However, from a device perspective we would expect a diffuse scattering of randomly adsorbed impurities. In these cases, we would expect impurities on VLDOS sites to only make up a third of the total impurities. It would be interesting to see if the strong signal from the center-adsorbed impurities survives in such an environment, or whether the lack of contribution from the VLDOS sites is sufficient to mask any difference between the different impurity type. In order to examine this, we must use configurational averaging.

7.3 CONFIGURATIONAL AVERAGES

Since engineering the adsorption of single impurities at specific sites is difficult experimentally, the question we would like to ask is how a specific type of confor-

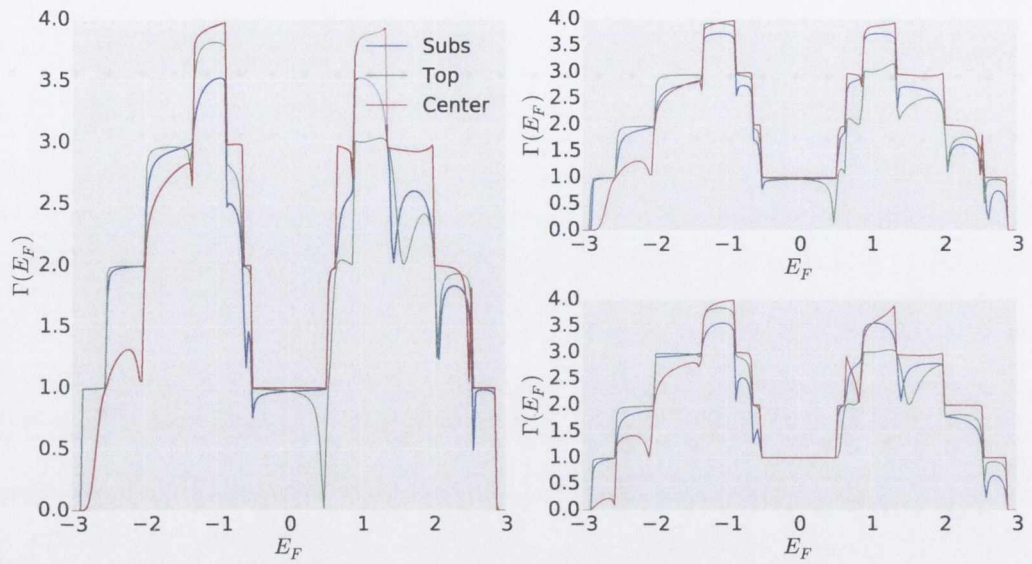


Figure 7.6: Comparison of the conductance for various kinds of impurity. The calculations were performed in a ribbon of width N = 8. The figure on the left has the impurity situated on the edge site i = 0. The superiority of the center-adsorbed case should be obvious. The figure on the top right maintains the center position, but the substitutional and top adsorbed impurities are situated at i = 1. Here too, the conductance is demonstrably better for the center-adsorbed case. Finally, in the bottom left, we plot the conductance against energy for impurities situated at i = 2. The substitutional and top-adsorbed impurities are situated at a VLDOS site and hence have little effect on the conductance.

mation *generally* effects the conductance. The most appropriate way of doing this is with a configurational average, where we sum and average all possible impurity configurations (A schematic of this process is shown in Fig.7.7). In this section we perform both *total* and *random* configurational averages. In the former, we examine every possible configuration, whereas in the random version we sample different systems until convergence is achieved. It should be obvious that performing a total configurational average is only possible for a small concentration of impurities, and that the addition of randomness is more important as the impurity concentration becomes larger.

In Fig.7.8 we plot the total configurational average for the different impurity conformations (for only a single impurity). The plot seems to confirm that the

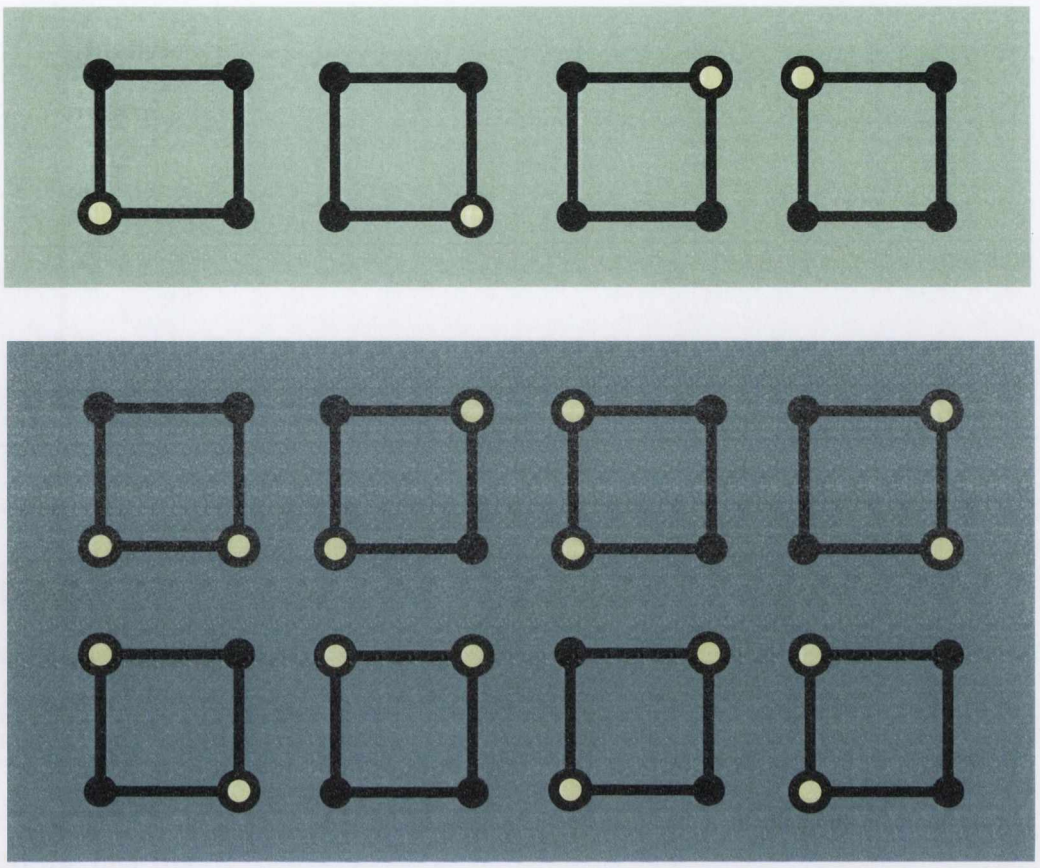


Figure 7.7: An illustration of the configurational average. Here we take the total configurational average over a small 2x2 grid. The single impurity case is presented above and the double impurity case below. Every single case is calculated and then averaged.

center-adsorbed impurities have the least effect on the conductance, even despite some possible configurations including VLDOS sties. However, to this point we have only examined the effect of single impurities on the conductance. This does not guarantee that a larger distribution of impurities has an equivalent effect, since impurities can interact and affect the overall scattering. In Fig.7.9 we produce the same plot for a much wider nanoribbon with a much larger scattering region and many more impurities. Now we must average over randomly sampled configurations, because to sample the whole configuration space would take an unreasonable amount of time. We keep sampling until we achieve a reasonable level of convergence, at which point we can see that roughly the same results are achieved as in

the smaller nanoribbon. These results were replicated for a number of different ribbon widths, scattering section sizes and impurity concentrations. We constantly obtained a higher conductance around the Fermi level for center-adsorbed impurities.

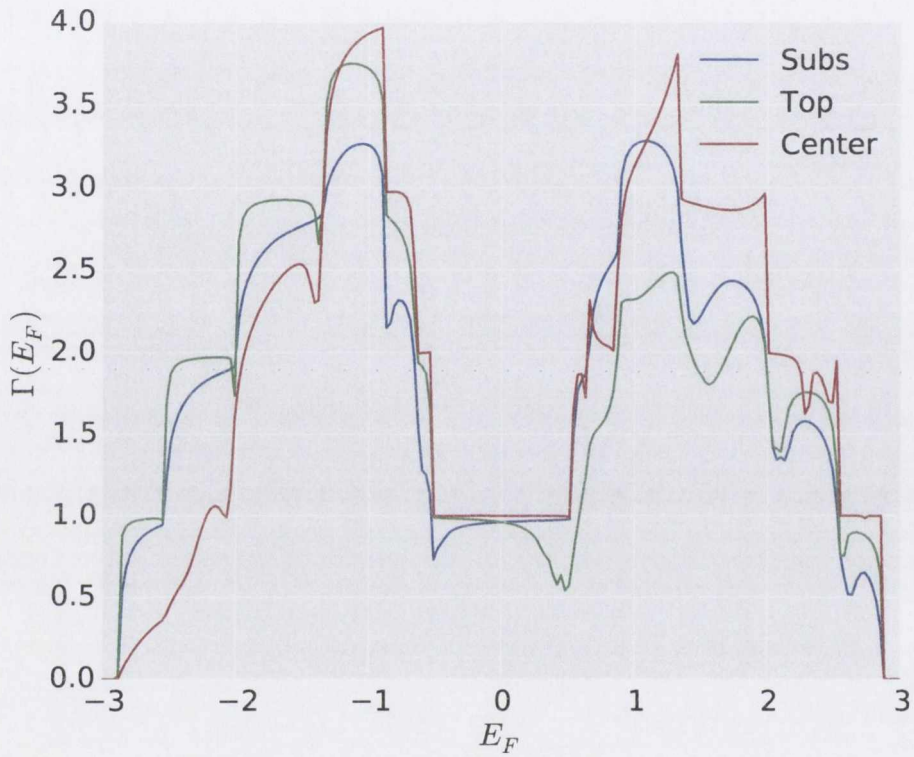


Figure 7.8: Configurational average of the conductance for various kinds of impurity. The calculations were performed in a ribbon of width N = 8, over a region of length p = 1 and with 1 impurity.

However, to better understand how the concentration affects the conductance, we can plot the configurational average of the conductance at the Fermi level against concentration. This should help demonstrate the superiority of the center-adsorbed coupling for any concentration of impurity. In Fig.7.10 we plot the configurational average of the conductance at the Dirac point against increasing impurity concentration for the different conformations. We find consistent superiority of the center-adsorbed case over all impurities concentrations. Furthermore, we should remark

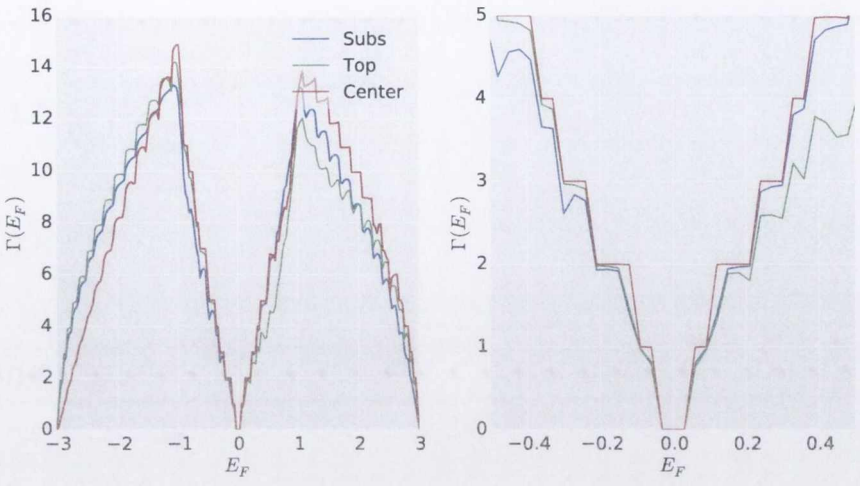


Figure 7.9: Random configurational average of the conductance for various kinds of impurity. The calculations were performed in a ribbon of width N = 30, over a region of length p = 2 and with 4 impurities. 500 iterations were performed until we began to achieve convergence. On the left we show the full plot and on the right we zoom in around the Dirac point.

upon the fact that this plot is essentially linear, which indicates that the main contribution of the impurities to the conductance is a first order effect, and not an interaction term. We can repeat these results using a much wider nanoribbon and the random configurational average in Fig.7.11. This figure essentially replicates our previous results, except now we see non-linear behaviour in the substitutional and top-adsorbed cases, which we would expect as impurity concentration increases. However, the center-adsorbed term still seems essentially linear, which makes sense given that all of our results indicate that center-adsorbed impurities do not interact with each other as much. This is an important result, especially in the case of graphene sensors, because it gives us an idea of a *general* impurity conformation that graphene will not be sensitive to.

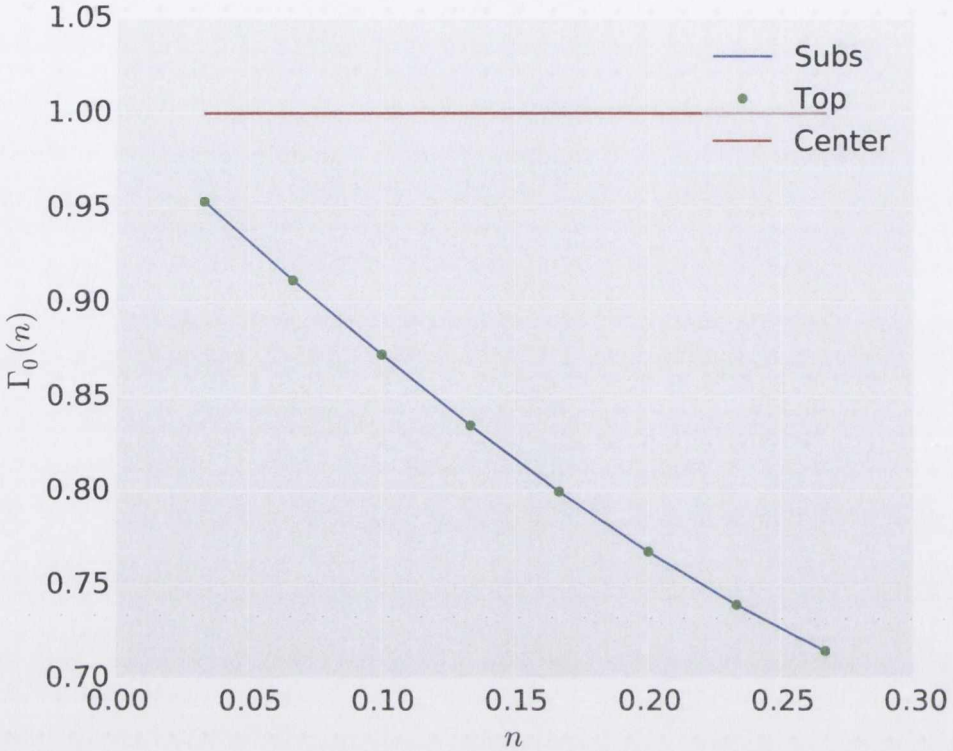


Figure 7.10: The total configurational average of the conductance at the Dirac point plotted against increasing impurity concentration for different conformations. n represents the fractional concentration of the number of impurities to the number of sites in the scattering region. Substitutional and top-adsorbed impurities behave identically, center-adsorbed impurities demonstrate a much higher conductance and a far slower decay with increasing impurity concentration.

7.4 AN ANALYTIC APPROACH

Unfortunately, in contrast to previous chapters, we can produce no completely analytic equation that completely describes the change in conductance. However, we can examine the reasons why such a change occurs on a more fundamental level. Throughout this chapter, we have drawn a lot of correlations between the change in the conductance and the LDOS. It would be nice if we could see this relation

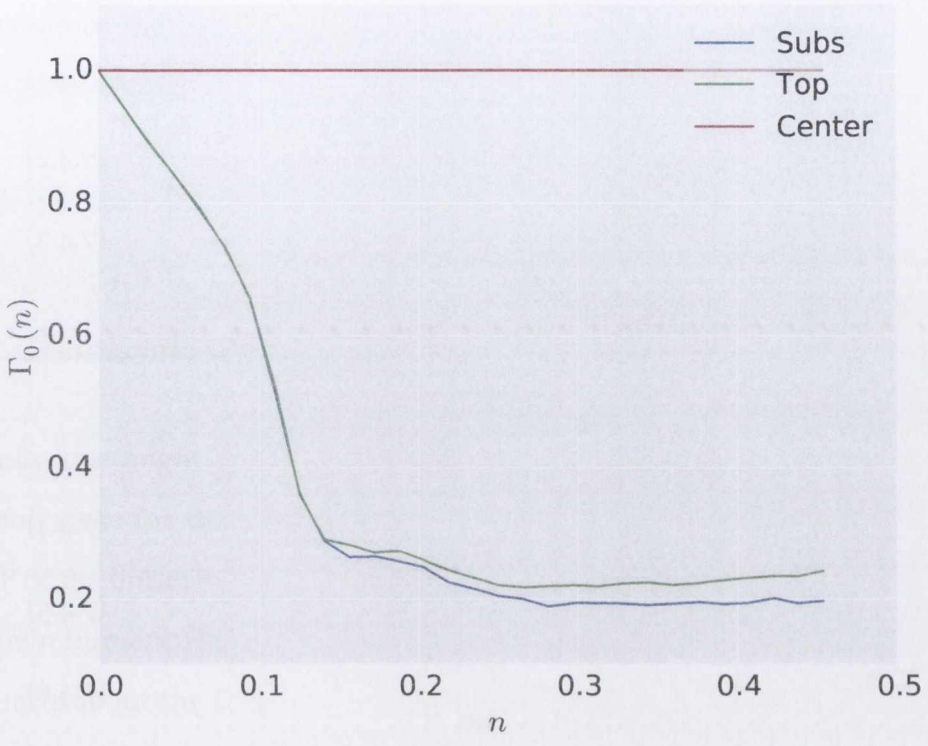


Figure 7.11: A random configurational average of the conductance at the Dirac point $\Gamma_0(n)$ plotted against increasing impurity concentration (n) for different conformations. Performed for a large ribbon, with $N = 32$ and $p = 40$. 5000 iterations were performed before convergence was obtained. Roughly the same results as before were obtained, however, the decay scheme of the substitutional and top-adsorbed cases are now even more dramatic. This may be due to the greater density of impurities making higher interaction terms important.

in a more transparent way. We can achieve this goal with a couple of reasonable assumptions and the use of the Dyson equation.

First of all, we know from our equation for the conductance that it can be written in terms of the imaginary parts of GFs. The GFs in question are the GFs between the sites of an arbitrary strip. Any change in conductance will be due to a change in the imaginary parts of these GFs. However, we can relate the change in an *arbitrary* GF to the GF of our impurity site using the Dyson equation.

The GF of an impurity site after being introduced into a nanoribbon is given by (where the equations are in order of substitutional, top-adsorbed, center-adsorbed)

$$G^S_{AA} = \frac{g_{AA}}{1 - g_{AA}\epsilon} \tag{7.4.1}$$

$$G^T_{AA} = \frac{g_{AA}}{1 - g_{AA}g_{aa}\tau^2} \tag{7.4.2}$$

$$G^C_{AA} = \frac{g_{AA}}{1 - g_{AA}\Gamma_{aa}\tau^2} \tag{7.4.3}$$

Where A is the impurity site, and a represents any connecting site. We can calculate the on-site GF at an arbitrary site using the same methods.

$$G^S_{00} = g_{00} + \frac{g_{0A}g_{A0}\epsilon}{1 - g_{AA}\epsilon} \tag{7.4.4}$$

$$G^T_{00} = g_{00} + \frac{g_{AA}g_{0a}g_{a0}\tau^2}{1 - g_{AA}g_{aa}\tau^2} \tag{7.4.5}$$

$$G^C_{00} = g_{00} + \frac{g_{AA}\Gamma_{0a}\Gamma_{a0}\tau^2}{1 - g_{AA}\Gamma_{aa}\tau^2} \tag{7.4.6}$$

Where o is an arbitrary site. We can now combine these equations to get

$$G^S_{00} = g_{00} + G_{AA}\frac{g_{0A}g_{A0}\epsilon}{g_{AA}} \tag{7.4.7}$$

$$G^T_{00} = g_{00} + G_{AA}g_{0a}g_{a0}\tau^2 \tag{7.4.8}$$

$$G^C_{00} = g_{00} + G_{AA}\Gamma_{0a}\Gamma_{a0}\tau^2 \tag{7.4.9}$$

From these we can see that the change in any on-site GF in the system can be written linearly in terms of the GF of the impurity site. Furthermore we seek the change in the imaginary part of the on-site GF, and the imaginary part of any GF is in one-to-one correspondence with the LDOS. The LDOS of the impurity site has already been discussed at length in this thesis, and we are well aware of the fact the center-adsorbed impurity has a much lower LDOS around the Dirac point than any of the other studied cases. Furthermore, this is in accordance with the top and substitutional impurities located at VLDOS sites. Hence, we have presented

a plausible theoretical mechanism through which the impurity LDOS affects the overall conductance. Of course, there are more than simply on-site elements in the calculation of the conductance, but as it turns out, it is possible to calculate also off-diagonal elements within the same scheme.

$$G^S_{00} = g_{00} + G_{AA}\frac{g_{0A}g_{A0}\epsilon}{g_{AA}} \tag{7.4.10}$$

$$G^T_{00} = g_{00} + G_{AA}g_{0a}g_{a0}\tau^2 \tag{7.4.11}$$

$$G^C_{00} = g_{00} + G_{AA}\Gamma_{0a}\Gamma_{a0}\tau^2 \tag{7.4.12}$$

Finally, one might point out that the above equations do not represent any kind of proof, since for the imaginary part of an arbitrary GF to be complete linear in the GF of the impurity site, we need the real part of the other term to vanish. It can be shown numerically that this is the case, and this can be determined from some basic facts about the GFs of nanoribbons, but we exclude this analysis here due to its length and lack of additional insight.

7.5 CHAPTER SUMMARY

In this chapter, we examined the conductance of armchair graphene nanoribbons in the presence of different species of impurity. The work in this chapter was motivated by the study of the indirect exchange coupling. We reasoned that since center-adsorbed impurity conformations are far more weakly coupling than others, and since both the IEC and the conductance are fundamentally scattering processes, these impurities should have little effect on the conductance. We examined single impurities first, with the results confirming our suspicions. Substitutional and top-adsorbed impurities caused a substantial dip in the conductance around the Fermi energy, except when located on a VLDOS site. Center-adsorbed impurities however, had little effect on the conductance regardless of their adsorption position.

We then wished to know if this analysis extended to the more complex case of multiple impurities randomly adsorbed on the nanoribbon. Therefore, we examined the previous impurities by taking configurational averages, and showed that our result was robust even in this case. Furthermore, we predicted that the difference in conductance would scale dramatically with impurity concentration. Finally, we showed that the coupling could be written linearly in terms of the LDOS. This indicated that the LDOS was the central quality determining the impact of an impurity on the conductance. We interpreted this to mean that impurities with low LDOS at the appropriate energies would not interact with the electronic states of the nanoribbon, and hence would not contribute to the conductance. The work in this chapter is in preparation for publication.

8

CONCLUSIONS

In this thesis we began with the intention of examining the static magnetic interaction in various forms of edged graphene. We determined that this interaction was strong dependent on the impurity conformation and the distance from the edge. This proved to be highly correlated with the LDOS, which was small where the interaction was weak, and large where it was strong. This led us to examine other forms of magnetic interaction, and we demonstrated that dynamic interactions also obeyed this law, and were strongly dependent on the distance from the edge in nanoribbons. Finally, we reasoned that since the RKKY was a scattering process, it should share considerable similarities with the conductance. This proved true, and we demonstrated that impurity conformation and distance from the edge were key characteristics in determining the conductance in nanoribbons.

In chapter 1 we examined the background to the materials we study, covering the most important results in the literature. We introduced graphene and also discussed the literature on its edged variants. We discussed the field of spintronics, graphene's role there and how it encourages the study of magnetic interactions. We discussed magnetic interactions in metals, introducing the indirect exchange interaction, and examined some of the recent literature on this interaction in graphene. Finally we discussed the conductance of graphene, and its applicability as a sensor.

In chapter 2 we introduced the mathematical methods that inform the rest of our thesis. We began by introducing the Green's function, which has the central role in our work, and showing how it can be used to describe the local density of states. Then we introduced the Dyson equation, which allows for perturbations to be applied to the GF, and we show how the impurities encountered in this work may be described using it. We also demonstrated its use in constructing

systems recursively. We introduced the Lloyd formula, used for describing energy differences in the wake of perturbations, and we discussed how integrals such as this may be cast over the imaginary axis, for easier numerical computation. Finally, we finished with a brief discussion of electron-electron interactions, and how they are incorporated into this work.

In chapter 3, we derived the GFs of the different graphene systems that we encountered in this work. We showed how the form of these GFs may be simplified using contour integration, and in some cases be written fully analytically using the stationary phase approximation. We also discuss how graphene nanoribbons can be built entirely recursively, using the techniques developed in chapter 2. Throughout this chapter, we used the GF to examine the LDOS. This produced the familiar linear regime around the Dirac point in bulk graphene, but in SI graphene and nanoribbons a triadic pattern emerged. We found that the LDOS every third site from the edge is different from other cases, exhibiting either a smoother structure or completely disappearing around the Dirac point. We called these sites vanishing local density of states sites.

In chapter 4 we examined the indirect exchange coupling between two magnetic impurities in edged graphene systems. We begin with a derivation of the IEC, demonstrating how it can be written in a very simple form using the Lloyd Formula. We further emphasized the computational advantage of this approach, since this calculation is often made by examining the complete energy of the system, which can be quite costly. We also showed that the coupling can be written in a completely analytic series form, which proves useful when extracting decay rates. We then examined the interaction in the various forms of edged graphene under discussion in this thesis. We reproduced the existing results for bulk graphene, demonstrating a D^{-3} decay with separation at the Dirac point and a D^{-2} decay elsewhere. We also show that the decay is ferromagnetic for same sublattice sites and antiferromagnetic otherwise. We repeated these calculations in semi-infinite graphene and armchair graphene nanoribbons, and here found the appearance of

the familiar triadic pattern we previously encountered in the LDOS. We found a greater decay every third site from the edge, one that slowly returns to the bulk case in SI graphene, and constantly decays exponentially in the ribbons. We interpreted these results as a lack of itinerant electrons to propagate the interaction in these cases. These results were very surprising, since the range of the IEC generally depends only on the dimensionality of the host, and finding a significant change in range based off the distance from the edge is very unsual. The results in this chapter were published as part of *RKKY Interaction Between Extended Magnetic Defect Lines in Graphene* (Physical Review B, 90, 125411, 2014).

In chapter 5 we examined the IEC for infinite lines of impurities in bulk graphene. This was motivated by the fact that the IEC might be more experimentally visible between finite sized objects. This necessitated that we introduce the *mixed representation*, whereby the GF is Fourier Transformed along one direction only. We used this representation to derive an expression for the IEC between infinite impurity lines, and cast it in series form as we had done in chapter 4. We obtain the coupling between lines both numerically and analytically. Around the Dirac point we find that the interaction decays with separation at a rate of $D^{-2.1}$ or $D^{-2.3}$, which matches reasonably well with our analytic prediction of $D^{-2.5}$. We find that our calculations are in complete agreement away from the Dirac point, where we obtain a decay of $D^{-1.5}$. We end the chapter with a discussion of finite lines of impurities, which we show quickly converges to the infinite case, even with relatively few impurities. The results in this chapter were published as part of *RKKY Interaction Between Extended Magnetic Defect Lines in Graphene* (Physical Review B, 90, 125411, 2014).

In chapter 6 we moved away from the static regime, examining the dynamic interaction between top-adsorbed impurities in graphene nanoribbons. The Dynamic interaction occurs whenever a magnetic system is subject to a time-dependent perturbation, and to that end we introduced a rotating magnetic field at one of the impurity sites. We then derived an expression for the dynamic transverse spin

susceptibility in this system, which contains the complete details of the magnetic response of the system. We first set about examining a single impurity, where we found the familiar triadic pattern that we observed in previous chapters. Here, we found that the excitation lifetime was very significantly long every site a multiple of 3 from the edge. We interpreted this with respect to the LDOS. Since there were no available states for the interaction to decay into, it was extremely long lived. We then began to examine multiple impurity systems. In two impurity systems we found that the linewidth oscillated as a function of distance where both impurities were away from VLDOS sites. However, when either impurity occupied a VLDOS site we found that the interaction quickly converged to the single impurity case. The same results was found for 3 impurities and we concluded that the very different responses from VLDOS and non-VLDOS sites should make for an easy signal to detect experimentally. The results in this chapter are in preparation for publication.

In chapter 7 we examined the conductance of graphene nanoribbon in the presence of impurities. We reasoned that since some impurities responded very differently to the RKKY interaction, which is essentially a scattering process, these same impurities should have a different effect on the conductance. We initially performed the calculations for single impurities, demonstrating that around the Dirac point, substitutional and top-adsorbed impurities had a considerably greater effect upon the conductance of the ribbon than center-adsorbed impurities, aside from at VLDOS sites. We then repeated the calculations for a random distribution of impurities, and demonstrated that the same effects were apparent. Finally, we showed that the coupling can be written linearly in terms of the LDOS at the impurity site, justifying the LDOS as the key predictive quantity of the conductance. The results in this chapter are in preparation for publication.

8.1 FUTURE WORK

There are many ways in which our current work can be expanded. For one, we have neglected to examine center adsorbed impurities in edged graphene, which themselves should display interesting results similar to those in bulk. Also, the method that we used to examine the infinite line of impurities could be extended to deal with infinite lines of center, top or bridge adsorbed impurities (which are not covered in this thesis). Wider, or multiple impurity lines would make an interesting topic of study, as would the introduction of disorder. It would also be worth examining the interaction between clusters of impurities, since this is often the quantity that is measured by experiment.

The dynamic interaction is an interesting and deep topic, and there is much more to examine there. Different impurity types can have a markedly different effect on the interaction. Furthermore, there are many other qualities of the interaction worth studying, of which the most obvious is its magnitude and distance dependence.

Finally, the conductance in the presence of impurities is worth studying in a number of different situations. Firstly, impurities are predicted to display an adsorption preference that varies across the width of the nanoribbon, and this would be an interesting quantity to account for in calculations. However, more importantly, it is essential to measure our results in the presence of disorder. It is shown that disorder can have a large effect on the properties of graphene nanoribbons, and hence it is essential to review our results with these features included. The presence of defects, functionalisation of the edge sites, buckling at the edge, or various types of strain should be examined with respect to their effect on the interaction. Really, it would be worth examining many of the effects mentioned in this thesis in these situations.

Finally, I should note that though the correlations between the IEC and the LDOS is both obvious and theoretically sensible, I was unable to derive an analytic expres-

sion that connected the two quantities. Perhaps another student can better me on this.

Part I

APPENDIX

A

DERIVATIONS

This part of the appendix contains parts of derivations considered too long or not relevant enough to remain in the main text.

A.1 THE GRAPHENE BRILLOUIN ZONE

The Brillouin zone is defined as the locus of points nearest the origin in reciprocal space, or equally, as the Wigner-Seitz cell in reciprocal space. Its value in this thesis is mainly in providing the integration area containing all unique k points and it is mostly used in the chapter on GFs. In this section, we will find the BZ of graphene, and then determine equivalent integration areas.

In order to examine the BZ we must first form the reciprocal lattice. The basis vectors for the reciprocal lattice vectors in an arbitrary solid are given by

$$\mathbf{b}_1 = \frac{2\pi}{\Omega_0}(\mathbf{a}_2 \times \mathbf{a}_3) \tag{A.1.1}$$

$$\mathbf{b}_2 = \frac{2\pi}{\Omega_0}(\mathbf{a}_3 \times \mathbf{a}_1) \tag{A.1.2}$$

$$\mathbf{b}_3 = \frac{2\pi}{\Omega_0}(\mathbf{a}_1 \times \mathbf{a}_2), \tag{A.1.3}$$

where $\Omega_0 = \mathbf{a}_1 \cdot (\mathbf{a}_2 \times \mathbf{a}_3)$. When working in 2 dimensions, we set $\mathbf{a}_3 = \mathbf{k}$. We can then substitute in our graphene basis vectors to get

$$\mathbf{b}_1 = \frac{2\pi}{\sqrt{3}a}(1, \sqrt{3}) \tag{A.1.4}$$

$$\mathbf{b}_2 = \frac{2\pi}{\sqrt{3}a}(1, -\sqrt{3}). \tag{A.1.5}$$

In Fig. A.1 we show a single point in the reciprocal lattice, along with all of its nearest neighbours. By bisecting the lines between them, we can create the Wigner-Seitz cell and hence, the Brillouin zone. This gives us all of the unique k points, however, its hexagonal shape is awkward for the purpose of integration.

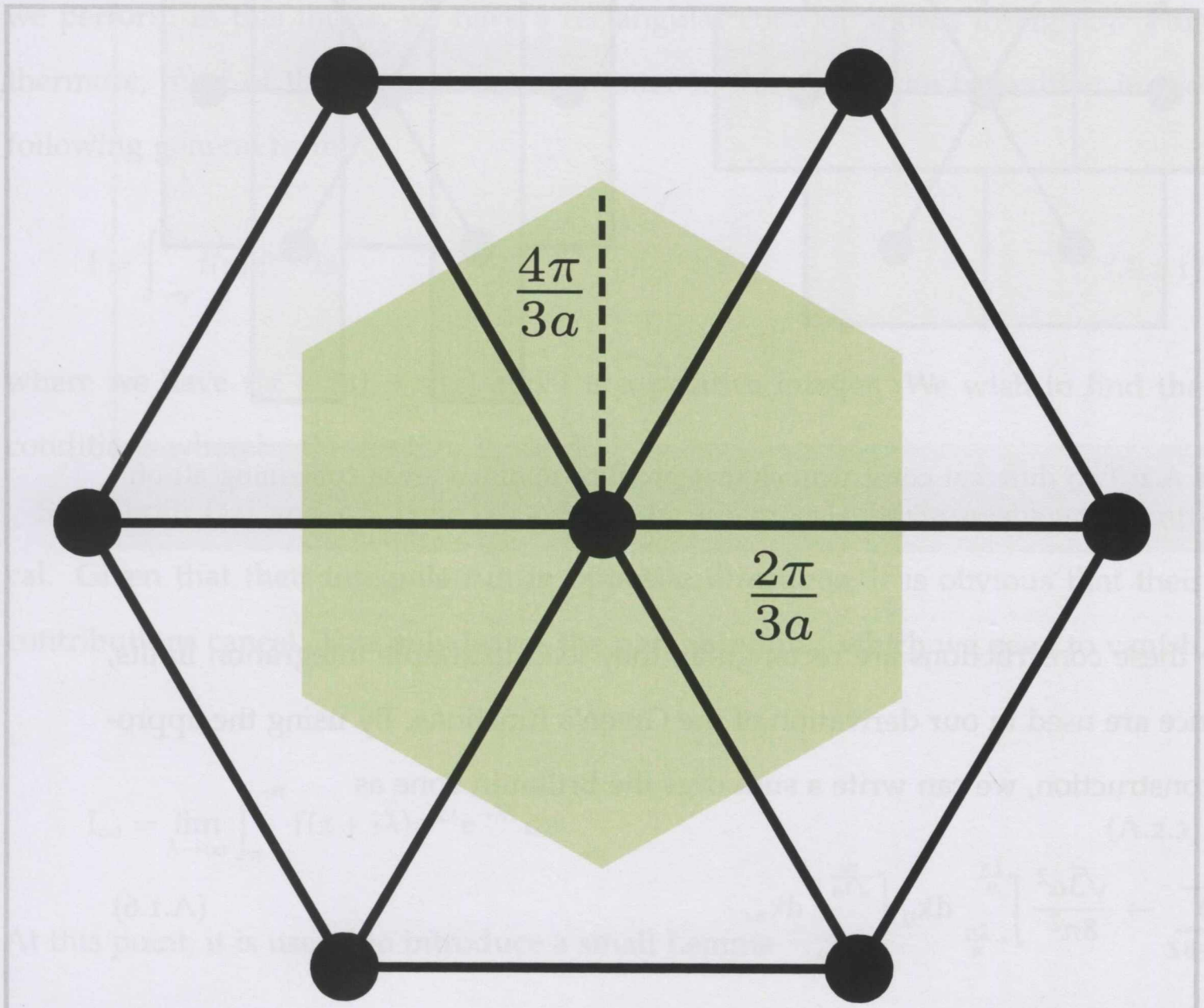


Figure A.1: The graphene Brillouin zone. This is found by creating a "star" in reciprocal space consisting of a single point and its nearest neighbours, and bisecting the perpendicular distance between them.

We wish to construct an equivalent integration region that contains all unique k points. This can be achieved by creating any minimal area that fills the space. Two such areas are shown in Fig. A.2, one bisects the distance between horizontal points, the other bisects the distance between vertical points, but both fill the space completely. They can be shown to be equivalent to the BZ by viewing it within the extended zone scheme.

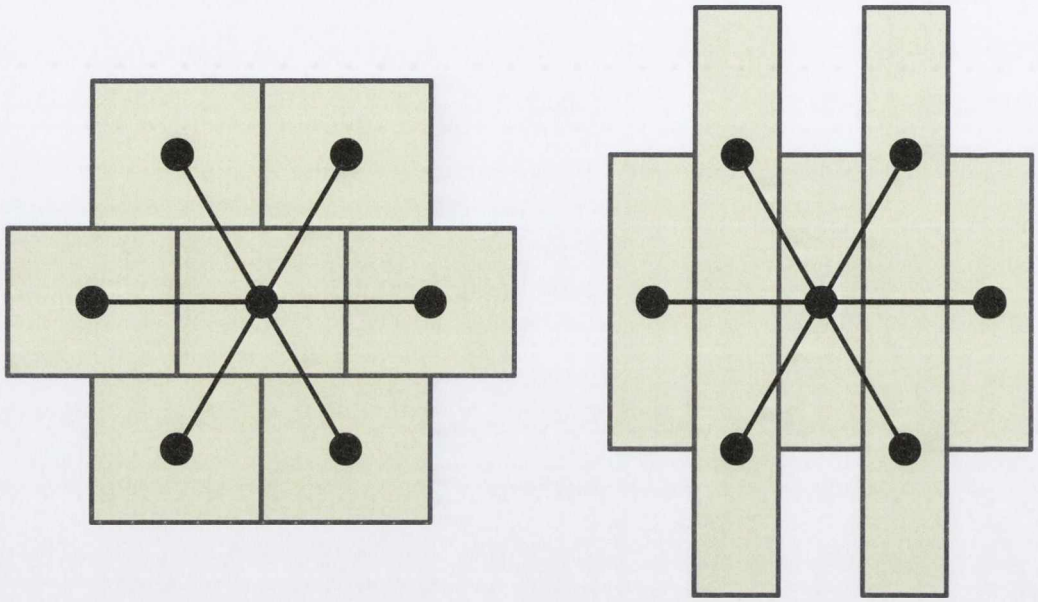


Figure A.2: Two different constructions that produce minimal areas containing all of the unique k points.

Since these constructions are rectangular, they lead to simple integration limits, and hence are used in our derivation of the Green's functions. By using the appropriate construction, we can write a sum over the Brillouin zone as

$$\sum_{k\in BZ} \rightarrow \frac{\sqrt{3}a^2}{8\pi^2} \int_{-\frac{2\pi}{a}}^{\frac{2\pi}{a}} dk_y \int_{-\frac{\pi}{\sqrt{3}a}}^{\frac{\pi}{\sqrt{3}a}} dk_x, \tag{A.1.6}$$

or

$$\sum_{k\in BZ} \rightarrow \frac{\sqrt{3}a^2}{8\pi^2} \int_{-\frac{\pi}{a}}^{\frac{\pi}{a}} dk_y \int_{-\frac{2\pi}{\sqrt{3}a}}^{\frac{2\pi}{\sqrt{3}a}} dk_x. \tag{A.1.7}$$

A.2 FINDING A CONTOUR

There are a number of integrations in this thesis, particularly when it comes to Green's functions, that are impossible to perform using standard integration methods. However, many of the integrations can be performed over a path in the com-

plex plane. The process of going from an integral over the real line to a complex contour is omitted in the main text. We examine it in detail here.

An integral over the real line may be extended into the complex plane if the integral over all of the complex parts vanishes. In most of the contour integrals we perform in this thesis, we have a rectangular contour shown in Fig.A.3. Furthermore, most of the integrals we encounter in this thesis can be written in the following general form

$$I = \int_{-\pi}^{\pi} f(z) e^{izl}\, dz, \tag{A.2.1}$$

where we have $f(z + 2\pi) = f(z)$ and l is a positive integer. We wish to find the conditions whereby the contour is valid.

Since both $f(z)$ and e^{izl} have period 2π, the integrands on the walls are identical. Given that their integrals run in opposite directions, it is obvious that their contributions cancel. This only leaves the part at infinity, which we need to vanish.

$$I_\infty = \lim_{\lambda\to\infty} \int_{\pi}^{-\pi} f(z + i\lambda) e^{izl} e^{-\lambda l}\, dz \tag{A.2.2}$$

At this point, it is useful to introduce a small Lemma

Lemma

$$\lim_{\lambda\to\infty} \frac{a_m e^{\lambda m} + \ldots + a_n e^{\lambda n}}{b_k e^{\lambda k} + \ldots + a_l e^{\lambda l}} = \begin{cases} 0 & \text{if } n < l \\ \infty & \text{if } n > l \\ \frac{a_n}{a_l} & \text{if } n = l \end{cases} \tag{A.2.3}$$

Where $m, n, k, l \in \mathbb{Z}$, $m < n$, $k < l$ and the coefficients are arbitrary complex numbers.

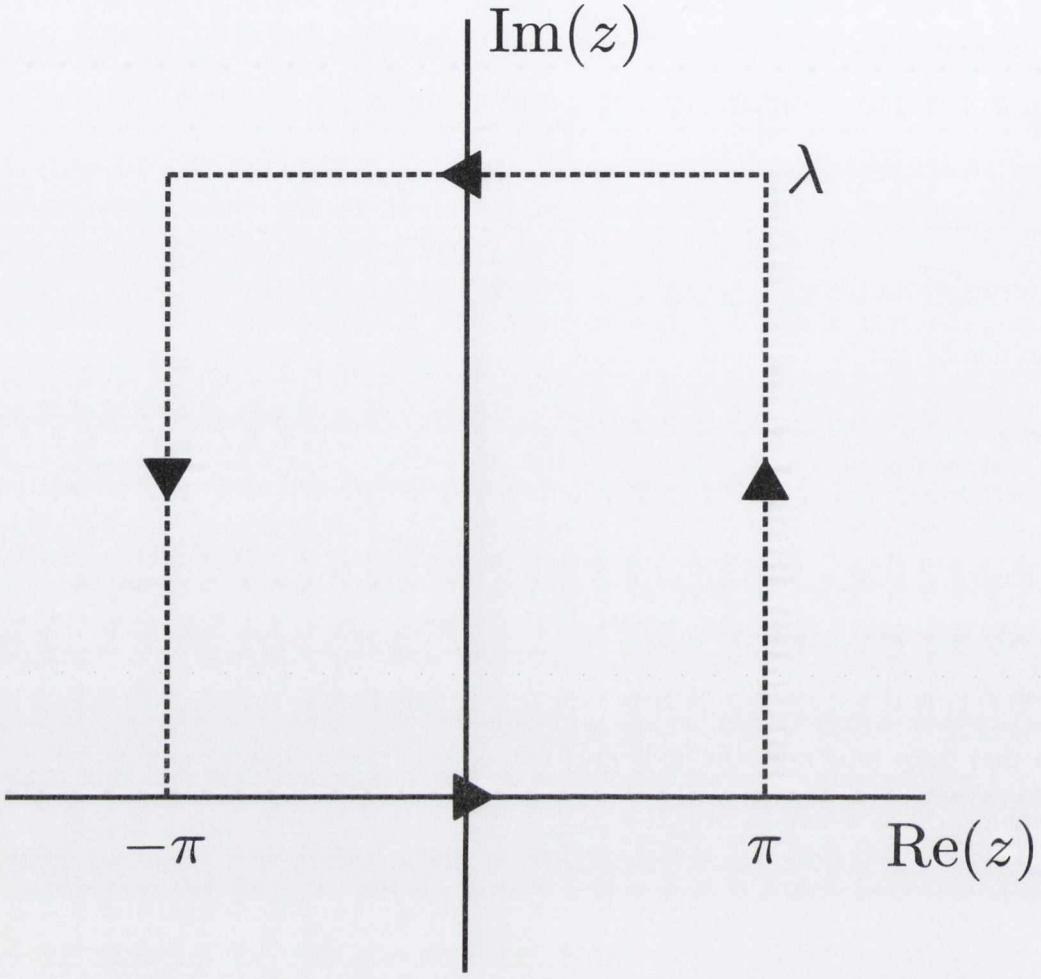


Figure A.3: We attempt to extend an integration on the real line, to a contour in the complex plane.

Proof

$$\begin{aligned}\lim_{\lambda\to\infty}\frac{a_m e^{m\lambda}+\ldots+a_n e^{n\lambda}}{b_k e^{k\lambda}+\ldots+a_l e^{l\lambda}} &= \lim_{\lambda\to\infty}\frac{a_m e^{(m-l)\lambda}+\ldots+a_n e^{(n-l)\lambda}}{b_k e^{(k-l)\lambda}+\ldots+a_l} \\ &= \lim_{\lambda\to\infty}\frac{a_m e^{(m-l)\lambda}+\ldots+a_n e^{(n-l)\lambda}}{a_l}\end{aligned} \tag{A.2.4}$$

If $n > l$ then $\lim_{\lambda\to\infty}\frac{a_n}{a_l}e^{(n-l)\lambda} = \infty$.

If $n < l$ then $m < l$ and all terms go to zero.

If $n = l$ then $m < l$ and the sole remaining term is $\frac{a_n}{a_l}$.

Most of the time, the limit behaviour of our $f(z)$ will be determined by exponentials. Separating out the λ dependent part of $f(z+i\lambda)$ gives $f(z+i\lambda) = g(z)e^{N\lambda}$ where e^N is the ratio between the largest exponentials in the numerator and denominator. This allows us to write

$$I_\infty = \lim_{\lambda\to\infty} \int_\pi^{-\pi} g(z)e^{izl}e^{-\lambda l}e^{N\lambda}\,dz, \tag{A.2.5}$$

which will disappear provided $l > N$.

When $l < N$ we can flip the sign of the integration variable. If $f(z) \neq f(-z)$ we must then repeat the process above. However, often we find that $f(z) = f(-z)$ and hence we can write down the answer immediately.

$$\begin{aligned} I &= \int_{-\pi}^{\pi} f(z)e^{izl}dz \qquad z \to -z \\ &= \int_{-\pi}^{\pi} f(z)e^{-izl}\,dz \end{aligned} \tag{A.2.6}$$

So now

$$\begin{aligned} I_\infty &= \lim_{\lambda\to\infty} \int_\pi^{-\pi} f(z+in)e^{-i(z+i\lambda)l}\,dz \\ &= \lim_{\lambda\to\infty} \int_\pi^{-\pi} g(z)e^{-izl}e^{\lambda l}e^{N\lambda}\,dz, \end{aligned} \tag{A.2.7}$$

which is 0 provided $l < -N$. This gives us the two conditions under which we can form a valid contour.

LOWER HALF PLANE We can also try closing the contour in the lower half plane, which will lead to a different constraint on l. We write $f(z-i\lambda) \to g(z)e^{N'\lambda}$ (where g is not necessarily the same function we encountered before). This gives us

$$I_\infty = \lim_{\lambda\to\infty} \int_\pi^{-\pi} e^{izl}e^{\lambda l}e^{N'\lambda}dz, \tag{A.2.8}$$

which goes to zero if $l < -N'$. Now we perform a sign change as in the previous section to get our other condition

$$I_\infty = \lim_{\lambda\to\infty} \int_{\pi}^{-\pi} g(z) e^{-izl} e^{-\lambda l} e^{N'\lambda} dz, \tag{A.2.9}$$

which goes to zero if $l > N'$. So now we can form a contour provided $l < -N'$ or $l > N'$.

SUMMARY For symmetric functions, we may close our contour in the upper half plane if

$$I = \int_{-\pi}^{\pi} f(z) e^{izl}\, dz \qquad l > N \tag{A.2.10}$$

$$I = \int_{-\pi}^{\pi} f(z) e^{-izl}\, dz \qquad l < -N, \tag{A.2.11}$$

and in the lower half plane if

$$I = \int_{-\pi}^{\pi} f(z) e^{izl}\, dz \qquad l < -N' \tag{A.2.12}$$

$$I = \int_{-\pi}^{\pi} f(z) e^{-izl}\, dz \qquad l > N', \tag{A.2.13}$$

It is instructive to apply these techniques to the bulk GFs

A.2.1 *Example: ZigZag Integration*

We attempt to perform the integration of the bulk GF over k_z, as in Eq.3.1.17 It is clear that the integration over both walls cancels identically (since everything is periodic with 2π). We need only show that the integration at infinity vanishes. We know from our lemma that we need only compare the largest exponential factors

in the numerator and denominator to find out if it is possible to form the contour. The part of the contour at infinity looks like

$$\int_{\pi}^{-\pi} dk_Z \frac{N^{\alpha\beta}(k_A, k_Z + i\lambda) e^{ik_A(m+n)+ik_Z(m-n)} e^{-\lambda(m-n)}}{E^2 - t^2|f(k_A, k_Z + i\lambda)|^2}. \tag{A.2.14}$$

The largest exponential in the denominator is $e^{2\lambda}$. For any choice of sublattices (bb, bw etc.) the largest exponential in the numerator is e^{λ}. So we can always form a contour when $m - n > -1$, or, since '$f(z)$' is symmetric, $m - n < 1$. Therefore if we change sign at -1 we can always have a valid integration contour.

A.2.2 *Armchair Integration*

Now we try to perform the integration of the bulk GF over k_A, as in Eq.3.1.23. If we expand the factor of $\cos(k_A)$ in $|f|^2$ the largest factor will be e^{λ}. The numerator will be different depending on what type of integral we are dealing with

$$bb : e^{-\lambda m+n} \tag{A.2.15}$$

$$bw : e^{-\lambda m+n} \tag{A.2.16}$$

$$wb : e^{-\lambda(m+n-1)}. \tag{A.2.17}$$

where bb refers to both sites on the black sublattice etc. To form a contour we require

$$bb : m + n > -1 \tag{A.2.18}$$

$$bw : m + n > -1 \tag{A.2.19}$$

$$wb : m + n > 0. \tag{A.2.20}$$

Once again we make a change of variables $k_z \to -k_z$ and re-examine.

$$bb : e^{\lambda m+n} \tag{A.2.21}$$

$$bw : e^{\lambda(m+n+1)} \tag{A.2.22}$$

$$wb : e^{\lambda m+n} \tag{A.2.23}$$

Now our conditions become

$$bb : m+n<1 \tag{A.2.24}$$

$$bw : m+n<0 \tag{A.2.25}$$

$$wb : m+n<1. \tag{A.2.26}$$

So when performing the armchair integral first we should let both bb and wb terms change sign at -1 but bw should change sign at 0.

B

DETAILS

Here we collect a couple of small mathematical results that will be of use in the main text.

B.1 BLOCK MATRIX INVERSE

Many of the chapters in this thesis examine the impact of magnetic impurities on a tight binding system. Almost all of the chapters invoke the Dyson formula at some point. The Dyson formula given involves an inverse of the entire system, but often we are interested in only a few sites. In this section we derive a relation demonstrating that we can restrict the range of the inversion to sites that interest us.

First we write our perturbation in block matrix form.

$$\hat{V} = \begin{pmatrix} \hat{V}_C & 0 \\ 0 & 0 \end{pmatrix} \tag{B.1.1}$$

Here $\hat{V}_C$ is a block matrix that represents all of the non-zero parts of the perturbing potential (which are the sites of interest). The Green's function of the system may be written similarly.

$$\hat{g} = \begin{pmatrix} \hat{g}_C & * \\ * & * \end{pmatrix} \tag{B.1.2}$$

Here $\hat{g}_C$ represents the block matrix of GFs between the same sites as $\hat{V}_C$. We represent all other sites by asterisks, which have arbitrary values, as they are not essential to our analysis.

The Dyson formula (Eq.2.2.1) is given by

$$\hat{G} = (1 - \hat{g}\hat{V})^{-1}\hat{g}, \tag{B.1.3}$$

and an elementary calculation will show that

$$1 - \hat{g}\hat{V} = \begin{pmatrix} 1 - \hat{g}_C\hat{V}_C & 0 \\ * & 1 \end{pmatrix}. \tag{B.1.4}$$

Now the inverse of a matrix of block matrices can be calculated as

$$\begin{pmatrix} A & B \\ C & D \end{pmatrix}^{-1} = \begin{pmatrix} A^{-1} + A^{-1}BS^{-1}CA^{-1} & -A^{-1}BS^{-1} \\ -S^{-1}CA^{-1} & S^{-1} \end{pmatrix}, \tag{B.1.5}$$

where S is the Schur complement and $S = (D - CA^{-1}B)$. This relation holds wherever A and S are non-singular. Therefore, we can write

$$\begin{pmatrix} A & 0 \\ C & D \end{pmatrix}^{-1} = \begin{pmatrix} A^{-1} & 0 \\ -SCA^{-1} & S \end{pmatrix}, \tag{B.1.6}$$

where now $S = D$.

Now we can easily calculate the Dyson formula as

$$(1 - \hat{g}\hat{V})^{-1} = \begin{pmatrix} (1 - \hat{g}_C\hat{V}_C)^{-1} & 0 \\ * & 1 \end{pmatrix}, \tag{B.1.7}$$

and we need only perform the inversion over the relevant area.

B.2 THE STATIONARY PHASE APPROXIMATION

Integrals with highly oscillatory integrands can often be reliably approximated through the stationary phase approximation. The SPA assumes that highly oscillatory integrands cancel over the bulk of the integration range, and hence may be evaluated solely by examining the *stationary points*. Generally, its function in this work is to put Green's functions in a fully analytic form. Our derivation focuses on a more specific case than the version often encountered in quantum field theory. However, it is sufficient for our purposes.

The SPA is used to approximate integrals of the following form.

$$I(x) = \int dy\, f(y) e^{i\phi(y)x}. \tag{B.2.1}$$

If x is very large the exponential term will oscillate rapidly and the integral will cancel over much of the range. The only significant contributions will come from around the stationary points $\left.\frac{d\phi}{dy}\right|_{y_0} = 0$, as shown in Fig.B.1. If we expand the phase around the stationary point we get

$$\phi(y) \approx \phi(y_0) + \frac{1}{2}\left.\frac{d^2\phi}{dy^2}\right|_{y_0} (y - y^0)^2 + \ldots, \tag{B.2.2}$$

which allows us to write the integral as

$$I_{y_0}(x) = \int dy f(y_0) e^{i[\phi(y_0)x + \frac{1}{2}\phi''(y_0)(y-y^0)^2 x]}, \tag{B.2.3}$$

where we have set $f(y) = f(y_0)$, since we have assumed that it is slowly varying over the range of the stationary point. Now the integral can be evaluated simply by removing the constant terms and using the familiar Gaussian identity.

$$\begin{aligned} I_{y_0}(x) &= f(y_0)e^{i\phi(y_0)x}\int dy\, f(y_0)e^{i\frac{1}{2}\phi''(y_0)(y-y^0)^2x} \\ &= f(y_0)e^{i\phi(y_0)x}\sqrt{\frac{\pi}{-\frac{i}{2}\phi''(y_0)x}} \\ &= f(y_0)e^{i\phi(y_0)x}\sqrt{\frac{2i\pi}{\phi''(y_0)x}} \end{aligned} \tag{B.2.4}$$

This final form is very useful, and underpins many for the analytic calculations in this thesis.

B.3 CONJUGATE OF THE GF

A couple of times in this thesis we will encounter the conjugate of the GF, or a combination of advanced and retarded GFs. Here we present a few identities that can prove useful in these situations.

Lemma: Conjugate Inverse The conjugate of the inverse is the inverse of the conjugate.

Proof We have

$$gg^{-1} = I \tag{B.3.1}$$

$$\Rightarrow \overline{gg^{-1}} = \bar{I} \tag{B.3.2}$$

$$\Rightarrow \bar{g}\overline{g^{-1}} = I, \tag{B.3.3}$$

where the distributive property over the product is standard. However, we also trivially have that

$$(\bar{g})(\overline{g^{-1}}) = I. \tag{B.3.4}$$

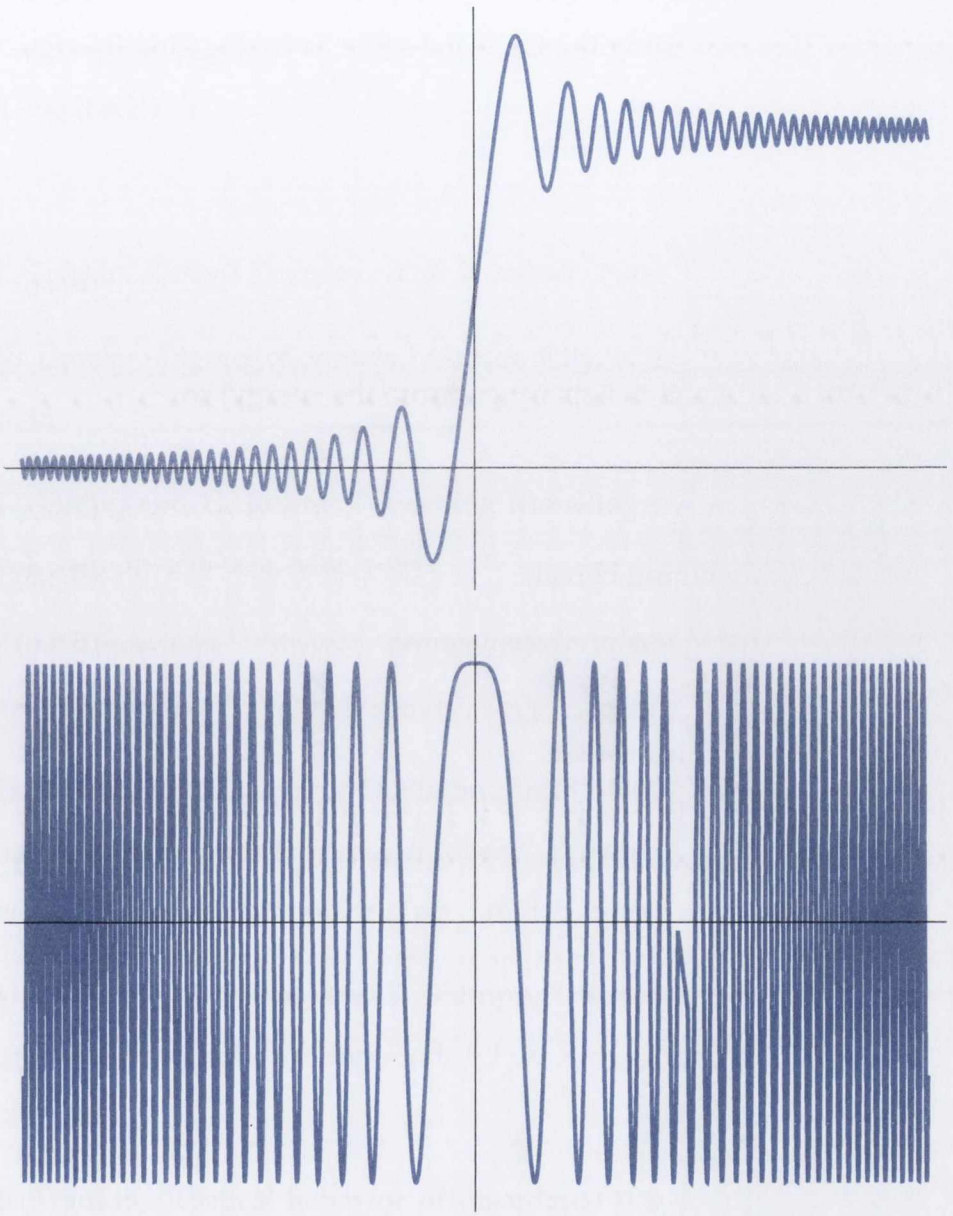


Figure B.1: A schematic of the stationary phase approximation. $\cos(20x^2)$ is used as an example of a quickly oscillating real function. The function is shown in the bottom figure, with the cumulative integral shown in the top. It is obvious that the main contribution to the integral comes from the slowly oscillating central region, which also happens to be the stationary point of $\cos(20x^2)$

Which gives us

$$\Rightarrow \overline{g^{-1}} = (\overline{g})^{-1}, \tag{B.3.5}$$

by uniqueness of the inverse

Lemma: Conjugate GF Conjugating the GF is the same as conjugating its argument

Proof We have

$$g(E) = (E\hat{I} - \hat{H})^{-1}, \tag{B.3.6}$$

(where we have absorbed the small imaginary part into the energy) so

$$g(\overline{E}) = (\overline{E}\hat{I} - \hat{H})^{-1} \tag{B.3.7}$$

$$= \overline{(E\hat{I} - \hat{H})}^{-1} \qquad \text{assuming H real} \tag{B.3.8}$$

$$= \overline{(E\hat{I} - \hat{H})^{-1}} \qquad \text{using our previous Lemma} \tag{B.3.9}$$

An important consequence of this is that

$$g(E + i\eta) + g(E - i\eta) = g + \overline{g} \tag{B.3.10}$$

$$= 2\mathrm{Re}(g), \tag{B.3.11}$$

and similarly we can write

$$\frac{g - \overline{g}}{2i} = \mathrm{Im}(g). \tag{B.3.12}$$

BIBLIOGRAPHY

[1] J. Gribbin, *Richard Feynman : a life in science*. New York: Plume, 1998.

[2] K. Drexler, *Engines of creation*. Garden City, N.Y: Anchor Press/Doubleday, 1986.

[3] G. Binnig and H. Rohrer, "Scanning tunneling microscopy," *Surface Science*, vol. 126, pp. 236–244, Mar. 1983.

[4] C. P. Inventory, "Project on emerging nanotechnologies." `http://www.nanotechproject.org/cpi/about/`, 2013. Accessed: 2015-10-23.

[5] H. P. Boehm, A. Clauss, G. O. Fischer, and U. Hofmann, "Das adsorptionsverhalten sehr dünner kohlenstoff-folien," *Zeitschrift für anorganische und allgemeine Chemie*, vol. 316, no. 3-4, pp. 119–127, 1962.

[6] H. P. Boehm, R. Setton, and E. Stumpp, "Nomenclature and terminology of graphite intercalation compounds," *Pure Appl. Chem.*, vol. 66, pp. 1893–1901, Jan. 1994.

[7] E. Fradkin, "Critical behavior of disordered degenerate semiconductors. II. Spectrum and transport properties in mean-field theory," *Physical Review B*, vol. 33, pp. 3263–3268, Mar. 1986.

[8] K. S. Novoselov, A. K. Geim, S. V. Morozov, D. Jiang, Y. Zhang, S. V. Dubonos, I. V. Grigorieva, and A. A. Firsov, "Electric field effect in atomically thin carbon films," *Science*, vol. 306, pp. 666–669, Oct. 2004.

[9] M. Hofmann, W.-Y. Chiang, T. D. Nguyễn, and Y.-P. Hsieh, "Controlling the properties of graphene produced by electrochemical exfoliation," *Nanotechnology*, vol. 26, no. 33, p. 335607, 2015.

[10] A. R. Kamali and D. J. Fray, "Molten salt corrosion of graphite as a possible way to make carbon nanostructures," *Carbon*, vol. 56, pp. 121–131, May 2013.

[11] L. Tang, X. Li, R. Ji, K. S. Teng, G. Tai, J. Ye, C. Wei, and S. P. Lau, "Bottom-up synthesis of large-scale graphene oxide nanosheets," *Journal of Materials Chemistry*, vol. 22, pp. 5676–5683, Feb. 2012.

[12] L. Jiao, L. Zhang, X. Wang, G. Diankov, and H. Dai, "Narrow graphene nanoribbons from carbon nanotubes," *Nature*, vol. 458, pp. 877–880, Apr. 2009.

[13] A. Nagashima, K. Nuka, H. Itoh, T. Ichinokawa, C. Oshima, and S. Otani, "Electronic states of monolayer graphite formed on TiC(111) surface," *Surface Science*, vol. 291, pp. 93–98, July 1993.

[14] T. Land, T. Michely, R. Behm, J. Hemminger, and G. Comsa, "STM investigation of single layer graphite structures produced on pt(111) by hydrocarbon decomposition," *Surface Science*, vol. 264, pp. 261–270, Mar. 1992.

[15] I. Forbeaux, J.-M. Themlin, and J.-M. Debever, "Heteroepitaxial graphite on 6H-SiC(0001): Interface formation through conduction-band electronic structure," *Physical Review B*, vol. 58, pp. 16396–16406, Dec. 1998.

[16] A. Van Bommel, J. Crombeen, and A. Van Tooren, "LEED and auger electron observations of the SiC(0001) surface," *Surface Science*, vol. 48, pp. 463–472, Mar. 1975.

[17] F. V. Kusmartsev, W. M. Wu, M. P. Pierpoint, and K. C. Yung, "Application of Graphene Within Optoelectronic Devices and Transistors," in *Applied Spectroscopy and the Science of Nanomaterials* (P. Misra, ed.), no. 2 in Progress in Optical Science and Photonics, pp. 191–221, Springer Singapore, 2015. DOI: 10.1007/978-981-287-242-5_9.

[18] L. Gao, G.-X. Ni, Y. Liu, B. Liu, A. H. Castro Neto, and K. P. Loh, "Face-to-face transfer of wafer-scale graphene films," *Nature*, vol. 505, pp. 190–194, Jan. 2014.

[19] D. A. Boyd, W.-H. Lin, C.-C. Hsu, M. L. Teague, C.-C. Chen, Y.-Y. Lo, W.-Y. Chan, W.-B. Su, T.-C. Cheng, C.-S. Chang, C.-I. Wu, and N.-C. Yeh, "Single-step deposition of high-mobility graphene at reduced temperatures," *Nature Communications*, vol. 6, p. 6620, Mar. 2015.

[20] J.-H. Lee, E. K. Lee, W.-J. Joo, Y. Jang, B.-S. Kim, J. Y. Lim, S.-H. Choi, S. J. Ahn, J. R. Ahn, M.-H. Park, C.-W. Yang, B. L. Choi, S.-W. Hwang, and D. Whang, "Wafer-Scale Growth of Single-Crystal Monolayer Graphene on Reusable Hydrogen-Terminated Germanium," *Science*, vol. 344, pp. 286–289, Apr. 2014.

[21] I. Vlassiouk, G. Polizos, R. Cooper, I. Ivanov, J. K. Keum, F. Paulauskas, P. Datskos, and S. Smirnov, "Strong and Electrically Conductive Graphene-Based Composite Fibers and Laminates," *ACS Applied Materials & Interfaces*, vol. 7, pp. 10702–10709, May 2015.

[22] K. R. Paton, E. Varrla, C. Backes, R. J. Smith, U. Khan, A. OâNeill, C. Boland, M. Lotya, O. M. Istrate, P. King, T. Higgins, S. Barwich, P. May, P. Puczkarski, I. Ahmed, M. Moebius, H. Pettersson, E. Long, J. Coelho, S. E. OâBrien, E. K. McGuire, B. M. Sanchez, G. S. Duesberg, N. McEvoy, T. J. Pennycook, C. Downing, A. Crossley, V. Nicolosi, and J. N. Coleman, "Scalable production of large quantities of defect-free few-layer graphene by shear exfoliation in liquids," *Nature Materials*, vol. 13, pp. 624–630, June 2014.

[23] C. Lee, X. Wei, J. W. Kysar, and J. Hone, "Measurement of the elastic properties and intrinsic strength of monolayer graphene," *Science*, vol. 321, pp. 385–388, July 2008.

[24] A. A. Balandin, S. Ghosh, W. Bao, I. Calizo, D. Teweldebrhan, F. Miao, and C. N. Lau, "Superior thermal conductivity of single-layer graphene," *Nano Letters*, vol. 8, pp. 902–907, Mar. 2008.

[25] A. K. Geim and K. S. Novoselov, "The rise of graphene," *Nature Materials*, vol. 6, no. 3, pp. 183–191, 2007.

[26] A. H. Castro Neto and F. Guinea, "Electron-phonon coupling and Raman spectroscopy in graphene," *Physical Review B*, vol. 75, p. 045404, Jan. 2007.

[27] T. Ando, "Anomaly of Optical Phonon in Monolayer Graphene," *Journal of the Physical Society of Japan*, vol. 75, p. 124701, Nov. 2006.

[28] A. K. Geim, "Graphene: Status and prospects," *Science*, vol. 324, pp. 1530–1534, June 2009.

[29] D. Pesin and A. H. MacDonald, "Spintronics and pseudospintronics in graphene and topological insulators," *Nature Materials*, vol. 11, no. 5, pp. 409–416, 2012.

[30] C. L. Kane and E. J. Mele, "Quantum spin hall effect in graphene," *Physical Review Letters*, vol. 95, p. 226801, Nov. 2005.

[31] R. R. Nair, P. Blake, J. R. Blake, R. Zan, S. Anissimova, U. Bangert, A. P. Golovanov, S. V. Morozov, A. K. Geim, K. S. Novoselov, and T. Latychevskaia, "Graphene as a transparent conductive support for studying biological molecules by transmission electron microscopy," *Applied Physics Letters*, vol. 97, pp. 153102–153102–3, Oct. 2010.

[32] A. Rycerz, J. Tworzydlo, and C. W. J. Beenakker, "Valley filter and valley valve in graphene," *Nat Phys*, vol. 3, pp. 172–175, Mar. 2007.

[33] J. T. Robinson, J. S. Burgess, C. E. Junkermeier, S. C. Badescu, T. L. Reinecke, F. K. Perkins, M. K. Zalalutdniov, J. W. Baldwin, J. C. Culbertson, P. E. Shee-

han, and E. S. Snow, "Properties of fluorinated graphene films," *Nano Letters*, vol. 10, pp. 3001–3005, Aug. 2010.

[34] M. H. F. Sluiter and Y. Kawazoe, "Cluster expansion method for adsorption: Application to hydrogen chemisorption on graphene," *Physical Review B*, vol. 68, p. 085410, Aug. 2003.

[35] J. O. Sofo, A. S. Chaudhari, and G. D. Barber, "Graphane: A two-dimensional hydrocarbon," *Physical Review B*, vol. 75, p. 153401, Apr. 2007.

[36] V. O. Özçelik and S. Ciraci, "Size Dependence in the Stabilities and Electronic Properties of α-Graphyne and Its Boron Nitride Analogue," *The Journal of Physical Chemistry C*, vol. 117, pp. 2175–2182, Feb. 2013.

[37] B. Lalmi, H. Oughaddou, H. Enriquez, A. Kara, S. Vizzini, B. Ealet, and B. Aufray, "Epitaxial growth of a silicene sheet," *Applied Physics Letters*, vol. 97, p. 223109, Nov. 2010.

[38] B. Aufray, A. Kara, S. Vizzini, H. Oughaddou, C. Léandri, B. Ealet, and G. L. Lay, "Graphene-like silicon nanoribbons on Ag(110): A possible formation of silicene," *Applied Physics Letters*, vol. 96, p. 183102, May 2010.

[39] Y. Kubota, K. Watanabe, O. Tsuda, and T. Taniguchi, "Deep Ultraviolet Light-Emitting Hexagonal Boron Nitride Synthesized at Atmospheric Pressure," *Science*, vol. 317, pp. 932–934, Aug. 2007.

[40] K. Watanabe, T. Taniguchi, and H. Kanda, "Direct-bandgap properties and evidence for ultraviolet lasing of hexagonal boron nitride single crystal," *Nat Mater*, vol. 3, pp. 404–409, June 2004.

[41] R. V. Gorbachev, A. K. Geim, M. I. Katsnelson, K. S. Novoselov, T. Tudorovskiy, I. V. Grigorieva, A. H. MacDonald, S. V. Morozov, K. Watanabe, T. Taniguchi, and L. A. Ponomarenko, "Strong coulomb drag and broken symmetry in double-layer graphene," *Nature Physics*, vol. 8, pp. 896–901, Dec. 2012.

[42] A. Kou, B. E. Feldman, A. J. Levin, B. I. Halperin, K. Watanabe, T. Taniguchi, and A. Yacoby, "Electron-hole asymmetric integer and fractional quantum Hall effect in bilayer graphene," *Science*, vol. 345, pp. 55–57, July 2014.

[43] K. Lee, B. Fallahazad, J. Xue, D. C. Dillen, K. Kim, T. Taniguchi, K. Watanabe, and E. Tutuc, "Chemical potential and quantum Hall ferromagnetism in bilayer graphene," *Science*, vol. 345, pp. 58–61, July 2014.

[44] P. Maher, L. Wang, Y. Gao, C. Forsythe, T. Taniguchi, K. Watanabe, D. Abanin, Z. PapiÄ, P. Cadden-Zimansky, J. Hone, P. Kim, and C. R. Dean, "Tunable fractional quantum Hall phases in bilayer graphene," *Science*, vol. 345, pp. 61–64, July 2014.

[45] M. Acik and Y. J. Chabal, "Nature of graphene edges: A review," *Japanese Journal of Applied Physics*, vol. 50, no. 7, p. 070101, 2011.

[46] O. V. Yazyev, "Emergence of magnetism in graphene materials and nanostructures," *Reports on Progress in Physics*, vol. 73, p. 056501, May 2010.

[47] c. O. Girit, J. C. Meyer, R. Erni, M. D. Rossell, C. Kisielowski, L. Yang, C.-H. Park, M. F. Crommie, M. L. Cohen, S. G. Louie, and A. Zettl, "Graphene at the edge: Stability and dynamics," *Science*, vol. 323, pp. 1705–1708, Mar. 2009. PMID: 19325110.

[48] Y.-W. Son, M. L. Cohen, and S. G. Louie, "Energy Gaps in Graphene Nanoribbons," *Physical Review Letters*, vol. 97, p. 216803, Nov. 2006.

[49] M. Y. Han, B. Özyilmaz, Y. Zhang, and P. Kim, "Energy band-gap engineering of graphene nanoribbons," *Physical Review Letters*, vol. 98, p. 206805, May 2007.

[50] S. R. Power, V. M. de Menezes, S. B. Fagan, and M. S. Ferreira, "Model of impurity segregation in graphene nanoribbons," *Physical Review B*, vol. 80, p. 235424, Dec. 2009.

[51] J. Klinovaja and D. Loss, "RKKY interaction in carbon nanotubes and graphene nanoribbons," *Physical Review B*, vol. 87, p. 045422, Jan. 2013.

[52] J. M. Duffy, P. D. Gorman, S. R. Power, and M. S. Ferreira, "Variable range of the RKKY interaction in edged graphene," *Journal of Physics: Condensed Matter*, vol. 26, p. 055007, Feb. 2014.

[53] M. Fujita, K. Wakabayashi, K. Nakada, and K. Kusakabe, "Peculiar Localized State at Zigzag Graphite Edge," *Journal of the Physical Society of Japan*, vol. 65, no. 7, pp. 1920–1923, 1996.

[54] D. V. Kosynkin, A. L. Higginbotham, A. Sinitskii, J. R. Lomeda, A. Dimiev, B. K. Price, and J. M. Tour, "Longitudinal unzipping of carbon nanotubes to form graphene nanoribbons," *Nature*, vol. 458, pp. 872–876, Apr. 2009.

[55] X. Wang and H. Dai, "Etching and narrowing of graphene from the edges," *Nature Chemistry*, vol. 2, no. 8, pp. 661–665, 2010.

[56] G. Lalwani, A. M. Henslee, B. Farshid, L. Lin, F. K. Kasper, Y.-X. Qin, A. G. Mikos, and B. Sitharaman, "Two-Dimensional Nanostructure-Reinforced Biodegradable Polymeric Nanocomposites for Bone Tissue Engineering," *Biomacromolecules*, vol. 14, pp. 900–909, Mar. 2013.

[57] G. Lalwani, X. Cai, L. Nie, L. V. Wang, and B. Sitharaman, "Graphene-based contrast agents for photoacoustic and thermoacoustic tomography," *Photoacoustics*, vol. 1, pp. 62–67, Dec. 2013.

[58] Z. F. Wang, Q. W. Shi, Q. Li, X. Wang, J. G. Hou, H. Zheng, Y. Yao, and J. Chen, "Z-shaped graphene nanoribbon quantum dot device," *Applied Physics Letters*, vol. 91, pp. 053109–053109–3, July 2007.

[59] V. Barone, O. Hod, and G. E. Scuseria, "Electronic structure and stability of semiconducting graphene nanoribbons," *Nano Letters*, vol. 6, pp. 2748–2754, Dec. 2006.

[60] K. Nakada, M. Fujita, G. Dresselhaus, and M. S. Dresselhaus, "Edge state in graphene ribbons: Nanometer size effect and edge shape dependence," *Physical Review B*, vol. 54, pp. 17954–17961, Dec. 1996.

[61] J. Kunstmann, C. Özdoğan, A. Quandt, and H. Fehske, "Stability of edge states and edge magnetism in graphene nanoribbons," *Physical Review B*, vol. 83, p. 045414, Jan. 2011.

[62] X. Zhang, O. V. Yazyev, J. Feng, L. Xie, C. Tao, Y.-C. Chen, L. Jiao, Z. Pedramrazi, A. Zettl, S. G. Louie, H. Dai, and M. F. Crommie, "Experimentally engineering the edge termination of graphene nanoribbons," *ACS Nano*, Nov. 2012.

[63] C.-I. Chia and V. H. Crespi, "Stabilizing the zigzag edge: Graphene nanoribbons with sterically constrained terminations," *Physical Review Letters*, vol. 109, p. 076802, Aug. 2012.

[64] F. Bloch, "Zur Theorie des Ferromagnetismus," *Zeitschrift für Physik*, vol. 61, pp. 206–219, Mar. 1930.

[65] B. N. Brockhouse, "Scattering of Neutrons by Spin Waves in Magnetite," *Physical Review*, vol. 106, pp. 859–864, June 1957.

[66] M. Johnson and R. H. Silsbee, "Interfacial charge-spin coupling: Injection and detection of spin magnetization in metals," *Physical Review Letters*, vol. 55, pp. 1790–1793, Oct. 1985.

[67] M. N. Baibich, J. M. Broto, A. Fert, F. N. Van Dau, F. Petroff, P. Etienne, G. Creuzet, A. Friederich, and J. Chazelas, "Giant magnetoresistance of (001)Fe/(001)Cr magnetic superlattices," *Physical Review Letters*, vol. 61, pp. 2472–2475, Nov. 1988.

[68] G. Binasch, P. Grünberg, F. Saurenbach, and W. Zinn, "Enhanced magnetoresistance in layered magnetic structures with antiferromagnetic interlayer exchange," *Physical Review B*, vol. 39, pp. 4828–4830, Mar. 1989.

[69] M. Julliere, "Tunneling between ferromagnetic films," *Physics Letters A*, vol. 54, pp. 225–226, Sept. 1975.

[70] S. Ikeda, J. Hayakawa, Y. Ashizawa, Y. M. Lee, K. Miura, H. Hasegawa, M. Tsunoda, F. Matsukura, and H. Ohno, "Tunnel magnetoresistance of 604% at 300K by suppression of Ta diffusion in CoFeB/MgO/CoFeB pseudo-spin-valves annealed at high temperature," *Applied Physics Letters*, vol. 93, pp. 082508–082508–3, Aug. 2008.

[71] J. Ãkerman, "Toward a Universal Memory," *Science*, vol. 308, pp. 508–510, Apr. 2005.

[72] B. Behin-Aein, D. Datta, S. Salahuddin, and S. Datta, "Proposal for an all-spin logic device with built-in memory," *Nature Nanotechnology*, vol. 5, pp. 266–270, Apr. 2010.

[73] O. V. Yazyev, "Hyperfine interactions in graphene and related carbon nanostructures," *Nano Letters*, vol. 8, pp. 1011–1015, Apr. 2008.

[74] D. Huertas-Hernando, F. Guinea, and A. Brataas, "Spin-orbit coupling in curved graphene, fullerenes, nanotubes, and nanotube caps," *Physical Review B*, vol. 74, p. 155426, Oct. 2006.

[75] A. T. Costa, M. S. Ferreira, T. Hallam, G. S. Duesberg, and A. H. C. Neto, "Origami-based spintronics in graphene," *EPL (Europhysics Letters)*, vol. 104, no. 4, p. 47001, 2013.

[76] L. Brey, H. A. Fertig, and S. Das Sarma, "Diluted graphene antiferromagnet," *Physical Review Letters*, vol. 99, p. 116802, Sept. 2007.

[77] Y.-W. Son, M. L. Cohen, and S. G. Louie, "Half-metallic graphene nanoribbons," *Nature*, vol. 444, pp. 347–349, Nov. 2006.

[78] O. V. Yazyev and M. I. Katsnelson, "Magnetic correlations at graphene edges: Basis for novel spintronics devices," *Physical Review Letters*, vol. 100, p. 047209, Jan. 2008.

[79] Y. Wang, Y. Huang, Y. Song, X. Zhang, Y. Ma, J. Liang, and Y. Chen, "Room-Temperature Ferromagnetism of Graphene," *Nano Letters*, vol. 9, pp. 220–224, Jan. 2009.

[80] H. S. S. R. Matte, K. S. Subrahmanyam, and C. N. R. Rao, "Novel Magnetic Properties of Graphene: Presence of Both Ferromagnetic and Antiferromagnetic Features and Other Aspects," *The Journal of Physical Chemistry C*, vol. 113, pp. 9982–9985, June 2009.

[81] A. Ney, P. Papakonstantinou, A. Kumar, N.-G. Shang, and N. Peng, "Irradiation enhanced paramagnetism on graphene nanoflakes," *Applied Physics Letters*, vol. 99, p. 102504, Sept. 2011.

[82] M. Sepioni, R. R. Nair, S. Rablen, J. Narayanan, F. Tuna, R. Winpenny, A. K. Geim, and I. V. Grigorieva, "Limits on Intrinsic Magnetism in Graphene," *Physical Review Letters*, vol. 105, p. 207205, Nov. 2010.

[83] R. R. Nair, M. Sepioni, I.-L. Tsai, O. Lehtinen, J. Keinonen, A. V. Krasheninnikov, T. Thomson, A. K. Geim, and I. V. Grigorieva, "Spin-half paramagnetism in graphene induced by point defects," *Nature Physics*, vol. 8, pp. 199–202, Mar. 2012.

[84] P. Grünberg, R. Schreiber, Y. Pang, M. B. Brodsky, and H. Sowers, "Layered magnetic structures: Evidence for antiferromagnetic coupling of Fe layers across Cr interlayers," *Physical Review Letters*, vol. 57, pp. 2442–2445, Nov. 1986.

[85] S. S. P. Parkin, N. More, and K. P. Roche, "Oscillations in exchange coupling and magnetoresistance in metallic superlattice structures: Co/Ru, Co/Cr, and Fe/Cr," *Physical Review Letters*, vol. 64, pp. 2304–2307, May 1990.

[86] D. M. Edwards, J. Mathon, R. B. Muniz, and M. S. Phan, "Oscillations in the exchange coupling of ferromagnetic layers separated by a nonmagnetic metallic layer," *Journal of Physics: Condensed Matter*, vol. 3, p. 4941, July 1991.

[87] D. M. Edwards, J. Mathon, R. B. Muniz, and M. S. Phan, "Oscillations of the exchange in magnetic multilayers as an analog of De Haas-van Alphen effect," *Physical Review Letters*, vol. 67, pp. 493–496, July 1991.

[88] M. A. Ruderman and C. Kittel, "Indirect exchange coupling of nuclear magnetic moments by conduction electrons," *Physical Review*, vol. 96, pp. 99–102, Oct. 1954.

[89] T. Kasuya, "A theory of metallic ferro- and antiferromagnetism on Zener's model," *Progress of Theoretical Physics*, vol. 16, pp. 45–57, July 1956.

[90] S. Doniach, "The Kondo lattice and weak antiferromagnetism," *Physica B+C*, vol. 91, pp. 231–234, July 1977.

[91] Y. Yafet, "Ruderman-Kittel-Kasuya-Yosida range function of a one-dimensional free-electron gas," *Physical Review B*, vol. 36, pp. 3948–3949, Sept. 1987.

[92] S. S. P. Parkin, "Systematic variation of the strength and oscillation period of indirect magnetic exchange coupling through the 3*d*, 4*d*, and 5*d* transition metals," *Physical Review Letters*, vol. 67, pp. 3598–3601, Dec. 1991.

[93] D. N. Aristov, "Indirect RKKY interaction in any dimensionality," *Physical Review B*, vol. 55, pp. 8064–8066, Apr. 1997.

[94] P. Bruno and C. Chappert, "Oscillatory coupling between ferromagnetic layers separated by a nonmagnetic metal spacer," *Physical Review Letters*, vol. 67, pp. 1602–1605, Sept. 1991.

[95] J. d'Albuquerque e Castro, M. S. Ferreira, and R. B. Muniz, "Theory of the exchange coupling in magnetic metallic multilayers," *Physical Review B*, vol. 49, pp. 16062–16065, June 1994.

[96] M. S. Ferreira, R. B. Muniz, J. d. e. Castro, and D. M. Edwards, "The nature and validity of the RKKY limit of exchange coupling in magnetic trilayers," *Journal of Physics: Condensed Matter*, vol. 6, pp. L619–L623, Oct. 1994.

[97] M. S. Ferreira, J. d. e. Castro, D. M. Edwards, and J. Mathon, "Fundamental oscillation periods of the interlayer exchange coupling beyond the RKKY approximation," *Journal of Physics: Condensed Matter*, vol. 8, pp. 11259–11276, Dec. 1996.

[98] M. A. H. Vozmediano, M. P. López-Sancho, T. Stauber, and F. Guinea, "Local defects and ferromagnetism in graphene layers," *Physical Review B*, vol. 72, p. 155121, Oct. 2005.

[99] V. K. Dugaev, V. I. Litvinov, and J. Barnas, "Exchange interaction of magnetic impurities in graphene," *Physical Review B*, vol. 74, p. 224438, Dec. 2006.

[100] S. Saremi, "RKKY in half-filled bipartite lattices: Graphene as an example," *Physical Review B*, vol. 76, p. 184430, Nov. 2007.

[101] M. Sherafati and S. Satpathy, "RKKY interaction in graphene from the lattice green's function," *Physical Review B*, vol. 83, p. 165425, Apr. 2011.

[102] A. M. Black-Schaffer, "RKKY coupling in graphene," *Physical Review B*, vol. 81, p. 205416, May 2010.

[103] B. Uchoa, T. G. Rappoport, and A. H. Castro Neto, "Kondo quantum criticality of magnetic adatoms in graphene," *Physical Review Letters*, vol. 106, p. 016801, Jan. 2011.

[104] A. M. Black-Schaffer, "Importance of electron-electron interactions in the RKKY coupling in graphene," *Physical Review B*, vol. 82, p. 073409, Aug. 2010.

[105] S. R. Power and M. S. Ferreira, "Electronic structure of graphene beyond the linear dispersion regime," *Physical Review B*, vol. 83, p. 155432, Apr. 2011.

[106] M. Sherafati and S. Satpathy, "Analytical expression for the RKKY interaction in doped graphene," *Physical Review B*, vol. 84, p. 125416, Sept. 2011.

[107] S. R. Power, P. D. Gorman, J. M. Duffy, and M. S. Ferreira, "Strain-induced modulation of magnetic interactions in graphene," *Physical Review B*, vol. 86, p. 195423, Nov. 2012.

[108] S. R. Power, F. S. M. Guimaraes, A. T. Costa, R. B. Muniz, and M. S. Ferreira, "Dynamic RKKY interaction in graphene," *Physical Review B*, vol. 85, May 2012. arXiv: 1112.0205.

[109] P. Venezuela, R. B. Muniz, A. T. Costa, D. M. Edwards, S. R. Power, and M. S. Ferreira, "Emergence of local magnetic moments in doped graphene-related materials," *Physical Review B*, vol. 80, p. 241413, Dec. 2009.

[110] F. Peng and W. Hongbin, "Strain enhanced exchange interaction between impurities in graphene," *Physica B: Condensed Matter*, vol. 407, pp. 3434–3436, Sept. 2012.

[111] P. D. Gorman, J. M. Duffy, M. S. Ferreira, and S. R. Power, "RKKY interaction between adsorbed magnetic impurities in graphene: Symmetry and strain effects," *Physical Review B*, vol. 88, p. 085405, Aug. 2013.

[112] S. Power and M. Ferreira, "Indirect Exchange and Ruderman-Kittel-Kasuya-Yosida (RKKY) Interactions in Magnetically-Doped Graphene," *Crystals*, vol. 3, pp. 49–78, Jan. 2013.

[113] O. Roslyak, G. Gumbs, and D. Huang, "Gap-modulated doping effects on indirect exchange interaction between magnetic impurities in graphene," *Journal of Applied Physics*, vol. 113, p. 123702, Mar. 2013.

[114] A. Allerdt, C. A. Büsser, G. B. Martins, and A. E. Feiguin, "Kondo versus indirect exchange: Role of lattice and actual range of RKKY interactions in real materials," *Physical Review B*, vol. 91, p. 085101, Feb. 2015.

[115] E. H. Lieb, "Two theorems on the hubbard model," *Physical Review Letters*, vol. 62, pp. 1201–1204, Mar. 1989.

[116] J. A. Lawlor, P. D. Gorman, S. R. Power, C. G. Bezerra, and M. S. Ferreira, "Sublattice imbalance of substitutionally doped nitrogen in graphene," *Carbon*, vol. 77, pp. 645–650, Oct. 2014.

[117] I. V. Krainov, I. V. Rozhansky, N. S. Averkiev, and E. Lähderanta, "Indirect exchange interaction between magnetic adatoms in graphene," *Physical Review B*, vol. 92, p. 155432, Oct. 2015.

[118] J. H. Sun, F. M. Hu, H. K. Tang, W. Guo, and H. Q. Lin, "Indirect exchange of magnetic impurities in zigzag graphene ribbon," *Journal of Applied Physics*, vol. 113, pp. 17B515–17B515–3, Mar. 2013.

[119] D. Soriano, F. Muñoz Rojas, J. Fernández-Rossier, and J. J. Palacios, "Hydrogenated graphene nanoribbons for spintronics," *Physical Review B*, vol. 81, p. 165409, Apr. 2010.

[120] J. E. Bunder and H.-H. Lin, "Ruderman-kittel-kasuya-yosida interactions on a bipartite lattice," *Physical Review B*, vol. 80, p. 153414, Oct. 2009.

[121] K. Szałowski, "Indirect RKKY interaction between localized magnetic moments in armchair graphene nanoribbons," *Journal of Physics: Condensed Matter*, vol. 25, p. 166001, Apr. 2013.

[122] A. Salehi-Khojin, D. Estrada, K. Y. Lin, M.-H. Bae, F. Xiong, E. Pop, and R. I. Masel, "Polycrystalline Graphene Ribbons as Chemiresistors," *Advanced Materials*, vol. 24, pp. 53–57, Jan. 2012.

[123] S. Winters, T. Hallam, H. Nolan, and G. S. Duesberg, "Production of 3d-shaped graphene via transfer printing," *physica status solidi (b)*, vol. 249, pp. 2515–2518, Dec. 2012.

[124] T. Hallam, M. T. Cole, W. I. Milne, and G. S. Duesberg, "Microtransfer Printing: Field Emission Characteristics of Contact Printed Graphene Fins (Small 1/2014)," *Small*, vol. 10, pp. 94–94, Jan. 2014.

[125] J. He, P. Zhou, N. Jiao, S. Y. Ma, K. W. Zhang, R. Z. Wang, and L. Z. Sun, "Magnetic Exchange Coupling and Anisotropy of 3d Transition Metal Nanowires on Graphyne," *Scientific Reports*, vol. 4, p. 4014, Feb. 2014.

[126] L. Jiang, X. Zhao, and Y. Zheng, "RKKY interaction in graphene with a line defect," *Journal of Physics: Condensed Matter*, vol. 27, no. 4, p. 046003, 2015.

[127] T. L. Makarova, A. L. Shelankov, A. A. Zyrianova, A. I. Veinger, T. V. Tisnek, E. Lähderanta, A. I. Shames, A. V. Okotrub, L. G. Bulusheva, G. N. Chekhova, D. V. Pinakov, I. P. Asanov, and v. Šljivančanin, "Edge state magnetism in zigzag-interfaced graphene via spin susceptibility measurements," *Scientific Reports*, vol. 5, p. 13382, Aug. 2015.

[128] J.-H. Chen, G. Autés, N. Alem, F. Gargiulo, A. Gautam, M. Linck, C. Kisielowski, O. V. Yazyev, S. G. Louie, and A. Zettl, "Controlled growth of a line defect in graphene and implications for gate-tunable valley filtering," *Physical Review B*, vol. 89, p. 121407, Mar. 2014.

[129] P. Venezuela, R. B. Muniz, A. T. Costa, D. M. Edwards, S. R. Power, and M. S. Ferreira, "Emergence of local magnetic moments in doped graphene-related materials," *Physical Review B*, vol. 80, p. 241413, Dec. 2009.

[130] C. B. Crook, C. Constantin, T. Ahmed, J.-X. Zhu, A. V. Balatsky, and J. T. Haraldsen, "Proximity-induced magnetism in transition-metal substituted graphene," *Scientific Reports*, vol. 5, p. 12322, Aug. 2015.

[131] E. J. G. Santos, A. Ayuela, and D. Sánchez-Portal, "First-principles study of substitutional metal impurities in graphene: structural, electronic and magnetic properties," *New Journal of Physics*, vol. 12, no. 5, p. 053012, 2010.

[132] I. C. Gerber, A. V. Krasheninnikov, A. S. Foster, and R. M. Nieminen, "A first-principles study on magnetic coupling between carbon adatoms on graphene," *New Journal of Physics*, vol. 12, p. 113021, Nov. 2010.

[133] E. J. G. Santos, D. Sánchez-Portal, and A. Ayuela, "Magnetism of substitutional Co impurities in graphene: Realization of single π vacancies," *Physical Review B*, vol. 81, p. 125433, Mar. 2010.

[134] F. M. Hu, L. Kou, and T. Frauenheim, "Controllable magnetic correlation between two impurities by spin-orbit coupling in graphene," *Scientific Reports*, vol. 5, p. 8943, Mar. 2015.

[135] U. Kaiser, A. Schwarz, and R. Wiesendanger, "Magnetic exchange force microscopy with atomic resolution," *Nature*, vol. 446, pp. 522–525, Mar. 2007.

[136] F. Meier, L. Zhou, J. Wiebe, and R. Wiesendanger, "Revealing Magnetic Interactions from Single-Atom Magnetization Curves," *Science*, vol. 320, pp. 82–86, Apr. 2008.

[137] L. Zhou, J. Wiebe, S. Lounis, E. Vedmedenko, F. Meier, S. Blügel, P. H. Dederichs, and R. Wiesendanger, "Strength and directionality of surface Ruderman Kittel Kasuya Yosida interaction mapped on the atomic scale," *Nature Physics*, vol. 6, pp. 187–191, Mar. 2010.

[138] C. F. Hirjibehedin, C. P. Lutz, and A. J. Heinrich, "Spin Coupling in Engineered Atomic Structures," *Science*, vol. 312, pp. 1021–1024, May 2006.

[139] A. A. Khajetoorians, J. Wiebe, B. Chilian, S. Lounis, S. Blügel, and R. Wiesendanger, "Atom-by-atom engineering and magnetometry of tailored nanomagnets," *Nature Physics*, vol. 8, pp. 497–503, June 2012.

[140] Y.-C. Lin, P.-Y. Teng, P.-W. Chiu, and K. Suenaga, "Exploring the Single Atom Spin State by Electron Spectroscopy," *Physical Review Letters*, vol. 115, p. 206803, Nov. 2015.

[141] D. F. Kirwan, C. G. Rocha, A. T. Costa, and M. S. Ferreira, "Sudden decay of indirect exchange coupling between magnetic atoms on carbon nanotubes," *Physical Review B*, vol. 77, p. 085432, Feb. 2008.

[142] E. Šimánek and B. Heinrich, "Gilbert damping in magnetic multilayers," *Physical Review B*, vol. 67, p. 144418, Apr. 2003.

[143] F. S. M. Guimarães, A. T. Costa, R. B. Muniz, and D. L. Mills, "Spin currents in metallic nanostructures: Explicit calculations," *Physical Review B*, vol. 84, p. 054403, Aug. 2011.

[144] F. S. M. Guimarães, A. T. Costa, R. B. Muniz, and M. S. Ferreira, "Graphene as a non-magnetic spin current lens," *Journal of Physics: Condensed Matter*, vol. 23, no. 17, p. 175302, 2011.

[145] A. A. Khajetoorians, S. Lounis, B. Chilian, A. T. Costa, L. Zhou, D. L. Mills, J. Wiebe, and R. Wiesendanger, "Itinerant Nature of Atom-Magnetization Excitation by Tunneling Electrons," *Physical Review Letters*, vol. 106, p. 037205, Jan. 2011.

[146] F. S. M. Guimarães, A. T. Costa, R. B. Muniz, and M. S. Ferreira, "Graphene-based spin-pumping transistor," *Physical Review B*, vol. 81, p. 233402, June 2010.

[147] F. S. M. Guimarães, D. F. Kirwan, A. T. Costa, R. B. Muniz, D. L. Mills, and M. S. Ferreira, "Carbon nanotube: A low-loss spin-current waveguide," *Physical Review B*, vol. 81, p. 153408, Apr. 2010.

[148] Y. Zhang, Y.-W. Tan, H. L. Stormer, and P. Kim, "Experimental observation of the quantum Hall effect and Berry's phase in graphene," *Nature*, vol. 438, pp. 201–204, Nov. 2005.

[149] K. S. Novoselov, A. K. Geim, S. V. Morozov, D. Jiang, M. I. Katsnelson, I. V. Grigorieva, S. V. Dubonos, and A. A. Firsov, "Two-dimensional gas of massless Dirac fermions in graphene," *Nature*, vol. 438, pp. 197–200, Nov. 2005.

[150] B. Ludbrook, G. Levy, P. Nigge, M. Zonno, M. Schneider, D. Dvorak, C. Veenstra, S. Zhdanovich, D. Wong, P. Dosanjh, C. Straßer, A. Stohr, S. Forti, C. Ast, U. Starke, and A. Damascelli, "Evidence for superconductivity in Li-decorated monolayer graphene," *arXiv:1508.05925 [cond-mat]*, Aug. 2015. arXiv: 1508.05925.

[151] C. Xu, H. Li, and K. Banerjee, "Graphene nano-ribbon (GNR) interconnects: A genuine contender or a delusive dream?," in *Electron Devices Meeting, 2008. IEDM 2008. IEEE International*, pp. 1–4, Dec. 2008.

[152] Z. Li, H. Qian, J. Wu, B.-L. Gu, and W. Duan, "Role of Symmetry in the Transport Properties of Graphene Nanoribbons under Bias," *Physical Review Letters*, vol. 100, p. 206802, May 2008.

[153] N. Gorjizadeh, A. A. Farajian, and Y. Kawazoe, "The effects of defects on the conductance of graphene nanoribbons," *Nanotechnology*, vol. 20, no. 1, p. 015201, 2009.

[154] Y. Wu and P. A. Childs, "Conductance of Graphene Nanoribbon Junctions and the Tight Binding Model," *Nanoscale Research Letters*, vol. 6, p. 62, Oct. 2010.

[155] M. Koch, F. Ample, C. Joachim, and L. Grill, "Voltage-dependent conductance of a single graphene nanoribbon," *Nature Nanotechnology*, vol. 7, pp. 713–717, Nov. 2012.

[156] J. Baringhaus, M. Ruan, F. Edler, A. Tejeda, M. Sicot, Taleb-IbrahimiAmina, A.-P. Li, Z. Jiang, E. H. Conrad, C. Berger, C. Tegenkamp, and W. A. de Heer, "Exceptional ballistic transport in epitaxial graphene nanoribbons," *Nature*, vol. 506, pp. 349–354, Feb. 2014.

[157] R. Stine, J. T. Robinson, P. E. Sheehan, and C. R. Tamanaha, "Real-Time DNA Detection Using Reduced Graphene Oxide Field Effect Transistors," *Advanced Materials*, vol. 22, pp. 5297–5300, Dec. 2010.

[158] N. Gorjizadeh, A. A. Farajian, K. Esfarjani, and Y. Kawazoe, "Spin and band-gap engineering in doped graphene nanoribbons," *Physical Review B*, vol. 78, p. 155427, Oct. 2008.

[159] T. C. Li and S.-P. Lu, "Quantum conductance of graphene nanoribbons with edge defects," *Physical Review B*, vol. 77, p. 085408, Feb. 2008.

[160] E. R. Mucciolo, A. H. Castro Neto, and C. H. Lewenkopf, "Conductance quantization and transport gaps in disordered graphene nanoribbons," *Physical Review B*, vol. 79, p. 075407, Feb. 2009.

[161] J. Wilhelm, M. Walz, and F. Evers, "*Ab-initio* spin-flip conductance of hydrogenated graphene nanoribbons: Spin-orbit interaction and scattering with local impurity spins," *Physical Review B*, vol. 92, p. 014405, July 2015.

[162] A. A. Sagade, D. Neumaier, D. Schall, M. Otto, A. Pesquera, A. Centeno, A. Z. Elorza, and H. Kurz, "Highly air stable passivation of graphene based field effect devices," *Nanoscale*, vol. 7, pp. 3558–3564, Feb. 2015.

[163] G. Lu, L. E. Ocola, and J. Chen, "Gas detection using low-temperature reduced graphene oxide sheets," *Applied Physics Letters*, vol. 94, p. 083111, Feb. 2009.

[164] F. Schedin, A. K. Geim, S. V. Morozov, E. W. Hill, P. Blake, M. I. Katsnelson, and K. S. Novoselov, "Detection of individual gas molecules adsorbed on graphene," *Nature Materials*, vol. 6, pp. 652–655, Sept. 2007.

[165] J. T. Robinson, F. K. Perkins, E. S. Snow, Z. Wei, and P. E. Sheehan, "Reduced Graphene Oxide Molecular Sensors," *Nano Letters*, vol. 8, pp. 3137–3140, Oct. 2008.

[166] J. W. Mintmire, B. I. Dunlap, and C. T. White, "Are fullerene tubules metallic?," *Physical Review Letters*, vol. 68, pp. 631–634, Feb. 1992.

[167] C. T. White, D. H. Robertson, and J. W. Mintmire, "Helical and rotational symmetries of nanoscale graphitic tubules," *Physical Review B*, vol. 47, pp. 5485–5488, Mar. 1993.

[168] M. P. L. Sancho, J. M. L. Sancho, and J. Rubio, "Quick iterative scheme for the calculation of transfer matrices: application to Mo (100)," *Journal of Physics F: Metal Physics*, vol. 14, pp. 1205–1215, May 1984.

[169] P. Lloyd, "Wave propagation through an assembly of spheres: II. the density of single-particle eigenstates," *Proceedings of the Physical Society*, vol. 90, pp. 207–216, Jan. 1967.

[170] A. T. Costa, D. F. Kirwan, and M. S. Ferreira, "Indirect exchange coupling between magnetic adatoms in carbon nanotubes," *Physical Review B*, vol. 72, p. 085402, Aug. 2005.

[171] D. A. Abanin, S. V. Morozov, L. A. Ponomarenko, R. V. Gorbachev, A. S. Mayorov, M. I. Katsnelson, K. Watanabe, T. Taniguchi, K. S. Novoselov, L. S. Levitov, and A. K. Geim, "Giant Nonlocality Near the Dirac Point in Graphene," *Science*, vol. 332, pp. 328–330, Apr. 2011.

[172] B. Heinrich, Y. Tserkovnyak, G. Woltersdorf, A. Brataas, R. Urban, and G. E. W. Bauer, "Dynamic exchange coupling in magnetic bilayers," *Physical Review Letters*, vol. 90, p. 187601, May 2003.

[173] M. V. Costache, S. M. Watts, C. H. van der Wal, and B. J. van Wees, "Electrical detection of spin pumping: dc voltage generated by ferromagnetic resonance at ferromagnet/nonmagnet contact," *Physical Review B*, vol. 78, p. 064423, Aug. 2008.

[174] N. Tombros, C. Jozsa, M. Popinciuc, H. T. Jonkman, and B. J. van Wees, "Electronic spin transport and spin precession in single graphene layers at room temperature," *Nature*, vol. 448, pp. 571–574, Aug. 2007.

[175] F. J. Culchac, A. Latgé, and A. T. Costa, "Spin waves in graphene nanoribbon devices," *Physical Review B*, vol. 86, p. 115407, Sept. 2012.

[176] R. Kubo, "Statistical-Mechanical Theory of Irreversible Processes. I. General Theory and Simple Applications to Magnetic and Conduction Problems," *Journal of the Physical Society of Japan*, vol. 12, pp. 570–586, June 1957.

[177] L. H. M. Barbosa, R. B. Muniz, A. T. Costa, and J. Mathon, "Spin waves in ultrathin ferromagnetic overlayers," *Physical Review B*, vol. 63, p. 174401, Mar. 2001.

[178] R. B. Muniz and D. L. Mills, "Theory of spin excitations in Fe(110) monolayers," *Physical Review B*, vol. 66, p. 174417, Nov. 2002.

[179] J. F. Cooke, "Neutron Scattering from Itinerant-Electron Ferromagnets," *Physical Review B*, vol. 7, pp. 1108–1116, Feb. 1973.

[180] J. F. Cooke, J. W. Lynn, and H. L. Davis, "Calculations of the dynamic susceptibility of nickel and iron," *Physical Review B*, vol. 21, pp. 4118–4131, May 1980.

[181] H. Tang, M. Plihal, and D. L. Mills, "Theory of the spin dynamics of bulk Fe and ultrathin Fe(100) films," *Journal of Magnetism and Magnetic Materials*, vol. 187, pp. 23–46, Aug. 1998.

[182] R. B. Muniz and D. L. Mills, "Local spin dynamics of magnetic moments on metal surfaces," *Physical Review B*, vol. 68, p. 224414, Dec. 2003.

[183] P. A. Lee and D. S. Fisher, "Anderson Localization in Two Dimensions," *Physical Review Letters*, vol. 47, pp. 882–885, Sept. 1981.

[184] J. Mathon, A. Umerski, and M. Villeret, "Oscillations with Co and Cu thickness of the current-perpendicular-to-plane giant magnetoresistance of a Co/Cu/Co(001) trilayer," *Physical Review B*, vol. 55, pp. 14378–14386, June 1997.